LEWIS AND BRØNSTED ACIDIC HOMOGENEOUS CATALYSIS FOR C–O BOND REDUCTION AND LATE-STAGE NATURAL PRODUCT FUNCTIONALIZATION

Anton I. Gudz

A dissertation submitted to the faculty at the University of North Carolina at Chapel Hill in partial fulfillment of the requirements for the degree of Doctor of Philosophy in the Department of Chemistry.

Chapel Hill
2020

Approved by:

Michel R. Gagné

Marcey L. Waters

Maurice S. Brookhart

Frank A. Leibfarth

Abigail S. Knight

© 2020
Anton I. Gudz
ALL RIGHTS RESERVED

ABSTRACT

Anton I. Gudz: Lewis and Brønsted Acidic Homogeneous Catalysis for C–O Bond Reduction and Late-stage Natural Product Functionalization
(Under the direction of Michel R. Gagné)

Diminishing fossil fuel resources and growing environmental concerns require the development of alternative methods for sustainable production of fine chemicals and pharmaceutically relevant compounds. Biomass and natural product resources constitute a large reservoir of organic carbon (C–O bonds) that can be converted into commodity chemicals or drug candidates on an industrially applicable scale. This dissertation aims to explore various homogeneous catalytic methods that help attain this goal.

The main objective of this work is to add to the existing methodology in the field of selective catalytic C–O bond reductions. Due to the complex regio- and chemoselectivities associated with these reactions, it is difficult to design and control such systems. In this vein, several Lewis and Brønsted acidic homogenous catalysts have emerged to allow for C–O bond reduction, and often subsequent generation of structural complexity.

The first half of this dissertation explores the fundamental reactivity of existing boron-based systems, specifically studying tris(pentafluorophenyl)borane $B(C_6F_5)_3$ as the primary workhorse catalyst. Silyl-phosphonium ions are explored as new silylium ion carriers in the modified Piers hydrosilylation catalytic cycle. This adds depth to the existing pool of knowledge, providing alternatives for chemoselective C–O bond reductions.

The second half of this work pushes the boundaries of late-stage natural product functionalization field by exploring catalytic methods to discover new molecules. Bioactive

natural products are used extensively with Lewis and Brønsted acids and nucleophiles to generate previously unreported molecular scaffolds. These new structures likely possess biological activity different from their parent molecules, making them ideal early candidates for biological assays.

Ultimately, the results presented benefit both the synthetic inorganic and organic catalysis communities, as well as the biological and pharmaceutical chemists studying natural products as potential drug candidates.

ACKNOWLEDGEMENTS

First and foremost, I would like to thank Dr. Mike Gagné for his support over the past five years to my education as an aspiring young researcher. Mike truly inspired me with his enthusiasm for science and continued encouragement, not making grad school feel like a never-ending grind. Mike's door is always open (literally), and he always has his students' best interests in mind, allowing us to pursue our endeavors.

I would also like to express my gratitude to the fellow graduate students and postdocs that I have worked with throughout my time in the lab. Pippa and Jen, Trandon and Brandon, Chrissy and Peruzzi have all helped me greatly in the beginning stages of my path, always being just a text message or a happy-hour wings trip away. Jared and Andreas have been with me at almost every step of the journey, helping me with a long list of bureaucratic checkpoints and interesting career discussions. The more recent lab members – Nick, Hannah, Neyen, Kat, and Eric – have all made life in the lab always vibrant and upbeat. Youngran Seo also deserves a special thank you for her willing nature and patience to discuss science and collaborate on a couple of challenging projects.

I would like to thank several people from my abroad research stint in Strasbourg, France in the lab of Dr. Joseph Moran. Thank you, Joseph, for welcoming me into your lab and allowing me to tap into your lab's expertise and resources far away from home. A special thank you goes to Moran lab members Lucas, Elodie, Paul, and Kamila who made me feel accepted and helped me adapt to life in France while also introducing new perspectives on science and on life. Thank you also to Jing, Shaofei, Flo, Sreejith, Vuk, Artem, and Abidjith for your willingness to help me through many helpful discussions.

In addition, I would like to mention my friends and roommates, who helped me adjust to life at UNC and made Chapel Hill feel like home. Thank you Tarun, Jared, Andrew, Eli, Jefferson, Kevin and David for putting up with me over the years. Also, a special thanks to Henry for choosing to come to UNC and to live at the house.

I am especially grateful to my cousin, Ryan Cody, for being there for me throughout my UNC journey and for inspiring me to challenge myself and succeed at any of my endeavors.

I would also like to thank my family, who have supported me each step of my life. My stepfather, Richard Cody, has been nothing but a tremendous positive influence on my personal and intellectual growth as a young man in a new country since the day I stepped foot on US soil.

Most importantly, my mother has always been my number one supporter. She has always pushed me to be a better, mentally stronger person, and for that there's not enough gratitude in the world.

TABLE OF CONTENTS

LIST OF TABLES

LIST OF SCHEMES

LIST OF FIGURES

LIST OF ABBREVIATIONS AND SYMBOLS

°C	degrees Celsius
Å	Angstroms
Ac	acetyl
aq	aqueous
$BAr_{2,4,6\text{-}F}$	tris(2,4,6-trifluorophenyl)borane
$BAr_{3,5\text{-}CF3}$	tris[3,5-bis(trifluoromethyl)phenyl]borane
BCF	tris(pentafluorophenyl)borane
Bn	benzyl
Bz	benzoate
C-PCM	conductor-like polarizable continuum model
δ	delta – chemical shift (NMR)
d	doublet
DCM	dichloromethane
DFT	density functional theory
DHMF	dihydrohydroxymethylfuran
DMSO	dimethylsulfoxide
E	electronic energy (density functional theory)
eq.	equivalent

equiv.	equivalent
Et	ethyl
EtOAc	ethyl acetate
FID	flame ionization detection (in gas chromatography)
FLP	frustrated Lewis pair
g	gram
GC	gas chromatography
GCMS	gas chromatography – mass spectrometry
Gibb	gibberellic acid
h	hour
HBCat	catecholborane
HFIP	hexafluoroisopropanol
HMB	hexamethylbenzene
HMF	hydroxymethylfurfural
HRMS	high resolution mass spectrum
Hz	hertz (NMR coupling constants)
K	Kelvin
L	liter

LA	Lewis acid
LSF	late-stage functionalization
M	molar – 1 mol / liter (concentration)
Me	methyl
MeOH	methanol
mg	milligram
MHz	megahertz
μL	microliter
mL	milliliter
mm	millimeter
min	minute
mmol	millimole (10^{-3} mol)
mol %	mole percent (catalyst loading)
m/z	mass-to-charge ration (mass spectrometry)
NMR	nuclear magnetic resonance
NW	northwest (direction)
Ph	phenyl
PPh_3	triphenylphosphine

ppm	part per million (NMR relative difference)
q	quartet (NMR)
R	any unspecified carbon-containing group
rt	room temperature
s	singlet (NMR)
Si-Gibb	silyl-protected gibberellic acid
t	triplet (NMR)
TES	triethylsilyl
TfOH	trifluoromethanesulfonic acid
THP	tetrahydropyran
TMS	trimethylsilyl
TMS-Me-Gibb	trimethylsilyl-protected methylated ester gibberellic acid

Chapter 1 – Introduction

1.1. Recent outlook and motivation

Diminishing fossil fuel resources, uncertain future supplies, and growing environmental concerns require the development of alternative methods for sustainable production of fuels, fine chemicals, and pharmaceutically relevant compounds.[1,2] Biomass and natural product resources constitute a large reservoir of renewable organic carbon (C–O bonds) that can be converted into commodity chemicals or drug candidates on an industrially applicable scale. Recently, it has been shown that biomass-derived small molecules can serve as chiral synthons for use in fine chemical synthesis applications,[3] while modified natural products are excellent candidates for facile development of bioactive drug compounds.[4–6]

One of the main challenges, and opportunities, in biomass and natural product modification field has been selective C–O bond reduction.[7] Removing or activating certain C–O bonds while leaving the others untouched allows for rapid generation of structural molecular complexity without having to adopt the traditional "ground up" approach that starts with simple small molecules or hydrocarbons. However, due to the complex regio- and chemoselectivities associated with C–O bond activation, it is challenging to design and control such systems. In this vein, novel catalytic methods have recently emerged to allow chemists to overcome some of the chemoselectivity problems associated with these challenging reactions. Lewis and Brønsted acidic homogenous catalysis, in particular, has been prominent in such undertakings.

1.2. Complete C–O bond reduction systems in place

While there are catalytic methods, both homogeneous and heterogeneous, to remove oxygen content from biomass, many of them result in complete deoxygenation of the parent structures. Experiments conducted by Dumesic and Huber,[8,9] for example, have relied on heterogeneous catalysis with solid-supported acid and a metal center to convert sorbitol to alkanes in water.[10] Chen et. al used a homogeneous N-heterocyclic carbene-catalyzed self-condensation reaction to dimerize the partially oxygenated hydroxymethylfurfural (HMF) to dihydrohydroxymethylfuran (DHMF), followed by metal-catalyzed hydrodeoxygenation to yield C_{12} jet fuel hydrocarbons.[11,12] Similarly, Toste et. al turned to a Rhenium-based system for dehydration of sorbitol to afford unsaturated hydrocarbons and aromatic compounds (Figure 1.1).[13]

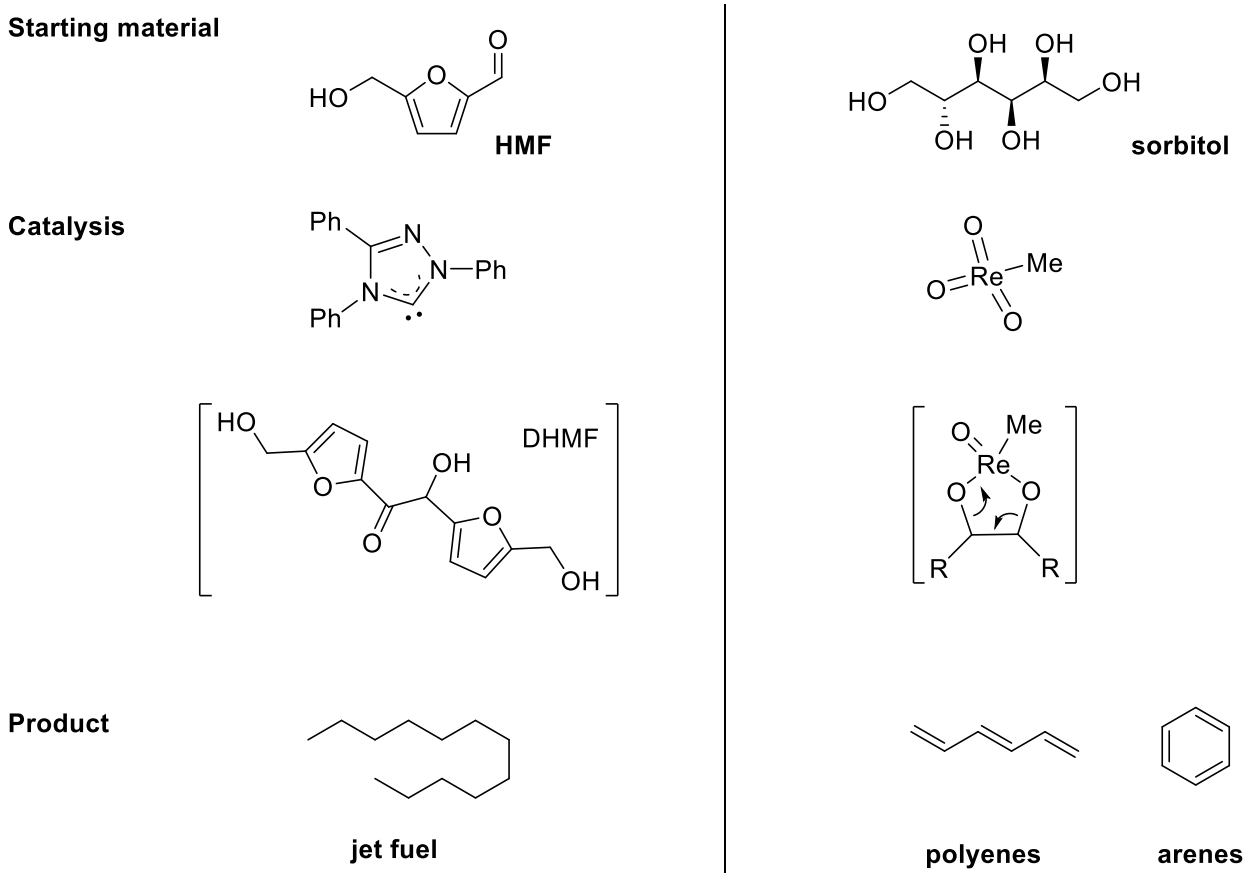

Figure 1.1. Catalytic deoxygenation of C–O bonds in biomass substrates

1.3. Lewis acid catalyzed hydrosilylation of C–O bonds

With a similar (biomass reduction) goal in mind, the Gagné lab has turned to hydrosilylation reactions aiming to transform C–O bonds to C–H bonds in sugar-derived structures, and later, in natural products.[3,5] Using a silane source as a reductant allows for heterolytic splitting of the Si–H bond and the subsequent use of the generated silylium ion as an activator and the hydride as the reducing agent.

Initial reports on Lewis acid-catalyzed hydrosilylation required stoichiometric quantities of Lewis acids to activate C–O bonds, making such systems atom-inefficient.[14,15] In these reactions, the role of the Lewis acid (LA), shown in Figure 1.2, is to increase the polarization of the C–O upon coordination, making the carbon center more electrophilic and thus more susceptible toward nucleophilic attack. For example, Lewis acid BF_3•OEt_2 was used to carry out such hydrosilylation.

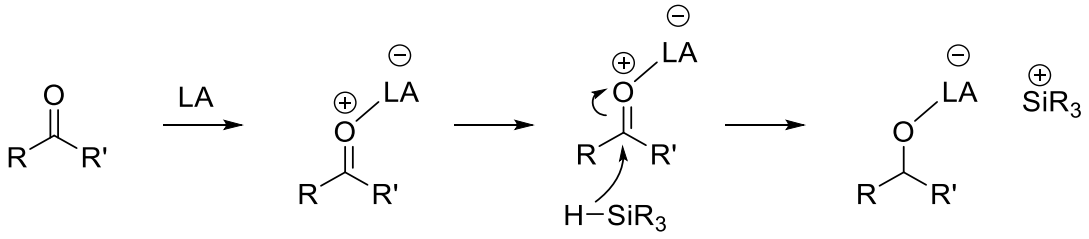

Figure 1.2. Lewis acid hydrosilylation of carbonyls

The BF_3•OEt_2 system has also shown excellent activity in stoichiometric reduction of alcohols to hydrocarbons, with selectivity preference for tertiary C–O bonds over the secondary and the primary ones.[16] This reactivity trend highlights the importance of building up and stabilizing positive charge at the reduction site prior to the nucleophilic attack. In the quest to render these types of systems catalytic, a number of both metal-based and metal-free catalysts have been studied since this method's initial inception, leading to many exciting developments in the field of C–O reduction catalysis.

As mentioned above, a powerful example of such Lewis acid catalytic system in action was demonstrated by Gagné et. al, when a homogeneous Iridium catalyst was successfully employed in conjunction with excess Et_2SiH_2 to completely deoxygenate glucose and generate saturated hydrocarbons (Figure 1.3).[17]

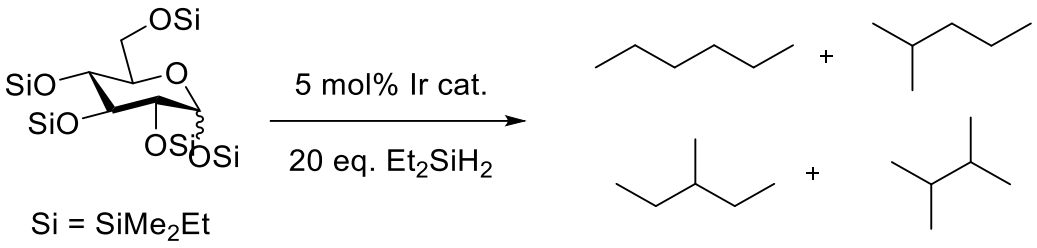

Figure 1.3. Iridium-catalyzed complete glucose deoxygenation

While this work is an excellent demonstration of the hydrosilylative chemistry, partial deoxygenation of the starting materials still remained elusive. Maintaining at least some of the stereocenters found in biomass derivatives or natural product starting materials would result in more useful partially oxygenated products for the synthesis of pharmaceuticals, high-value synthetic precursors, or commodity chemicals.

1.4. Progress towards partial and selective C–O deoxygenation

In recent years, Lewis acidic catalyst tris(pentafluorophenyl)borane $B(C_6F_5)_3$ (BCF) has received much attention in projects aimed towards selective C–O bond reductions.[18] Pioneering work on hydrosilylation of aldehydes, ketones, and esters was conducted in the late 1990's by both the Piers[19,20] and the Yamamoto[21] research groups. Piers et. al have initially demonstrated the reduction of aldehydes and ketones to alcohols by BCF and Ph_3SiH. In these experiments, the rate of substrate reduction to the corresponding silyl protected alcohol followed a trend: ethyl benzoate >> acetophenone > benzaldehyde. While first considering a mechanism consistent with the

classical Lewis-acid catalyzed hydrosilylation similar to the BF_3•OEt_2 system, an inverse dependence of reaction rate on the substrate concentration was observed (Figure 1.4).

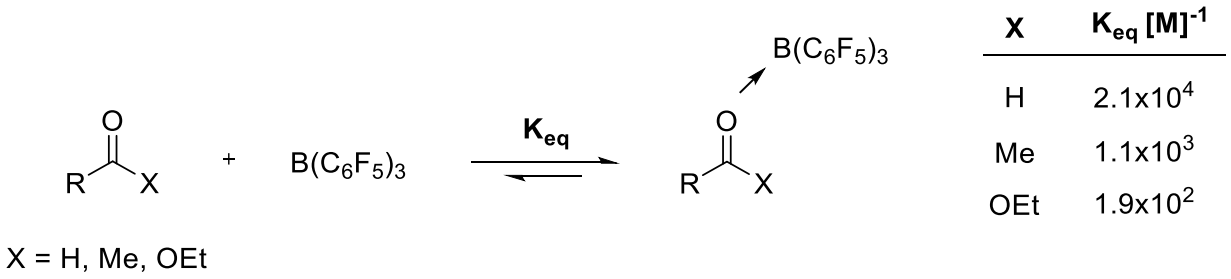

X	K_{eq} $[M]^{-1}$
H	$2.1x10^4$
Me	$1.1x10^3$
OEt	$1.9x10^2$

Figure 1.4. Carbonyl-BCF stabilities and K_{eq} constants

Since the stoichiometric hydrosilylation mechanism requires the formation of the Lewis acid-substate adduct prior to the C–O bond reduction, this inverse rate dependence observation pointed to a change in the mechanism. The most rapidly reduced substrate, ethyl benzoate, had the lowest calculated equilibrium constant K_{eq}, indicating that an alternate silane activation pathway was occurring. Thus, instead of the catalyst binding to the C–O bond of the substrate, it was proposed that the boron center of BCF activates the silane directly (Figure 1.5).

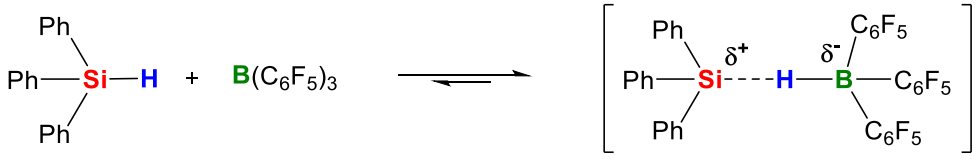

Figure 1.5. Proposed silane activation pathway by BCF

This proposed silane activation route, later supported by several in-depth mechanistic experiments,[22] involves generation of a transient borane/silane adduct and subsequent heterolytic cleavage of the Si–H bond. It is discussed in detail in the following sections.

1.5. BCF catalysis and the Piers mechanism

The true potential of BCF and related fluoroarylborane reagents is the balance of hydride affinity/electrophilicity with a muted oxophilicity that enables transformations in functional group

rich environments.[23] Following the initial groundbreaking Piers report, the latest examples report high selectivities and yields for such important organic transformations as selective reductions of carboxylic acids to aldehydes (Scheme 1.1)[24] via the Si–H bond activation mechanism introduced in Section 1.4 and detailed further in Figure 1.6.[3]

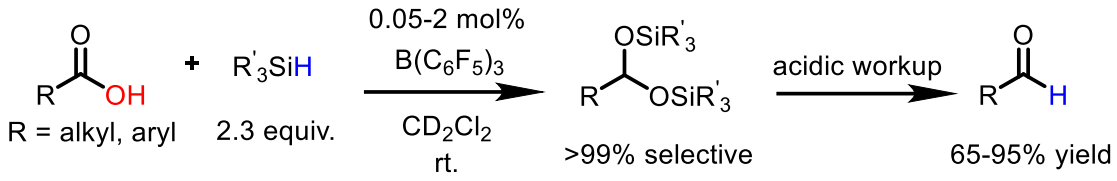

Scheme 1.1. Reduction of carboxylic acids to aldehydes

In the Piers mechanism, the key intermediate for BCF-activation of a silane is the weak BCF--H–SiR_3 adduct (**1**, Figure 1.6), which is susceptible to nucleophilic attack at Si by a Lewis base (e.g. ether or carbonyl) to generate a reactive ion pair composed of an $H–B(C_6F_5)_3^-$ nucleophile and a $R_3Si–LB^+$ electrophile. Their recombination leads to C–O reduction. This mechanistic scheme has been supported by the isolation of the BCF-silane adduct with an exceptionally electrophilic version of BCF,[25] by stereochemical studies demonstrating that attack of the Lewis base is invertive at Si,[26] and by computational studies of ketone hydrosilylation.[27]

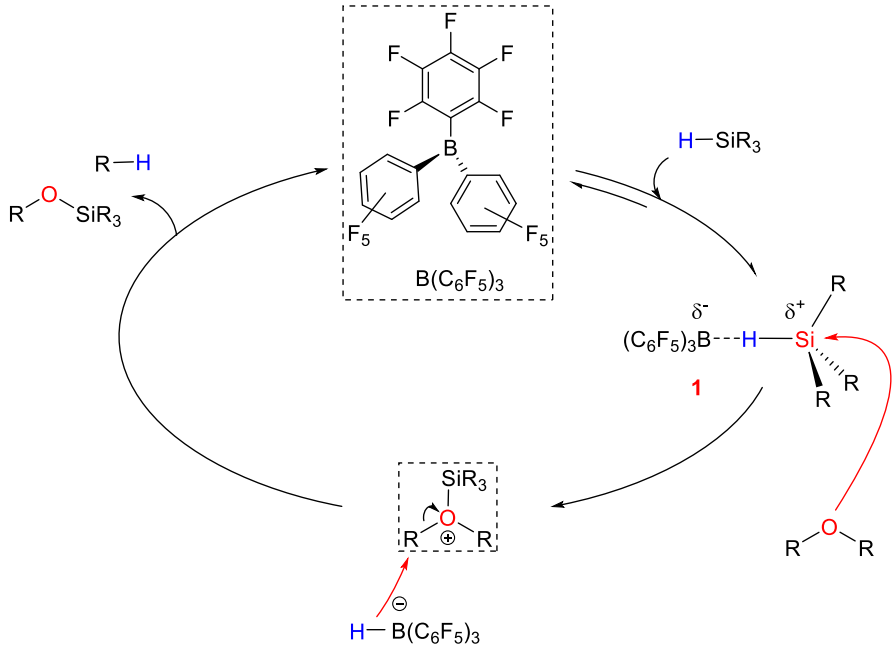

Figure 1.6. BCF-catalyzed reduction of ethers via the Piers mechanism

1.6. Frustrated Lewis pairs

As the chemistry of BCF and its catalytic potential continued to evolve, the concept of frustrated Lewis pairs (FLPs) involving fluoroarylboranes has also come to the forefront as a productive methodology for catalytic heterolytic activation of reactants such as H_2[28] or R_3SiH.[29] An FLP is a compound or mixture containing a Lewis acid and a Lewis base component that cannot combine to form a classical adduct due to steric hindrance.[30] Certain combinations of such Lewis acids and bases lead to small molecule activation, such as splitting H_2. Fluoroarylborane catalysts, led by BCF, generally constitute the Lewis acidic component of the reported FLPs, while nitrogen and phosphine-derived compounds serve as the Lewis basic partners. Such systems have been utilized extensively in a wide variety of applications,[31] including catalytic hydrogenation of imines[32] and carbonyls,[33] and the hydrosilylation of carbonyls,[19,34] ethers,[21] imines,[35–37] pyridines,[38] and enones.[39]

When it comes to C–O bond reductions, many new FLP-type systems have shown superb chemoselectivities in reactions on complex biomass-derived sugars,[3,40,41] ether-containing alkyl tosylates,[42] and even natural products.[5] Rapid development of this chemistry called for a more in-depth look at the fundamental concepts initially established in the field, thus prompting the study reported in Chapter 2 of this work analyzing the phosphine-modified version of the Piers catalytic cycle.

1.7. Phosphine-modified Piers mechanism

Highlighting its unique reactivity, BCF and its variants can mediate chemoselective reductions in complex biomass molecule and natural product environments.[5] In these studies, it was noted that selectivity and functional group tolerance could be improved with phosphine additives. It was previously noted by Klankermayer,[32] and then Du,[43,44] that phosphine additives enhance turnover rates and selectivities for the enantioselective hydrosilylations of imines. The mechanistic role of added phosphine in the mediation of reactivity and selectivity was not well understood and presented an opportunity for catalyst development and optimization.

Extensive mechanistic investigations on the hydrosilylation of ethers have led to the Piers mechanism shown in Figure 1.6, where the BCF preferentially activates the Si–H bond of the silane via the borane-silane adduct. This activated borane-silane species transfers R_3Si^+ to the substrate to generate the undetectable ion pair $R_2O–SiR_3^+$ and $H–B(C_6F_5)_3^-$. The C–O bond of the silyl oxonium is then cleaved by $H–B(C_6F_5)_3^-$ to regenerate the BCF catalyst. Most of the catalyst thus speciates as free BCF and the ionic compounds are all reactive intermediates. In the phosphine modified version of this reaction, Klankermayer and co-workers have shown that the combination of a trialkyl silane, a moderately basic triaryl Mes_3P phosphine, and BCF will stoichiometrically ionize the silane into $H–B(C_6F_5)_3^-$ and $R_3Si–PMes_3^+$.[32] Although the mechanistic role of these

additives was not determined, it can be surmised that if the BCF/PR_3 pair is (at least partially) frustrated then an equilibrium accessible η^1-silane adduct of $B(C_6F_5)_3$ can react with free phosphine to yield the thermodynamically favorable ion pair.[45–47]

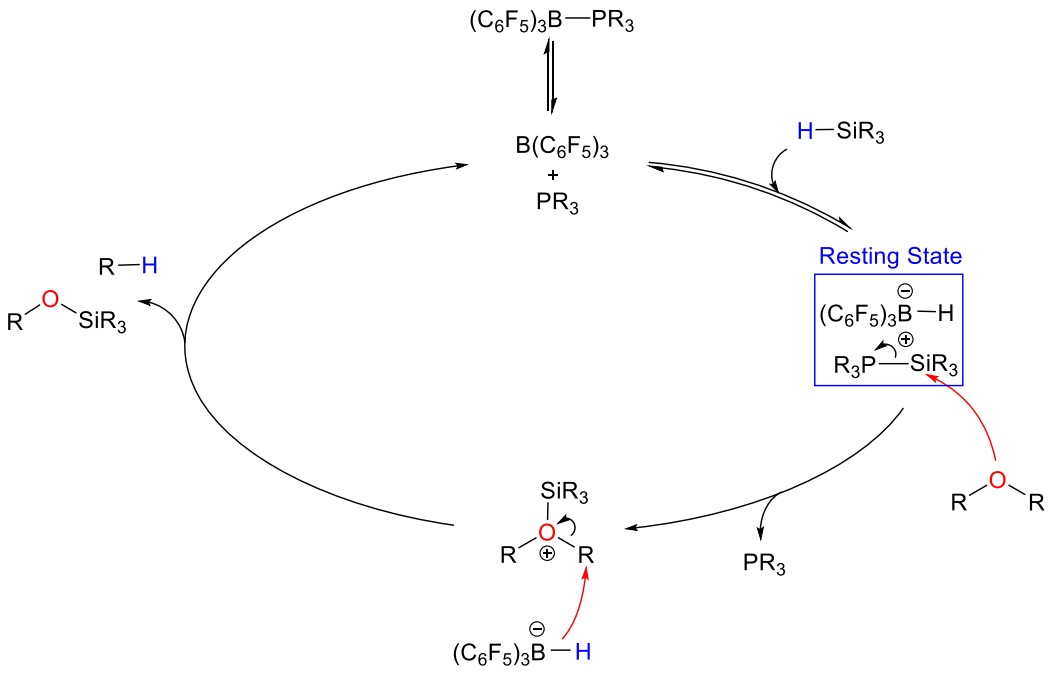

Figure 1.7. Proposed phosphine-modified Piers mechanism

Transfer of silylium ion from the phosphine to the imine substrate would generate a similarly activated substrate poised to undergo hydride attack. A mechanism for the reduction of ethers consistent with these observations is shown in Figure 1.7.

Further details of this mechanism, along with catalytic studies, are extensively discussed in Chapter 2. We performed stoichiometric, kinetic, and computational analyses of the silane activation component of this proposed phosphine-modified catalytic cycle, in combination with a full cycle analysis of the anisole reduction. Together, these data delineate the importance of silyl-phosphonium intermediates and the potential pitfalls of phosphine modified catalyst systems.

1.8. Late-stage functionalization of natural products

Recently, a novel research direction in the Gagné group has highlighted the utility of the Piers and the phosphine-modified Piers catalytic cycles in selective late-stage functionalization (LSF) of natural products.[5] This is an important new area because diversification of complex molecules provides important information on structure-activity relationships and optimized bioactivity of such molecules.[4,5] In fact, the main aim of the LSF strategy is to use natural products themselves to experimentally populate the chemical space surrounding each natural product. Doing so successfully would provide structurally similar, yet chemically distinct, molecules that can be studied in biological assays and beyond. Chemoselectivity in these transformations, much like in the case of aforementioned biomass experiments, is a significant challenge considering the complexity of a given natural product containing multiple functional groups. Targeting a specific part of a molecule while avoiding the diverse array of off-target reactive groups is not trivial and requires careful manipulations.[48]

Figure 1.8 demonstrates the LSF principle for the site-selective deoxygenation of erythromycin A (highlighted reduction sites), enabled either by a selectively-defining *O*-thiocarbonylation or -phosphitylation with a peptide catalyst.[49,50] This is an interesting application of the LSF strategy towards deoxygenation in that the desired transformation is achieved while preserving the core structural integrity of the parent molecule.

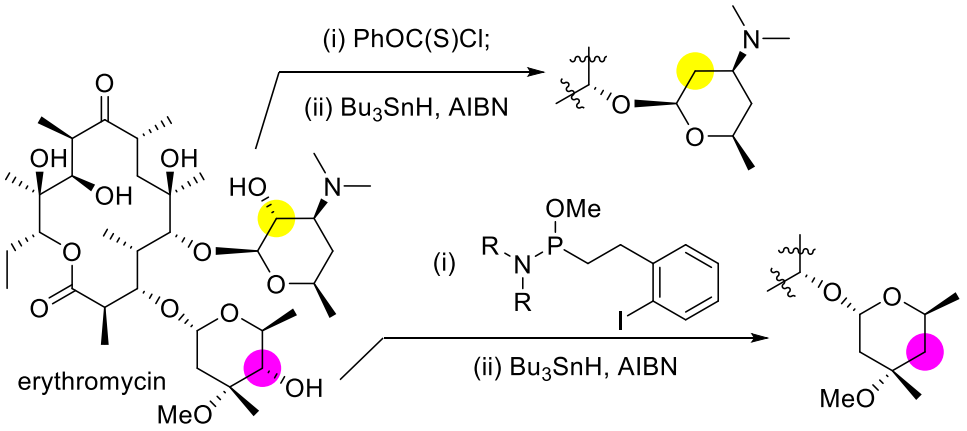

Figure 1.8. Late-stage functionalization of erythromycin

Metal catalysts for deoxygenation are also feasible as recently demonstrated for the ruthenium-catalyzed primary alcohol reduction of cholic alcohol (highlighted, Figured 1.9).[51]

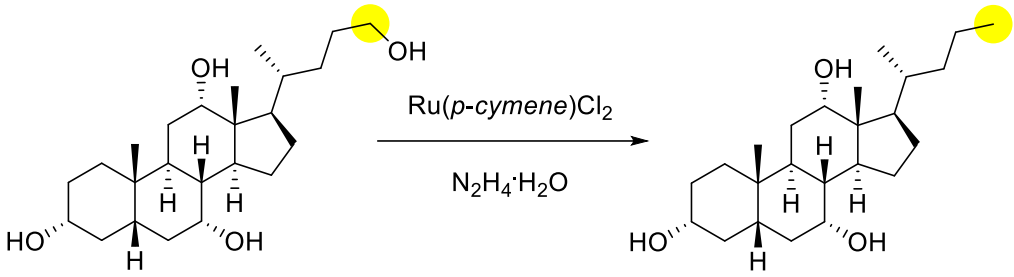

Figure 1.9. Ru-catalyzed deoxygenation of cholic alcohol

1.9. LSF of natural products via BCF catalysis

Both of the examples in Figure 1.8 and 1.9 are interesting applications of the LSF strategy, yet the catalytic approach is generally well-defined and does not involve the same chemoselectivity challenges as when a BCF/silane system is employed. This can be attributed to the fact that BCF/silane-driven transformations are unique in that silylium ions are typically very aggressive electrophiles and would seemingly be poor at facilitating selective chemistry on complex molecular scaffolds. However, the Gagné lab's recent work[5] shows that R_3Si^+ ions can be used to activate Lewis bases and carry out selective transformations on natural products as complex as gibberellic acid, dihydroartemisinin, and natamycin (Figure 1.10).

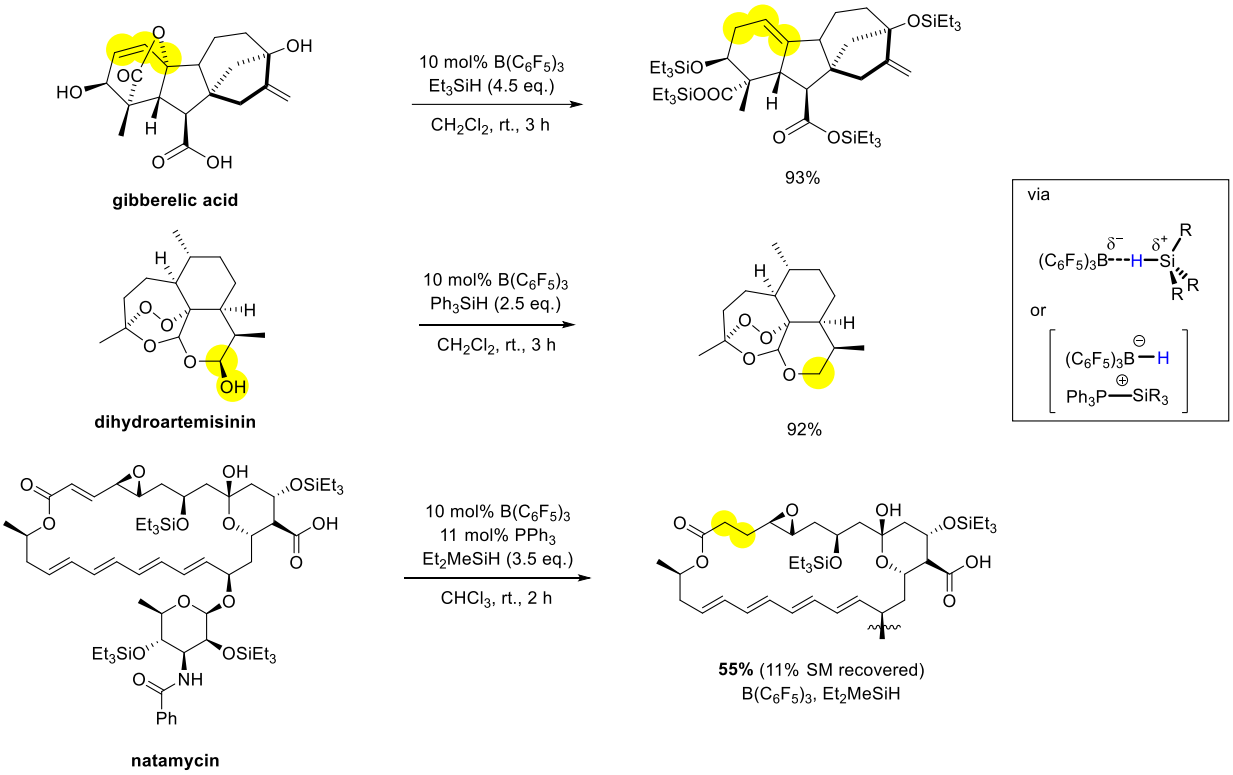

Figure 1.10. Chemoselective C–O bond reductions of natural products with BCF

As can be surmised from Figure 1.10, BCF-catalyzed hydrosilylative deoxygenations are achieved via chemoselective reduction of the hemiacetal of dihydroartemisinin or via the lactone ring opening of gibberellic acid with an accompanying allylic transposition. In the case of natamycin, a highly selective enoate conjugate reduction is achieved without affecting any of the other functional groups in the molecule, including the neighboring epoxide.[5] Studying these interesting phenomena is the focal point of Chapter 4 in this dissertation, with the results leading not only to discovery of new natural product derivatives but also to explanations and predictive strategies for the catalytic reactivity given a certain catalyst/reductant combination.

1.10. Selective catalysis with Brønsted acids

In addition to being a powerful Lewis acid catalyst, BCF has also been shown to act as a Brønsted acid in chemoselective reactions. Several examples of this have been demonstrated recently on a variety of substrates.[52] For example, Moran's work on the azidation of tertiary aliphatic alcohols in nitromethane is an important example of such Brønsted acidic activity (Figure 1.11).[53]

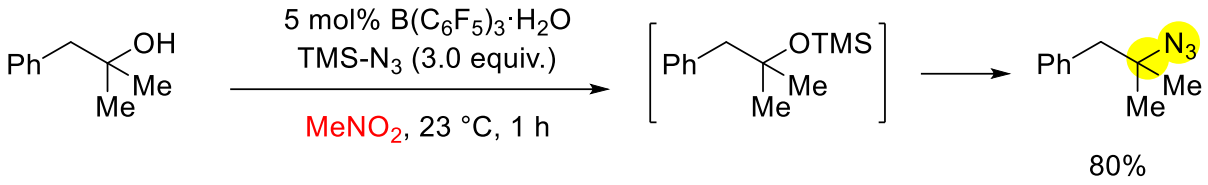

Figure 1.11. Azidation of tertiary aliphatic alcohols by BCF•H_2O

According to Moran's report, the active catalytic species is BCF•H_2O with nitromethane acting as the key co-catalyst. Unlike in the classical Piers mechanism-based chemistry above, the role of the Lewis acidic boron center is not to heterolytically active a silane, but to bind a molecule of water and provide an H^+ source for the catalytic reaction. In fact, IR experiments show evidence of hydrogen bonding between the OH of BCF•H_2O and the nitro compounds.[53] Further studying the Brønsted acidic catalytic systems proved fruitful in terms of diversifying molecular structures and activating C–O bonds of several biologically active substrates, with the details outlined in Chapter 3.

1.11. Selective TMS–X chemistry and new chemical space

In the greater context of LSF chemistry and catalysis, we explored the possibility of building novel molecular scaffolds, employing TMS–X type reagents to make new bonds. Moran's aforementioned work demonstrated an unprecedented example of co-catalysis between nitro compounds and Brønsted acids, resulting in the first azidation of tertiary aliphatic alcohols with

catalytic turnover.[53] While these results highlighted the utility of BCF•H_2O as a Brønsted acid catalyst, the substrate scope was fairly limited to tertiary aliphatic alcohols. Thus, we expanded this methodology onto complex natural product structures, highlighting the importance of facile BCF•H_2O catalysis and leading not only to selective C–O bond reductions, but also to the formation of novel C–X derivatives. Where possible, we carried out the comparison to the Lewis acid catalyzed systems, as well as other classical Brønsted acids not involving boron. Ultimately, the gathered results provide a synthetic toolbox for facile population of chemical space around a given bioactive compound.

1.12. Functional group reactivity ranking

Throughout relevant literature and this dissertation project itself, the LSF often resulted in (desired) excellent chemoselectivities and good yields for a host of new natural product derivatives. Despite this success, some of reported results were exciting serendipitous discoveries rather than targeted predetermined synthetic outcomes. Since a chemoselective reaction is inherently a competition between functional groups, baseline reactivity trends are needed to gain insight into the structure-activity relationships of the chosen natural products. Baseline kinetic data on simple small molecules provides important context for how structure can enhance or diminish reactivity. Changing the reaction conditions such as catalyst, reductant, or temperature also helps us gain important insights into the chemoselectivity trends observed in natural product reactions. Ultimately, the vast complexity and diversity of natural products mean that the reported reactivity trends vary on a case by case basis, but the baseline data can help in *a priori* selection of the catalyst/reductant combinations with the highest chance of success for a given structure or region of a molecule. As such, we conducted competition experiments with the BCF/silane system between various functional groups found in our previously analyzed natural products. These

experiments, discussed in Chapter 4, contextualize the prior deoxygenation and functionalization results and help with understanding the factors responsible for the observations of certain reactivities in the broader sense of BCF/silane C–O bond activation catalysis.

Chapter 2 – Phosphines as silylium ion carries for controlled C–O deoxygenation

2.1. Introduction and relevant background

As the potential of BCF and metal free catalysts in catalytic C–O reduction reactions has evolved, so has the need for fundamental analysis of the various aspects of such catalysis. In recent years, metal-free FLP catalysts have been utilized in a wide variety of applications,[31] with fluoroarylborane catalysts generally constituting the Lewis acidic component of such FLPs, while nitrogen and phosphine-derived compounds serve as the Lewis basic partners. Most recently, BCF and its derivatives have shown superb chemoselectivities in the deoxygenation of complex biomass-derived sugars,[3,40,41] ether-containing alkyl tosylates,[42] and natural products.[5]

Most recent examples highlighting the potential of BCF-based systems report high selectivities and yields for many important organic transformations, including selective reductions of carboxylic acids to aldehydes (Scheme 2.1).[24] This reaction occurs via a Si–H bond activation mechanism first described independently by Piers[19] and later supported by Yamamoto and co-workers (Figure 2.1).[21]

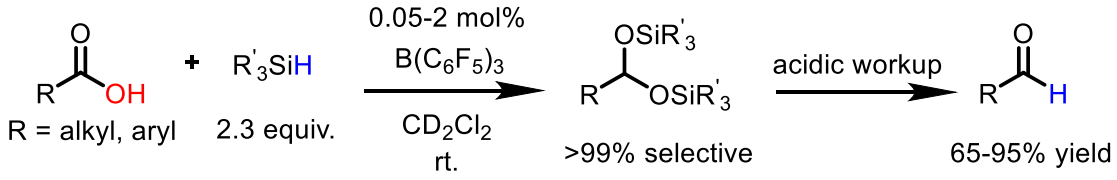

Scheme 2.1. Reduction of carboxylic acids to aldehydes with BCF

In the Piers mechanism, the key intermediate for BCF-activation of a silane is the weak BCF--H–SiR_3 adduct (**1**, Figure 2.1a), which is susceptible to nucleophilic attack at Si by a Lewis base (e.g. ether or carbonyl) to generate a reactive ion pair composed of an H–$B(C_6F_5)_3^-$ nucleophile and a R_3Si–LB^+ electrophile. Their recombination leads to C–O reduction. This mechanistic scheme has been supported by the isolation of the BCF-silane adduct with an exceptionally electrophilic version of BCF,[25] by stereochemical studies demonstrating that attack of the Lewis base is invertive at Si,[26] and by computational studies of ketone hydrosilylation.[27]

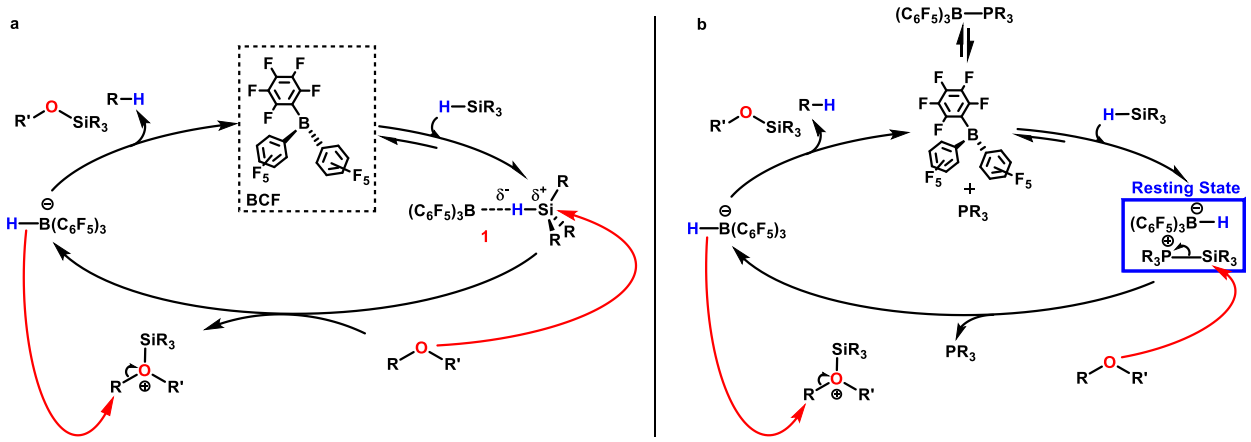

Figure 2.1. BCF or BCF/phosphine catalyzed reduction of ethers

Highlighting its unique reactivity, BCF and its variants can also mediate chemoselective reductions in complex natural product environments.[5] In these studies, it was noted that selectivity and functional group tolerance could be improved with phosphine additives. It was previously noted by Klankermayer,[32] and then Du,[43,44] that phosphine additives enhance turnover rates and selectivities for the enantioselective hydrosilylations of imines. The mechanistic role of added phosphine in the mediation of reactivity and selectivity was not well understood and presented an opportunity for catalyst development and optimization.

While extensive mechanistic investigations on the hydrosilylation of ethers have led to the mechanism in Figure 2.1a, the phosphine-modified cycle was yet to be extensively analyzed. In

the phosphine modified version of the cycle, BCF can stoichiometrically ionize a chosen silane into $H–B(C_6F_5)_3^-$ and $R_3Si–PR_3^+$ ion pair.[32] Although the mechanistic role of these additives has not been determined, it can be surmised that if the BCF/PR_3 pair is (at least partially) frustrated then an equilibrium accessible η^1-silane adduct of $B(C_6F_5)_3$ can react with free phosphine to yield this thermodynamically favorable ion pair.[45–47] Transfer of silylium ion from the phosphine to the imine substrate would generate a similarly activated substrate poised to undergo hydride attack. A mechanism for the reduction of ethers consistent with these observations is shown in Figure 2.1b. Consistent with the Klankermayer work on imine reduction, *in situ* monitoring of the BCF/PAr_3 catalyzed reduction of anisole to PhOTES (Scheme 2.2), showed at early times that the catalyst rests at the $H–B(C_6F_5)_3^-$ and $R_3Si–PR_3^+$ ion pair, with no other BCF species detectable.

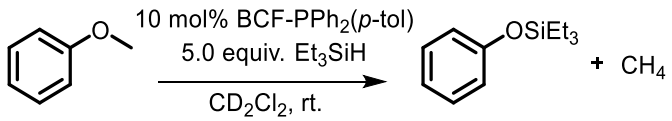

Scheme 2.2. BCF-catalyzed reduction of anisole

In this chapter, we detail stoichiometric, kinetic, and computational analysis of the silane activation component of this proposed phosphine-modified catalytic cycle, in combination with a full cycle analysis of the anisole reduction. Together, these data delineate the importance of silyl-phosphonium intermediates and the potential pitfalls of phosphine modified catalyst systems.

2.2. Initial speciation studies

Initial investigations focused on determining how steric and electronic changes in the various triaryl phosphines, BCF, and alkyl silanes components impacted speciation to ionic products. As shown in Figure 2.2, multiple equilibria are possible, including Lewis adduct formation (**2**) and the silane ionization ion pair, $H–B(C_6F_5)_3^-$ and $R_3Si–PAr_3^+$ (**3**). The η^1-silane adduct (**1**) plays a

key role in silane activation, but is only experimentally observable with an exceptionally strong Lewis acid;[25] and thus was not observed with the conditions and reagents studied in this chapter.

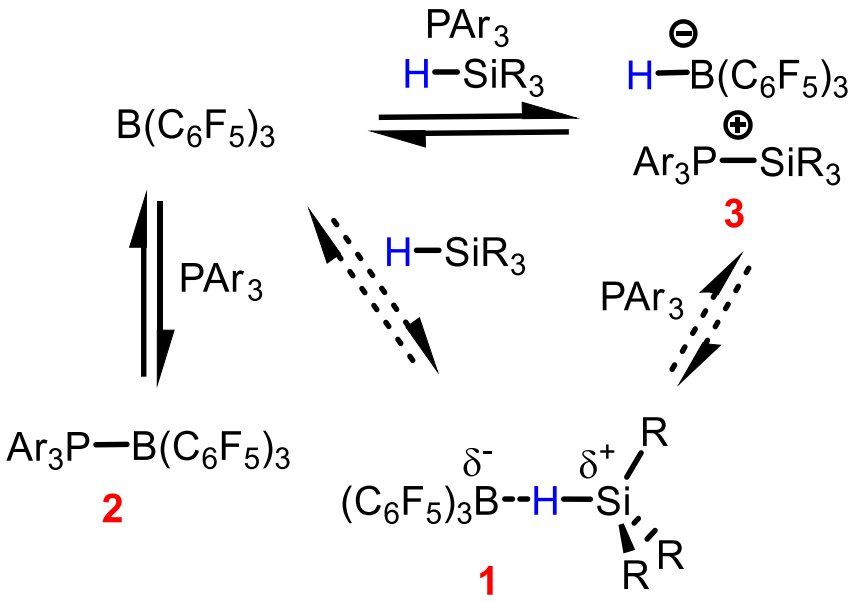

Figure 2.2. Potential speciation outcomes of BCF, R_3SiH, and PAr_3

The combination of BCF and 1.1 equivalents of PPh_3 in CH_2Cl_2 rapidly precipitates the BCF•PPh_3 Lewis adduct **2** as a white solid. The addition of a 50-fold excess of Et_3SiH dissolves the solid in <10 min and cleanly speciates the components to the $[H–B(C_6F_5)_3^-][Et_3Si–PPh_3^+]$ ion pair. The ^{19}F NMR resonances of $H–B(C_6F_5)_3^-$ are diagnostic,[54] and the ^{31}P NMR spectrum indicates a shift from free phosphine (-5.6 ppm) to a sharp singlet at -2.9 ppm of the silyl-phosphonium (Figure 2.3).[46]

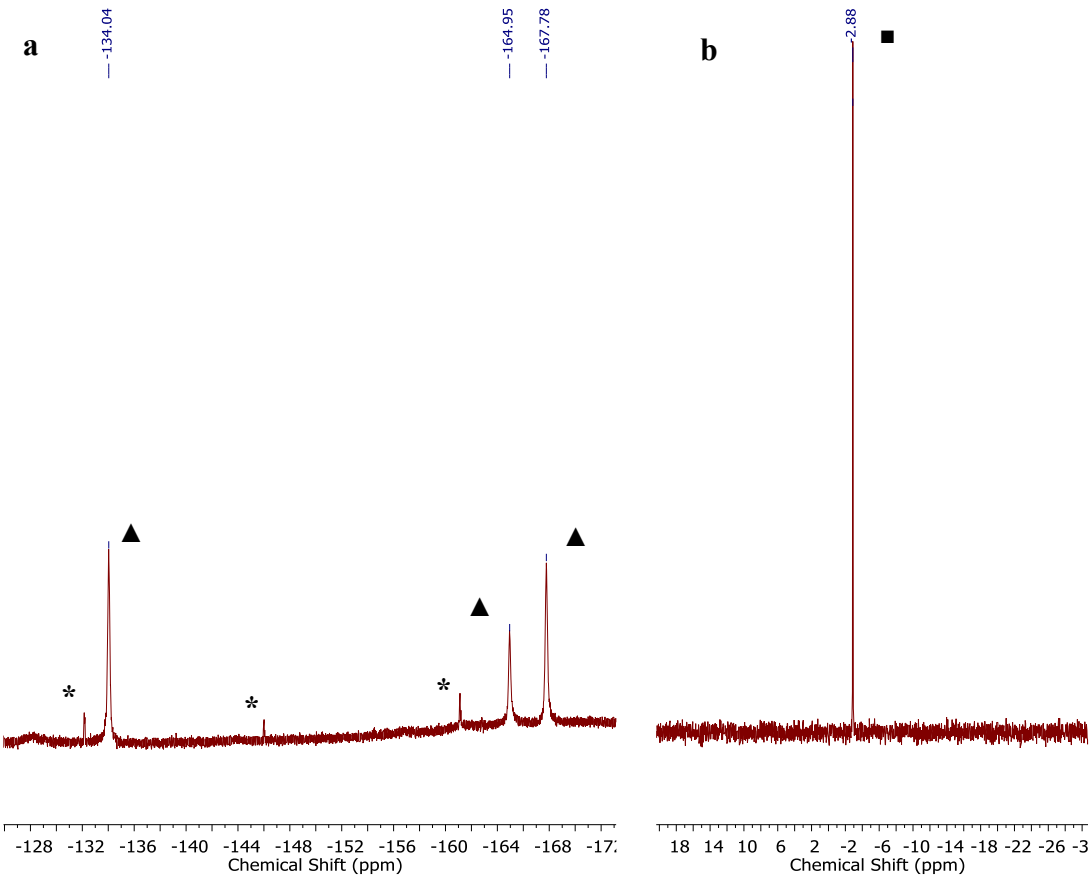

Figure 2.3. BCF•PPh_3 and silane speciation experiment

a. $^{19}F\{^1H\}$ NMR spectrum of the solution obtained from the combination of BCF, PPh_3, and Et_3SiH. The spectrum is consistent with complete speciation of the starting materials to the $Et_3Si–PPh_3^+$ / $H–B(C_6F_5)_3^-$ ion pair. The peaks indicated with (*) correspond to unreacted $(C_6F_5)_3B–PPh_3$. The peaks indicated with (▲) correspond to the $H–B(C_6F_5)_3^-$ anion.[46] b. $^{31}P\{^1H\}$ NMR spectrum of the solution obtained from the combination of BCF, PPh_3, and Et_3SiH. The spectrum is consistent with complete speciation of the starting materials to the $Et_3Si–PPh_3^+$ / $H–B(C_6F_5)_3^-$ ion pair. The peak indicated with (■) is assigned to the $Et_3Si–PPh_3^+$ cation.[54]

At lower concentrations of excess silane (10 equiv.), this reaction is sensitive to order of addition; if silane is added to pre-formed BCF•PPh_3, a slower dissolution rate ensues and conversion to the ion pair is still incomplete after 2h, as evidenced by a small amount of white precipitate. If the silane is instead added to the borane before PPh_3 then clean conversion to the

ion pair is observed without precipitation of the Lewis adduct. Since the Lewis adduct is most likely off-cycle, this observation may be an important element to consider during catalytic applications. Because PPh_2(*p*-tol) behaves like PPh_3 but forms a more soluble Lewis adduct with BCF in CH_2Cl_2, we continued our studies with this phosphine.

2.3. Silane and phosphine effects on ionization efficiency

Changing the silane and phosphine directly impacts the thermodynamics of speciation. This was determined by qualitatively assessing the extent of ion pair formation for a variety of trialkyl silanes upon addition to preformed BCF•PPh_2(*p*-tol) (Table 2.1).

Table 2.1. Extent of silyl-phosphonium formation using PPh_2(*p*-tol)[a]

Silane	Extent of Speciation[b]	$[R_3Si–PAr_3]^+$ peak?[c]
Me_2EtSiH	Full	Yes; -3.1 ppm
Me_2PhSiH	Full	Yes; -6.8 ppm
Et_3SiH	Full	Yes; -3.4 ppm
Ph_3SiH	Partial	No; unclear/broad
$Me_2tBuSiH$	None	None
$(i\text{-}Pr)_3SiH$	None	None

[a]Speciation studies carried out at 20 mM BCF, 20 mM PPh2(*p*-tol), and 200 mM silane in CH_2Cl_2. [b]Determined by ^{19}F NMR spectroscopy. [c]In the $^{31}P\{^1H\}$ NMR spectrum.

The less sterically hindered Me_2EtSiH and Me_2PhSiH rapidly and fully form the ion pair, with both the $H–B(C_6F_5)_3^-$ and $R_3Si–PPh_2(p\text{-tol})^+$ peaks being clearly observable in the ^{19}F and ^{31}P NMR spectra. Ph_3SiH, on the other hand, only partially ionizes as reported by the trace quantities of $H–B(C_6F_5)_3^-$. Finally, the bulkier $Me_2tBuSiH$ and $(i\text{-}Pr)_3SiH$ are unreactive, with only BCF•PPh_2(*p*-tol) being observable by ^{19}F and ^{31}P NMR spectroscopy. The phosphine basicity was

similarly varied[55] to study the extent of ion pair formation with Et_3SiH (Table 2.2). As mentioned above, BCF•PPh_2(*p*-tol) is relatively soluble in CH_2Cl_2, and full speciation to H–$B(C_6F_5)_3^-$ / Et_3Si–PPh_2(*p*-tol)$^+$ occurs within minutes; 2-(diphenylphosphino) biphenyl, PPh_2(*o*-biphen), behaves similarly. While tri(*o*-tolyl)phosphine, P(*o*-tol)$_3$, does not form an adduct with BCF or ionize 10 equiv. of Et_3SiH (by ^{19}F and ^{31}P NMR), it does fully ionize 10 equiv. of the less bulky Me_2EtSiH to Me_2EtSi–P(*o*-tol)$_3^+$ and H–$B(C_6F_5)_3^-$ as noted by ^{31}P NMR (2.2 ppm) and ^{19}F NMR spectroscopy.

Table 2.2. Extent of silyl-phosphonium formation using Et_3SiH[a]

Phosphine	Extent of Speciation[b]	Et_3Si–PAr_3^+ peak?[c]
PPh_2(*p*-tol)	Full	Yes; -3.4 ppm
PPh_3	Full	Yes; -2.9 ppm
PPh_2(*o*-biphen)	Full	Yes, -0.4 ppm
P(*o*-tol)$_3$	None	None[d]
P(*p*-Cl-Ph)$_3$	Partial[e]	Yes, -1.6 ppm
P(*p*-F-Ph)$_3$	Partial[e]	Yes, -3.8 ppm
PCy_3	None	None
P(*n*-Bu)$_3$	None[f]	None[g]

[a]Speciation studies carried out at 20 mM BCF, 20 mM PPh_2(*p*-tol), and 200 mM silane in CH_2Cl_2. [b]Determined by ^{19}F spectroscopy. [c]In the $^{31}P\{^1H\}$ NMR spectrum. [d]Free P(*o*-tol)$_3$ peak only. [e]solution heterogeneous (forms insoluble BCF•PR_3); full ionization occurs with Me_2EtSiH. [f]Partial ionization occurs with Me_2EtSiH. [g]BCF•PR_3 peaks only (see Experimental section).

The attenuated Lewis base tris(4-chlorophenyl)phosphine, P(*p*-Cl-Ph)$_3$, also forms the Et_3Si–P(*p*-Cl-Ph)$_3^+$ / H–$B(C_6F_5)_3^-$ ion pair with 10 equiv. of Et_3SiH. However, as in the case with

PPh_3, the BCF•PAr_3 is relatively insoluble, and the precipitate and free P(*p*-Cl-Ph)$_3$ remains after silane addition. A similar situation occurs with tris(4-fluorophenyl)phosphine, P(*p*-F-Ph)$_3$, whose Lewis adduct with BCF is poorly soluble, though 10 equiv. of Et_3SiH does provide traces of H–$B(C_6F_5)_3^-$ by ^{19}F NMR spectroscopy. The trialkyl phosphines PCy_3 and P(*n*-Bu)$_3$ were found to be less well behaved, with PCy_3 especially providing multiple unidentified products. Neither PCy_3 nor P(*n*-Bu)$_3$were found to substantially ionize Et_3SiH, but in the case of P(*n*-Bu)$_3$, the less bulky Me_2EtSiH was more promoting of this reactivity and partial speciation was observed.

The above studies demonstrate that the extent of silane ionization by the combination of BCF and a phosphine depend on the size and basicity of both silane and phosphine. The solubility of BCF•PPh_2(*p*-tol) in CH_2Cl_2 and its ability to cleanly generate H–$B(C_6F_5)_3^-$ / Et_3Si–PPh_2(*p*-tol)$^+$ on treating with Et_3SiH led us to choose this system for a more detailed kinetic analysis of ion pair formation.

2.4. Kinetic investigations

2.4.1 Spectroscopic characterization

The BCF•PPh_2(*p*-tol) Lewis pair for this investigation was prepared as a stable white solid by mixing the components in a 1:1 CH_2Cl_2/pentane mixture and drying the pentane washed precipitate under vacuum.[56] The ^{31}P and *m*-^{19}F resonances are broad in the adduct, but the *o*- and *p*-F resonances are sharp and easily distinguished (-156.8 and -165.1 ppm, respectively) from free BCF. A 20 mM solution of BCF•PPh_2(*p*-tol) appears as a cloudy white mixture, which, upon addition of 10 equiv. of Et_3SiH at room temperature, becomes clear within 5 min (Scheme 2.3).

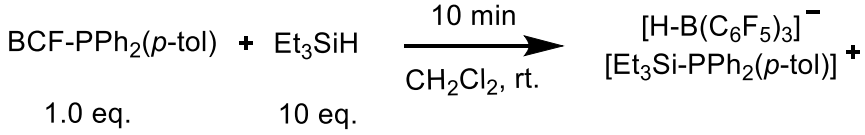

Scheme 2.3. BCF•PPh_2(*p*-tol) adduct reaction excess Et_3SiH

The resulting ion pair can be identified by characteristic signals in ^{19}F, ^{31}P, ^{11}B, and ^{29}Si NMR spectra. The borohydride anion, $H–B(C_6F_5)_3^-$ provides a set of peaks at -133.9, -164.7, and -167.6 ppm in the ^{19}F NMR spectrum (Figure 2.4a) and a doublet at -25.4 ppm in the proton-coupled ^{11}B NMR (Figure 2.5) spectrum ($^1J_{H,B}$ = 93 Hz).[54] The silyl-phosphonium ion, $Et_3Si–PPh_2(p\text{-tol})^+$ exhibits a singlet at -3.4 ppm in its ^{31}P NMR spectrum (Figure 2.4b) and a doublet at 18.6 ppm in its ^{29}Si NMR (Figure 2.6) spectrum ($^1J_{Si,P}$ = 19 Hz).

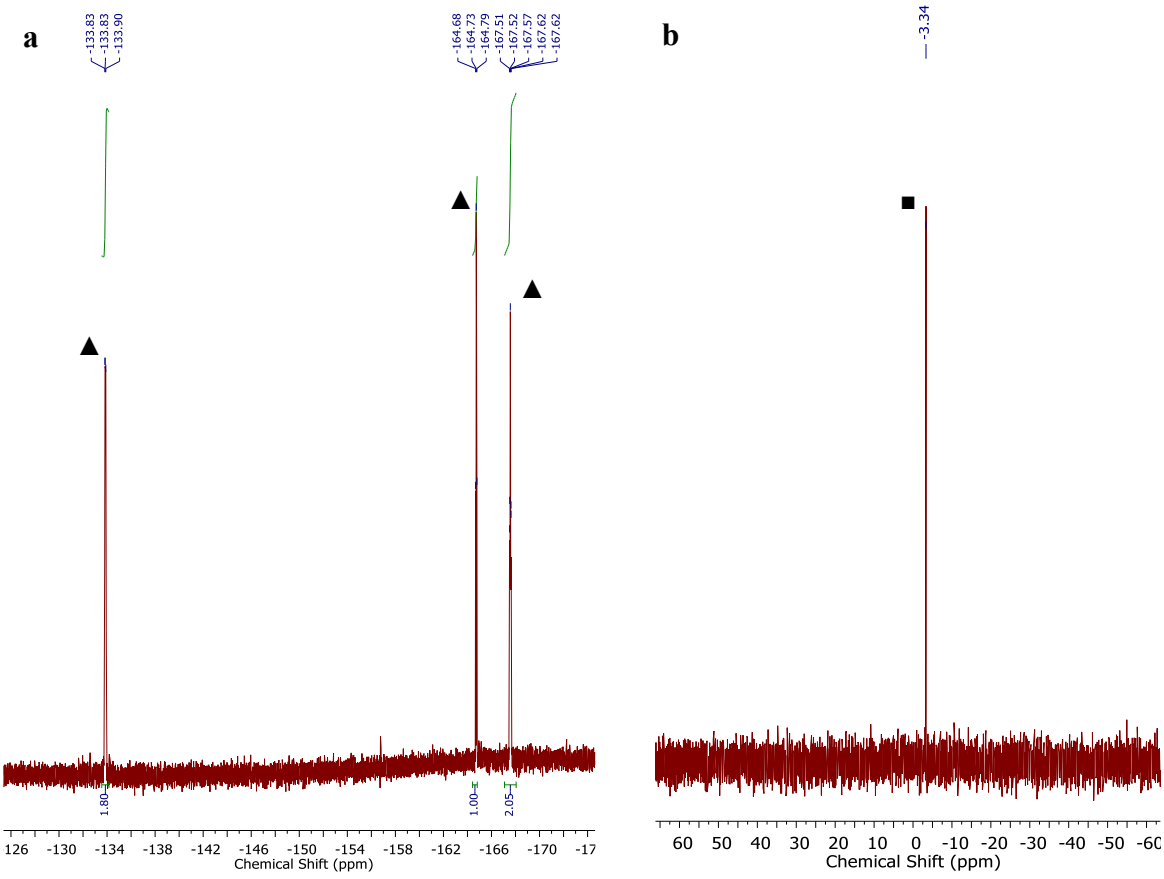

Figure 2.4. $B(C_6F_5)_3$, $PPh_2(p\text{-tol})$, and Et_3SiH speciation

a. $^{19}F\{^1H\}$ NMR spectrum of the solution obtained from the combination of $B(C_6F_5)_3$, $PPh_2(p\text{-tol})$, and Et_3SiH. The spectrum is consistent with complete speciation of the starting materials to the $Et_3Si–PPh_2(p\text{-tol})^+$ / $H–B(C_6F_5)_3^-$ ion pair. The peaks indicated with (▲) correspond to the $H–B(C_6F_5)_3^-$ anion.[54]

b. $^{31}P\{^{1}H\}$ NMR spectrum of the solution obtained from the combination of $B(C_6F_5)_3$, PPh_2(*p*-tol), and Et_3SiH. The spectrum is consistent with complete speciation of the starting materials to the $Et_3Si–PPh_2$(*p*-tol)$^+$ / H–$B(C_6F_5)_3^-$ ion pair. The peak indicated with (■) is assigned to the $Et_3Si–PPh_2$(*p*-tol)$^+$ cation.

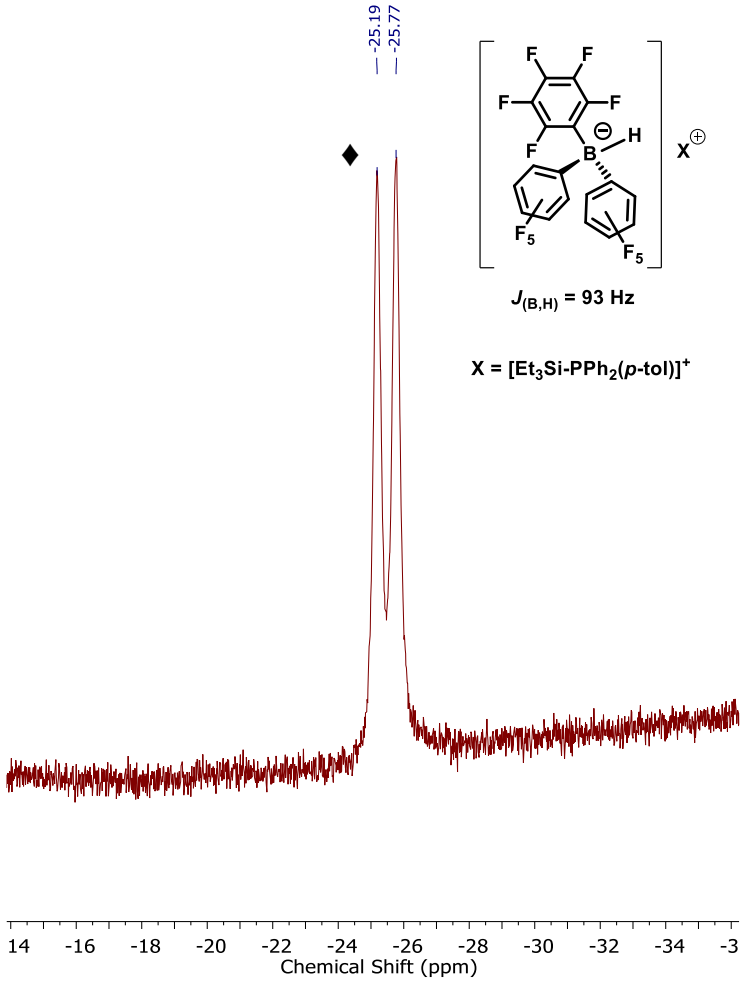

Figure 2.5. ^{11}B NMR spectrum of H–$B(C_6F_5)_3^-$ ion

^{11}B NMR spectrum (proton coupled) of [$Et_3Si–PPh_2$(p-tol)$^+$][H–$B(C_6F_5)_3^-$]. The peak indicated with (♦) corresponds to the H–$B(C_6F_5)_3^-$ anion.[54]

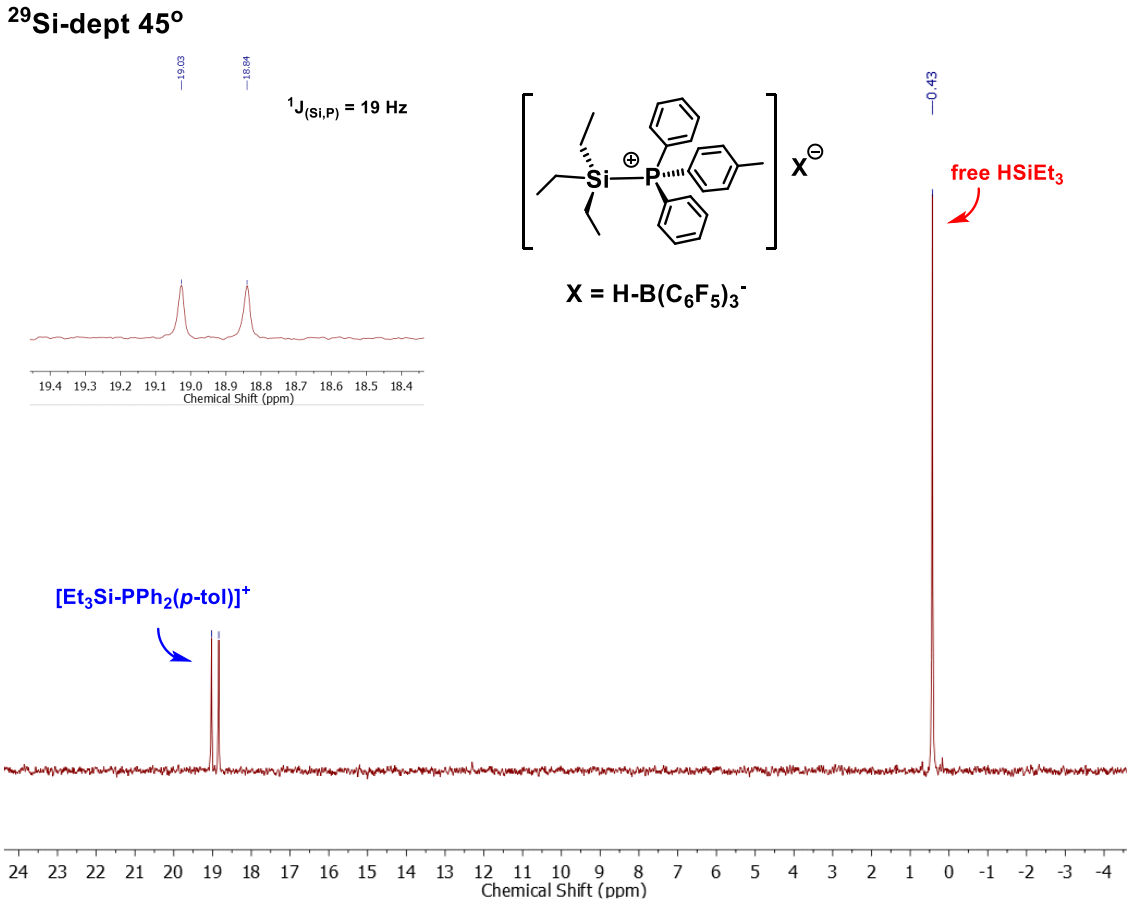

Figure 2.6. ^{29}Si-dept 45° NMR spectrum of $Et_3Si–PPh_2(p\text{-tol})^+$ ion

^{29}Si-dept 45° NMR spectrum of $Et_3Si–PPh_2(p\text{-tol})^+$ / $H–B(C_6F_5)_3^-$ ion pair in CD_2Cl_2. The residual Et_3SiH signal at 0.4 ppm is greatly enhanced. The $Et_3Si–PPh_2(p\text{-tol})^+$ peak is not observed under standard ^{29}Si NMR experimental conditions due to the presence of a broad peak from the SiO_2 present in the probe of the spectrometer.

Consistent with a marked preference for less sterically hindered phosphines and with slow silylium transfer from one phosphine to another on the NMR timescale, the addition of 5 equiv. of $PPh_2(p\text{-tol})$ to $Et_3Si–PPh_2(o\text{-biphen})^+$ / $H–B(C_6F_5)_3^-$ quantitatively transfers Et_3Si^+ to $PPh_2(p\text{-tol})$, Figure 2.7, which also displays independent resonances for silyl-phosphonium and free phosphine at -3.4 and -6.5 ppm, respectively.

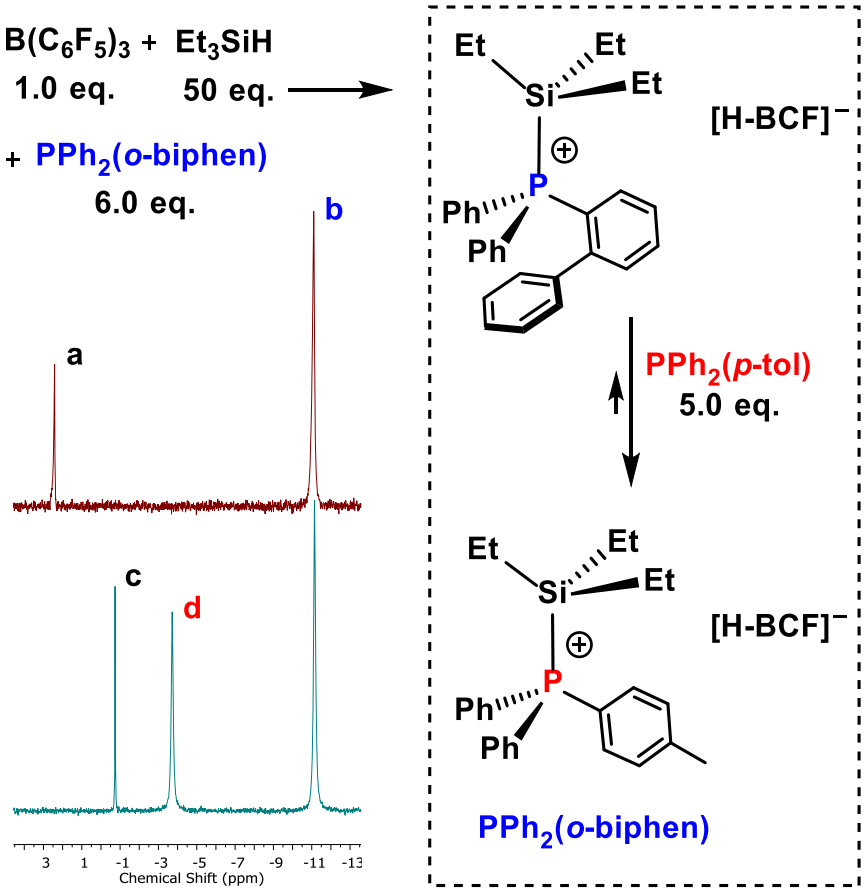

Figure 2.7. Silylium ion transfer experiment

Silylium ion transfer from $Et_3Si\text{-}PPh_2(o\text{-biphen})^+$ to the more nucleophilic $PPh_2(p\text{-tol})$ *a*: $Et_3Si\text{-}PPh_2(o\text{-biphen})^+$; *b*: $PPh_2(o\text{-biphen})$; *c*: $Et_3Si\text{-}PPh_2(p\text{-tol})^+$; *d*: $PPh_2(p\text{-tol})$.

2.4.2 Silane and phosphine order determination

Kinetics for the rate of ion pair formation were obtained under pseudo-first order conditions in triethylsilane. A constant concentration of BCF•PPh_2(*p*-tol) was reacted with increasing concentrations of Et_3SiH to provide 10-50-fold excesses. The disappearance of the Lewis adduct and the appearance of the H–$B(C_6F_5)_3^-$ were tracked *in situ* by ^{19}F NMR spectroscopy using monofluorobenzene, in CD_2Cl_2 as an external standard (capillary insert). Unique chemical shifts of the *p*-F peak of BCF•PPh_2(*p*-tol) and the *o*-F peak of H–$B(C_6F_5)_3^-$ were used to monitor the loss and growth of the starting material and product, respectively; both methods gave the same result.

The appearance of the $Et_3Si–PPh_2(p\text{-tol})^+$ cation was verified *in situ* by ^{31}P NMR (-3.4 ppm). A plot of k_{obs} vs. [Et_3SiH], as shown in Figure 2.8, was linear and confirmed a first order dependence on silane.

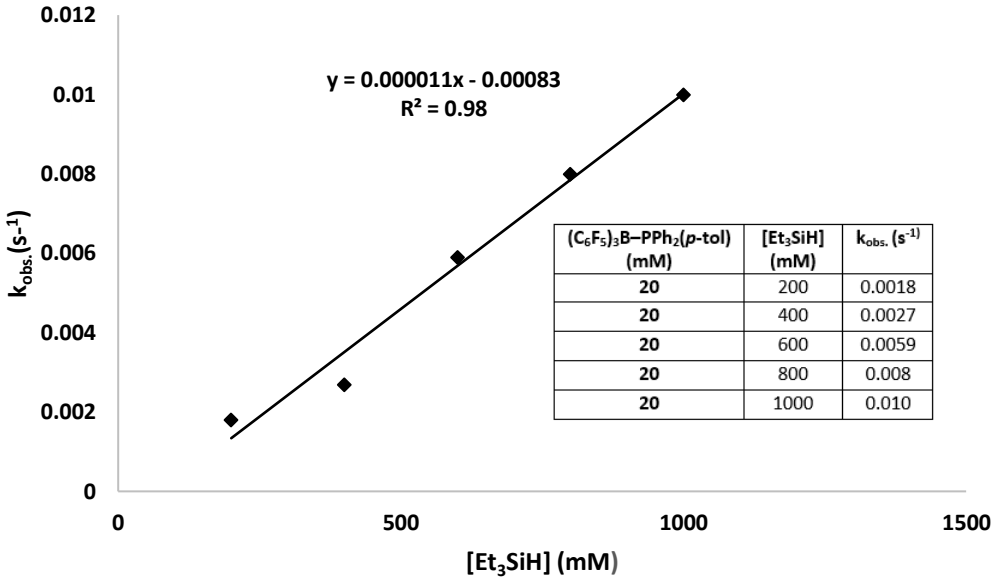

$(C_6F_5)_3B–PPh_2(p\text{-tol})$ (mM)	[Et_3SiH] (mM)	$k_{obs.}$ (s^{-1})
20	200	0.0018
20	400	0.0027
20	600	0.0059
20	800	0.008
20	1000	0.010

Figure 2.8. $k_{obs.}$ vs. silane concentration plot

To determine the reaction order in $PPh_2(p\text{-tol})$, a similar set of experiments was carried out, holding the Lewis pair and silane concentrations constant and varying the concentration of excess $PPh_2(p\text{-tol})$. The results are summarized in Table 2.3. Using the same spectroscopic handles as for Table 2.1, k_{obs} was found to be insensitive to [$PPh_2(p\text{-tol})$], consistent with a reaction that is zero order in $PPh_2(p\text{-tol})$.

Table 2.3. Reaction of $(C_6F_5)_3B–PPh_2(p\text{-tol})$ with $H–SiEt_3$

Run	$(C_6F_5)_3B–PPh_2(p\text{-tol})$			$H–SiEt_3$			$PPh_2(p\text{-tol})$			k_{obs} (s^{-1})[a]
	Eq.	mmol	conc. (mM)	Eq.	mmol	conc. (mM)	Eq.	mmol	conc. (mM)	
1	1.0	0.01	20	20	0.20	400	5	0.05	100	0.0023
2	1.0	0.01	20	20	0.20	400	10	0.10	200	0.0023
3	1.0	0.01	20	20	0.20	400	15	0.15	300	0.0026
4	1.0	0.01	20	20	0.20	400	20	0.20	400	0.0026

[a]**Raw data for the reaction of $(C_6F_5)_3B–PPh_2(p\text{-tol})$ and $H–SiEt_3$ with varying amounts of $PPh_2(p\text{-tol})$. The $H–SiEt_3$ concentration is kept in large excess with respect to $(C_6F_5)_3B–PPh_2(p\text{-tol})$. $PPh_2(p\text{-tol})$ concentration is kept in 10-fold or more excess with respect to $(C_6F_5)_3B–PPh_2(p\text{-tol})$ and varied to detemine the order in phopsine.**

Together, the data in Figure 2.8 and Table 2.3 indicate that silane heterolysis is α $[R_3SiH]^1[PAr_3]^0$. Loss of $PPh_2(p\text{-tol})$ from the Lewis pair, followed by its re-engagement in the transition state with one equivalent of triethylsilane would provide the observed kinetic dependence on silane and phosphine.

2.5. Computational investigations

To further understand the effect of the phosphine Lewis base on BCF and silane speciation, and by extension to catalytic cycles that involve these intermediates (e.g. Figure 2.1b), density functional theory (DFT) was used to compute relative free energies of the geometry optimized key proposed intermediates (DCM solvent model) for the conversion of $BCF•PPh_2(p\text{-tol})$ to $Et_3Si–PPh_2(p\text{-tol})^+$ and $H–B(C_6F_5)_3^-$. Figure 2.9 shows the calculated Gibbs free energy (ΔG) for the proposed reaction coordinate. Free BCF, PPh_2(p-tol), and Et_3SiH are assigned the starting 0.0 kcal/mol point, with $BCF•PPh_2(p\text{-tol})$ adduct (**4**) formation depicted to the left and the silane

reaction leading to borohydride and the silyl-phosphonium ion pair (**7**) to the right. As shown, Lewis adduct formation is computed to be exergonic (-14.3 kcal/mol) while net silane ionization to the individual ions is favorable by -9.9 kcal/mol. Along the proposed silane activation pathway, the η^1-silane adduct **5** is calculated to be +2.3 kcal/mol relative to free BCF and free silane, in agreement with the results reported by Fujimoto.[27]

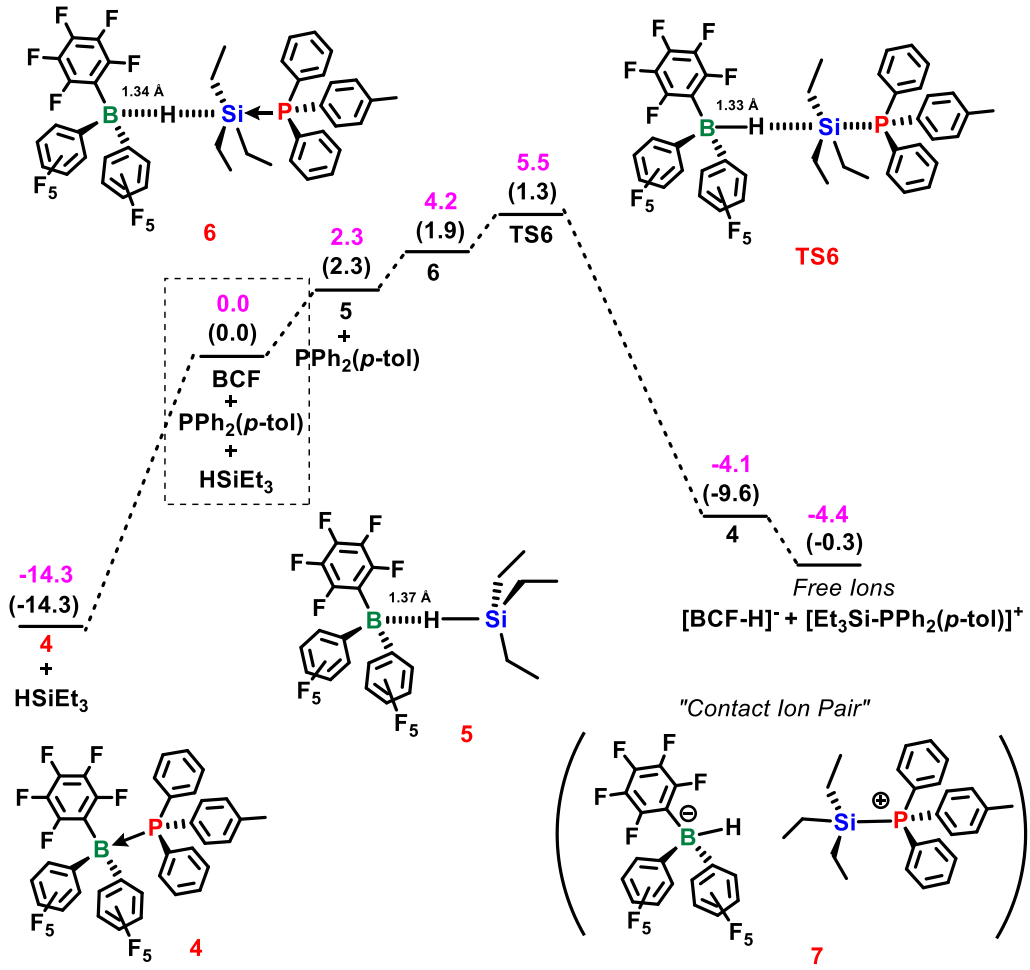

Figure 2.9. DFT data for ion pair formation

Gibbs free energy (ΔG) diagram at the M06-2X(C-PCM)/6-311++G level of theory (kcal/mol). Numbers above the parentheses indicate free energy changes relative to the zero point (free BCF, PPh_2(*p*-tol), and Et_3SiH); numbers inside the parentheses indicate free energy changes from the previous step of**

the calculation (left to right). TS6 structure was calculated using the Berny QST2 transition state optimization from species 6 to 7.

A transition state for the addition of PPh_2(*p*-tol) to the BCF--silane adduct and inversion of the silicon center,[26] is located at +5.5 kcal/mol, which is +19.8 kcal/mol higher than the BCF•PPh_2(*p*-tol) Lewis pair. An intermediate adduct between BCF--H–$SiEt_3$ and PPh_2(*p*-tol) was found computationally (Species **6**, Figure 2.9), though its barrier for completing the inversion of Si and ion pair generation is low (+1.3 kcal/mol).

These computed energies are consistent with experimental observation apart from the relative free energy of BCF•PPh_2(*p*-tol) Lewis pair and the free ions, which at equilibrium (with excess silane) favors the ions. Since the above free energies are computed from the individual free ions, and it is reasonable to assume that the ions exist as an additionally stabilized contact ion pair, we briefly explored several starting geometries for the ion pair. This proved challenging and computationally expensive. In one such species, a computationally stable pair was computed to be slightly higher in energy than the free ions (Species **7**, Figure 2.9). In computing a reaction coordinate for the reduction of acetone with a BCF-based FLP system, Sakata and Fujimoto found a contact ion pair to be 15.2 kcal/mol *lower* in energy than the free ions.[27] Since ^{19}F and ^{31}P NMR spectroscopy confirm a complete conversion of BCF and PPh_2(*p*-tol) on reacting with 10 equiv. of Et_3SiH, we presume that the correct contact ion pair in the current system would be additionally stabilizing.

2.6. Speciation studies of catalytic anisole reduction

In situ monitoring of the BCF-catalyzed demethylation of anisole[21] proved informative and shed additional light on the possible roles of the phosphine during catalysis (Scheme 2.4).

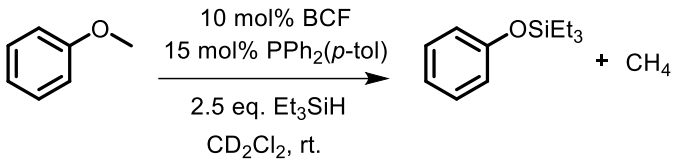

Scheme 2.4. BCF and excess phosphine catalyzed reduction of anisole

In the presence of excess phosphine, the reaction proceeeds significantly slower than when catalyzed solely by BCF. In addition to the expected free phosphine and the silyl-phosphonium ion described earlier, a new phosphorus-containing species was observed to grow at 20.1 ppm in the ^{31}P NMR spectrum. This species, identified as $[H_3C–PPh_2(p\text{-tol})^+][H–B(C_6F_5)_3^-]$, likely results from phosphine attack on the silylium activated anisole intermediate **8** (Figure 2.10). Over time, the initially observed silyl-phosphonium is consumed and converted to methyl phosphonium.

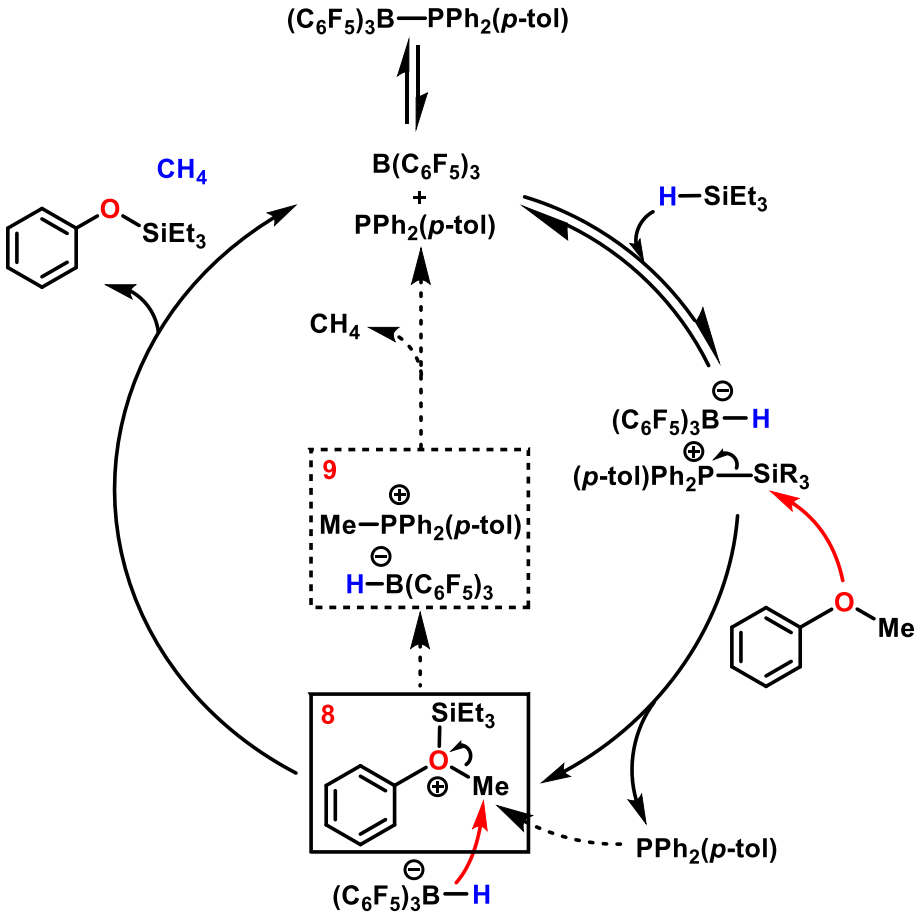

Figure 2.10. Phosphine-modified catalytic reduction of anisole

Although loss of a silylium ion source should lower catalytic efficiency, if $H–B(C_6F_5)_3^-$ were to reduce $Me–PPh_2(p\text{-tol})^+$ and liberate methane, then a path to close the cycle would ensue. Control experiments, however, indicate that $Me–PPh_2(p\text{-tol})^+$ does not react with $H–B(C_6F_5)_3^-$ at catalytically relevant rates (Figure 2.11), and its growth (and concomitant loss of $Et_3Si–PPh_2(p\text{-tol})^+$) correlates with a loss of catalytic activity. Even though the DFT studies indicate that the free energy change for CH_4 generation is -3.9 kcal/mol, experimental data shows that even after 300 h no additional ctalysis and CH_4 liberation occurs.

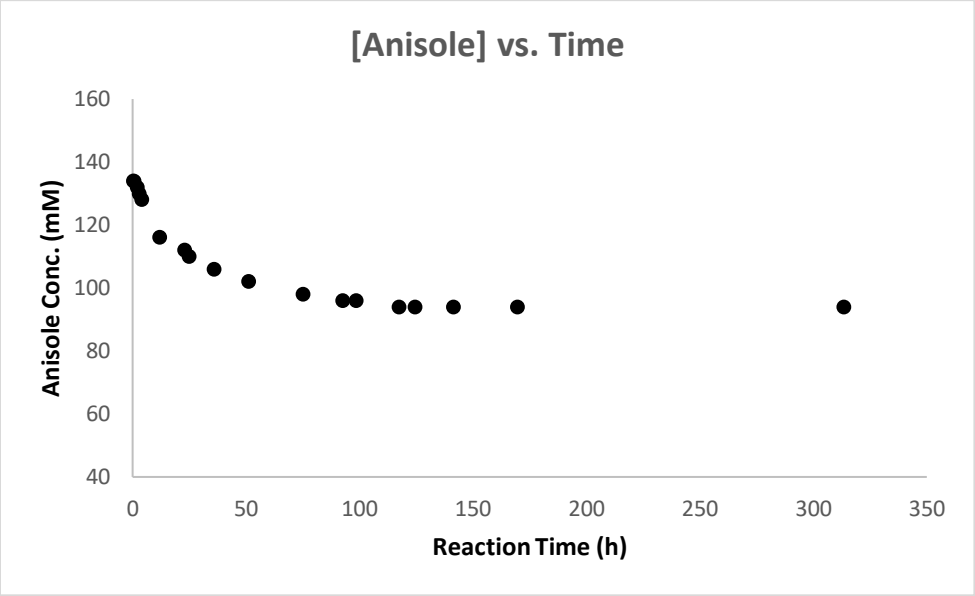

Figure 2.11. [Anisole] vs. time plot with excess phosphine

A plot showing [anisole] vs. time, in the presence of excess phosphine, based on ^{1}H NMR spectra of the *in situ* solution of the BCF, Et_3SiH, anisole, and excess $PPh_2(p\text{-tol})$ mixture. The spectrum is consistent with anisole demethylation being impeded by $PPh_2(p\text{-tol})$ and not proceeding to completion, even after 300 h.

The mechanistic picture that is revealed by the desribed experiments is shown in Figure 2.10 above. Under conditions of excess silane and phosphine, anisole reduction only occurs while silyl-phosphonium is present. The competitive reactivity of intermediate **8** with a phosphine or hydride nucleophile defines whether the cycle turns over $H–B(C_6F_5)_3^-$ attacks at Me or is shunted

to an off-cycle state (**9**, Me-PPh_2(*p*-tol)$^+$) through phosphine attack at Me. Even if hydride reduction of **8** is kinetically preferred, the irreversible (or at least slow relative to catalysis) formation of H_3C–PPh_2(*p*-tol)$^+$ acts to pull active silylium out of the catalytic cycle. Once Et_3Si–PPh_2(*p*-tol)$^+$ is consumed, turnover ceases and the only species observable by ^{31}P and ^{19}F NMR spectroscopy are the methyl-phosphonium and the borohydride, respectively.

2.7. Conclusions

The results summarized in this chapter demonstrate that phosphine additivies significantly alter the catalyst speciation in BCF-catalyzed C–O defunctionalization reactions. In the absence of PAr_3, the catalyst rests in the Lewis acidic form (free BCF), which for some substrate types (e.g. natural products)[18] is detrimental to stability. The presence of phosphine, however, can completely shift the speciation to the nucleophilic form (H–$B(C_6F_5)_3^-$). In these cases it is the silyl-phosphonium, which is the electrophilic form of Si that activates the substrate. The advantage of this species over **1** (Figure 2.1) is that the phosphine is readily manipulated to be more or less basic and more less sterically conjested, thereby providing a handle for affecting the reactivity and selectivity of reactions they catalyze.

2.8. Experimental section

2.8.1. General experimental considerations

All catalytic reactions were performed in oven (130 °C) and/or flame-dried glassware in a nitrogen-filled glovebox. All reactions were performed at room temperature (23 ºC, rt.) unless otherwise specified. All deuterated solvents were purchased from Cambridge Isotope Laboratories, Inc., and degassed prior to use in the glovebox.

All NMR spectra were acquired on either a Bruker Avance 600 MHz, 500 MHz, or 400 MHz spectrometer at standard temperature and pressure. All ^{19}F NMR spectra reported herein were

obtained with proton decoupling under the following experimental conditions: Number of scans n.s. = 8; Delay D_1 = 1.00 sec; Sweep Width SW = 237 ppm; Acquisition Time AQ = 0.73 sec. Time per scan = D_1 + AQ = 1.73 sec. All ^{31}P NMR spectra reported herein were obtained with proton decoupling under the following experimental conditions: Number of scans n.s. = 32; Delay D_1 = 2.00 sec; Sweep Width SW = 396 ppm; Acquisition Time AQ = 0.51 sec. Time per scan = D_1 + AQ = 2.51 sec. All ^{11}B NMR spectra (proton coupled) reported herein were obtained under the following experimental conditions: Number of scans n.s. = 128; Delay D_1 = 1.00 sec; Sweep Width SW = 199 ppm; Acquisition Time AQ = 1.02 sec. Time per scan = D_1 + AQ = 2.02 sec.

2.8.2. Preparation of $(C_6F_5)_3B–PPh_2(p\text{-tol})$[56]

Inside a nitrogen-filled glovebox at room temperature, 1.0 equivalent of $B(C_6F_5)_3$ (76.8 mg, 0.15 mmol) was added to a 1-dram vial and dissolved in 1:1 CH_2Cl_2/pentane mixture (1.5 mL). 1.0 equivalent of PPh_2(*p*-tol) (41.4 mg, 0.15 mmol) was added to a separate 1-dram vial and dissolved in a 1:1 CH_2Cl_2/pentane mixture (1.5 mL). The contents of the two vials were combined in a 20-mL scintillation vial and allowed to stir for 1 hour at room temperature. After 1 h, the stirring was stopped and the mixture was allowed to sit overnight. The next day, the supernatant was decanted from the solid, it was washed with pentane (2 mL), and dried *in vacuo* (1 h) to give the product as a white solid in approximately 80% yield. $^{19}F\{^1H\}$ NMR (CH_2Cl_2, 376 MHz, 298K): δ -127.3 (br, *m*-C_6F_5), -156.8 (t, J_{FF} = 21 Hz, *p*-C_6F_5), -165.1 (br s, *o*-C_6F_5). $^{31}P\{^1H\}$ NMR (CH_2Cl_2, 162 MHz, 298K): δ 16.8 (br s).

2.8.3. Experiments to generate catalytic ion pairs

Generating the $R_3Si–PPh_2(p\text{-tol})^+$ / $H–B(C_6F_5)_3^-$ ion pairs

Inside a nitrogen-filled glovebox at room temperature, 1.0 equivalent of $(C_6F_5)_3B–PPh_2$(*p*-tol) (7.9 mg, 0.01 mmol) was added to a 1-dram vial and the solid dissolved in CH_2Cl_2 (0.5 mL). To the same 1-dram vial, 10 equivalents (0.10 mmol) of the appropriate trialkyl silane was added.

The resulting mixtures were transferred via syringe to an NMR tube, which was sealed with a septum and removed from the glovebox. The mixtures were then analyzed by ^{19}F and ^{31}P NMR spectroscopy. Relevant NMR spectra of these compounds can be found below.

This combination of reagents provides ^{19}F and ^{31}P NMR spectra consistent with complete speciation of the starting materials to the $Me_2EtSi–PPh_2(p\text{-tol})^+$ / $H–B(C_6F_5)_3$ ion pair. **^{19}F NMR** (CH_2Cl_2, 376 MHz, 298K): δ -133.9 (d, 2F, J_{FF} = 24 Hz, *m*-C_6F_5), -164.7 (t, 1F, J_{FF} = 20 Hz, *p*-C_6F_5), -167.6 (m, 2F, *o*-C_6F_5). **^{31}P NMR** (CH_2Cl_2, 162 MHz, 298K): δ -3.1 (s).

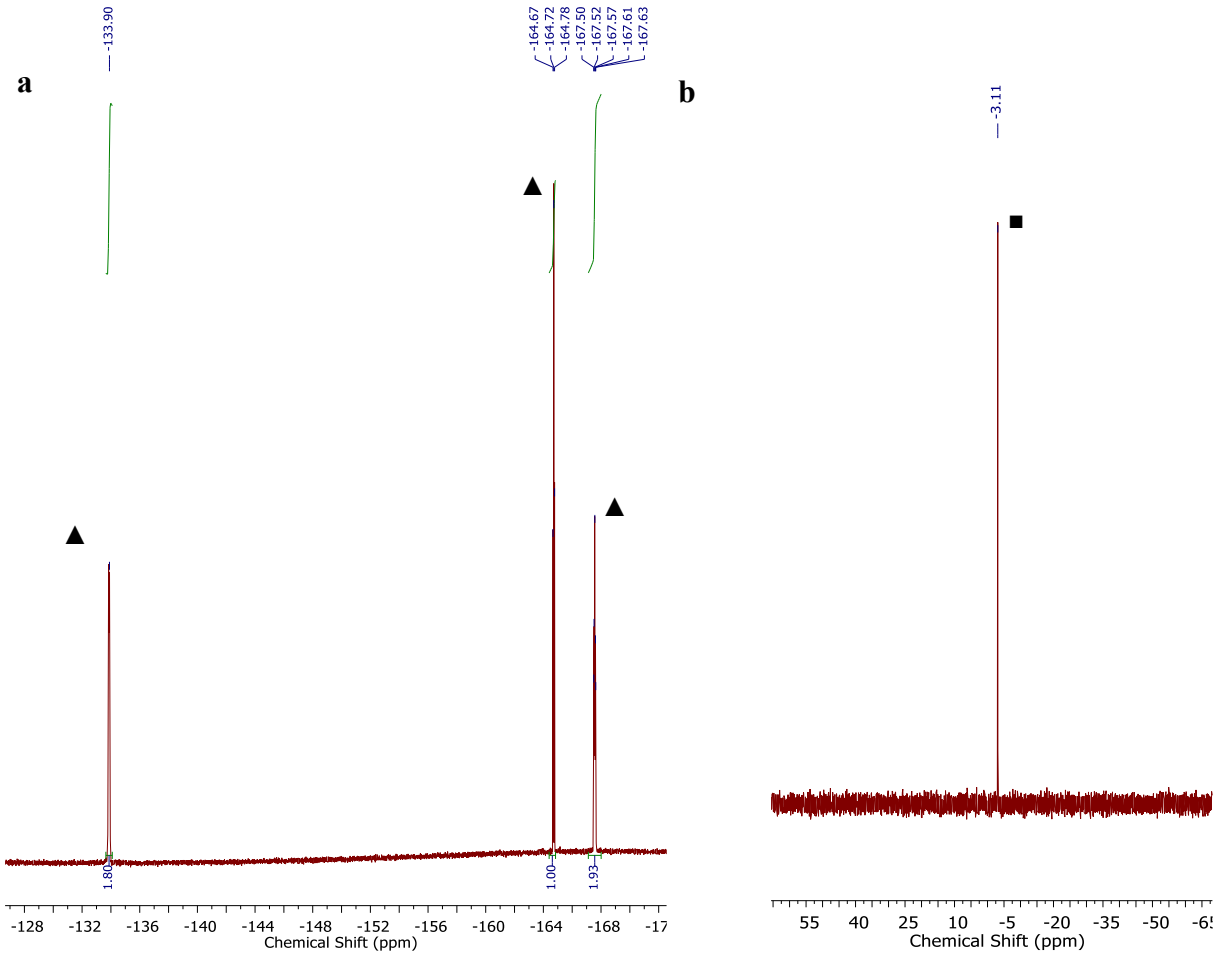

Figure 2.12. $B(C_6F_5)_3$, $PPh_2(p\text{-tol})$, and Me_2EtSiH speciation

a. $^{19}F\{^1H\}$ NMR spectrum of the solution obtained from the combination of $B(C_6F_5)_3$, $PPh_2(p\text{-tol})$, and Me_2EtSiH. The spectrum is consistent with complete speciation of the starting materials to the

$Me_2EtSi–PPh_2(p\text{-tol})^+$ / $H–B(C_6F_5)_3^-$ ion pair. The peaks indicated with (▲) correspond to the $H–B(C_6F_5)_3^-$ anion.[54] b. $^{31}P\{^1H\}$ NMR spectrum of the solution obtained from the combination of $B(C_6F_5)_3$, $PPh_2(p\text{-tol})$, and Me_2EtSiH. The spectrum is consistent with complete speciation of the starting materials to the $Me_2EtSi–PPh_2(p\text{-tol})^+$ / $H–B(C_6F_5)_3^-$ ion pair. The peak indicated with (■) is assigned to the $Me_2EtSi–PPh_2(p\text{-tol})^+$ cation.

This combination of reagents provides ^{19}F and ^{31}P NMR spectra consistent with complete speciation of the starting materials to the $Me_2PhSi–PPh_2(p\text{-tol})^+$ / $H–B(C_6F_5)_3^-$ ion pair. **$^{19}F\{^1H\}$ NMR** (CH_2Cl_2, 376 MHz, 298K): δ -133.9 (d, 2F, J_{FF} = 24 Hz, *m*-C_6F_5), -164.7 (t, 1F, J_{FF} = 20 Hz, *p*-C_6F_5), -167.6 (m, 2F, *o*-C_6F_5). **$^{31}P\{^1H\}$ NMR** (CH_2Cl_2, 162 MHz, 298K): δ -6.8 (s).

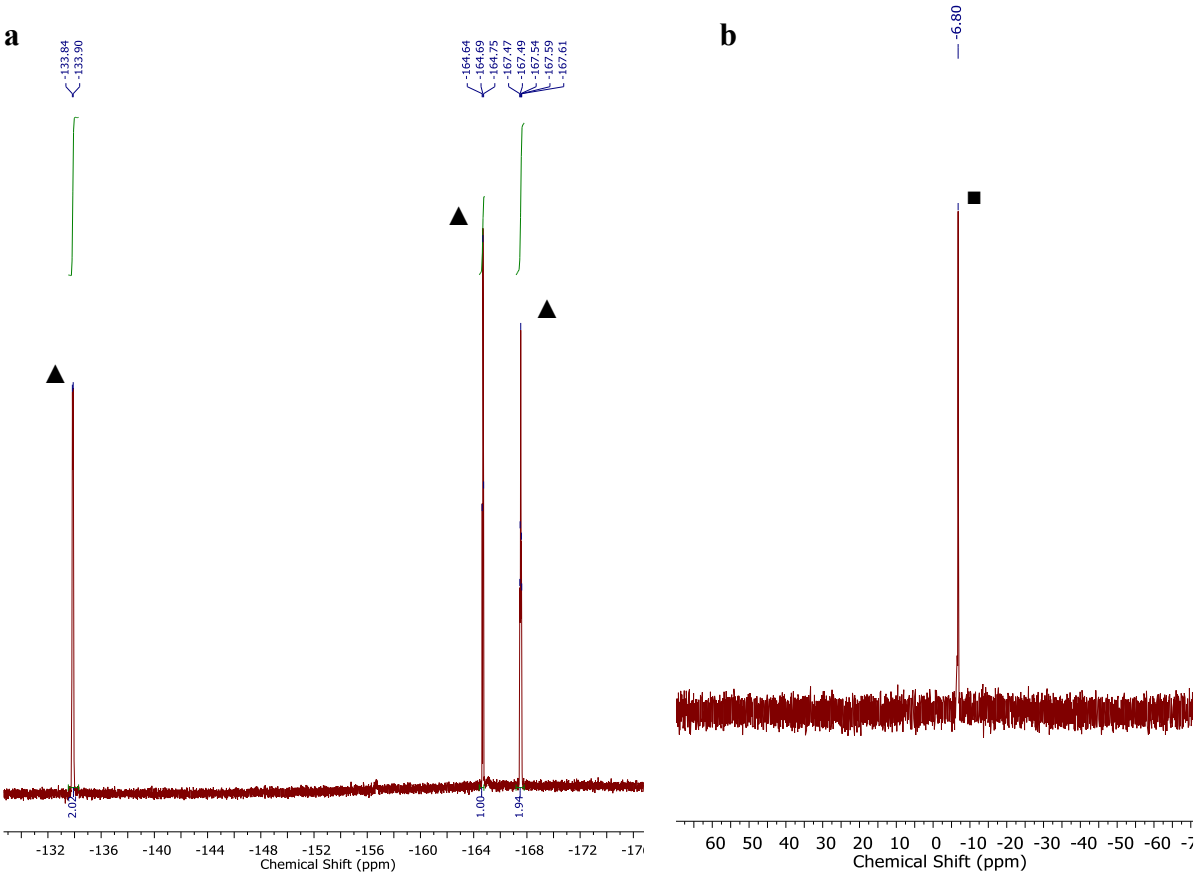

Figure 2.13. $B(C_6F_5)_3$, $PPh_2(p\text{-tol})$, and Me_2PhSiH speciation

a. $^{19}F\{^1H\}$ NMR spectrum of the solution obtained from the combination of $B(C_6F_5)_3$, $PPh_2(p\text{-tol})$, and Me_2PhSiH. The spectrum is consistent with complete speciation of the starting materials to the

$Me_2PhSi–PPh_2(p\text{-tol})^+$ / $H–B(C_6F_5)_3^-$ ion pair. The peaks indicated with (▲) correspond to the $H–B(C_6F_5)_3^-$ anion.[54] b. $^{31}P\{^1H\}$ NMR spectrum of the solution obtained from the combination of $B(C_6F_5)_3$, $PPh_2(p\text{-tol})$, and Me_2PhSiH. The spectrum is consistent with complete speciation of the starting materials to the $Me_2PhSi–PPh_2(p\text{-tol})^+$ / $H–B(C_6F_5)_3^-$ ion pair. The peak indicated with (■) is assigned to the $Me_2PhSi–PPh_2(p\text{-tol})^+$ cation.

This ^{31}P NMR spectrum shows speciation of the starting materials to the $Et_3Si–PPh_2(p\text{-tol})^+$ / $H–B(C_6F_5)_3^-$ ion pair in the presence of excess $PPh_2(p\text{-tol})^+$, which has a chemical shift of -6.5 ppm.

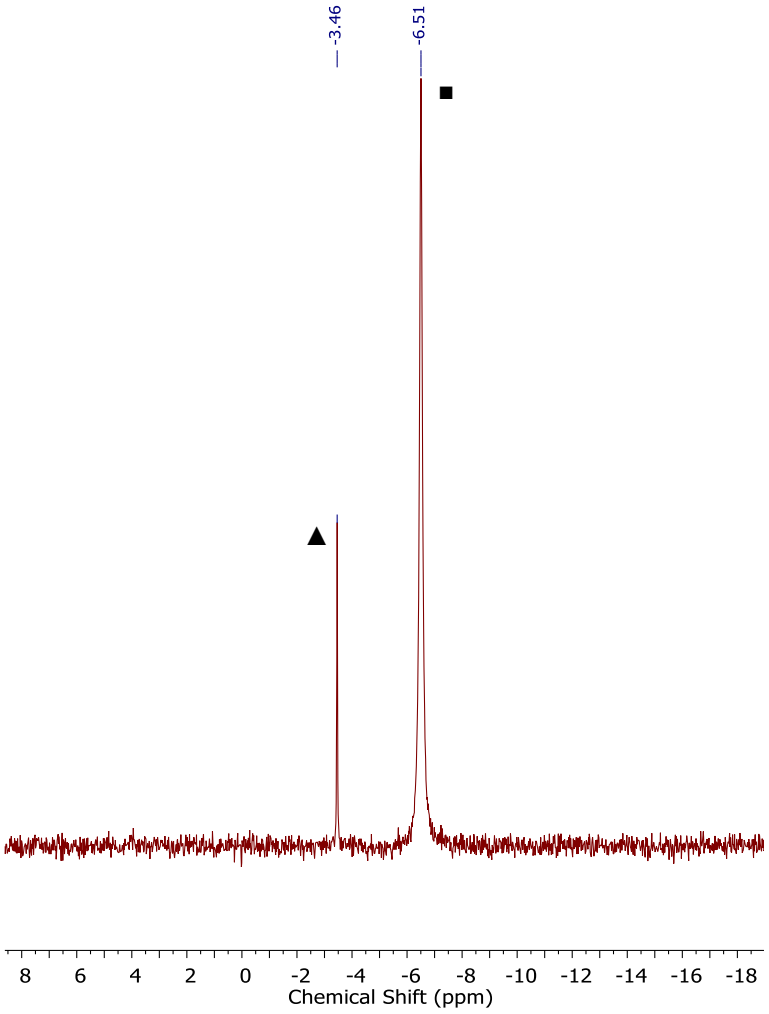

Figure 2.14. Excess phosphine speciation experiment

$^{31}P\{^1H\}$ NMR spectrum of $[Et_3Si–PPh_2(p\text{-tol})^+][H–B(C_6F_5)_3^-]$ with excess $PPh_2(p\text{-tol})$;

▲ = $Et_3Si–PPh_2(p\text{-tol})^+$; ■ = excess $PPh_2(p\text{-tol})$

H–SiPh$_3$ and (C$_6$F$_5$)$_3$B–PPh$_2$(*p*-tol) : This combination of reagents provides ^{19}F and ^{31}P NMR spectra consistent with partial speciation of the starting materials to the Me$_2$EtSi–PPh$_2$(*p*-tol)$^+$ / H–B(C$_6$F$_5$)$_3^-$ ion pair, i.e. a mixture of starting material and ion pair. ^{19}F NMR spectrum shows a mixture of B(C$_6$F$_5$)$_3$–PPh$_2$(*p*-tol) and H–B(C$_6$F$_5$)$_3^-$ peaks. **^{19}F{^{1}H} NMR** (CH$_2$Cl$_2$, 376 MHz, 298K): δ -133.9 (d, 2F, J_{FF} = 24 Hz, *m*-C$_6$F$_5$), -156.7 (br s), -164.7 (t, 1F, J_{FF} = 20 Hz, *p*-C$_6$F$_5$), -165.0 (br s), -167.6 (m). **^{31}P{^{1}H} NMR** (CH$_2$Cl$_2$, 162 MHz, 298K): no clear identifiable peaks.

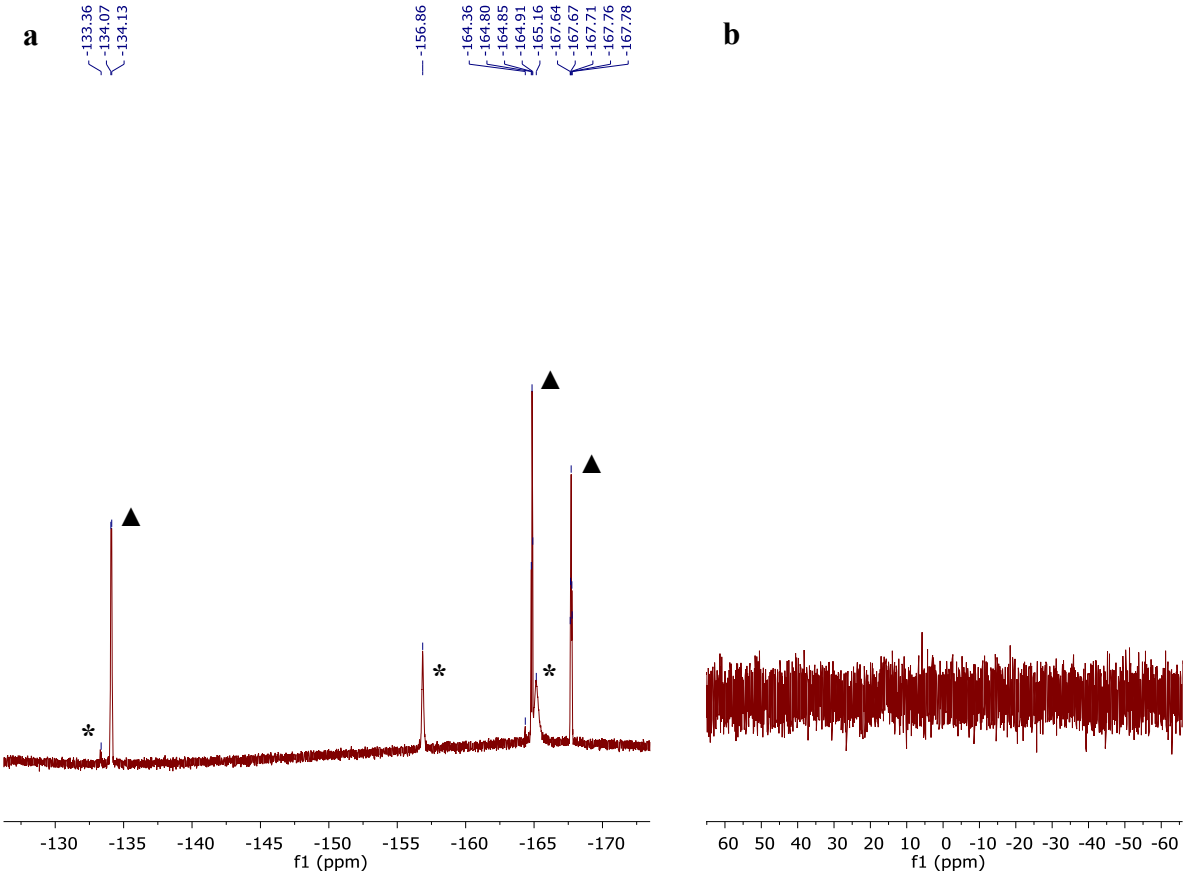

Figure 2.15. B(C$_6$F$_5$)$_3$, PPh$_2$(*p*-tol), and Ph$_3$SiH speciation

a. ^{19}F{^{1}H} NMR spectrum of the solution obtained from the combination of B(C$_6$F$_5$)$_3$, PPh$_2$(*p*-tol), and Ph$_3$SiH. The spectrum is consistent with partial speciation of the starting materials to the Ph$_3$Si–PPh$_2$(*p*-tol)$^+$ / H–B(C$_6$F$_5$)$_3^-$ ion pair. The peaks indicated with (*) correspond to unreacted B(C$_6$F$_5$)$_3$–PPh$_2$(*p*-tol). The peaks indicated with (▲) correspond to the H–B(C$_6$F$_5$)$_3^-$ anion.[54] b. ^{31}P{^{1}H} NMR

spectrum of the solution obtained from the combination of $B(C_6F_5)_3$, PPh_2(*p*-tol), and Ph_3SiH. No clear identifiable peaks are visible.

H–SiMe$_2$*t*Bu and (C_6F_5)$_3$B–PPh$_2$(*p*-tol) : This combination of reagents provides ^{19}F and ^{31}P NMR spectra predominantly consistent with unreacted starting materials. No speciation of the starting materials to the Me$_2$*t*BuSi–PPh$_2$(*p*-tol)$^+$ / H–B(C_6F_5)$_3^-$ ion pair is evident. **$^{19}F\{^1H\}$ NMR** (CH_2Cl_2, 376 MHz, 298K): δ -127.3 (br s), -156.8 (t), -165.0 (br s). **$^{31}P\{^1H\}$ NMR** (CH_2Cl_2, 162 MHz, 298K): δ 16.9 (br s).

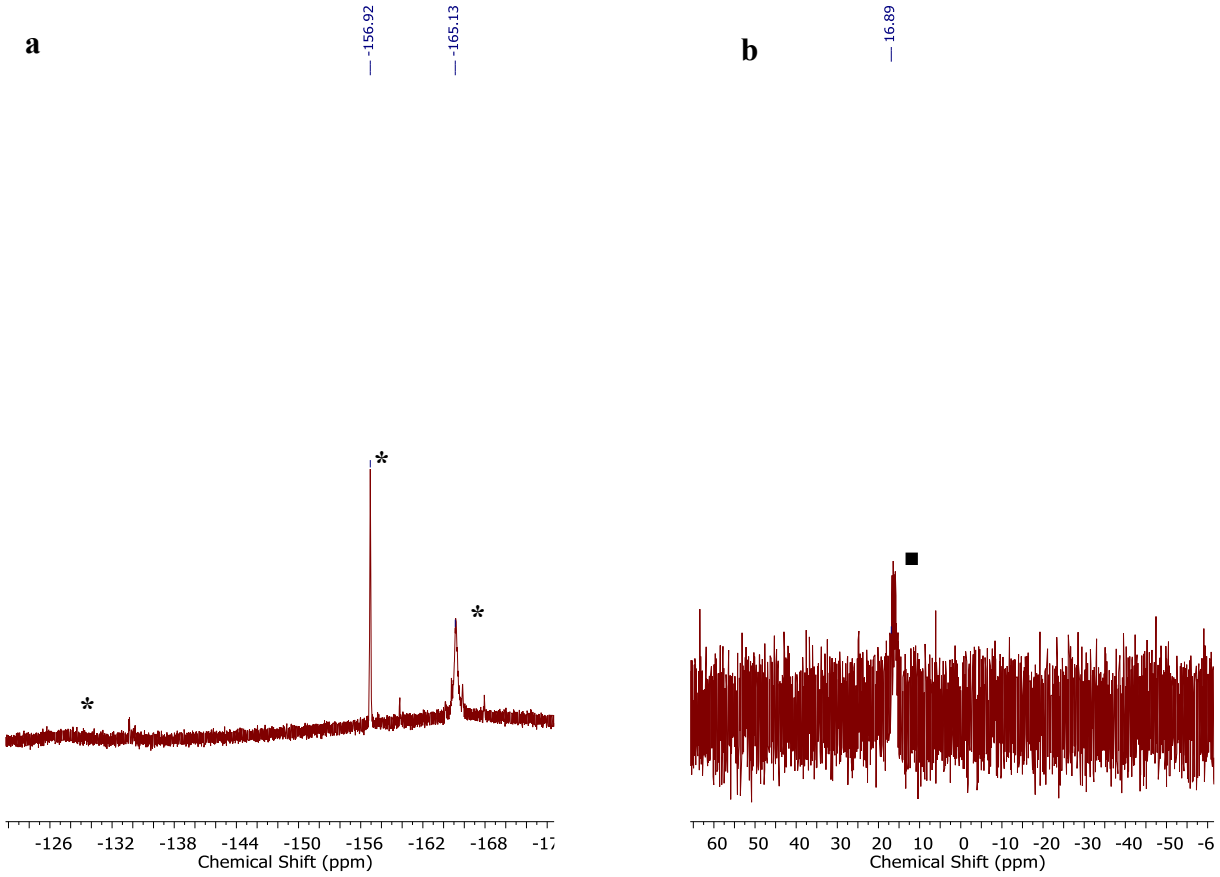

Figure 2.16. $B(C_6F_5)_3$, PPh_2(*p*-tol), and Me$_2$*t*BuSiH speciation

a. $^{19}F\{^1H\}$ NMR spectrum of the solution obtained from the combination of $B(C_6F_5)_3$, PPh_2(*p*-tol), and Me$_2$*t*BuSiH. No evidence for significant ion pair formation is evident. The peaks indicated with (*) correspond to unreacted (C_6F_5)$_3$B–PPh$_2$(*p*-tol). b. $^{31}P\{^1H\}$ NMR spectrum of the solution obtained from

the combination of $B(C_6F_5)_3$, PPh_2(*p*-tol), and Me_2*t*BuSiH. No evidence for significant ion pair formation is evident. The peak indicated with (■) corresponds to unreacted $(C_6F_5)_3B–PPh_2$(*p*-tol).

H–Si(*i*-Pr)$_3$ and $(C_6F_5)_3B–PPh_2$(*p*-tol) : This combination of reagents provides ^{19}F and ^{31}P NMR spectra predominantly consistent with unreacted starting materials. No speciation of the starting materials to $iPr_3Si–PPh_2(p\text{-tol})^+$/ $H–B(C_6F_5)_3^-$ ion pair is evident. **$^{19}F\{^1H\}$ NMR** (CH_2Cl_2, 376 MHz, 298K): δ -127.3 (br s), -156.8 (t), -165.1 (br s). **$^{31}P\{^1H\}$ NMR** (CH_2Cl_2, 162 MHz, 298K): δ 16.8 (br s).

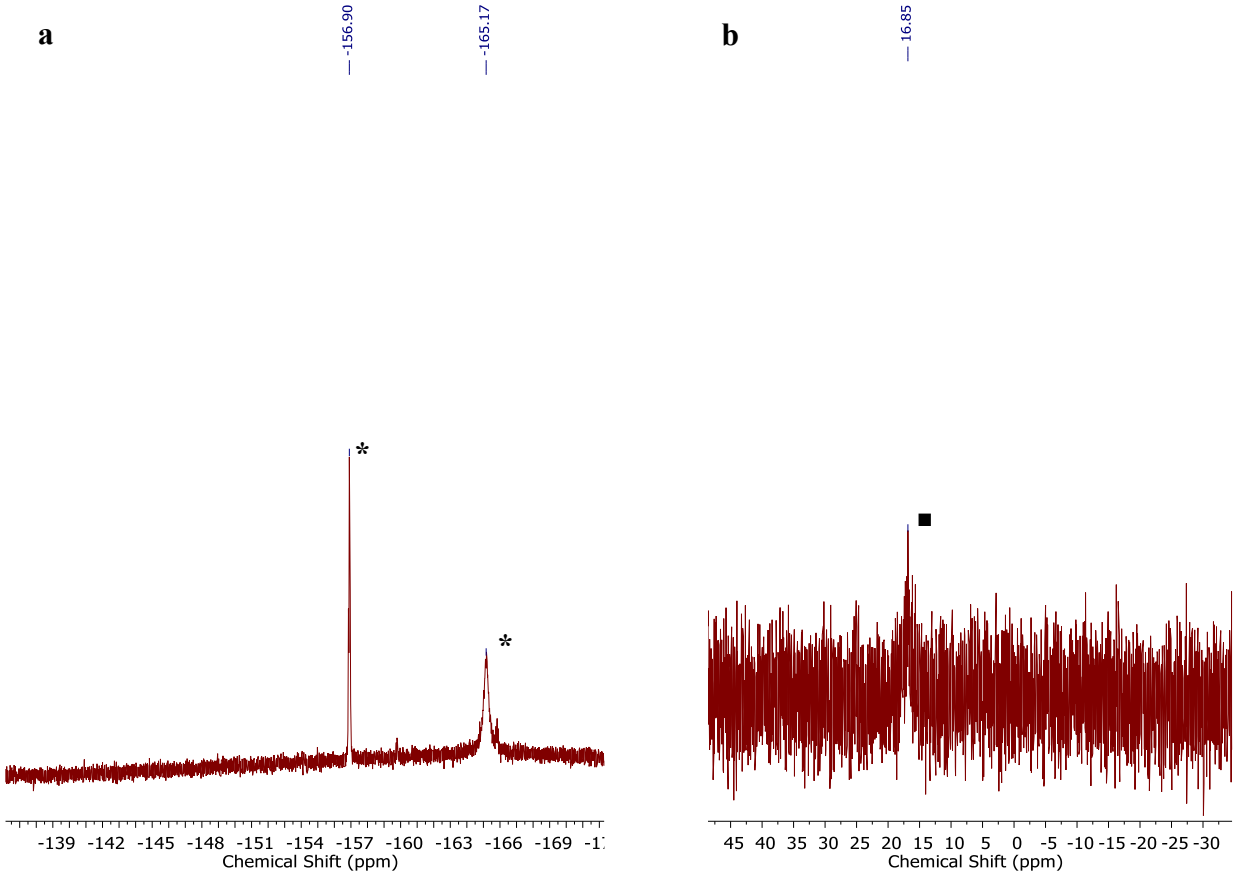

Figure 2.17. $B(C_6F_5)_3$, PPh_2(*p*-tol), and *i*Pr_3SiH speciation

a. $^{19}F\{^1H\}$ NMR spectrum of the solution obtained from the combination of $B(C_6F_5)_3$, PPh_2(*p*-tol), and *i*Pr_3SiH. No evidence for significant ion pair formation is evident. The peaks indicated with (*) correspond to unreacted $(C_6F_5)_3B–PPh_2$(*p*-tol). b. $^{31}P\{^1H\}$ NMR spectrum of the solution obtained from

the combination of $B(C_6F_5)_3$, PPh_2(*p*-tol), and *i*Pr_3SiH. No evidence for significant ion pair formation is evident. The peak indicated with (■) corresponds to unreacted $(C_6F_5)_3B–PPh_2$(*p*-tol).

Generating the $Et_3Si–PAr_3^+$ / $H–B(C_6F_5)_3^-$ ion pairs

Inside a nitrogen-filled glovebox at room temperature, a 1-dram vial was loaded with 1.0 equivalent of $B(C_6F_5)_3$ (5.1 mg, 0.01 mmol), followed by 1.0 equivalent (0.01 mmol) of the appropriate triaryl phosphine (PAr_3) and CH_2Cl_2 (0.5 mL) to dissolve the mixture. The solution was then transferred via syringe to an NMR tube, which was septum sealed and removed from the glovebox. 10 equivalents of $H–SiEt_3$ (16.0 μL, 0.10 mmol) were added to the NMR tube via syringe through the septum, and the resulting mixture analyzed by ^{19}F and ^{31}P NMR spectroscopy. Relevant NMR spectra of these compounds can be found below.

This combination of reagents provides ^{19}F and ^{31}P NMR spectra consistent with complete speciation to the $Et_3Si–PPh_2$(*o*-biphen)$^+$ / $H–B(C_6F_5)_3^-$ ion pair. **$^{19}F\{^1H\}$ NMR** (CH_2Cl_2, 376 MHz, 298K): δ -133.9 (br s), -164.8 (br s), -167.6 (br s). **$^{31}P\{^1H\}$ NMR** (CH_2Cl_2, 162 MHz, 298K): δ -0.4 (s).

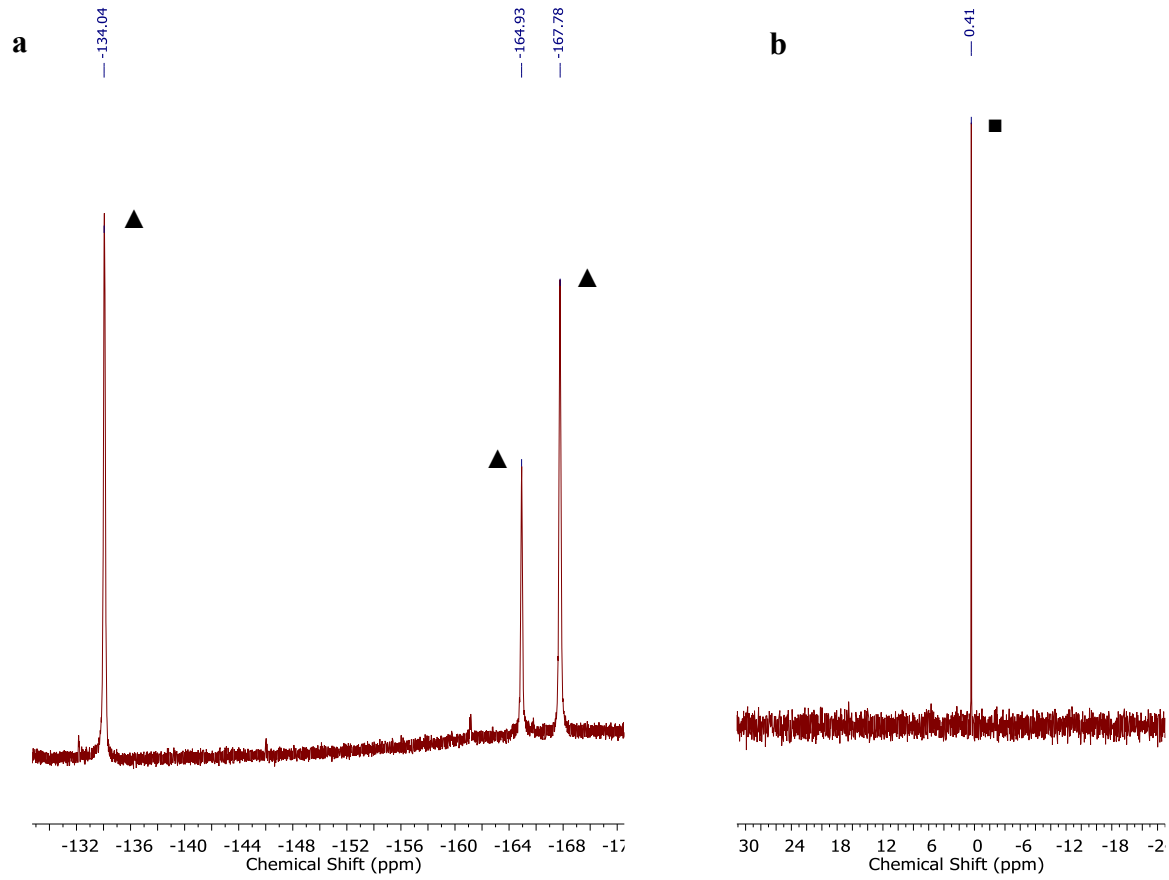

Figure 2.18. $B(C_6F_5)_3$, PPh_2(*o*-biphen), and Et_3SiH speciation

a. $^{19}F\{^1H\}$ NMR spectrum of the solution obtained from the combination of $B(C_6F_5)_3$, PPh_2(*o*-biphen), and Et_3SiH. The spectrum is consistent with complete speciation of the starting materials to the $Et_3Si–PPh_2$(*o*-biphen)$^+$ / $H–B(C_6F_5)_3^-$ ion pair. The peaks indicated with (▲) correspond to the $H–B(C_6F_5)_3^-$ anion.[54] b. $^{31}P\{^1H\}$ NMR spectrum of the solution obtained from the combination of $B(C_6F_5)_3$, PPh_2(*o*-biphen), and Et_3SiH. The spectrum is consistent with complete speciation of the starting materials to the $Et_3Si–PPh_2$(*o*-biphen)$^+$ / $H–B(C_6F_5)_3^-$ ion pair. The peak indicated with (■) is assigned to the $Et_3Si–PPh_2$(*o*-biphen)$^+$ cation. . The peak indicated with (■) is assigned to the $Et_3Si–PPh_2$(*o*-biphen)$^+$ cation.

This combination of reagents provides ^{19}F and ^{31}P NMR spectra predominantly consistent with unreacted starting materials. No speciation of the starting materials to $Et_3Si–P(o\text{-tol})_3^+$/ $H–B(C_6F_5)_3^-$ ion pair is evident. **$^{19}F\{^1H\}$ NMR** (CH_2Cl_2, 376 MHz, 298K): δ -128.9 (br s), -144.7 (br s), -161.7 (br s). **$^{31}P\{^1H\}$ NMR** (CH_2Cl_2, 162 MHz, 298K): δ -29.0 (s).

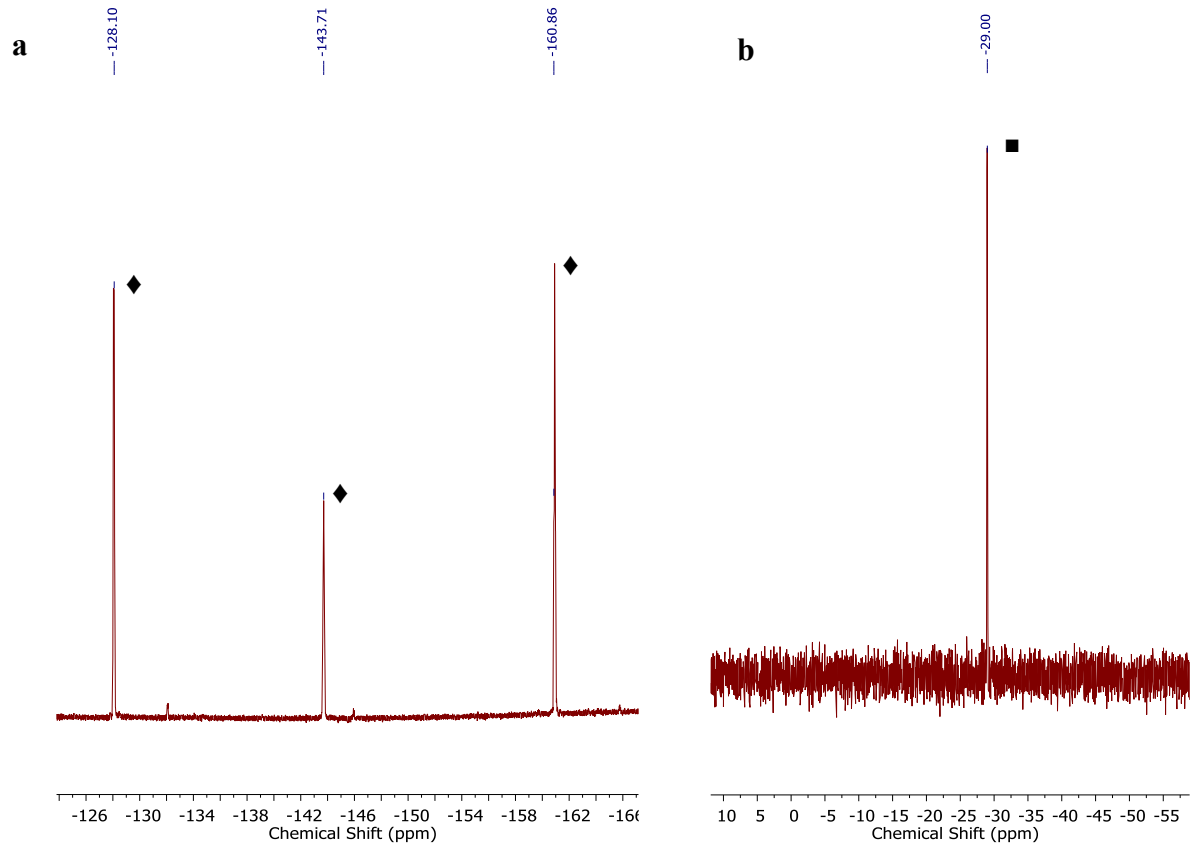

Figure 2.19. $B(C_6F_5)_3$, P(*o*-tol)$_3$, and Et_3SiH speciation

a. $^{19}F\{^1H\}$ NMR spectrum of the solution obtained from the combination of $B(C_6F_5)_3$, P(*o*-tol)$_3$, and Et_3SiH. No evidence for significant ion pair formation is evident. The peaks indicated with (♦) correspond to the free $B(C_6F_5)_3$ species. b. $^{31}P\{^1H\}$ NMR spectrum of the solution obtained from the combination of $B(C_6F_5)_3$, P(*o*-tol)$_3$, and Et_3SiH. No evidence for significant ion pair formation is evident. The peak indicated with (■) corresponds to the free P(*o*-tol)$_3$ species.

This combination of reagents provides ^{19}F and ^{31}P NMR spectra consistent with partial speciation to the $Et_3Si–P(p\text{-Cl-Ph})_3$ / $H–B(C_6F_5)_3^-$ ion pair, i.e. a mixture of starting material and ion pair. Traces of the relatively insoluble $(C_6F_5)_3B–P(p\text{-Cl-Ph})_3$ remain as observed inside the NMR tube, and confirmed by the presence of the corresponding peaks in ^{19}F NMR spectrum(*). **$^{19}F\{^1H\}$ NMR** (CH_2Cl_2, 376 MHz, 298K): δ -127.3 (br s), -134.0 (d, J_{FF} = 24 Hz), -154.9 (br s), -

164.0 (br s), -164.7 (t, J_{FF} = 20 Hz), -167.6 (m). **$^{31}P\{^{1}H\}$ NMR** (CH_2Cl_2, 162 MHz, 298K): δ -1.6 (s).

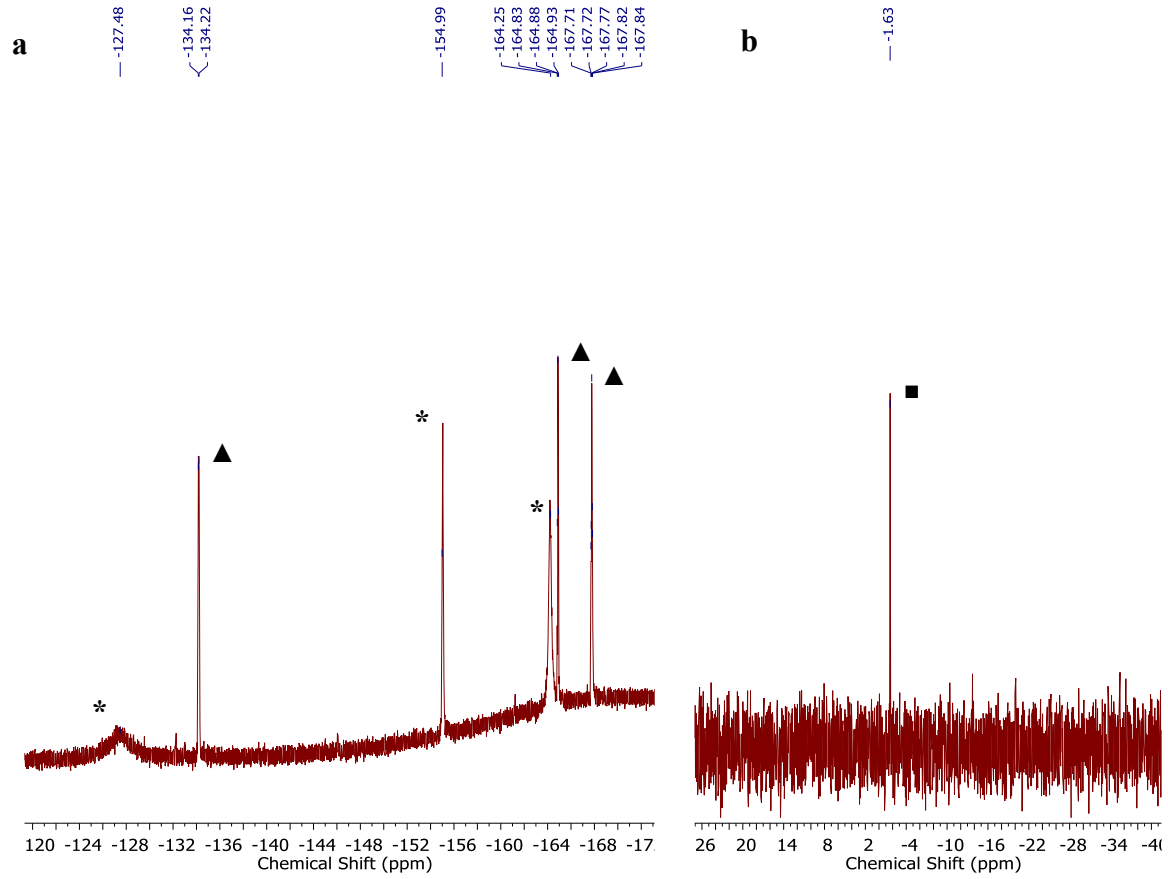

Figure 2.20. $B(C_6F_5)_3$, P(*p*-Cl-Ph)$_3$, and Et_3SiH speciation

a. $^{19}F\{^{1}H\}$ NMR spectrum of the solution obtained from the combination of $B(C_6F_5)_3$, P(*p*-Cl-Ph)$_3$, and Et_3SiH. The spectrum is consistent with partial speciation of the starting materials to the Et_3Si–P(*p*-Cl-Ph)$_3^+$ / H–$B(C_6F_5)_3^-$ ion pair. The peaks indicated with (*) correspond to unreacted $(C_6F_5)_3$B–P(*p*-Cl-Ph)$_3$. The peaks indicated with (▲) correspond to the H–$B(C_6F_5)_3^-$ anion.[54] b. $^{31}P\{^{1}H\}$ NMR spectrum of the solution obtained from the combination of $B(C_6F_5)_3$, P(*p*-Cl-Ph)$_3$, and Et_3SiH. The spectrum is consistent with partial speciation of the starting materials to the Et_3Si–P(*p*-Cl-Ph)$_3^+$ / H–$B(C_6F_5)_3^-$ ion pair. The peak indicated with (■) is assigned to the Et_3Si–P(*p*-Cl-Ph)$_3^+$ cation.

This combination of reagents provides ^{19}F and ^{31}P NMR spectra consistent with partial speciation to the Et_3Si–P(*p*-F-Ph)$_3^+$ / H–$B(C_6F_5)_3^-$ ion pair. Traces of the relatively insoluble

$(C_6F_5)_3B–P(p\text{-Cl-Ph})_3$ remain as observed inside the NMR tube, and confirmed by the presence of the corresponding peaks in ^{19}F NMR spectrum(*). **$^{19}F\{^1H\}$ NMR** (CH_2Cl_2, 376 MHz, 298K): δ -100.5 (s), -134.0 (br s), -155.4 (br s), -164.3 (br s), -164.7 (t), -167.6 (m) **$^{31}P\{^1H\}$ NMR** (CH_2Cl_2, 162 MHz, 298K): δ -3.8 (s).

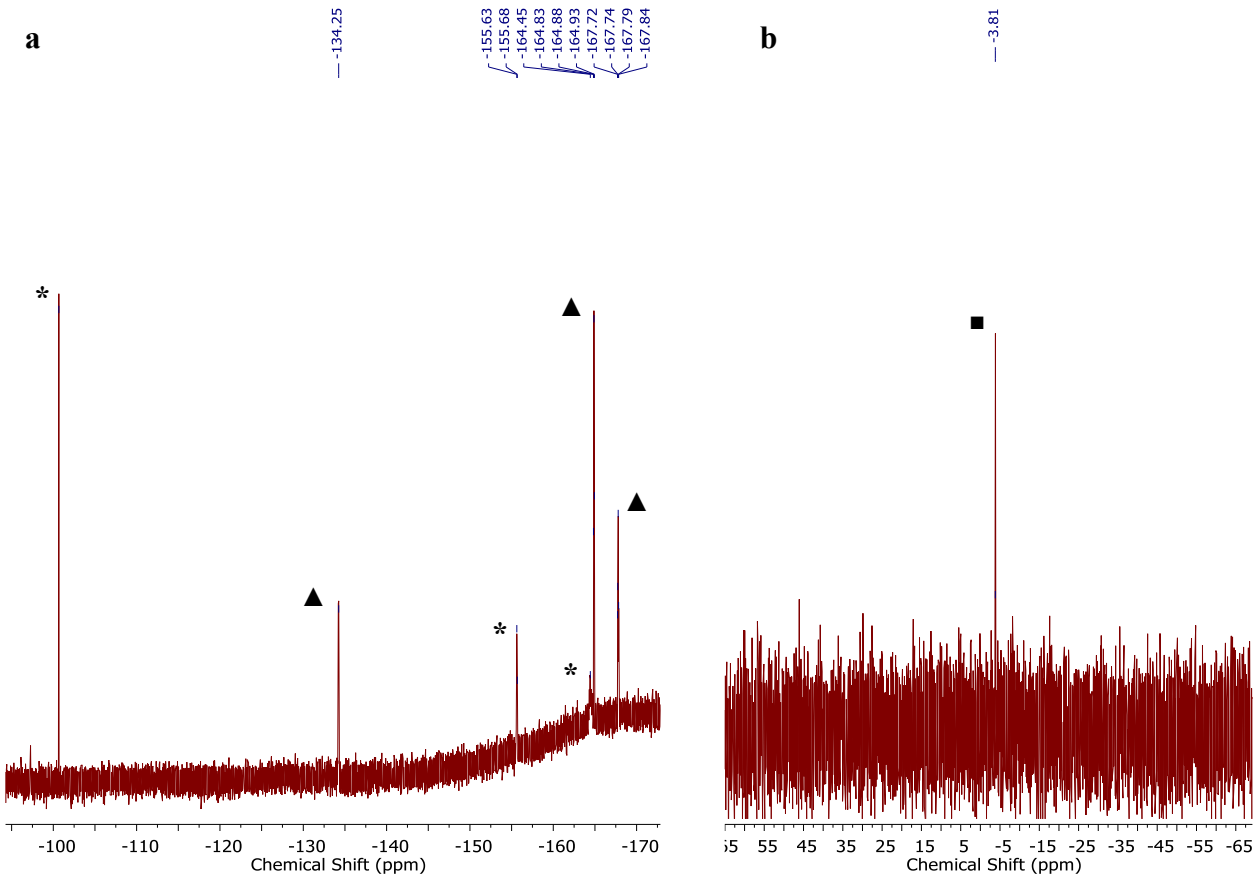

Figure 2.21. $B(C_6F_5)_3$, $P(p\text{-F-Ph})_3$, and Et_3SiH speciation

a. $^{19}F\{^1H\}$ NMR spectrum of the solution obtained from the combination of $B(C_6F_5)_3$, $P(p\text{-F-Ph})_3$, and Et_3SiH. The spectrum is consistent with partial speciation of the starting materials to the $Et_3Si–P(p\text{-F-Ph})_3^+$ / $H–B(C_6F_5)_3^-$ ion pair. The peaks indicated with (*) correspond to unreacted $(C_6F_5)_3B–P(p\text{-F-Ph})_3$. The peaks indicated with (▲) correspond to the $H–B(C_6F_5)_3^-$ anion.[54] b. $^{31}P\{^1H\}$ NMR spectrum of the solution obtained from the combination of $B(C_6F_5)_3$, $P(p\text{-F-Ph})_3$, and Et_3SiH. The spectrum is consistent with partial speciation of the starting materials to the $Et_3Si–P(p\text{-F-Ph})_3^+$ / $H–B(C_6F_5)_3^-$ ion pair. The peak indicated with (■) is assigned to the $Et_3Si–P(p\text{-F-Ph})_3^+$ cation.

This combination of reagents provides ^{19}F and ^{31}P NMR spectra depicting a complex mixture, including unreacted $B(C_6F_5)_3$. No speciation of the starting materials to the $Et_3Si–PCy_3^+$ / $H–B(C_6F_5)_3^-$ ion pair is evident. **$^{19}F\{^1H\}$ NMR** (CH_2Cl_2, 376 MHz, 298K): δ -131.9 (s), -132.6 (s), -133.4 (s), -133.5 (s), -143.6 (br s), -145.8 (br s), -160.8 (s), -163.5 (m), -167.1 (m), -175.8 (m). **$^{31}P\{^1H\}$ NMR** (CH_2Cl_2, 162 MHz, 298K): δ 40.6 (s).

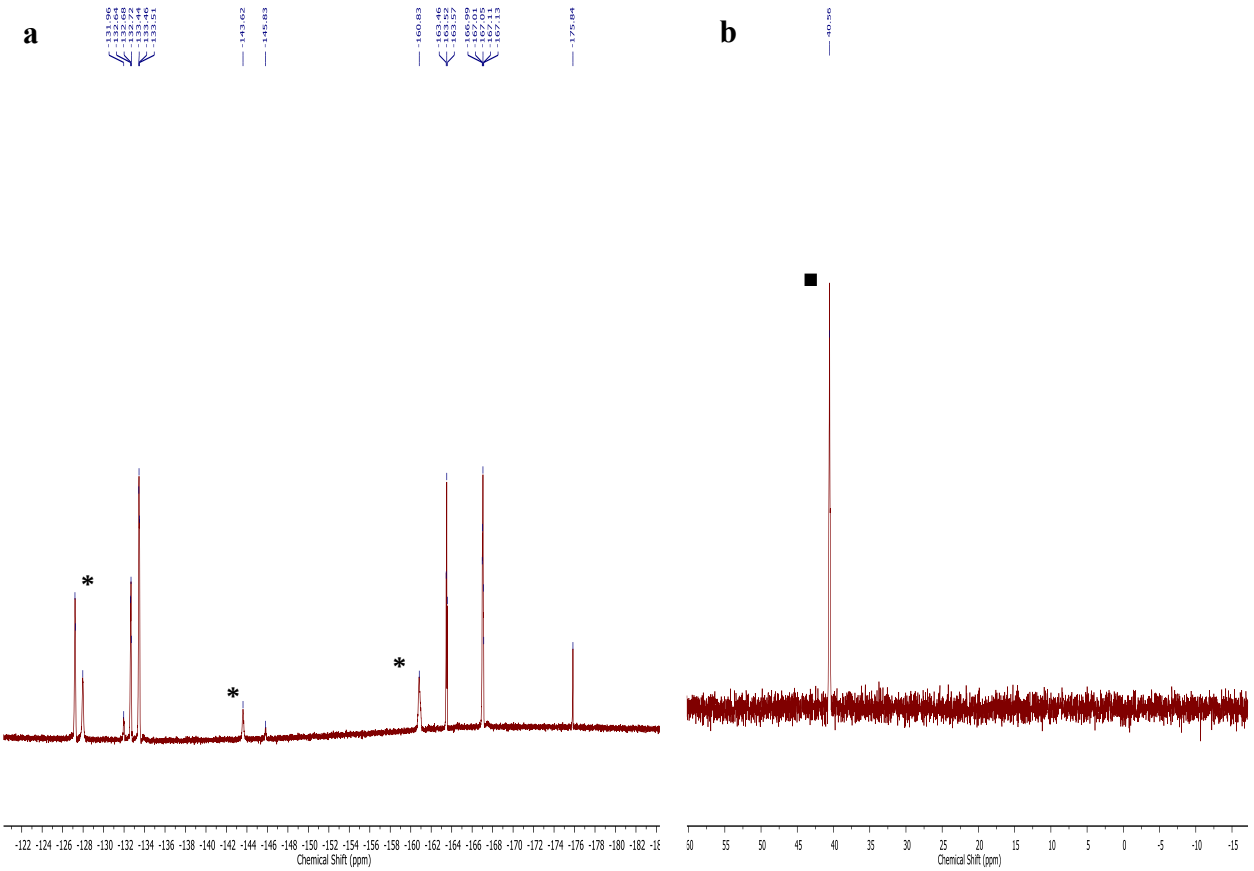

Figure 2.22. $B(C_6F_5)_3$, PCy_3, and Et_3SiH speciation

a. $^{19}F\{^1H\}$ NMR spectrum of the solution obtained from the combination of $B(C_6F_5)_3$, PCy_3, and Et_3SiH. No evidence for ion pair formation is evident. The peaks indicated with (*) correspond to unreacted $B(C_6F_5)_3$. The remaining peaks do correspond to the $H–B(C_6F_5)_3^-$ anion. b. $^{31}P\{^1H\}$ NMR spectrum of the solution obtained from the combination of $B(C_6F_5)_3$, PCy_3, and Et_3SiH. No evidence for significant ion pair formation is evident. The peak indicated with (■) is assigned to $(C_6F_5)_3B–PCy_3$.

This combination of reagents provides ^{19}F and ^{31}P NMR spectra predominantly consistent with unreacted starting materials. No speciation of the starting materials to the $Et_3Si–P(n\text{-}Bu)_3^+$ / $H–B(C_6F_5)_3^-$ ion pair is evident. **$^{19}F\{^1H\}$ NMR** (CH_2Cl_2, 376 MHz, 298K): δ -128.0 (s), -129.5 (m), -143.6 (br s), -157.1 (d, J_{FF} = 21 Hz), -160.9 (br s), -164.0 (m). **$^{31}P\{^1H\}$ NMR** (CH_2Cl_2, 162 MHz, 298K): δ -0.07 (br s).

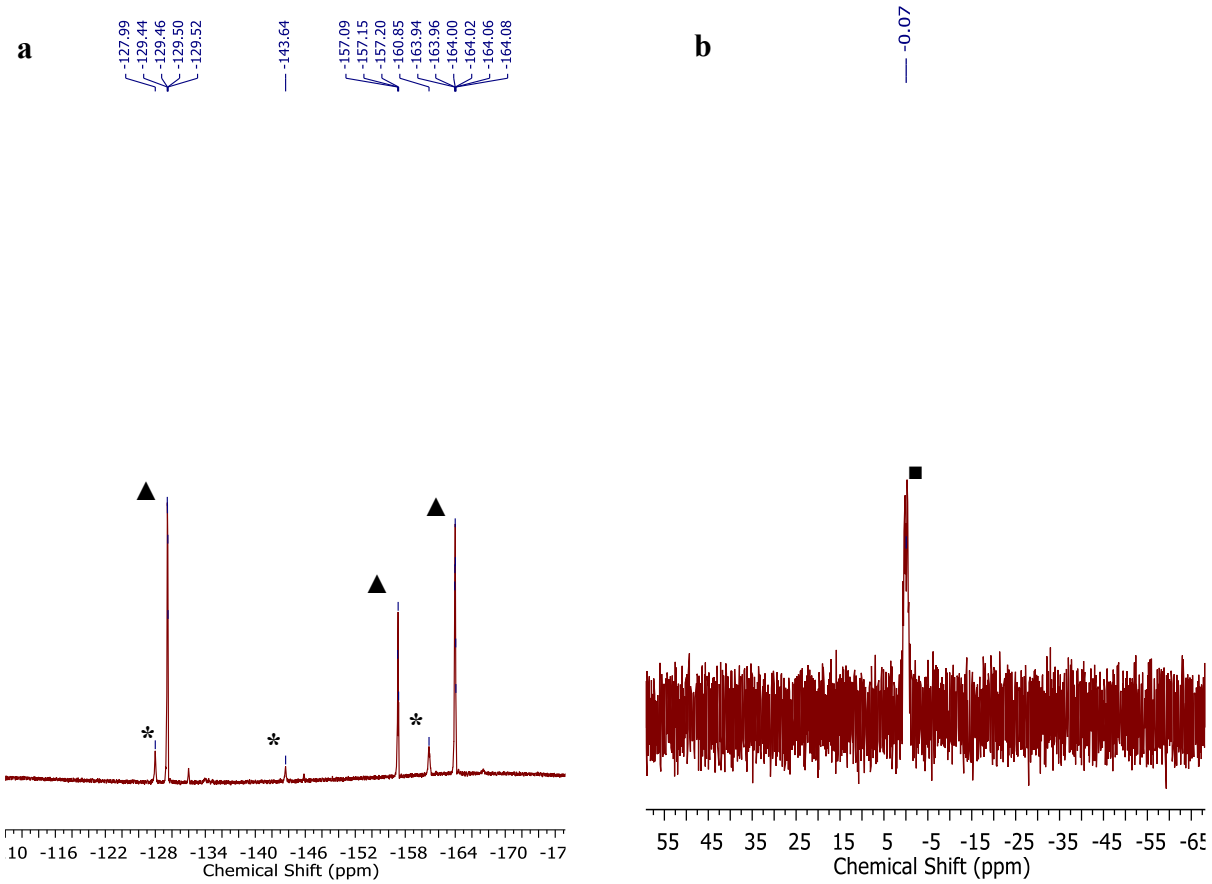

Figure 2.23. $B(C_6F_5)_3$, $P(n\text{-}Bu)_3$, and Et_3SiH speciation

a. $^{19}F\{^1H\}$ NMR spectrum of the solution obtained from the combination of $B(C_6F_5)_3$, $P(n\text{-}Bu)_3$, and Et_3SiH. No evidence for significant ion pair formation is evident. The peaks indicated with (▲) correspond to unreacted (C6F5)3B–P(n-Bu)$_3$. The peaks indicated with (*) correspond to unreacted $B(C_6F_5)_3$. b.$^{31}P\{^1H\}$ NMR spectrum of the solution obtained from the combination of $B(C_6F_5)_3$, $P(n\text{-}Bu)_3$, and Et_3SiH. No evidence for significant ion pair formation is evident. The peak indicated with (■) corresponds to unreacted (C6F5)3B–P(n-Bu)$_3$.

This combination of reagents provides ^{19}F and ^{31}P NMR spectra depicting a complex mixture. No speciation to the $Me_2EtSi–PCy_3^+$ / $H–B(C_6F_5)_3^-$ ion pair is evident. **$^{19}F\{^1H\}$ NMR** (CH_2Cl_2, 376 MHz, 298K): δ -127.4 (br s), -132.8 (m), -133.6 (m), -163.6 (t, 1F, J_{FF} = 20 Hz), -164.0 (br s), -167.2 (m). **$^{31}P\{^1H\}$ NMR** (CH_2Cl_2, 162 MHz, 298K): δ 41.0 (s), 40.5 (t), 10.5 (s).

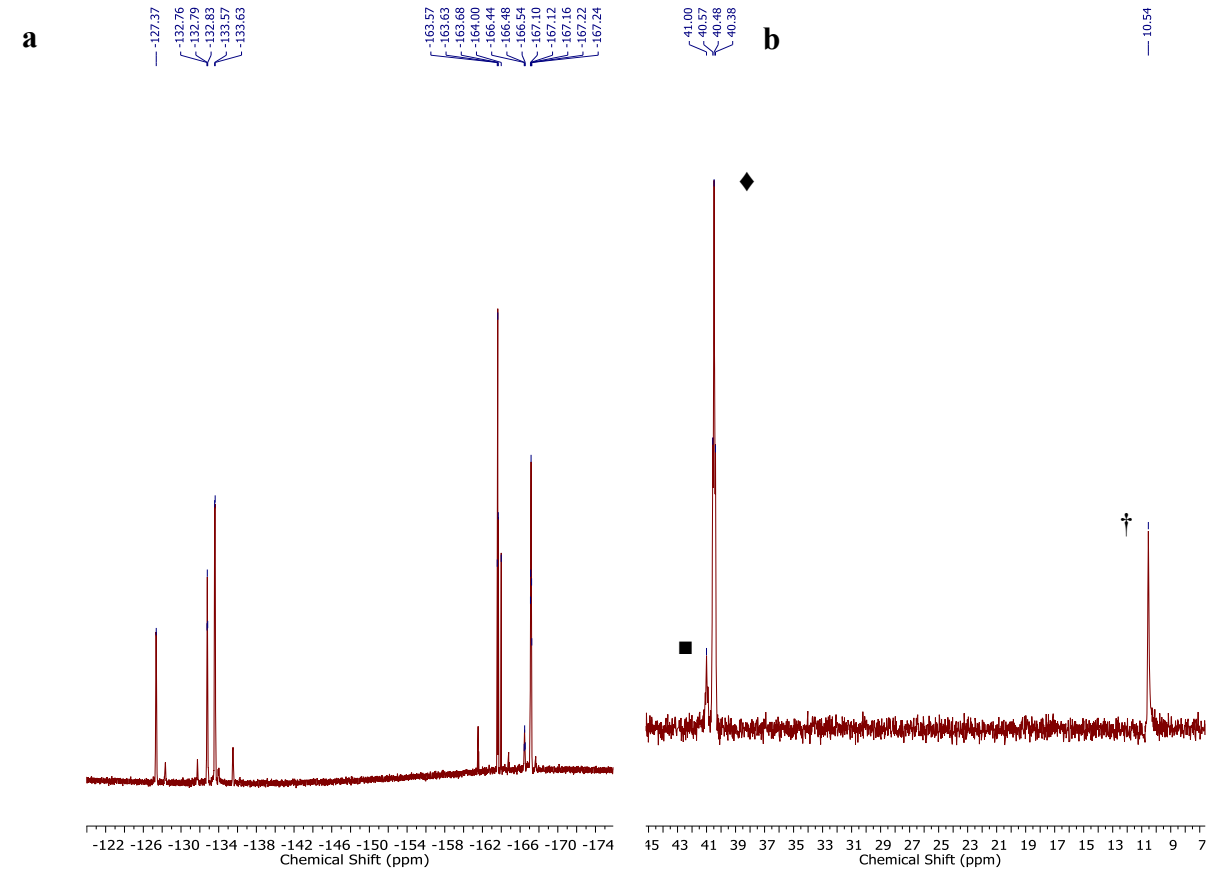

Figure 2.24. $B(C_6F_5)_3$, PCy_3, and Me_2EtSiH speciation

a. $^{19}F\{^1H\}$ NMR spectrum of the solution obtained from the combination of $B(C_6F_5)_3$, PCy_3, and Me_2EtSiH. No evidence for ion pair formation is evident (complex mixture). No peaks correspond to the $H–B(C_6F_5)_3^-$ anion. b. $^{31}P\{^1H\}$ NMR spectrum of the solution obtained from the combination of $B(C_6F_5)_3$, PCy_3, and Me_2EtSiH. The peaks indicated with (■) and with (♦) are assigned to unreacted $(C_6F_5)_3B–PCy_3$. The peak indicated with (†) corresponds to the free PCy_3.

This combination of reagents provides ^{19}F and ^{31}P NMR spectra consistent with partial speciation of the starting materials to the $Me_2EtSi–P(n\text{-}Bu)_3^+$ / $H–B(C_6F_5)_3^-$ ion pair. ^{19}F NMR spectrum shows a mixture of $B(C_6F_5)_3–P(n\text{-}Bu)_3$ and $H–B(C_6F_5)_3^-$ peaks. **$^{19}F\{^1H\}$ NMR** (CH_2Cl_2, 376 MHz, 298K): δ -129.6 (m), -134.0 (d, J_{FF} = 24 Hz), -157.3 (br s), -164.1 (m), -164.8 (t, J_{FF} = 20 Hz), -167.7 (m). **$^{31}P\{^1H\}$ NMR** (CH_2Cl_2, 162 MHz, 298K): δ -0.07 (br s), -11.0 (s).

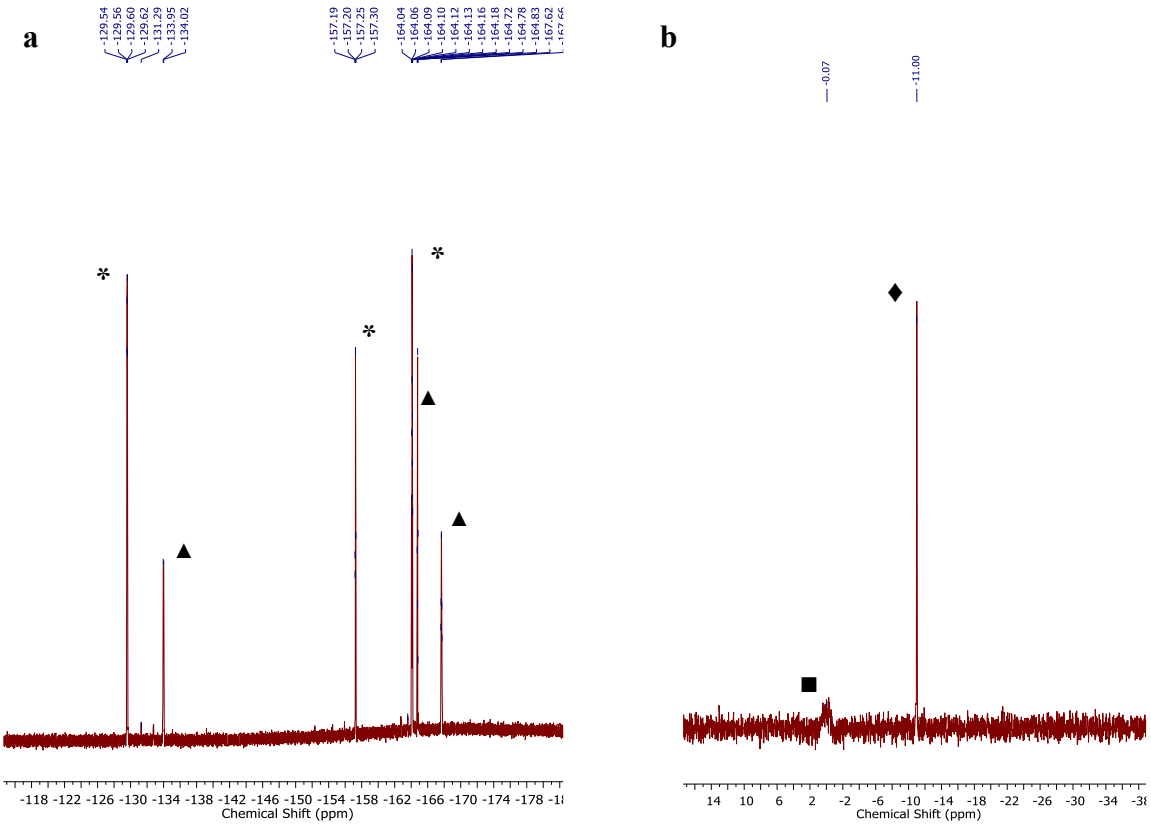

Figure 2.25. $B(C_6F_5)_3$, $P(n\text{-}Bu)_3$, and Me_2EtSiH speciation

a. $^{19}F\{^1H\}$ NMR spectrum of the solution obtained from the combination of $B(C_6F_5)_3$, $P(n\text{-}Bu)_3$, and Me_2EtSiH. The spectrum is consistent with partial speciation of the starting materials to the $Me_2EtSi–P(n\text{-}Bu)_3$ / $H–B(C_6F_5)_3^-$ ion pair. The peaks indicated with (*) correspond to unreacted $B(C_6F_5)_3–P(n\text{-}Bu)_3$. The peaks indicated with (▲) correspond to the $H–B(C_6F_5)_3^-$ anion.[54] b. $^{31}P\{^1H\}$ NMR spectrum of the solution obtained from the combination of $B(C_6F_5)_3$, $P(n\text{-}Bu)_3$, and Me_2EtSiH. The peak indicated with (■) corresponds to unreacted $(C_6F_5)_3B–P(n\text{-}Bu)_3$. The peak indicated with (♦) is assigned to the $Me_2EtSi–P(n\text{-}Bu)_3^+$ cation.

2.8.4. Kinetic experiments – determining the order in Et_3SiH

Inside a nitrogen-filled glovebox at room temperature, 1.0 equivalent of $(C_6F_5)_3B–PPh_2$(*p*-tol) (7.9 mg, 0.01 mmol) was added to a 1-dram vial followed by CH_2Cl_2 (0.5 mL) to dissolve the solid. The resulting mixture was transferred via syringe to an NMR tube containing a C_6H_5F (in C_6D_6 for spectrometer solvent lock) standard capillary insert (80 mM). The NMR tube was sealed with a septum and removed from the glovebox. 10 equivalents of $H–SiEt_3$ (16.0 μL, 0.10 mmol) were added to the NMR tube via syringe through the septum, the resulting tube quickly mixed, inserted into the probe, and [$(C_6F_5)_3B–PPh_2$(*p*-tol)] vs. time data obtained by ^{19}F NMR spectroscopy over the course of 5 minutes. Upon locking to the C_6D_6 solvent of the standard capillary insert, ^{19}F NMR spectra (8 scans) were consecutively obtained. The C_6H_5F standard signal at -112.96 ppm was used as a reference to monitor the disappearance of $B(C_6F_5)_3–PPh_2$(*p*-tol) and the growth of $H–B(C_6F_5)_3^-$. ^{31}P NMR spectra were taken at the end of the reaction to confirm the presence of the $Et_3Si–PPh_2$(*p*-tol)$^+$ species.

Table 2.4. Raw data for the reaction of $(C_6F_5)_3B–PPh_2$(*p*-tol) with $H–SiEt_3$[a]

Run	$(C_6F_5)_3B–PPh_2$(*p*-tol)			$H–SiEt_3$			k_{obs} (s^{-1})
	Equiv.	mmol	conc. (mM)	Equiv.	mmol	conc. (mM)	
1	1.0	0.01	20	10	0.10	200	0.0018
2	1.0	0.01	20	20	0.20	400	0.0027
3	1.0	0.01	20	30	0.30	600	0.0059
4	1.0	0.01	20	40	0.40	800	0.0080
5	1.0	0.01	20	50	0.50	1000	0.0100

[a]Raw data for the reaction of $(C_6F_5)_3B–PPh_2$(*p*-tol) adduct with varying amounts of $H–SiEt_3$. $H–SiEt_3$ concentration is kept in 10-fold or more excess and varied to detemine the order in silane.

Table 2.5. Adduct disappearance over time raw data

Time after H–$SiEt_3$ addition (sec)	$(C_6F_5)_3B$–PPh_2(*p*-tol) para peak[a]	H–$B(C_6F_5)_3^-$ ortho peak integral[b]
0	8.12	0
33	4.11	6.86
72	3.38	9.50
114	2.78	11.79
154	1.72	13.35
195	1.18	14.29
233	0.82	14.77
274	0.69	15.37

[a]Referenced to the C_6H_5F external standard (-112.96 ppm). [b]Relative to the C_6F_5H external standard (set to 1.00). Starting material para peak integration was tracked with respect to the internal standard vs. H–$B(C_6F_5)_3^-$ anion product peak integration to determine the ratio of starting material conversion to the product anion.

Table 2.6. $(C_6F_5)_3B–PPh_2(p\text{-tol})$ adduct concentration vs. time

Time (sec)	SM rem.	SM Conc. (mM)
0	1.00	20
33	0.51	10.12
72	0.42	8.33
114	0.34	6.85
154	0.21	4.24
195	0.15	2.91
233	0.10	2.02
274	0.085	1.70

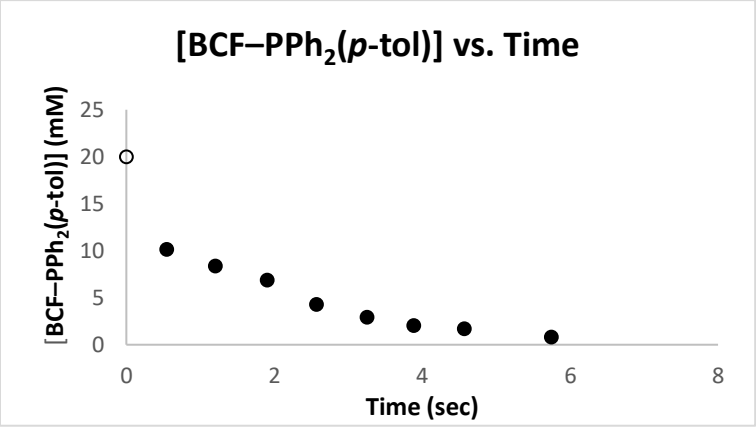

Figure 2.26. $[(C_6F_5)_3B–PPh_2(p\text{-tol})]$ vs. time plot

Concentration of $(C_6F_5)_3B–PPh_2(p\text{-tol})$ starting material vs. time as determined from ^{19}F NMR data by tracking the amount of starting material remaining at a given time point.

Table 2.7. ln[$(C_6F_5)_3B$–PPh_2(*p*-tol)] adduct concentration vs. time

Time (sec)	ln [SM]
0	2.99
33	2.31
72	2.12
114	1.92
154	1.44
195	1.07
233	0.70
274	0.53

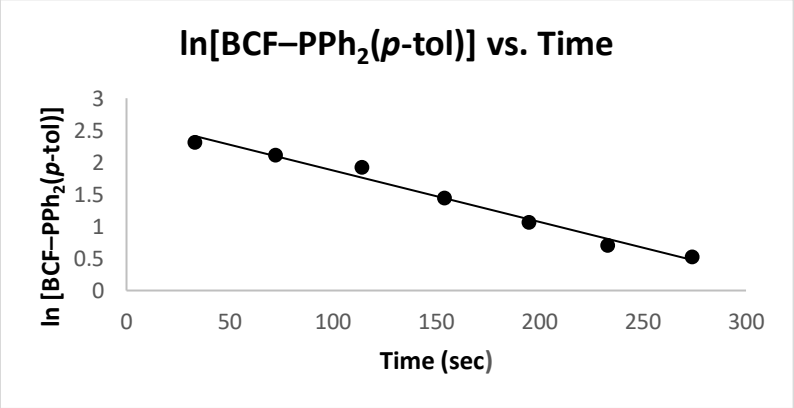

Figure 2.27. ln[$(C_6F_5)_3B$–PPh_2(*p*-tol)] vs. time plot

An example plot of ln[$(C_6F_5)_3B$–PPh_2(*p*-tol)] vs. time as determined from ^{19}F NMR data by tracking the amount of starting material remaining at a given time point.

2.8.5. Kinetic experiments – determining the order in PPh_2(*p*-tol)

Inside a nitrogen-filled glovebox at room temperature, 1.0 equivalent of $B(C_6F_5)_3$–PPh_2(*p*-tol) (7.9 mg, 0.01 mmol) was added to a 1-dram vial. To the same vial, 5-20 equivalents of excess

PPh_2(*p*-tol) (13.8-55.3 mg, 0.05-0.20 mmol) were added followed by CH_2Cl_2 (0.5 mL) to dissolve the solids. The resulting mixture was transferred via syringe to an NMR tube containing a C_6H_5F (in C_6D_6) standard capillary insert (80 mM). The NMR tube was sealed with a septum and removed from the glovebox. 20 equivalents of H–$SiEt_3$ (31.9 μL, 0.20 mmol) were added to the NMR tube via syringe through the septum, the resulting tube quickly mixed, inserted into the probe, and analyzed by ^{19}F NMR spectroscopy over the course of 5 minutes. The C_6H_5F signal from the external standard at -112.96 ppm was used as a reference to monitor the disappearance of $(C_6F_5)_3B$–PPh_2(*p*-tol) and the growth of H–$B(C_6F_5)_3^-$. ^{31}P NMR spectroscopy was used to confirm the presence of the Et_3Si–PPh_2(*p*-tol)$^+$ and the excess PPh_2(*p*-tol) species at the end of the reaction.

2.8.6. Ion pair preparation for the ^{29}Si NMR Experiment

Inside a nitrogen-filled glovebox at room temperature, 1.0 equivalent of $B(C_6F_5)_3$ (76.8 mg, 0.15 mmol) and 1.0 equivalent of PPh_2(*p*-tol) (41.4 mg, 0.15 mmol) were added to a 1-dram vial and dissolved in CD_2Cl_2 (0.5 mL). 1.0 equivalent of H–$SiEt_3$ (23.9 μL, 0.15 mmol) was added to the same 1-dram vial and the solution was transferred via syringe to an NMR tube, which was sealed with a septum and removed from the glovebox. A ^{29}Si NMR spectrum was acquired on the Bruker Avance 500 MHz spectrometer at standard temperature and pressure using a Dept-45° pulse program with the following experimental conditions: Number of scans = 1200; Delay D_1 = 5.00 sec; Sweep Width SW = 80 ppm; Acquisition Time AQ = 4.12 sec; Time per scan = D_1 + AQ = 9.12 sec. Relevant NMR spectrum can be found in Figure 2.6.

2.8.7. Silylium transfer experiment details

Inside a nitrogen-filled glovebox at room temperature, 1.0 equivalent $B(C_6F_5)_3$ (5.1 mg, 0.01 mmol) and 6.0 equivalents PPh_2(*o*-biphen) (20.3 mg, 0.06 mmol) were combined in a 1-dram vial and dissolved in CD_2Cl_2 (0.4 mL). 50 equivalents H–$SiEt_3$ (79.8 μL, 0.50 mmol) were added

to the same vial and the resulting solution transferred via syringe to an NMR tube, which was sealed with a septum cap and removed from the glovebox. The solution in the NMR tube was analyzed by ^{31}P and ^{19}F NMR spectroscopy to observe speciation to the $Et_3Si–PPh_2(o\text{-biphen})^+$ / $H–B(C_6F_5)_3^-$ ion pair. After 10 minutes, a solution of 5.0 equivalents $PPh_2(p\text{-tol})$ (13.8 mg, 0.05 mmol) in CD_2Cl_2 (0.2 mL) was added to the same NMR tube via syringe through the septum, and the resulting mixture analyzed by ^{31}P and ^{19}F NMR spectroscopy. Relevant NMR spectra can be found below.

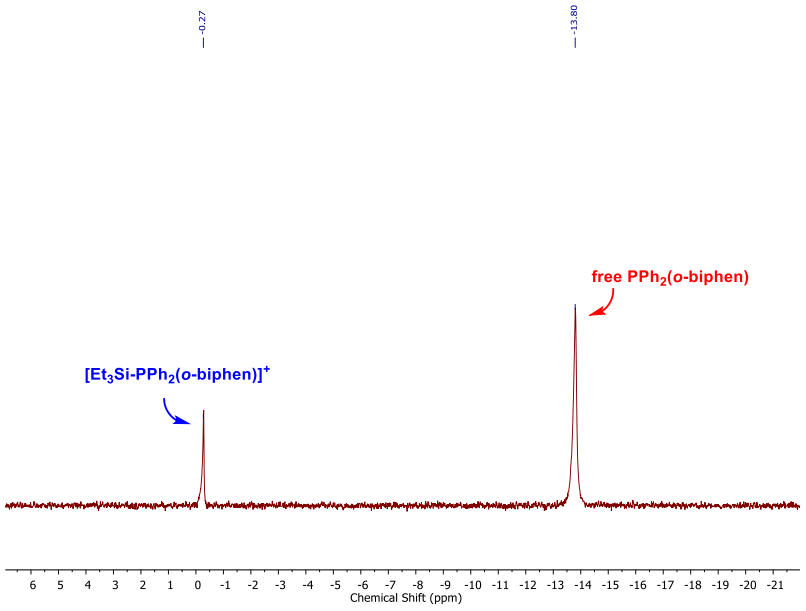

Figure 2.28. Excess $PPh_2(o\text{-biphen})$ transfer experiment

$^{31}P\{^1H\}$ NMR spectrum of the $Et_3Si–PPh_2(o\text{-biphen})^+$ / $H–B(C_6F_5)_3^-$ ion pair and excess $PPh_2(o\text{-biphen})$ in CD_2Cl_2.

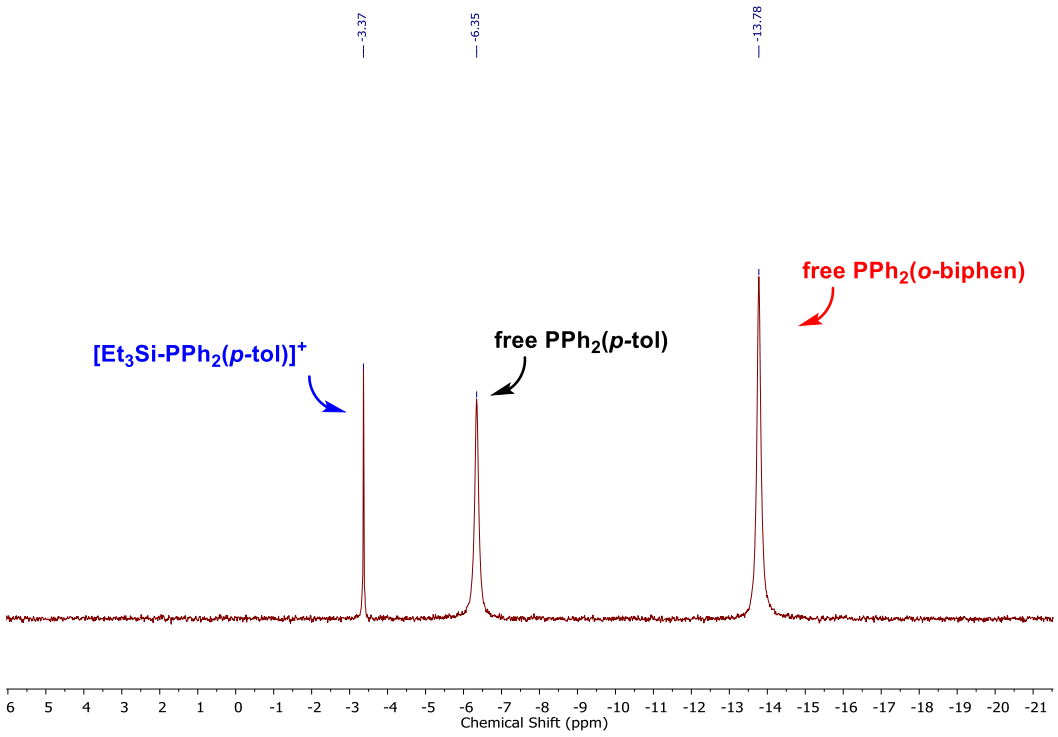

Figure 2.29. Excess PPh_2(*o*-biphen) and PPh_2(*p*-tol) transfer experiment

$^{31}P\{^1H\}$ NMR spectrum of the $Et_3Si–PPh_2$(*p*-tol)$^+$ / H–$B(C_6F_5)_3^-$ ion pair and excess PPh_2(*o*-biphen) and PPh_2(*p*-tol) in CD_2Cl_2, indicating that 1) Et_3Si^+ transfer is rapid from one phosphine to another, 2) that it favorably coordinates to PPh_2(*p*-tol), and 3) that it exchanges between phosphines at a rate that is slower than the NMR timescale.

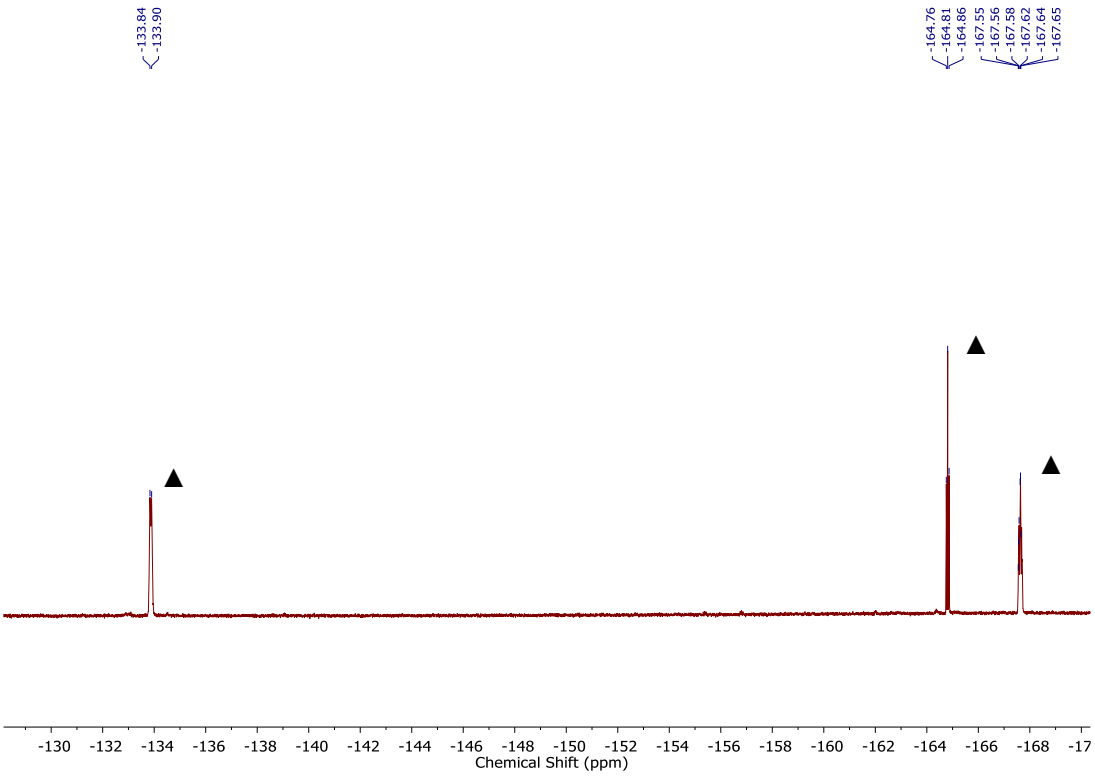

Figure 2.30. $^{19}F\{^{1}H\}$ NMR spectrum during phosphine exchange

$^{19}F\{^{1}H\}$ NMR spectrum of $Et_3Si–PPh_2(p\text{-tol})^+$ / $H–B(C_6F_5)_3^-$ ion pair confirming the presence of the $H–B(C_6F_5)_3^-$ anion throughout the phosphine exchange experiment. The peaks indicated with (▲) correspond to the $H–B(C_6F_5)_3^-$ anion.[54]

2.8.8. Catalytic anisole reduction studies

Inside a nitrogen-filled glovebox at room temperature, 0.1 equivalent $B(C_6F_5)_3–PPh_2$(*p*-tol) (7.9 mg, 0.01 mmol) was added to a 1-dram vial and dissolved in CD_2Cl_2 (0.5 mL). 5.0 equivalents $H–SiEt_3$ (79.8 µL, 0.50 mmol) were added to the same vial and the resulting solution was transferred via syringe to an NMR tube, which was sealed with a septum and removed from the glovebox. 1.0 equivalent anisole (10.9 µL, 0.10 mmol) was added to the NMR tube via syringe through the septum, and the resulting mixture was analyzed over time by ^{1}H, ^{19}F, and ^{31}P NMR spectroscopy.

Based on Klankermayer's prior work[32] documenting the effect of phosphine additivies in imine reduction, our model system composed of the combination of $(C_6F_5)_3B–PPh_2(p\text{-tol})$ and Et_3SiH was similarly examined for the catalytic reduction of anisole. *In situ* ^{1}H, ^{19}F, and ^{31}P NMR studies confirmed that at early times (< 3 h), the catalyst rests as the $Et_3Si\text{-}PPh_2(p\text{-tol})^+$ / $H–B(C_6F_5)_3^-$ ion pair, with no other $B(C_6F_5)_3$ species detectable.

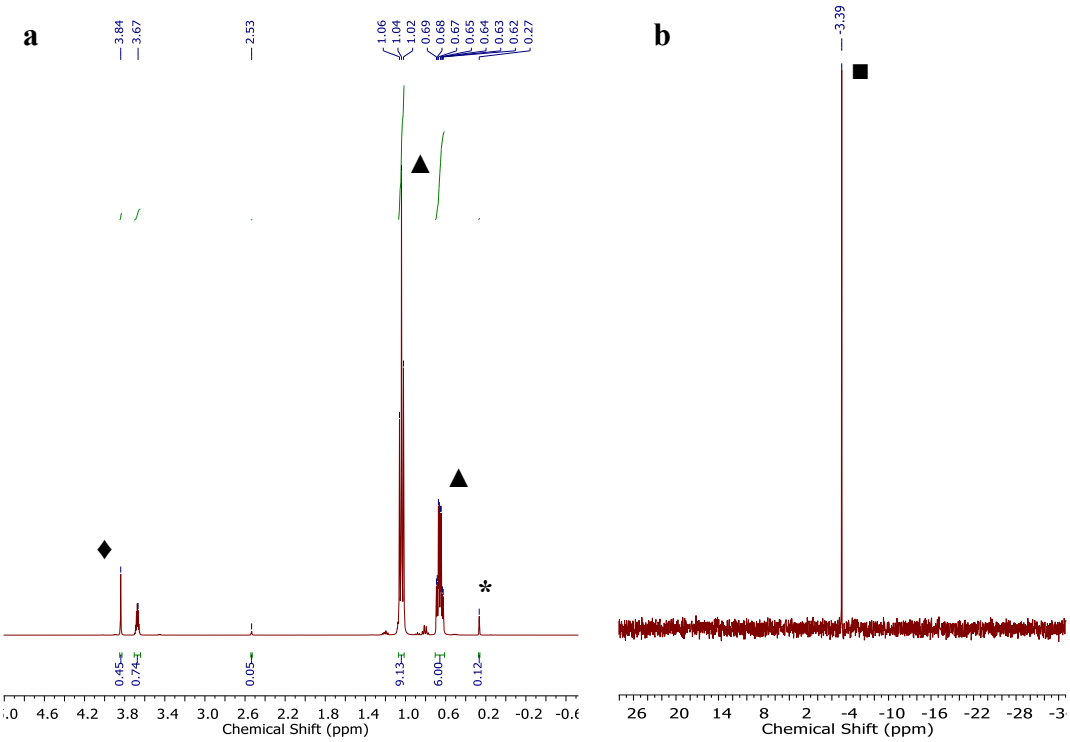

Figure 2.31. ^{1}H and $^{31}P\{^{1}H\}$ NMR spectra during anisole reduction

a. ^{1}H NMR spectrum of the *in situ* solution of the anisole, $(C_6F_5)_3B–PPh_2(p\text{-tol})$, and Et_3SiH mixture after 3 h. The spectrum is consistent with demethylation of anisole to generate CH_4 (*). Excess Et_3SiH is indicated with (▲) and anisole $–OCH_3$ peak is indicated with (♦). b. $^{31}P\{^{1}H\}$ NMR spectrum of the *in situ* solution of the anisole, $(C_6F_5)_3B–PPh_2(p\text{-tol})$, and Et_3SiH mixture after 3 h. The spectrum is consistent with the presence of $Et_3Si\text{-}PPh_2(p\text{-tol})^+$ cation, indicated with (■).

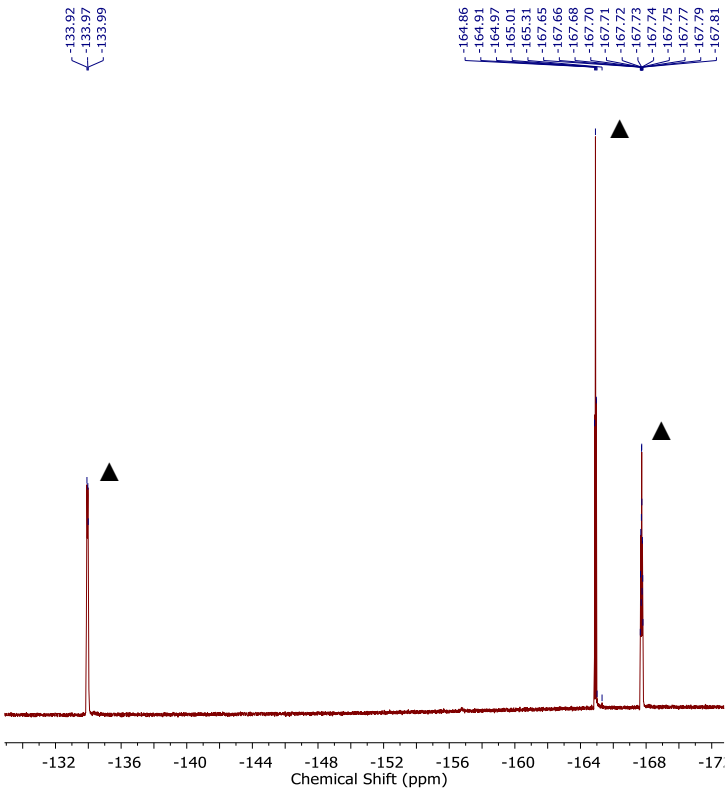

Figure 2.32. $^{19}F\{^{1}H\}$ NMR spectrum during anisole reduction

$^{19}F\{^{1}H\}$ NMR spectrum of the *in situ* solution of the anisole, $(C_6F_5)_3B–PPh_2$(*p*-tol), and Et_3SiH mixture after 3 h. The peaks indicated with (▲) correspond to the $H–B(C_6F_5)_3^-$ anion.[2]

2.8.9. Catalytic anisole reduction– excess PPh_2(*p*-tol) experiment

Inside a nitrogen-filled glovebox at room temperature, 0.1 equivalent $B(C_6F_5)_3$ (5.1 mg, 0.01 mmol), 0.15 equivalents PPh_2(*p*-tol) (4.1 mg, 0.015 mmol), and 0.17 equivalents hexamethylbenzene internal standard (2.7 mg, 0.017 mmol) were added to a 1-dram vial and dissolved in CD_2Cl_2 (0.5 mL). To the same vial, 2.5 equivalents $H–SiEt_3$ (39.9 µL, 0.25 mmol) were added via syringe and the resulting solution was transferred to a J-Young NMR tube. 1.0 equivalent anisole (10.9 µL, 0.10 mmol) was added to the same J-Young NMR tube via syringe, the tube was sealed, and the resulting mixture was analyzed over time by ^{1}H, ^{19}F, and ^{31}P NMR spectroscopy. Relevant NMR spectra can be found below. In the presence of excess phosphine, a new species was observed to grow by ^{31}P NMR. This species, identified as $[H_3C–PPh_2(p\text{-tol})^+][H–$

$B(C_6F_5)_3^-$], likely results from phosphine attack on the silylium activated anisole intermediate (see Figure 2.10).

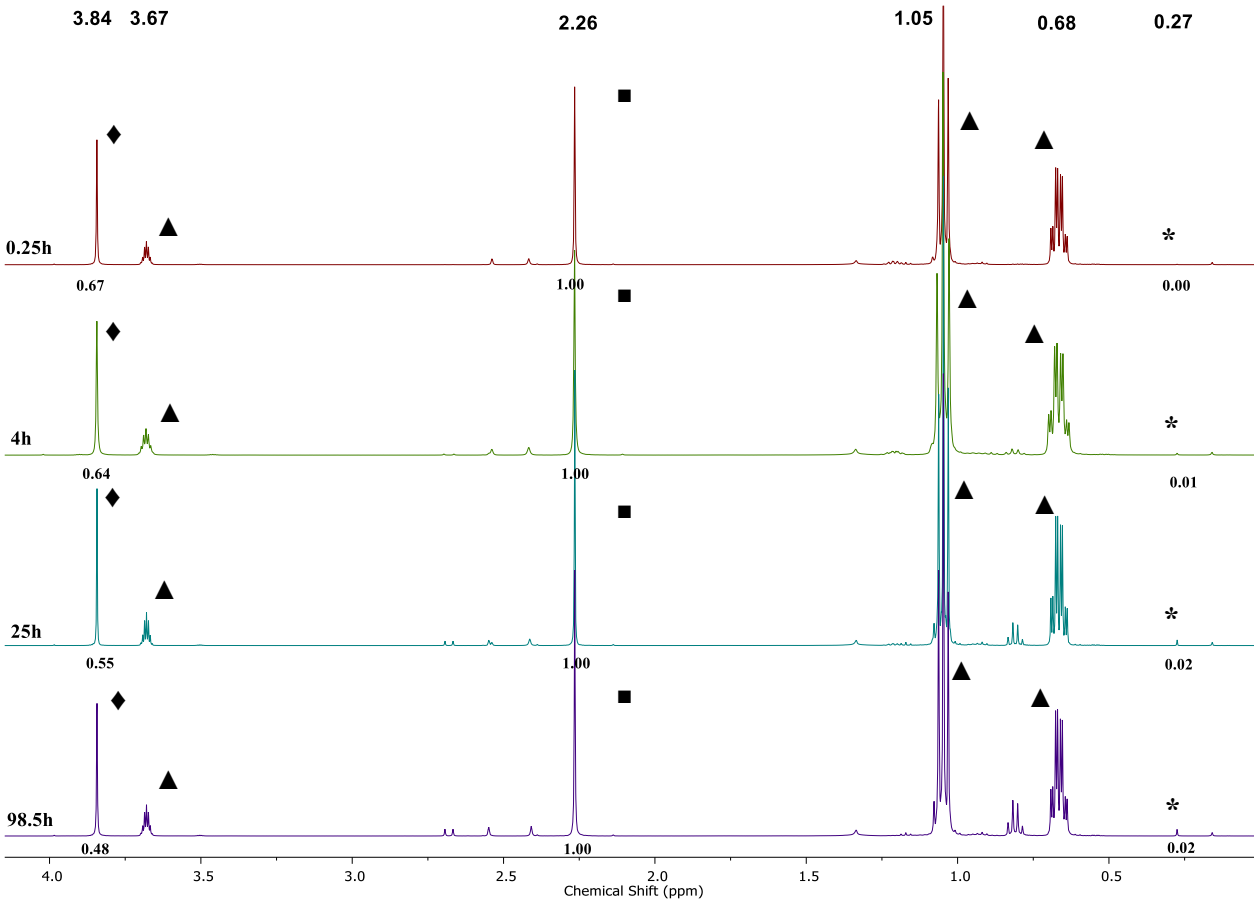

Figure 2.33. ^{1}H NMR spectra over time during anisole reduction

^{1}H NMR spectra of the *in situ* solution of the $B(C_6F_5)_3$, Et_3SiH, anisole, and excess PPh_2(*p*-tol) mixture after 0.25, 4, 25, and 98.5 h during active catalysis. The spectra are consistent with slow demethylation of anisole to generate trace amounts of CH_4 (*). Excess Et_3SiH is indicated with (▲), internal standard hexamethylbenzene is indicted with (■) and integrated to 1.00, and the anisole –OCH_3 peak is indicated with (♦).

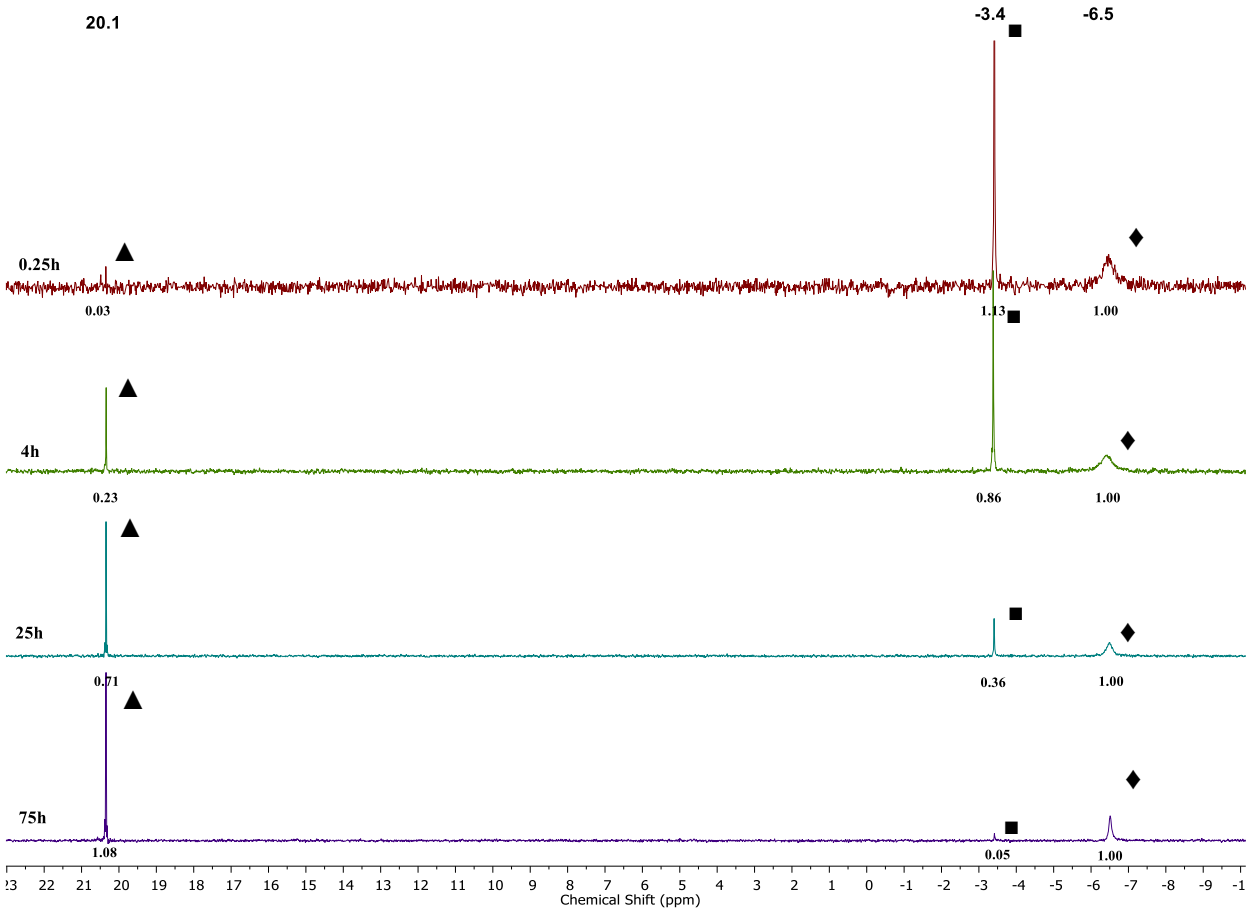

Figure 2.34. $^{31}P\{^{1}H\}$ NMR spectra over time during anisole reduction

$^{31}P\{^{1}H\}$ NMR spectra of the *in situ* solution of the $B(C_6F_5)_3$, Et_3SiH, anisole, and excess PPh_2(*p*-tol) mixture after 0.25, 4, 25, and 75 h during active catalysis. The spectra are consistent with demethylation of anisole by free PPh_2(*p*-tol) to generate the methyl-phosphonium cation indicated with (▲). The spectra show a disappearance of the silyl-phosphonium ion, indicated with (■), over time. Excess PPh_2(*p*-tol) is indicated with (♦) and is integrated to 1.00.

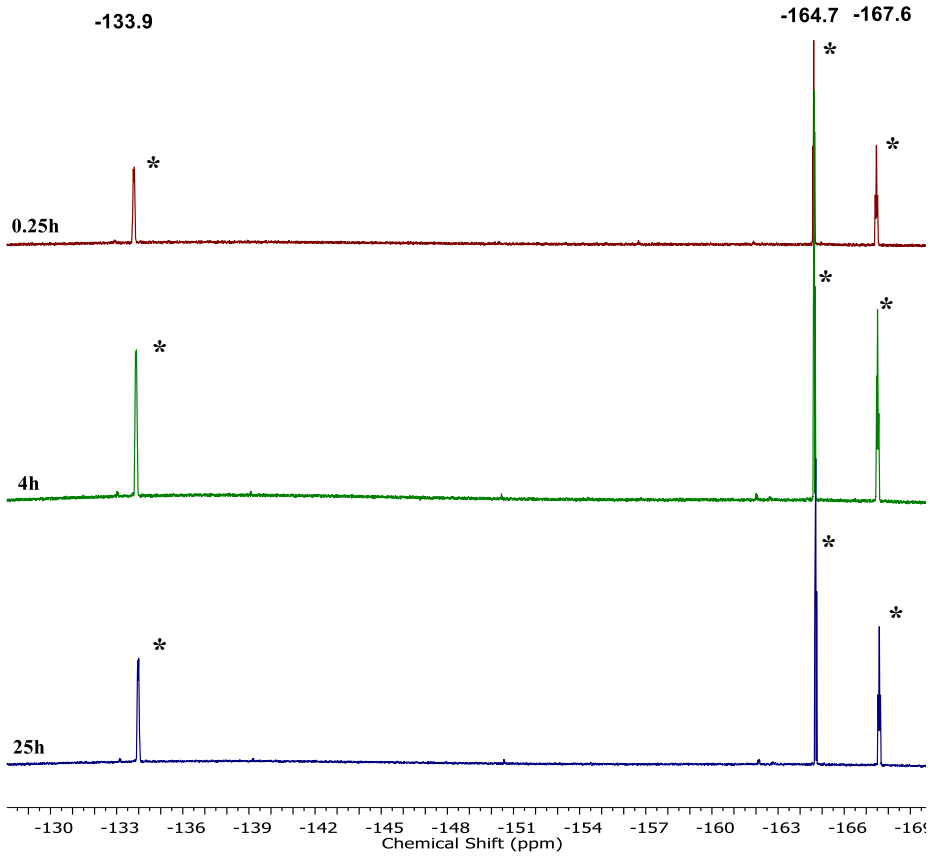

Figure 2.35. $^{19}F\{^{1}H\}$ NMR spectra over time during anisole reduction

$^{19}F\{^{1}H\}$ NMR spectra of the *in situ* solution of the $B(C_6F_5)_3$, Et_3SiH, anisole, and excess PPh_2(*p*-tol) mixture after 0.25, 4, and 25 h. The spectra are consistent with the presence of $H–B(C_6F_5)_3^-$ anion[2] (*) throughout active catalysis.

2.8.10. Computational approach

To carry out the relevant calculations, the system was examined using the Gaussian09 software suite.[57] Geometry optimization and frequency calculations were performed, without symmetry constraints, using the M06-2X density functional[58] in conjunction with the 6-311^{++}G** basis set[59] for all the atoms in the system. In addition, to closely represent the reaction environment and the effects of the dichloromethane solvent, secondary solvent interactions were studied using the conductor-like polarizable continuum (C-PCM) model.[60] The M06-2X functional was chosen

based on literature precedent in depiction of accurate thermodynamic data in related Lewis pair systems.[27] Relevant computational data can be found below.

2.8.11. Computation investigation of the ion pair generation

Table 2.8. On-cycle total Energy *E* in dichloromethane (au)[a]

Molecule	M06-2X (C-PCM)/6-311++G**	
	E	*Free Energy*
$B(C_6F_5)_3$–PPh_2(*p*-tol) (1)	-3283.751748	-3283.371746
$B(C_6F_5)_3$	-2208.222169	-2208.124568
PPh_2(*p*-tol)	-1075.478649	-1075.22425
H–$SiEt_3$	-527.7069723	-527.5389773
$B(C_6F_5)_3$–H–$SiEt_3$ (2)	-2735.952692	-2735.659923
$B(C_6F_5)_3$–H–$SiEt_3$–PPh_2(*p*-tol) (3)	-3811.450011	-3810.88112
$B(C_6F_5)_3$–H–$SiEt_3$–PPh_2(*p*-tol) (TS3)	-3811.450208	-3810.879061
[Et_3Si–PPh_2(*p*-tol)$^+$][H–$B(C_6F_5)_3^-$] (4)	-3811.471096	-3810.894579
H–$B(C_6F_5)_3^-$	-2208.983557	-2208.879313
Et_3Si–PPh_2(*p*-tol)$^+$	-1602.457416	-1602.015622

[a]Total electronic energy and free energy values for all of the species in Figure 2.9 as determined by DFT (Gaussian 09, M06-2X functional, C-PCM model, 6-311++G basis set).**[57–60]

2.8.12. Computational investigation of anisole reduction

To computationally investigate the propensity of H–$B(C_6F_5)_3^-$ to reduce Me–PPh_2(*p*-tol)$^+$ and liberate methane (Scheme 2.5), the relevent calculations were carried out.

$$[Me\text{-}PPh_2(p\text{-}tol)]^+ + [H\text{-}B(C_6F_5)_3]^- \xrightarrow[CH_2Cl_2]{} B(C_6F_5)_3 + PPh_2(p\text{-}tol) + CH_4$$

$$\Delta G_{calc.} = -3.9 \text{ kcal/mol}$$

Scheme 2.5. Proposed reduction of Me–PPh_2(*p*-tol)$^+$ to liberate CH_4

Table 2.9. Off-cycle processes total Energy *E* in dichloromethane (au)[a]

Molecule	M06-2X (C-PCM)/6-311++G**	
	E	*Free Energy*
Me–PPh$_2$(*p*-tol)$^+$	-1115.225762	-1114.935247
H–B(C$_6$F$_5$)$_3^-$	-2208.983557	-2208.879313
B(C$_6$F$_5$)$_3$	-2208.222169	-2208.124568
PPh$_2$(*p*-tol)	-1075.478649	-1075.22425
CH$_4$	-40.49701977	-40.4719667

[a]Total electronic energy and free energy values for all of the species involved in liberation of methane starting from the H–B(C$_6$F$_5$)$_3^-$ / Me–PPh$_2$(*p*-tol)$^+$ ion pair as determined by DFT (Gaussian 09, M06-2X functional, C-PCM model, 6-311++G basis set).**[57–60]

2.8.13. Computation coordinates of the reported sctructures

1. B(C$_6$F$_5$)$_3$–PPh$_2$(*p*-tol) – computed adduct between BCF and PPh$_2$(*p*-tol)

Energy: -2060583.7820300 Ha

B	-0.28036	0.04667	0.78491
C	-0.67744	1.58912	0.43678
C	-1.53492	2.30552	1.26787
C	-0.20423	2.32307	-0.64708
C	-1.86155	3.63634	1.10291
C	-0.50406	3.66338	-0.85367
C	-1.32963	4.33019	0.03029

C	-1.54991	-0.96057	0.95380
C	-1.35522	-2.25290	1.43483
C	-2.88132	-0.65131	0.69518
C	-2.36574	-3.15315	1.70355
C	-3.93203	-1.52279	0.95170
C	-3.67717	-2.77854	1.46789
C	0.92254	-0.54720	-0.14015
C	0.84485	-1.69131	-0.92852
C	2.16400	0.08119	-0.18001
C	1.92058	-2.20362	-1.64119
C	3.26125	-0.39093	-0.87160
C	3.14138	-1.55779	-1.60577
F	4.42515	0.25393	-0.83033
F	4.17919	-2.04008	-2.27846
F	2.34267	1.23081	0.49256
F	-0.10356	-2.68264	1.67019
F	-2.09400	-4.36067	2.19364
F	-4.67295	-3.61970	1.71971

F	-2.09834	1.68836	2.31993
F	-2.66724	4.25444	1.96347
F	-0.29897	-2.37650	-1.05993
F	1.77979	-3.31069	-2.36778
F	-3.23806	0.52341	0.15959
F	-5.18620	-1.15687	0.69321
F	0.57496	1.77035	-1.58613
F	-0.00742	4.30779	-1.90800
F	-1.62139	5.61193	-0.15337
P	0.55909	0.13522	2.79087
C	-0.32587	-0.93293	3.98888
C	-1.70989	-0.79554	4.14828
C	0.36035	-1.88747	4.74167
C	-2.39535	-1.60803	5.04247
H	-2.25642	-0.05656	3.57790
C	-0.33299	-2.70249	5.63259
H	1.43147	-2.00610	4.63572
C	-1.70856	-2.56784	5.78167

H	-3.46663	-1.49237	5.15636
H	0.20795	-3.44369	6.20831
H	-2.24523	-3.20577	6.47381
C	2.30967	-0.37847	2.90618
C	3.23171	0.38715	3.62213
C	2.73733	-1.57149	2.31067
C	4.55643	-0.02511	3.72284
H	2.92706	1.30609	4.10757
C	4.06143	-1.97235	2.41901
H	2.04158	-2.19584	1.76490
C	4.99511	-1.20269	3.11842
H	5.25794	0.58230	4.28440
H	4.37459	-2.89995	1.95122
C	0.52192	1.81129	3.52786
C	1.06604	2.88625	2.81561
C	-0.01561	2.03008	4.79773
C	1.06126	4.16239	3.36540
H	1.49528	2.73484	1.83356

C	-0.02178	3.31178	5.34070
H	-0.43209	1.20969	5.36829
C	0.51196	4.37860	4.62641
H	1.48500	4.98707	2.80493
H	-0.44469	3.47102	6.32537
H	0.50357	5.37530	5.05121
C	6.43485	-1.63117	3.19930
H	6.51415	-2.71044	3.33938
H	6.95690	-1.38007	2.27199
H	6.94942	-1.13169	4.02051

2. $B(C_6F_5)_3$ – free BCF catalyst

Energy: -1385679.2848650 Ha

B	-0.00013	-0.00528	0.00832
C	0.87606	1.29252	0.00763
C	2.09828	1.36518	-0.66125
C	0.48323	2.45490	0.67204
C	2.87664	2.50770	-0.68436
C	1.24583	3.60819	0.68656

C	2.44826	3.63377	-0.00081
C	0.68355	-1.41418	0.00696
C	0.13299	-2.50774	-0.66246
C	1.88811	-1.65677	0.66854
C	0.73406	-3.75232	-0.69100
C	2.50596	-2.89303	0.67789
C	1.92584	-3.94530	-0.01173
C	-1.56180	0.10909	0.00506
C	-2.37717	-0.79904	0.68042
C	-2.22904	1.12869	-0.67474
C	-3.75637	-0.70352	0.69682
C	-3.60645	1.24191	-0.69745
C	-4.37332	0.32125	-0.00228
F	-4.19840	2.22010	-1.37266
F	-5.69134	0.42072	-0.00552
F	-1.54219	2.04335	-1.36141
F	-1.01154	-2.38231	-1.33572
F	0.18374	-4.76032	-1.35753

F	2.50906	-5.13116	-0.02176
F	2.56362	0.31257	-1.33538
F	4.02862	2.53422	-1.34419
F	-1.83944	-1.80678	1.36923
F	-4.49236	-1.58156	1.36829
F	2.49222	-0.68094	1.34820
F	3.64555	-3.08091	1.33309
F	-0.66566	2.48986	1.34884
F	0.83720	4.68641	1.34502
F	3.18588	4.73067	-0.00371

3. PPh_2(*p*-tol) – free phosphine

Energy: -674872.5312981 Ha

P	0.50979	0.08285	0.06134
C	1.42644	0.80138	1.49260
C	0.93470	2.00100	2.01854
C	2.56284	0.22648	2.06628
C	1.57558	2.62427	3.08417
H	0.04410	2.45045	1.58992

C	3.19832	0.84509	3.14075
H	2.95556	-0.70610	1.67554
C	2.70892	2.04481	3.64921
H	1.18552	3.55540	3.47871
H	4.07867	0.38915	3.57887
H	3.20535	2.52409	4.48489
C	1.26294	-1.59478	-0.05029
C	2.32940	-1.93201	-0.88472
C	0.72323	-2.58723	0.77567
C	2.84346	-3.22680	-0.88552
H	2.76912	-1.18500	-1.53678
C	1.24900	-3.87259	0.78080
H	-0.11294	-2.34906	1.42658
C	2.31537	-4.21561	-0.05530
H	3.67444	-3.46951	-1.54015
H	0.82166	-4.62394	1.43725
C	1.32454	0.93895	-1.35425
C	0.72029	0.79800	-2.60864

C	2.49211	1.69802	-1.24770
C	1.28203	1.38538	-3.73721
H	-0.19601	0.22278	-2.70191
C	3.04768	2.29698	-2.37630
H	2.97311	1.82343	-0.28378
C	2.44747	2.13905	-3.62192
H	0.80583	1.26289	-4.70315
H	3.95361	2.88461	-2.28157
H	2.88282	2.60460	-4.49832
C	2.85484	-5.62157	-0.07568
H	2.87169	-6.04948	0.92813
H	2.22497	-6.26418	-0.69717
H	3.86579	-5.65007	-0.48365

4. H–$SiEt_3$ – free silane

Energy: -331140.8744942 Ha

Si	0.74932	0.48725	0.15868
H	-0.72957	0.54221	0.37061
C	1.14103	1.26734	-1.51150

C	0.84769	2.77383	-1.55750
H	0.56820	0.74902	-2.28748
H	2.19767	1.08284	-1.73780
H	1.04252	3.19394	-2.54709
H	-0.19767	2.98096	-1.31141
H	1.46661	3.31844	-0.84010
C	1.58647	1.44592	1.55009
C	1.43918	0.76938	2.92072
H	1.16956	2.45764	1.58455
H	2.64747	1.56086	1.29971
H	1.88976	1.36636	3.71714
H	0.38656	0.61823	3.17628
H	1.92183	-0.21109	2.93033
C	1.28478	-1.32008	0.18992
C	0.75120	-2.12810	-1.00160
H	0.94807	-1.76965	1.12994
H	2.38014	-1.35531	0.20917
H	1.03630	-3.18087	-0.93712

H	-0.34052	-2.08443	-1.05188
H	1.13769	-1.73897	-1.94701

5. $B(C_6F_5)_3$–H–$SiEt_3$ – BCF-silane adduct formation transition state

Energy: -1716397.7962535 Ha

Si	-0.38971	-0.24317	0.13600
C	0.25797	0.77661	-1.29914
C	0.59162	2.25821	-1.01160
H	-0.45688	0.68822	-2.12598
H	1.15566	0.24425	-1.64182
H	1.63275	2.47730	-1.26317
H	-0.03374	2.92402	-1.61260
H	0.44469	2.54003	0.03537
C	0.06701	0.41451	1.82677
C	1.60180	0.46879	1.96177
H	-0.34981	-0.24452	2.59707
H	-0.36858	1.40795	1.98219
H	1.88834	0.83143	2.95339
H	2.05287	-0.52116	1.83131

H	2.05028	1.14005	1.22150
C	-0.19963	-2.10500	-0.04298
C	0.53479	-2.57321	-1.30726
H	-1.19610	-2.56110	0.01510
H	0.32958	-2.45168	0.85498
H	0.56197	-3.66632	-1.35344
H	0.04520	-2.21291	-2.21746
H	1.56957	-2.21618	-1.32232
B	-3.34172	0.06398	-0.00942
C	-3.45779	1.31944	-1.00553
C	-2.79095	2.50344	-0.69775
C	-4.16462	1.33864	-2.20423
C	-2.80489	3.63111	-1.50170
C	-4.20861	2.44834	-3.04073
C	-3.52221	3.59996	-2.68995
C	-3.68252	0.31718	1.54058
C	-3.17608	-0.54920	2.50602
C	-4.46209	1.35736	2.03467

C	-3.39733	-0.40703	3.86556
C	-4.71985	1.53359	3.38936
C	-4.18043	0.64939	4.31076
C	-3.72511	-1.38006	-0.60125
C	-4.65901	-2.25185	-0.05016
C	-3.08970	-1.85066	-1.74747
C	-4.94214	-3.50103	-0.59217
C	-3.33295	-3.08797	-2.31847
C	-4.27371	-3.92325	-1.73025
F	-2.68271	-3.48143	-3.41503
F	-4.53389	-5.11602	-2.25898
F	-2.17069	-1.07088	-2.34759
F	-2.42520	-1.59803	2.11526
F	-2.87517	-1.26688	4.74239
F	-4.41458	0.80776	5.61125
F	-2.08396	2.57783	0.44476
F	-2.14010	4.73432	-1.15210
F	-5.35398	-1.91574	1.04716

F	-5.85160	-4.29526	-0.02422
F	-5.02256	2.25077	1.20480
F	-5.47992	2.54675	3.80983
F	-4.85976	0.26652	-2.61342
F	-4.90313	2.41182	-4.17975
F	-3.55167	4.66819	-3.48314
H	-1.96759	-0.03256	0.06431

6. $B(C_6F_5)_3$–H–$SiEt_3$ – BCF-silane adduct upon completed formation

Energy: -1716834.9380678 Ha

Si	-0.24081	-0.09769	-0.01699
C	0.17506	0.91867	-1.54046
C	0.79837	2.29680	-1.27733
H	-0.73745	1.01848	-2.13731
H	0.85300	0.31026	-2.14860
H	0.96929	2.82165	-2.21917
H	0.15499	2.92345	-0.65691
H	1.76090	2.20719	-0.76952
C	0.19110	0.67355	1.63891

C	0.84287	-0.27196	2.65802
H	-0.72249	1.11118	2.05465
H	0.85117	1.52259	1.43372
H	1.04770	0.25772	3.59030
H	0.19605	-1.12002	2.88987
H	1.79102	-0.66670	2.28659
C	0.02071	-1.95092	-0.16626
C	0.61519	-2.43484	-1.49685
H	-0.93811	-2.44288	0.02737
H	0.66968	-2.24733	0.66450
H	0.70712	-3.52263	-1.49784
H	-0.00634	-2.15073	-2.34808
H	1.61150	-2.01899	-1.66121
B	-3.19613	0.06961	-0.00847
C	-3.38647	1.32381	-0.99347
C	-2.72018	2.51146	-0.71289
C	-4.12326	1.32493	-2.16936
C	-2.75798	3.62739	-1.52632

C	-4.19350	2.42402	-3.01350
C	-3.50565	3.58004	-2.69235
C	-3.48167	0.32376	1.55103
C	-2.87556	-0.48675	2.50251
C	-4.28701	1.33215	2.06018
C	-3.02994	-0.32259	3.86558
C	-4.47778	1.52877	3.42016
C	-3.84382	0.69937	4.32751
C	-3.54888	-1.38983	-0.57867
C	-4.37383	-2.31614	0.04376
C	-2.95479	-1.82685	-1.75674
C	-4.59285	-3.58975	-0.46314
C	-3.13811	-3.08610	-2.29362
C	-3.97017	-3.97786	-1.63508
F	-2.53457	-3.44725	-3.42270
F	-4.17036	-5.19287	-2.12825
F	-2.13674	-0.99143	-2.41877
F	-2.07910	-1.48915	2.09201

F	-2.41429	-1.12597	4.72894
F	-4.01377	0.87936	5.63093
F	-1.97243	2.59286	0.40127
F	-2.09078	4.73353	-1.20788
F	-5.01290	-2.01576	1.18053
F	-5.39630	-4.44051	0.16981
F	-4.93193	2.17238	1.24205
F	-5.26285	2.50919	3.85943
F	-4.81360	0.24311	-2.54820
F	-4.91421	2.37368	-4.13073
F	-3.56213	4.63664	-3.49262
H	-1.83821	0.00292	0.00269

7. $B(C_6F_5)_3$–H–$SiEt_3$–PPh_2(*p*-tol) – BCF-silane-phosphine adduct formation transition state

Energy: -2391154.1207851 Ha

Si	0.20568	-0.07042	-0.28109
C	0.43043	0.97323	-1.81999
C	1.87994	1.48010	-1.95092
H	-0.25681	1.82763	-1.78265

H	0.14597	0.38393	-2.69883
H	1.98780	2.10256	-2.84462
H	2.17152	2.08954	-1.08866
H	2.59708	0.65545	-2.03499
C	0.97951	0.67413	1.25507
C	2.39290	0.10858	1.47942
H	0.34988	0.48226	2.13200
H	1.01774	1.76224	1.12808
H	2.87378	0.57620	2.34531
H	2.37336	-0.97242	1.65469
H	3.03810	0.28470	0.61050
C	0.53660	-1.89861	-0.52797
C	1.81599	-2.13880	-1.35089
H	-0.31983	-2.36028	-1.03436
H	0.61533	-2.38226	0.45206
H	2.00395	-3.21133	-1.46284
H	1.73339	-1.71022	-2.35548
H	2.69836	-1.69697	-0.87366

P	5.60861	-0.45914	-0.65444
C	6.88323	-1.53643	-1.43758
C	7.84821	-2.25566	-0.72200
C	6.87931	-1.61355	-2.83614
C	8.79183	-3.03216	-1.39458
H	7.86583	-2.21039	0.36437
C	7.82965	-2.37919	-3.51035
H	6.12361	-1.06962	-3.39912
C	8.78689	-3.09247	-2.78864
H	9.53502	-3.58694	-0.82875
H	7.81584	-2.42643	-4.59543
H	9.52413	-3.69615	-3.31006
C	6.50132	1.14614	-0.51791
C	5.76811	2.26085	-0.08364
C	7.84796	1.32523	-0.84503
C	6.37033	3.50979	0.03225
H	4.71793	2.15062	0.18424
C	8.44338	2.58393	-0.74090

H	8.44336	0.48281	-1.18751
C	7.71918	3.69323	-0.29886
H	5.78276	4.35911	0.37451
H	9.49118	2.70151	-1.00856
C	5.63797	-1.06543	1.08737
C	6.24108	-0.38446	2.14921
C	4.97326	-2.27259	1.34838
C	6.18235	-0.90160	3.44547
H	6.75975	0.55389	1.97008
C	4.92790	-2.79744	2.63723
H	4.48279	-2.80429	0.53412
C	5.52982	-2.10807	3.69236
H	6.65404	-0.36087	4.26126
H	4.41374	-3.73661	2.82102
H	5.48649	-2.50934	4.70076
C	8.36621	5.04812	-0.16301
H	8.58932	5.26758	0.88725
H	9.30481	5.09633	-0.72142

H	7.70509	5.83939	-0.52916
B	-2.71635	0.02762	0.24476
C	-3.12492	1.34787	-0.57457
C	-2.42618	2.53488	-0.36909
C	-4.17271	1.43126	-1.48562
C	-2.72253	3.72662	-1.00973
C	-4.50989	2.60670	-2.14676
C	-3.78004	3.76053	-1.90882
C	-2.74042	0.15181	1.84651
C	-1.98736	-0.72208	2.62601
C	-3.50039	1.07211	2.56160
C	-1.96238	-0.69872	4.01031
C	-3.51313	1.12666	3.95070
C	-2.73757	0.23859	4.67930
C	-3.17081	-1.38295	-0.37594
C	-3.93862	-2.33757	0.28338
C	-2.80728	-1.71739	-1.67820
C	-4.32160	-3.53857	-0.30349

C	-3.15968	-2.90319	-2.30028
C	-3.92798	-3.82456	-1.60113
F	-2.77139	-3.16791	-3.54893
F	-4.28087	-4.97289	-2.17312
F	-2.06004	-0.85217	-2.38914
F	-1.22987	-1.65348	2.01679
F	-1.21322	-1.56101	4.69964
F	-2.73754	0.28147	6.00961
F	-1.39343	2.54560	0.49577
F	-2.01239	4.83114	-0.77352
F	-4.36604	-2.13255	1.53882
F	-5.06332	-4.41822	0.37248
F	-4.28863	1.95484	1.92908
F	-4.26687	2.02470	4.58785
F	-4.93417	0.36065	-1.75986
F	-5.53096	2.63324	-3.00558
F	-4.08951	4.89339	-2.53504
H	-1.36049	-0.00781	0.00235

8. [$Et_3Si–PPh_2(p\text{-tol})^+$][$H–B(C_6F_5)_3^-$] – BCF-silane-phosphine adduct in formed state

Energy: -2391719.1851409 Ha

Si	0.31729	-0.12776	-0.02155
C	0.63144	0.56276	-1.73643
C	1.29781	1.94512	-1.78507
H	-0.31958	0.58353	-2.27735
H	1.24510	-0.18184	-2.25632
H	1.48595	2.24260	-2.81939
H	0.66832	2.71082	-1.32867
H	2.25418	1.95649	-1.25484
C	0.66946	0.98078	1.44918
C	1.22646	0.27483	2.69356
H	-0.24937	1.51915	1.70074
H	1.36662	1.74749	1.09283
H	1.44705	1.00132	3.47912
H	0.51380	-0.44599	3.09812
H	2.14873	-0.27061	2.47456
C	0.47329	-1.98067	0.22054

C	1.02361	-2.76533	-0.97874
H	-0.50801	-2.37114	0.50728
H	1.10932	-2.12015	1.10181
H	1.11876	-3.82511	-0.73109
H	0.36580	-2.68394	-1.84565
H	2.00913	-2.40468	-1.28591
P	3.70292	-0.32887	-0.04438
C	4.44450	-0.95118	-1.61142
C	5.35331	-2.00960	-1.66804
C	4.04275	-0.33831	-2.80531
C	5.84587	-2.44908	-2.89557
H	5.68330	-2.49537	-0.75738
C	4.54399	-0.77041	-4.02752
H	3.34974	0.49658	-2.78117
C	5.44406	-1.83281	-4.07543
H	6.54949	-3.27280	-2.92514
H	4.22961	-0.28035	-4.94138
H	5.82997	-2.17597	-5.02795

C	4.59132	1.26071	0.21222
C	4.20842	2.04554	1.30741
C	5.61183	1.72780	-0.61624
C	4.83219	3.25853	1.56471
H	3.43269	1.69679	1.98182
C	6.22509	2.95215	-0.35864
H	5.93976	1.13894	-1.46497
C	5.84626	3.73729	0.72946
H	4.52733	3.84477	2.42546
H	7.01784	3.29695	-1.01447
C	4.47965	-1.42177	1.21830
C	5.55704	-1.03054	2.01574
C	3.94562	-2.70591	1.38131
C	6.08662	-1.90664	2.96094
H	5.98837	-0.04283	1.90217
C	4.48251	-3.58286	2.31708
H	3.11805	-3.03305	0.75999
C	5.55260	-3.18181	3.11353

H	6.92177	-1.59043	3.57493
H	4.06337	-4.57604	2.42654
H	5.96754	-3.86126	3.84850
C	6.49195	5.07178	0.99226
H	5.85761	5.88239	0.62342
H	6.64035	5.23128	2.06153
H	7.45725	5.14771	0.49088
B	-2.65603	0.06655	-0.00977
C	-2.89496	1.09871	-1.22239
C	-2.21145	2.30875	-1.22685
C	-3.70322	0.87776	-2.32796
C	-2.29261	3.23932	-2.24432
C	-3.82112	1.78656	-3.37069
C	-3.10960	2.97117	-3.33148
C	-2.91896	0.62761	1.47637
C	-2.35270	-0.03248	2.56021
C	-3.64330	1.76650	1.79628
C	-2.46796	0.39111	3.86992

C	-3.79177	2.22601	3.09776
C	-3.19827	1.53775	4.13968
C	-3.06886	-1.46631	-0.27955
C	-3.92761	-2.22357	0.50370
C	-2.50828	-2.14072	-1.35746
C	-4.20735	-3.55816	0.24349
C	-2.75198	-3.46825	-1.65110
C	-3.61447	-4.18510	-0.83681
F	-2.17644	-4.05901	-2.69576
F	-3.87077	-5.46167	-1.09470
F	-1.66845	-1.47879	-2.17180
F	-1.63712	-1.14876	2.33952
F	-1.89330	-0.28214	4.86397
F	-3.32893	1.96833	5.38845
F	-1.40911	2.60519	-0.18993
F	-1.60424	4.37740	-2.19303
F	-4.54380	-1.68871	1.56527
F	-5.04108	-4.23991	1.02571

F	-4.24939	2.48696	0.84436
F	-4.49858	3.32514	3.35092
F	-4.42580	-0.24377	-2.44033
F	-4.61205	1.52603	-4.40910
F	-3.21023	3.84675	-4.32397
H	-1.32636	-0.02362	-0.01530

9. $B(C_6F_5)_3$–H–$SiEt_3$–PPh_2(*p*-tol) – BCF-silane-phosphine adduct to ion pair formation transition state

Energy: -2391719.3083773 Ha

Si	0.42056	-0.11379	-0.03250
C	0.73379	0.58330	-1.74566
C	1.40060	1.96509	-1.78635
H	-0.21896	0.60964	-2.28347
H	1.34347	-0.16062	-2.27110
H	1.58992	2.26869	-2.81872
H	0.76848	2.72647	-1.32611
H	2.35599	1.97439	-1.25441
C	0.74334	0.99987	1.44180
C	1.31669	0.31306	2.68912

H	-0.19406	1.50547	1.69307
H	1.41346	1.79157	1.08841
H	1.49922	1.04674	3.47791
H	0.62768	-0.43531	3.08494
H	2.26261	-0.19433	2.48052
C	0.57954	-1.96659	0.21000
C	1.13217	-2.75634	-0.98482
H	-0.40287	-2.35579	0.49387
H	1.21213	-2.10571	1.09379
H	1.23394	-3.81360	-0.72852
H	0.47251	-2.68766	-1.85166
H	2.11501	-2.39362	-1.29799
P	3.79844	-0.31197	-0.03651
C	4.54652	-0.95642	-1.59243
C	5.46330	-2.00856	-1.63271
C	4.14830	-0.35771	-2.79429
C	5.96650	-2.45629	-2.85287
H	5.79264	-2.48297	-0.71566

C	4.66037	-0.79787	-4.00921
H	3.44955	0.47280	-2.78290
C	5.56815	-1.85406	-4.04105
H	6.67529	-3.27597	-2.87033
H	4.34833	-0.31867	-4.92971
H	5.96245	-2.20411	-4.98781
C	4.70961	1.26684	0.21199
C	4.30811	2.09125	1.26944
C	5.77808	1.67953	-0.58519
C	4.96361	3.28890	1.52435
H	3.49255	1.78707	1.91805
C	6.42251	2.88738	-0.33139
H	6.11842	1.05788	-1.40524
C	6.02738	3.71132	0.72252
H	4.64414	3.90622	2.35763
H	7.25351	3.18855	-0.96106
C	4.54510	-1.40411	1.24577
C	5.58108	-1.00060	2.09022

C	4.01995	-2.69490	1.38510
C	6.07817	-1.87057	3.05876
H	6.00546	-0.00783	1.99528
C	4.52424	-3.56505	2.34461
H	3.22467	-3.03276	0.72832
C	5.55276	-3.15168	3.18829
H	6.88172	-1.54452	3.70879
H	4.11199	-4.56306	2.43597
H	5.94211	-3.82663	3.94129
C	6.71019	5.02871	0.97779
H	6.18716	5.83669	0.45854
H	6.71480	5.26884	2.04200
H	7.73972	5.01417	0.61820
B	-2.55433	0.04959	-0.02985
C	-2.81897	1.07878	-1.23952
C	-2.15385	2.29890	-1.25193
C	-3.64566	0.85004	-2.32976
C	-2.26960	3.23203	-2.26369

C	-3.79881	1.76144	-3.36547
C	-3.10534	2.95685	-3.33445
C	-2.83154	0.60445	1.45655
C	-2.27031	-0.05485	2.54362
C	-3.56698	1.73712	1.77493
C	-2.40697	0.35832	3.85453
C	-3.73389	2.18809	3.07708
C	-3.15018	1.49713	4.12237
C	-2.93880	-1.48971	-0.30618
C	-3.78157	-2.26756	0.47422
C	-2.36911	-2.14786	-1.38912
C	-4.03736	-3.60570	0.20779
C	-2.58931	-3.47808	-1.68968
C	-3.43672	-4.21561	-0.87797
F	-2.00681	-4.05088	-2.74084
F	-3.66960	-5.49525	-1.14251
F	-1.54087	-1.46814	-2.20083
F	-1.53883	-1.16134	2.32555

F	-1.84224	-0.31812	4.85202
F	-3.30353	1.91607	5.37263
F	-1.34075	2.60626	-0.22657
F	-1.60121	4.38236	-2.21989
F	-4.40295	-1.75131	1.54208
F	-4.85693	-4.30530	0.98922
F	-4.16798	2.46040	0.82191
F	-4.45067	3.28148	3.32733
F	-4.35452	-0.28144	-2.43233
F	-4.60900	1.49406	-4.38729
F	-3.24135	3.83701	-4.31887
H	-1.22498	-0.01060	-0.03389

10. [$Et_3Si–PPh_2(p\text{-}tol)^+$][$H–B(C_6F_5)_3^-$] – formed ion pair upon speciation completion

Energy: -2391732.4025323 Ha

Si	4.22766	-0.05986	-0.22454
C	2.88576	1.22782	-0.46696
C	1.73973	0.84190	-1.40920
H	3.43116	2.09035	-0.87271

H	2.49803	1.55505	0.50190
H	1.09770	1.70225	-1.61050
H	2.11150	0.47265	-2.36919
H	1.10354	0.06405	-0.98124
C	5.27767	-0.25018	-1.76983
C	6.25830	-1.42981	-1.81844
H	5.83915	0.69325	-1.79825
H	4.63924	-0.23072	-2.65817
H	6.94988	-1.31968	-2.65558
H	6.85242	-1.49796	-0.90326
H	5.74283	-2.38494	-1.94100
C	5.29893	0.30143	1.27328
C	4.60717	0.34117	2.64283
H	5.70732	1.29500	1.04349
H	6.16323	-0.36885	1.28504
H	5.28535	0.73499	3.40198
H	3.72027	0.97966	2.62546
H	4.28325	-0.64926	2.97149

P	3.19190	-2.13078	0.15157
C	2.21425	-2.11887	1.68088
C	2.23031	-3.21317	2.54951
C	1.43258	-0.99913	1.97092
C	1.47466	-3.17127	3.71633
H	2.82907	-4.08763	2.32195
C	0.68274	-0.96347	3.14079
H	1.39346	-0.15889	1.28983
C	0.71157	-2.04489	4.01677
H	1.48704	-4.01732	4.39264
H	0.08282	-0.08891	3.36412
H	0.13659	-2.01293	4.93540
C	2.11158	-2.64465	-1.20744
C	2.55948	-2.57592	-2.53188
C	0.85249	-3.16971	-0.92821
C	1.75595	-3.05596	-3.55466
H	3.53819	-2.17191	-2.76725
C	0.05501	-3.64510	-1.96484

H	0.48508	-3.21055	0.08822
C	0.49774	-3.61047	-3.28636
H	2.11262	-3.01156	-4.57815
H	-0.92716	-4.04634	-1.73293
C	4.46606	-3.41541	0.35114
C	4.49745	-4.53546	-0.47947
C	5.43551	-3.24930	1.34526
C	5.51105	-5.47713	-0.32601
H	3.74200	-4.67492	-1.24360
C	6.44202	-4.19463	1.49347
H	5.40062	-2.39556	2.01296
C	6.48393	-5.30488	0.65273
H	5.53547	-6.34627	-0.97192
H	7.19176	-4.06462	2.26424
H	7.27201	-6.03946	0.76717
C	-0.33940	-4.16735	-4.40636
H	0.19741	-4.96917	-4.91904
H	-1.28090	-4.57088	-4.03169

H	-0.56058	-3.39634	-5.14816
B	-1.87726	-0.72159	0.23639
C	-2.22977	0.87264	0.18975
C	-1.29635	1.85022	0.49767
C	-3.47114	1.36031	-0.19376
C	-1.54619	3.21037	0.40488
C	-3.77009	2.70866	-0.30045
C	-2.79499	3.64409	-0.00233
C	-2.28865	-1.44636	1.64318
C	-2.04700	-2.80450	1.82234
C	-2.74362	-0.80288	2.78593
C	-2.22754	-3.48261	3.01272
C	-2.94124	-1.43955	4.00524
C	-2.68044	-2.79024	4.12293
C	-2.47223	-1.42783	-1.11419
C	-3.48768	-2.36860	-1.20248
C	-1.90772	-1.08118	-2.33570
C	-3.88810	-2.95995	-2.39233

C	-2.28698	-1.62671	-3.54980
C	-3.28181	-2.58727	-3.57847
F	-1.69324	-1.24928	-4.68665
F	-3.65080	-3.14289	-4.73267
F	-0.92090	-0.17139	-2.38383
F	-1.60292	-3.54443	0.78781
F	-1.96067	-4.78738	3.11019
F	-2.85383	-3.41658	5.28641
F	-0.07063	1.50924	0.94160
F	-0.60214	4.10537	0.70879
F	-4.15908	-2.75839	-0.10503
F	-4.86196	-3.87391	-2.40817
F	-3.01172	0.51586	2.78264
F	-3.37667	-0.75490	5.06592
F	-4.47480	0.50569	-0.46137
F	-4.98402	3.11775	-0.67736
F	-3.05755	4.94676	-0.10135
H	-0.67535	-0.83274	0.15536

11. $H–B(C_6F_5)_3^-$ – borohydride anion

Energy: -1386157.0628821 Ha

B	0.03344	0.19871	0.91791
C	-0.44456	1.64687	0.32757
C	-1.71113	2.11859	0.65856
C	0.30302	2.52873	-0.43911
C	-2.21598	3.34293	0.26262
C	-0.15926	3.76989	-0.85869
C	-1.42884	4.18229	-0.50779
C	-0.99822	-1.02335	0.54715
C	-0.92239	-2.20103	1.28199
C	-1.94511	-1.04251	-0.46681
C	-1.72371	-3.30800	1.05799
C	-2.77177	-2.12614	-0.72659
C	-2.66144	-3.26964	0.04139
C	1.51322	-0.27752	0.41885
C	1.76072	-0.60148	-0.90823
C	2.58911	-0.45722	1.27263

C	2.97684	-1.06382	-1.37635
C	3.82897	-0.91913	0.84972
C	4.02390	-1.22577	-0.48349
F	4.83475	-1.07308	1.71615
F	5.20654	-1.67182	-0.90742
F	2.48463	-0.17913	2.58223
F	-0.02343	-2.31203	2.27518
F	-1.60133	-4.40940	1.80433
F	-3.44517	-4.32214	-0.19447
F	-2.53267	1.34995	1.39560
F	-3.44837	3.72551	0.60899
F	0.78302	-0.44210	-1.81749
F	3.15821	-1.35191	-2.66832
F	-2.11719	0.02085	-1.27054
F	-3.67032	-2.07912	-1.71443
F	1.55487	2.22663	-0.82981
F	0.61592	4.57158	-1.59477
F	-1.89026	5.36991	-0.90020

H	0.04468	0.30240	2.11924

12. $Et_3Si–PPh_2(p\text{-tol})^+$ – silyl-phosphonium cation

Energy: -1005556.4474000 Ha

Si	-0.82616	-0.01640	2.15507
C	-0.05005	1.48971	2.95917
C	1.46719	1.66406	2.80058
H	-0.29250	1.35016	4.02138
H	-0.58560	2.39483	2.65939
H	1.83108	2.45746	3.45556
H	2.00484	0.74797	3.05764
H	1.74684	1.92607	1.77715
C	-0.16458	-1.60568	2.90055
C	-0.55066	-2.91868	2.20585
H	-0.58083	-1.59334	3.91668
H	0.91862	-1.53204	3.03348
H	-0.26154	-3.77518	2.81716
H	-1.62841	-2.98038	2.03529
H	-0.06423	-3.02698	1.23362
C	-2.69997	0.05120	2.22428

C	-3.39263	1.18701	1.45803
H	-2.90084	0.16103	3.29830
H	-3.11770	-0.92222	1.95128
H	-4.45338	1.22713	1.71159
H	-2.95634	2.15922	1.70045
H	-3.31730	1.05993	0.37520
P	-0.20678	-0.00518	-0.10634
C	-0.87935	1.45117	-0.95323
C	-1.60924	1.32188	-2.13517
C	-0.66619	2.71360	-0.38972
C	-2.13772	2.45720	-2.74228
H	-1.77015	0.34749	-2.58130
C	-1.19356	3.84119	-1.00487
H	-0.08279	2.82274	0.51813
C	-1.93525	3.71173	-2.17693
H	-2.70670	2.35806	-3.65849
H	-1.02864	4.81831	-0.56775
H	-2.35236	4.59189	-2.65118

C	1.59573	0.02403	-0.27560
C	2.35810	-0.92521	0.41493
C	2.23181	0.98569	-1.05913
C	3.74069	-0.89903	0.32432
H	1.87895	-1.69537	1.01029
C	3.62066	1.00265	-1.13616
H	1.65555	1.72332	-1.60521
C	4.39419	0.07092	-0.44439
H	4.32392	-1.64112	0.85849
H	4.10792	1.75432	-1.74712
C	-0.83937	-1.48423	-0.94576
C	0.00864	-2.31206	-1.68177
C	-2.19762	-1.79460	-0.82332
C	-0.50439	-3.45805	-2.28241
H	1.06044	-2.07287	-1.78477
C	-2.70153	-2.93719	-1.43005
H	-2.86621	-1.14546	-0.26832
C	-1.85285	-3.77271	-2.15290

H	0.15295	-4.10316	-2.85236
H	-3.75365	-3.17577	-1.33565
H	-2.24627	-4.66835	-2.61838
C	5.89631	0.10845	-0.50566
H	6.30168	0.51854	0.42312

13. Me–PPh_2(*p*-tol)$^+$ – methyl-phosphonium cation

Energy: -699814.2025174 Ha

C	1.49203	0.83342	1.52207
C	0.93538	2.01023	2.03229
C	2.61101	0.25632	2.12571
C	1.50286	2.60347	3.15283
H	0.07103	2.46721	1.56392
C	3.17338	0.86096	3.24428
H	3.03884	-0.65845	1.73107
C	2.61965	2.02986	3.75631
H	1.07314	3.51281	3.55420
H	4.04028	0.41520	3.71570
H	3.05799	2.49615	4.63040

C	1.32863	-1.63480	-0.04747
C	2.35588	-2.01619	-0.91120
C	0.75561	-2.57404	0.81736
C	2.80391	-3.33195	-0.90659
H	2.80926	-1.29465	-1.58174
C	1.21242	-3.88238	0.80762
H	-0.03488	-2.29201	1.50440
C	2.24161	-4.28140	-0.05235
H	3.60609	-3.62233	-1.57557
H	0.76882	-4.60653	1.48199
C	1.38514	0.96236	-1.41801
C	0.79880	0.68725	-2.65803
C	2.43391	1.87683	-1.31376
C	1.26514	1.33761	-3.79225
H	-0.00799	-0.03244	-2.74613
C	2.89396	2.52188	-2.45743
H	2.88850	2.08553	-0.35202
C	2.31084	2.25333	-3.69088

H	0.81370	1.13010	-4.75445
H	3.70661	3.23342	-2.38089
H	2.67089	2.75828	-4.57919
C	2.71266	-5.70904	-0.06430
H	2.70453	-6.13091	0.94155
H	2.04905	-6.31837	-0.68393
H	3.72002	-5.78906	-0.47269
P	0.79842	0.08031	0.03925
C	-1.00364	0.16079	0.10062
H	-1.35664	-0.29177	1.02731
H	-1.31997	1.20293	0.05505
H	-1.41208	-0.38125	-0.75253

14. CH_4 – methane

Energy: -25412.2443761 Ha

C	0.29787	-0.28034	0.00000
H	0.66108	-1.30736	-0.00000
H	0.66098	0.23306	0.88946
H	0.66098	0.23306	-0.88946

H	-0.79143	-0.28029	0.00000

Chapter 3 – Catalytic methods for late-stage functionalization of natural products

3.1. Late-stage functionalization concept to build new structures

3.1.1 Adding molecular complexity – new chemical bonds

C–O bonds are ubiquitous in a wide variety of chemicals, ranging from simple small molecules to biomass-derived sugar compounds to complex natural products. Selective deoxygenation (i.e. removal of these bonds) is important because it leads to generation of new chemical compounds that could be used in chemical synthesis or pharmaceutical applications.[3,17,18] Additionally, reduction of C–O bonds followed by functionalization adds complexity and creates new chemical space around a given starting material. Selective installation of new bonds (i.e. C–N, C–C) to replace the C–O ones in bioactive compounds is an intriguing prospect that generates new compound libraries. This may lead to the discovery of new pre-drug candidates with increased biological activities over their unmodified counterparts.[4,61]

Recently, a novel research direction in the Gagné group has highlighted the utility of the fluoroarylborane-catalyzed hydrosilylation reactions in selective late-stage functionalization (LSF) of natural products.[5] The main objective of LSF is facile diversification of molecular complexity around the chosen natural product scaffolds, ideally resulting in increased biological activity of the generated compounds. Chemoselectivity in these transformations, however, is a significant challenge considering that typically a given natural product contains multiple potentially reactive functional groups. Targeting a specific part of a molecule while avoiding the diverse array of off-target reactive groups is not trivial and requires careful manipulations.[48]

3.1.2. Piers mechanism and its importance in LSF

A representative catalytic cycle, utilizing BCF as the catalyst has been explored comprehensively by Piers and coworkers and extensively discussed in previous chapters. In this mechanism, the BCF catalyst heterolytically activates an alkyl silane and generates a highly reactive silylium ion (R_3Si^+) and a borohydride anion ($H–B(C_6F_5)_3^-$), which then facilitates net C–O bond cleavage and the formation of partially deoxygenated products. Sometimes, as in the case of the anti-fungal natural product natamycin, the BCF/silane system on its own is too aggressive and leads to starting material decomposition. In such cases, adding a triaryl phosphine is helpful as it attenuates the silylium ion electrophilicity and changes the catalyst speciation tendencies as discussed in Chapter 2. This chapter outlines several catalytic strategies for selective natural product deoxygenation and functionalization using both phosphine-modified and the original Piers catalysis with Lewis acidic BCF.

3.1.3. Brønsted acid catalysis for LSF

In addition to the powerful Lewis acidic methodologies in place, sometimes Brønsted acid catalysis is more effective in LSF when it comes to generating new chemical bonds. In fact, BCF has been shown to act as a Brønsted acid in chemoselective reactions on a variety of substrates.[52] For example, Moran's work on the azidation of tertiary aliphatic alcohols in nitromethane is an important example of such Brønsted acidic activity (Figure 3.1).[53]

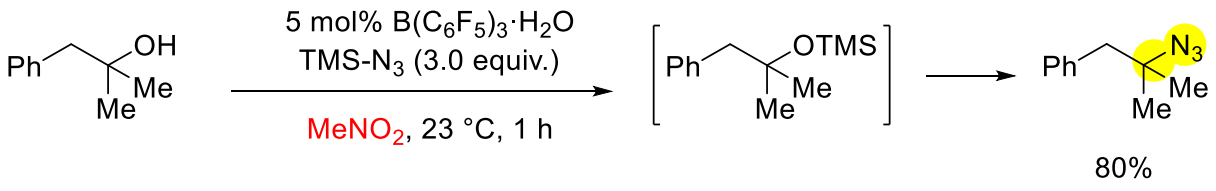

Figure 3.1. Azidation of tertiary aliphatic alcohols by BCF•H_2O

According to Moran's report, the active catalytic species is BCF•H_2O with nitromethane acting as the key co-catalyst. Further studying this and other Brønsted acidic catalytic systems is the focal point of the second part of this chapter, leading to unprecedented reactivity with a variety of TMS–X type reagents and various other nucleophiles that are otherwise unreactive in Lewis acidic systems.

3.2 Deoxygenation of gibberellic acid with fluoroarylboranes

3.2.1. Diversifying the fluoroarylborane catalysts

Although the commercially available BCF has been the workhorse catalyst in the majority of examples discussed thus far, other fluorinated arylboranes have also been investigated for the reduction of diverse functional groups, with one form typically exhibiting superior reactivity to the others.[62–64] Our group recently discovered that tuning the position of fluorination led to catalysts for site-selective deoxygenation that yielded divergent products from a set of common cellulosic starting materials.[65] Several site-selective modifications in natamycin have been reported using fluoroarylborane catalysts other than BCF and silanes as reductants.[5] The choice of reductant (i.e. borane versus silane) can also alter which product is formed, as seen with carbohydrates under BCF-catalyzed conditions.[66] These results led us to ask how modifications to the fluoroaryl borane catalyst and the reductant influences the selectivity for the deoxygenation of a multi-functional test molecule such as gibberellic acid.[61] Trialkylsilanes (Me_2EtSiH or Et_3SiH) and catecholborane (HBCat) were selected as the reductants while the following three fluoroarylboranes (Figure 3.2) were chosen based on their differing Lewis acidity and steric profiles: $B(C_6F_5)_3$, $B((3,5\text{-}CF_3)_2C_6H_3)_3$ ($BAr_{3,5\text{-}CF3}$), and $B(2,4,6\text{-}F_3C_6H_2)_3$ ($BAr_{2,4,6\text{-}F}$).[67]

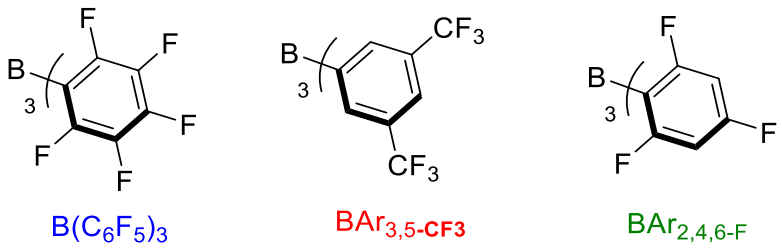

Figure 3.2. Lewis acidic fluoroarylborane catalysts

3.2.2. Free versus pre-protected gibberellic acid reactivity

In the study comparing the three aforementioned catalysts for the site-selective deoxygenation of cellulose-derived carbohydrates, the most significant differences were noted between BCF and $BAr_{3,5\text{-}CF3}$.[65] For multiple carbohydrate starting materials the two catalysts favored different products. Although no definitive reasons were apparent, it was noted that the boron resting state for BCF-catalyzed reactions was $H–B(C_6F_5)_3^-$ while for $BAr_{3,5\text{-}CF3}$, it was the Lewis acid form. The higher nucleophilicity of $H–BAr_{3,5\text{-}CF3}^-$ presumably promoted its consumption. In this study, $BAr_{2,4,6\text{-}F}$ was typically a less reactive version of BCF.[68]

The previously reported BCF-catalyzed hydrosilylative deoxygenation of free gibberellic acid afforded the tetrasilyl-protected diester **1** in 93% yield via a cascade of dehydrosilylation, and reductive olefin migration/ lactone opening (Scheme 3.1).[5]

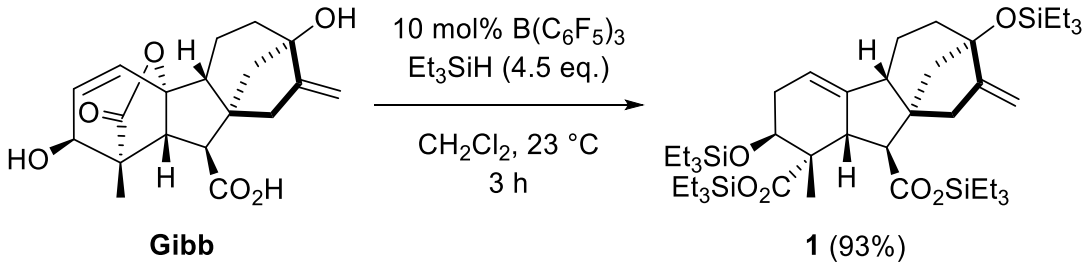

Scheme 3.1 Hydrosilylative deoxygenation of Gibb and Si-Gibb

To enhance the starting material solubility and to avoid vigorous hydrogen evolution, the allylic alcohols of gibberellic acid were pre-silylated (Me_2EtSi-, Et_3Si-; Si-Gibb), and tested under

ambient reaction conditions with excess Et_3SiH. Unlike the results obtained with Gibb in Scheme 3.1, Si-Gibb provided **2** (83%) along with the conjugated diene **3** (16%) (Scheme 3.2). Although it is unclear why pre-silylated Si-Gibb promotes elimination to **3**, all BCF-catalyzed deoxygenations favor product **2** as the major species.

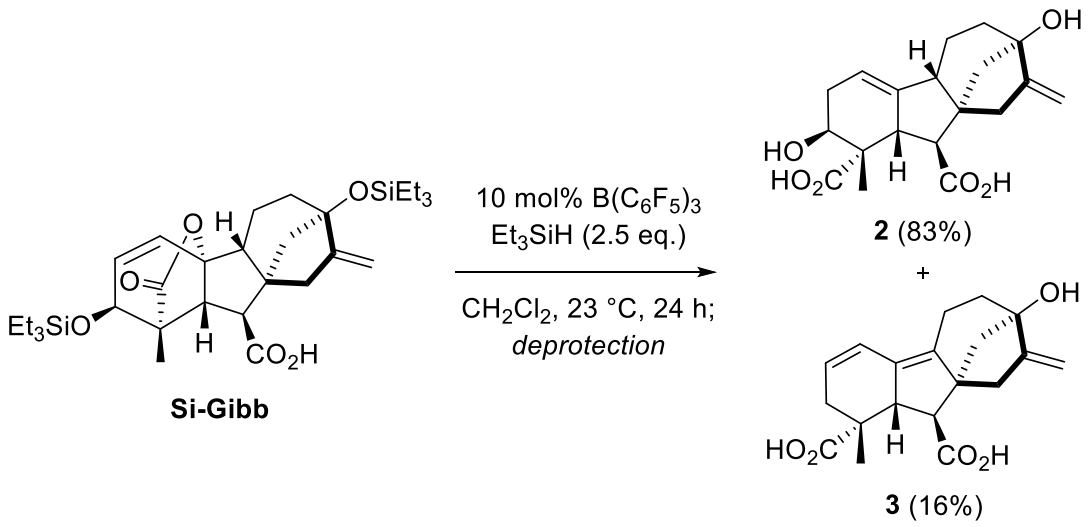

Scheme 3.2. Hydrosilylative deoxygenation of Si-Gibb with BCF and Et_3SiH

3.2.3. Gibberellic acid reactivity with HBCat as the reductant

Since free gibberellic acid and silyl protected gibberellic acid react slightly differently, both forms were tested with the alternative reductant, catecholborane (HBCat). Interestingly, different products, **2** or **4**, were obtained from Si-Gibb and Gibb after hydrolysis (Scheme 3.3).

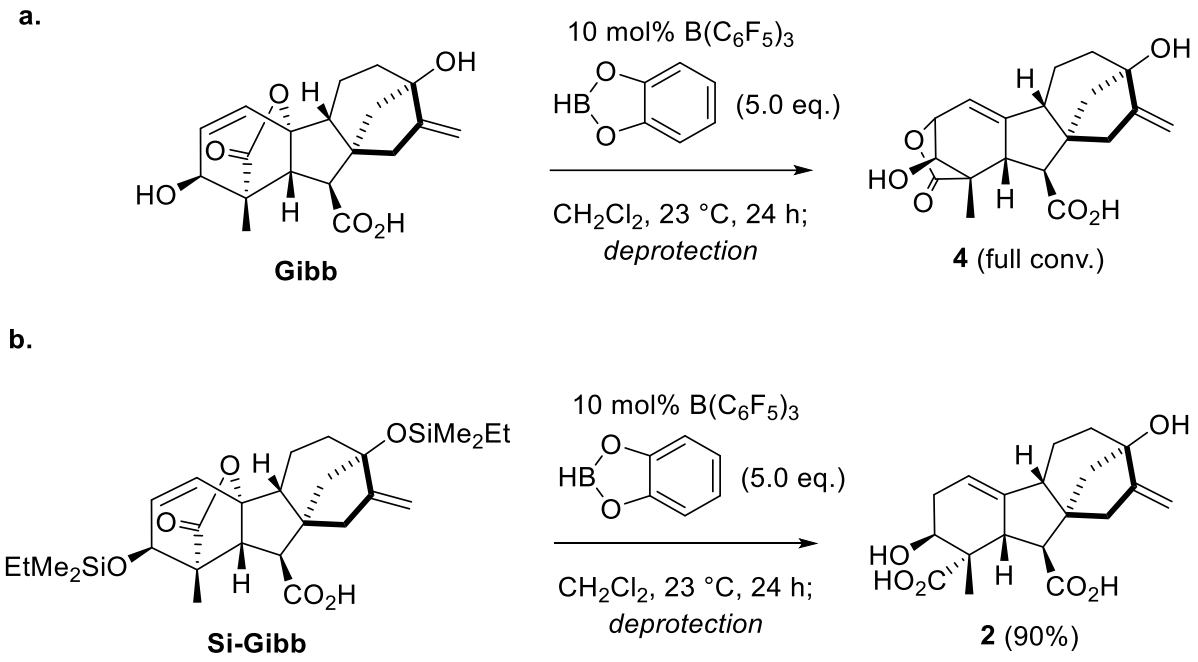

Scheme 3.3. Deoxygenation with HBCat as reductant

As evidenced from gas evolution on mixing either Gibb or Si-Gibb with HBCat (no catalyst necessary), the free alcohols and carboxylic acids become borylated, making the resulting borylated compounds the actual starting materials. Under these conditions, isomerization to known **4** occurs in contrast to Si-Gibb, which converts to **2** (Scheme 3.3). *In situ* monitoring of the reactions by ^{19}F and ^{11}B NMR spectroscopy reveal that the fluoroarylborane catalyst rests as H–$B(C_6F_5)_3^-$ in the reaction using Si-Gibb whereas it rests as various BCF Lewis adducts in reactions using Gibb. These observations agree with previously reported DFT study on the silyl/boryl oxonium ions that can be formed from 2-propanol.[66] These calculations showed that a diboryl oxonium is significantly higher in energy than a mixed silyl-boryl or disilyloxonium ion. In other words, boryl protected ethers are insufficiently Lewis basic to support the formation of a putative [(diboryl oxonium$^+$)][(H–$B(C_6F_5)_3^-$)] Lewis pair. In this situation a Lewis acid catalyzed allylic transposition becomes competitive over heterolytic cleavage of HBCat. Thus, the formation of **2** through C–O bond activation/cleavage predominates when relatively more basic silyl ethers are

present under BCF-catalyzed conditions, while non-reductive pathways dominate when the less basic boryl ester intermediates are involved.

3.2.4. Gibberellic acid reactivity with other fluoroarylboranes

Next, the less Lewis acidic fluoroarylboranes, $BAr_{2,4,6\text{-}F}$ and $BAr_{3,5\text{-}CF3}$, were tested with Si-Gibb and silane reductants. Although BCF generates a mixture of **2** and **3**, each compound can be prepared as the sole product by changing the catalyst (Figure 3.3). With 10 mol% $BAr_{2,4,6\text{-}F}$, Me_2EtSi-protected gibberellic acid was fully converted to **2** and isolated in a good yield (82%). Even though the yield was a little lower than that obtained with BCF and Gibb, **2** was not detectable by *in situ* $^{13}C\{^1H\}$ NMR. In contrast, using 10 mol% of $BAr_{3,5\text{-}CF3}$ resulted in allylic alcohol reduction coupled with lactone opening and elimination. *In situ* $^{13}C\{^1H\}$ NMR monitoring indicated a lack of detectable intermediates, with Si-Gibb being smoothly converted to **3**.

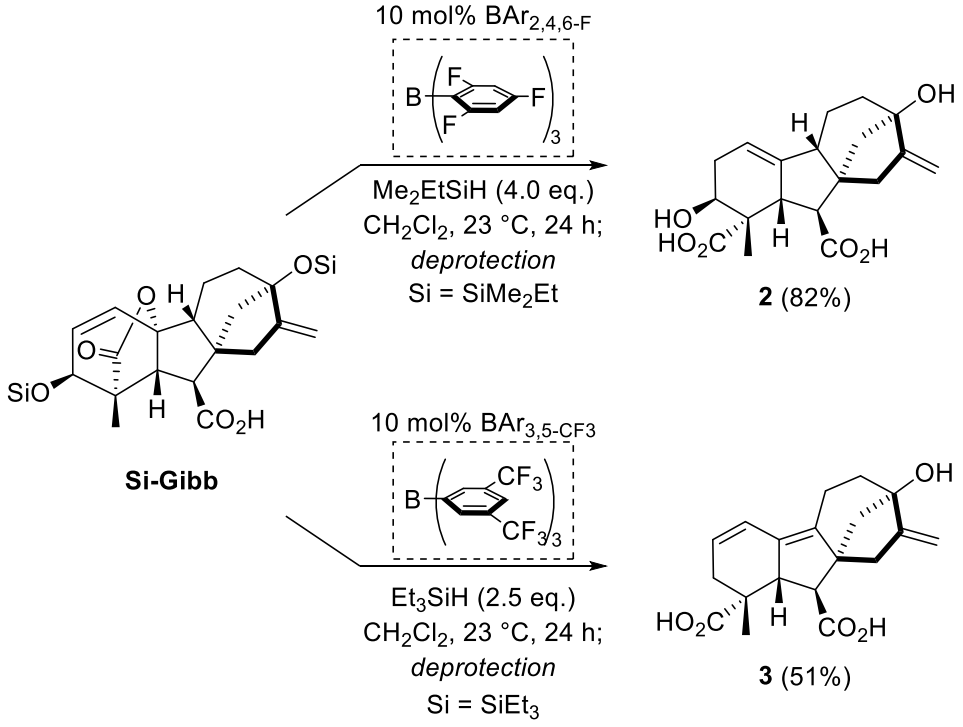

Figure 3.3. Deoxygenation with $BAr_{2,4,6\text{-}F}$ and $BAr_{3,5\text{-}CF3}$

We next sought to synthesize **3** from conjugated diene **5** *via* selective allylic alcohol reduction using a fluoroarylborane catalyst and silane (Scheme 3.4).

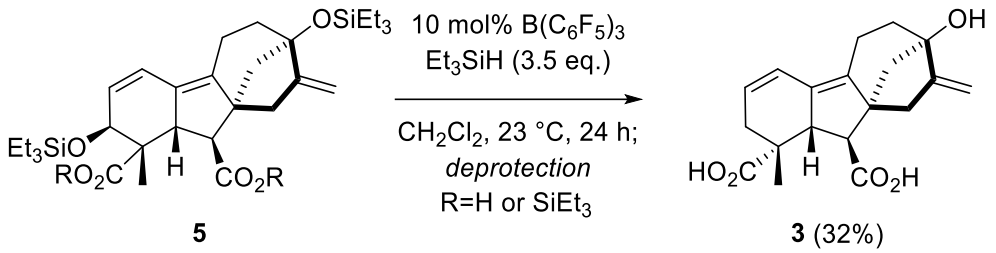

Scheme 3.4. Stepwise synthesis of gibberellic acid derivative 3

Silyl protected diene **5** was prepared *via* a previously reported procedure in 64% yield from gibberellic acid.[61] Under BCF-catalyzed hydrosilylative deoxygenation conditions, 32% of reduced allylic alcohol **3** was obtained after 24 h, with only trace amounts of **3** being formed when $BAr_{3,5\text{-}CF3}$ was the catalyst. Few examples of hydrosilylative allylic alcohol reductions with fluoroarylborane catalysts are known although several examples of C–O reductions on cyclic ethers have been reported.[69,70]

3.3. Brønsted acid catalyzed reduction of gibberellic acid

As mentioned above, BCF can act as a Brønsted acid in chemoselective reactions. According to Moran's report on BCF•H_2O catalysis, the role of the boron center is not to heterolytically active a silane, but to bind a molecule of water and provide an H^+ source for the catalytic reaction. In fact, IR experiments show evidence of hydrogen bonding between the OH of BCF•H_2O and the nitro compounds.[53]

In the context of gibberellic acid deoxygenation, BCF•H_2O performed similar transformations to its "dry" fluoroarylborane counterparts discussed earlier (Scheme 3.5). Both products **2** and **3** were observed, however, the relative yield of elimination product **2** was higher when BCF•H_2O catalyst was employed. The yield of **2** significantly dropped, irrespective of the silyl protecting group, while the yield of **3** was slightly higher.

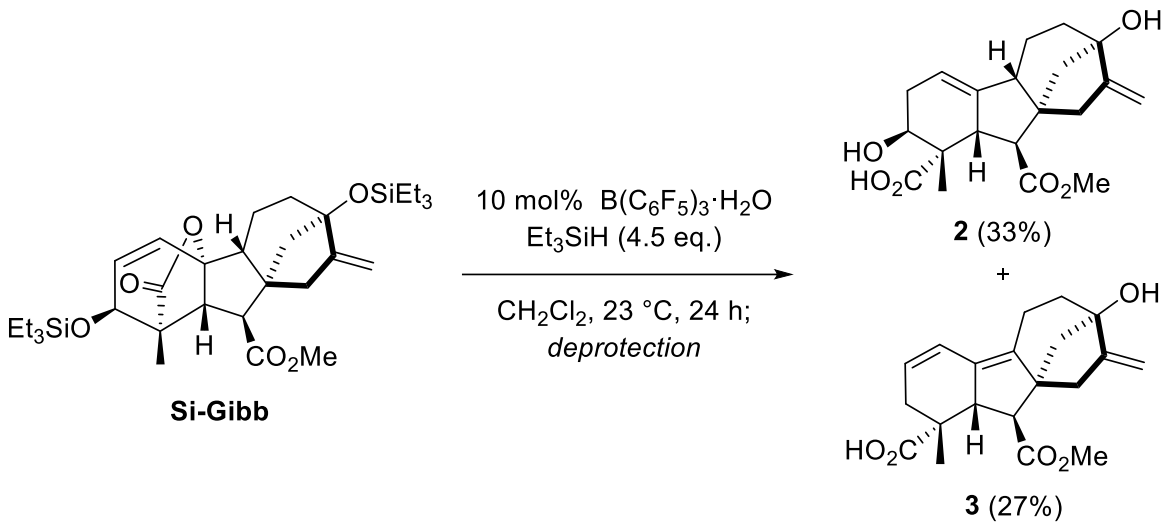

Scheme 3.5. BCF•H_2O-catalyzed hydrosilylative deoxygenation of Si-Gibb

Encouraged by the Brønsted acid activity of BCF•H_2O toward deoxygenation of gibberellic acid, we explored its utility in building novel molecular scaffolds, employing TMS–X type reagents and other nucleophiles to make new bonds. Moran's work established an unprecedented example of co-catalysis between nitro compounds and Brønsted acids, resulting in the first azidation of tertiary aliphatic alcohols with catalytic turnover. While these results highlighted the utility of BCF•H_2O as a Brønsted acid catalyst, the substrate scope was fairly limited to tertiary aliphatic alcohols. Thus, we expanded this methodology onto complex natural product structures, highlighting the importance of facile BCF•H_2O catalysis and leading not only to selective C–O bond reductions, but also to the formation of novel C–X derivatives. Ultimately, the results of this study provide a synthetic toolbox for facile population of chemical space around a given bioactive compound.

3.4. LSF of gibberellic acid with Brønsted acidic catalysis

3.4.1. Azidation of gibberellic acid

While late-stage azidation of natural products has been previously reported by Hartwig et. al.,[4] it has not been shown with BCF or a similar type catalyst in conjunction with a TMS–N_3

reagent. Installing an azide functional group is a useful synthetic transformation since the azidated products can be further derivatized by, for example, a Click-type reaction providing potentially more bioactive products than the parent molecules.[71] Starting from the known TMS-protected methylated ester gibberellic acid (TMS-Me-Gibb)[72] and using 10% of BCF•H_2O with excess TMS–N_3 at room temperature in $MeNO_2$ led to the discovery of two new azidated products and an alcohol derivate (Figure 3.4).

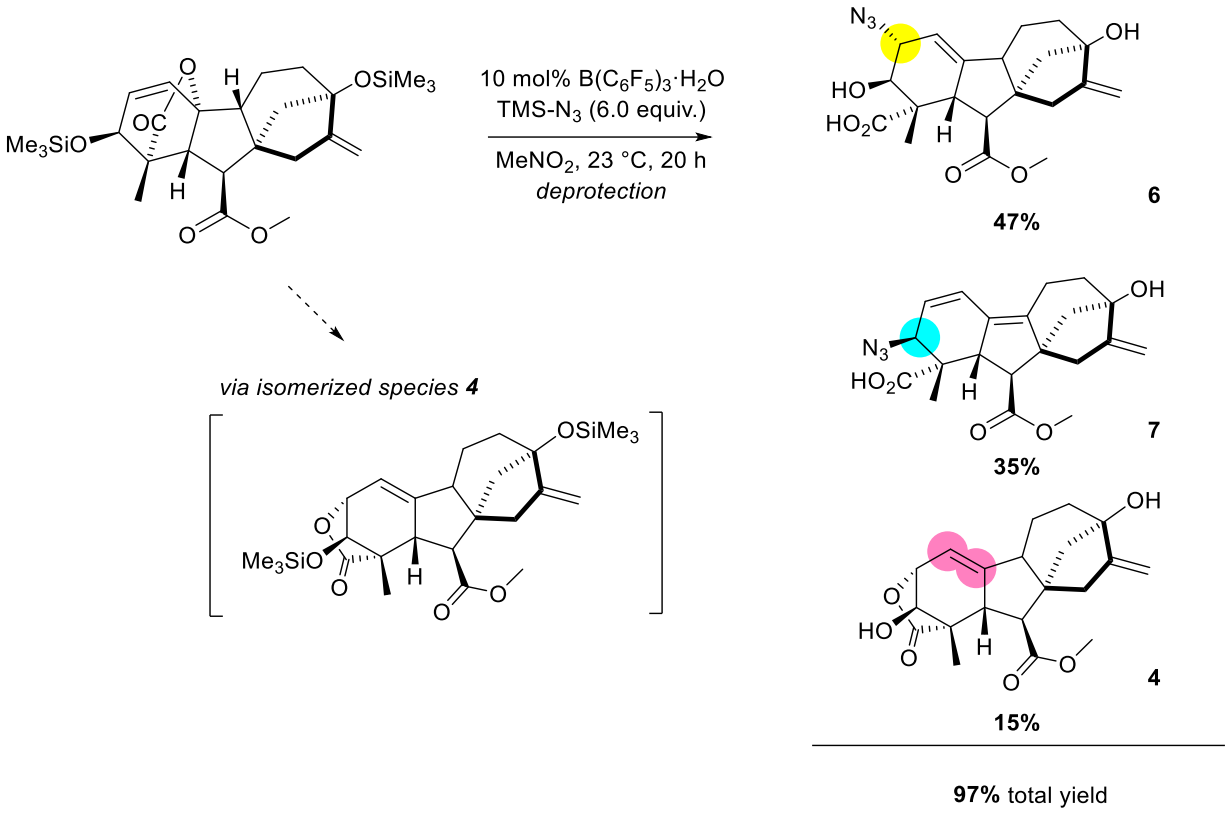

Figure 3.4. BCF•H_2O-catalyzed azidation of gibberellic acid

Three new products resulting from an azidation reaction (4, 6, and 7) are shown. Product 4 is an isomerized gibberellic acid species that serves as an intermediate to the azidation products 6 and 7. Stereochemistry of 6 and 7 was determined by ^{1}H NMR analysis.

Unlike Gagne's BCF/silane LSF catalytic systems in CH_2Cl_2, this reaction does not proceed via the Piers' mechanism but is Brønsted acid catalyzed. The first step is the H^+-catalyzed lactone

isomerization to species **4**, followed by lactone opening and nucleophilic attack on the resultant carbocation to form **6**. Species **4** does not fully react and was isolated in its unprotected form in 15% yield. If species **4** reacts through a different pathway, the diene core of product **7** can form via elimination of the proton beta to the isomerized alkene. The subsequent secondary alcohol activation leads to azidated product **7**. To the best of our knowledge, product **7** is the first example of BCF-catalyzed secondary alcohol activation in a complex molecule that results in a new azidated species. This result adds to the complexity and highlights the importance of Moran's prior report on azidation of tertiary aliphatic alcohols in $MeNO_2$. It is especially useful as it is relevant in the context of LSF of more structurally challenging bioactive systems like gibberellic acid. This reaction also worked reasonably well in a similar manner in CH_2Cl_2 solvent.

3.4.2. Other nucleophiles with gibberellic acid

In addition to the azidation reaction shown in Figure 3.4, several other nucleophiles were tested and successfully installed onto TMS-Me-Gibb. Employing 10 mol% of BCF•H_2O with excess thiophenol led to the formation of a new C–S bond (Scheme 3.6), presumably via a similar mechanistic route to that which led to formation of product **6** with TMS–N_3. While stereochemical assignment for product **8** proved to be challenging, the compound was isolated as a single major diastereomer by column chromatography. The reaction likely proceeds in the same sequence as the azidation reaction, going through isomerized species **4** before the attack of the thiophenol nucleophile.

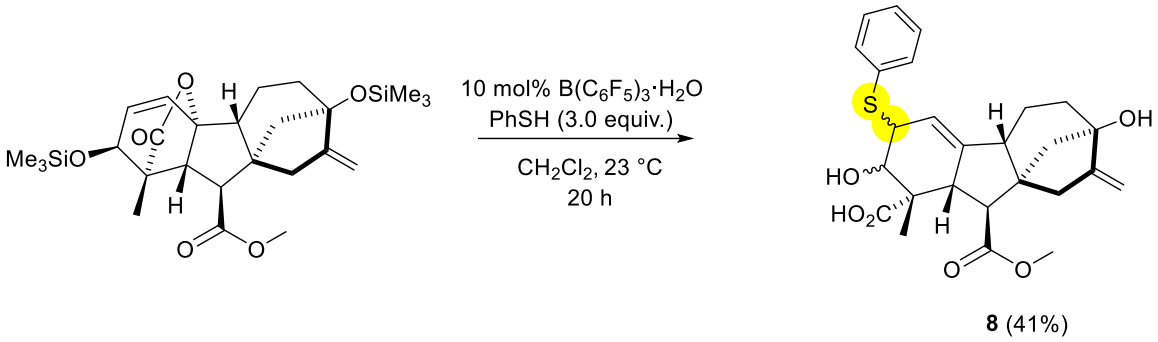

Scheme 3.6. TMS-Me-Gibb reaction with thiophenol to form a C–S bond

Mixture of diastereomers was isolated and product structure was confirmed by ^{1}H and ^{13}C NMR.

Similarly, secondary alcohol activation that resulted in product **7** formation with TMS–N_3 occurred when 1-methylindole was reacted with TMS-Me-Gibb and 10 mol% of BCF•H_2O (Scheme 3.7). This reaction resulted in formation of a new C–C bond in the major isolated product **9** as well as the previously observed isomerization to isolated product **4**. The indole stereochemistry is assigned based on the relatively low ^{1}H NMR coupling constant (J = 2.5 Hz) between the highlighted indole stereocenter proton and the neighboring olefin proton.

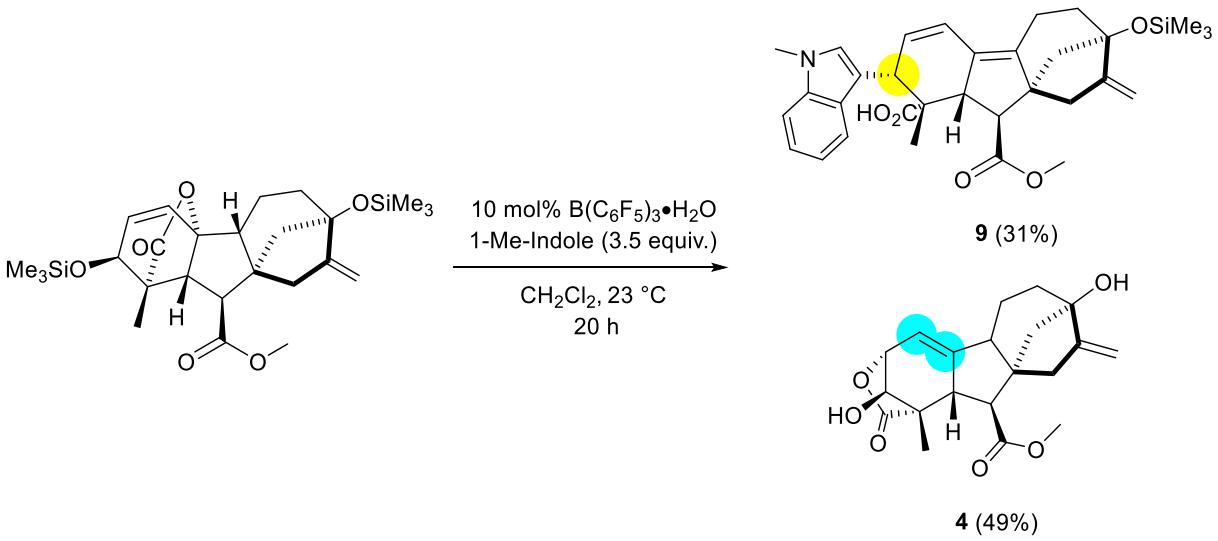

Scheme 3.7. TMS-Me-Gibb reaction with 1-methylindole to form a C–C bond

3.5. LSF of baccatin with fluoroarylborane catalysts

3.5.1. Relevant background

To demonstrate the broad utility and the synergy of combining Lewis and Brønsted acidic fluoroarylborane catalysis methodology, we investigated functionalization reactions of 10-deacetoxy baccatin III (baccatin). The following study allowed us to expand the breadth of the work beyond gibberellic acid by creating new chemical space around a structurally distinct class of natural products. Baccatin is a precursor to the commonplace chemotherapeutic drug Taxol, and thus its derivatization with various functionalities presents much interest to the medicinal chemistry community. Based on prior reports in which baccatin was studied in reactions with BCF or similar fluoroarylborane catalysts (but no nucleophiles),[5] we hypothesized that it would be feasible to install TMS–X reagents onto this molecule. Creating new baccatin derivatives in only one or two synthetic steps once again highlights the advantages of our methodology when it comes to rapidly populating chemical space around a given natural product substrate.

3.5.2. Lewis acid catalyzed azidation of baccatin

To test our hypothesis about installing new TMS–X bonds onto the baccatin structure, unprotected starting material was subjected to 10 mol% of the dry Lewis acidic BCF catalyst and 3.5 equiv. TMS–N_3 inside the glovebox in CH_2Cl_2. As a result, a new interesting azidated product **10** was observed (Scheme 3.8) along with 35% of the previously reported aldehyde **11**. To the best of our knowledge, azidated product **10** is the first example of the ring-opening of baccatin oxetane moiety followed by a skeletal rearrangement and formation of a new ring system (via a mechanism outlined in steps a-e in Scheme 3.8) . A crystal structure of **10** (Figure 3.5) confirms the installation of the N_3 functionality and the acetate migration (see Experimental section for full XRD

characterization of **10**). It is noteworthy that no side reactions occurred on the left-hand-side of the molecule, with the ketone, benzoate and allyl alcohols remaining untouched.

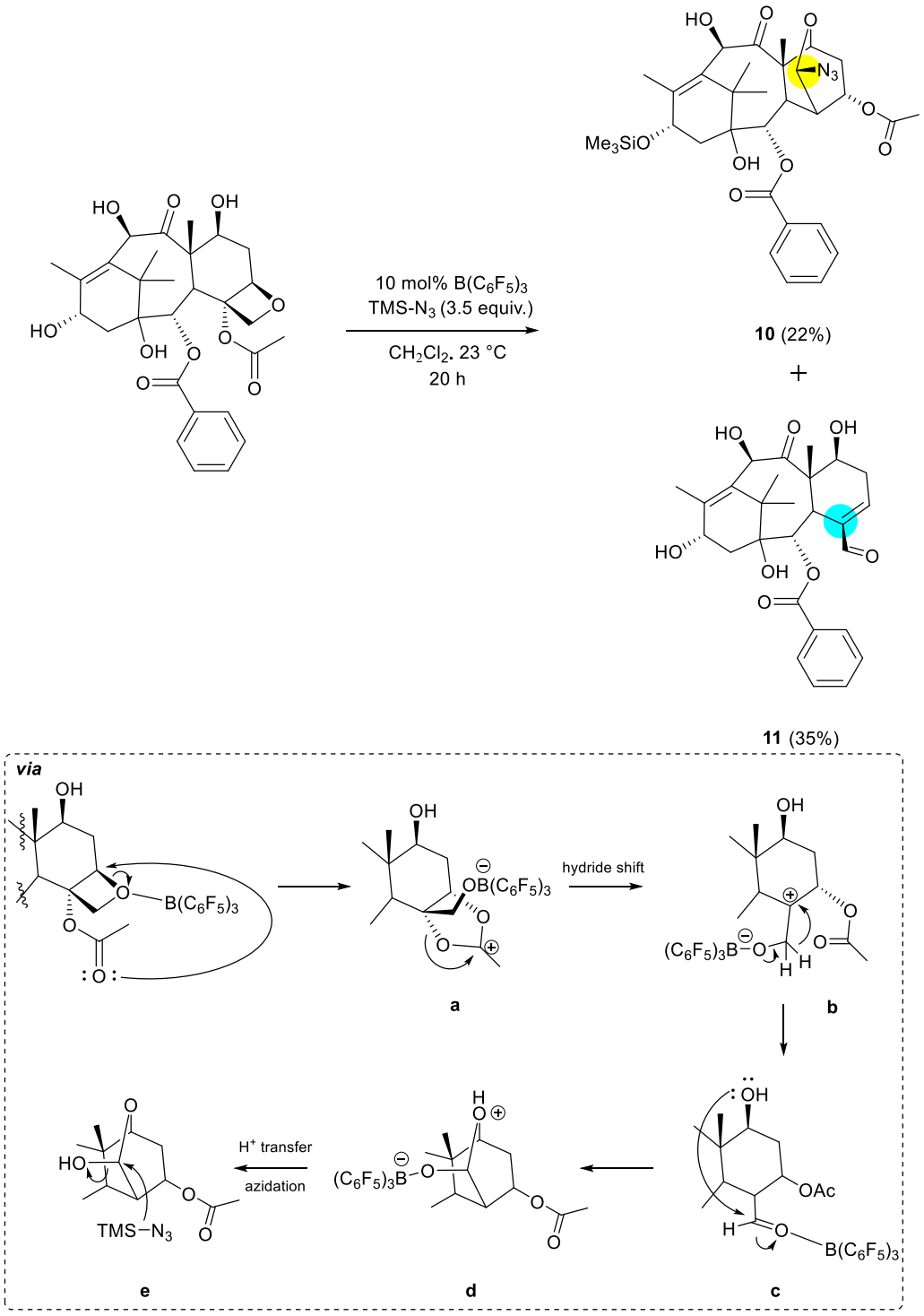

Scheme 3.8. Azidation of baccatin with TMS–N_3 and dry BCF

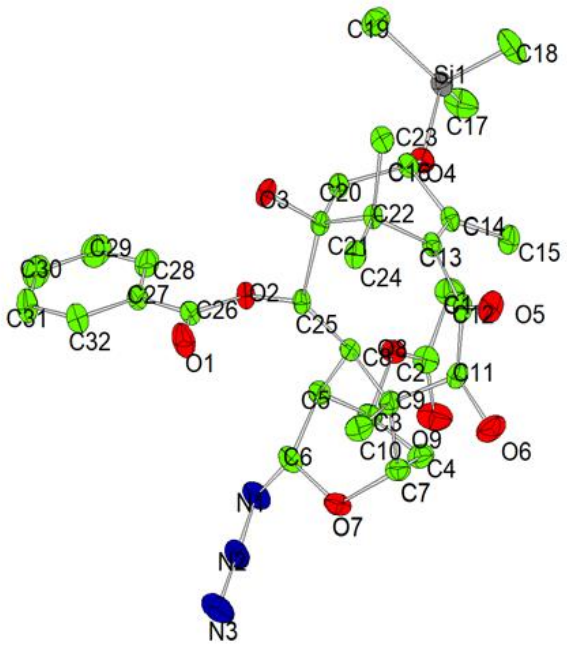

Figure 3.5. Crystal structure of the azidated product 10

Because the parent structure of baccatin was drastically changed to form **10**, this reaction presented us with an interesting diversification tool to increase the chemical space around its original structure. Further functionalization of the azide should enable one to rapidly generate a library of new baccatin derivatives which have the same structural core. Additionally, spectral evidence obtained by *in situ* ^{13}C NMR points to the formation of a new lactol-type intermediate prior to the final azidation step. Starting with such an intermediate could be useful when designing future reactions that target specific regions on the chosen molecule.

3.5.3. Functionalization of baccatin with additional nucleophiles

While the baccatin azidation result above was unexpected and arose from an unknown structural rearrangement of the parent molecule, the use of TMS–CN and 1-methylindole nucleophiles resulted in reactivity that is based on a previously reported dioxocarbenium ion intermediate.[73] Based on the results obtained so far, several new baccatin derivatives are postulated (Figure 3.6). *In situ* ^{1}H and ^{13}C NMR data provides initial spectroscopic evidence for these

structures. They key steps to form products **12-14** are the oxetane ring-opening and acetate rearrangement, followed by the nucleophile trapping the formed dioxocarbenium ion.

Starting with unprotected baccatin, a cyano functional group is installed in this fashion to generate major product **12** (35%). Selective 1D and 2D NMR experiments (DEPT 135, HSQC, and HMBC) suggest the presence of the highlighted quaternary carbon center containing both the methyl and the cyano groups, with exact stereochemistry yet to be determined. Previously reported ring-contraction of the left-hand-side of the molecule followed by dioxocarbenium trapping resulted in minor product **13** (12%).[73] It is interesting to note that only a mixture of products **12** and **13** were observed when TMS–CN was used regardless of the reaction conditions, with no spectral evidence suggesting a reaction pathway similar to the prior TMS–N_3 example.

As in the cyanide experiments, the same spectroscopic handles were used to arrive at proposed product **14** (40%) – the result of the 1-methylindole nucleophilic attack. Selective 2D NMR data confirmed the shown regioselectivity for **14** (i.e. 1-methylindole reaction at C3), with exact stereochemistry to be determined. It is also noteworthy that product **14** was only observed under Brønsted acidic conditions in the presence of the BCF•H_2O catalyst and the 1:1 CH_2Cl_2:hexafluoroisopropanol (HFIP) solvent mixture. Since this reaction does not occur at all in neat CH_2Cl_2 or $MeNO_2$ solvents, we propose that the high H-bonding donor ability and dielectric constant of HFIP (see the following section) are responsible for stabilizing the key intermediates and allowing the reaction to take place.

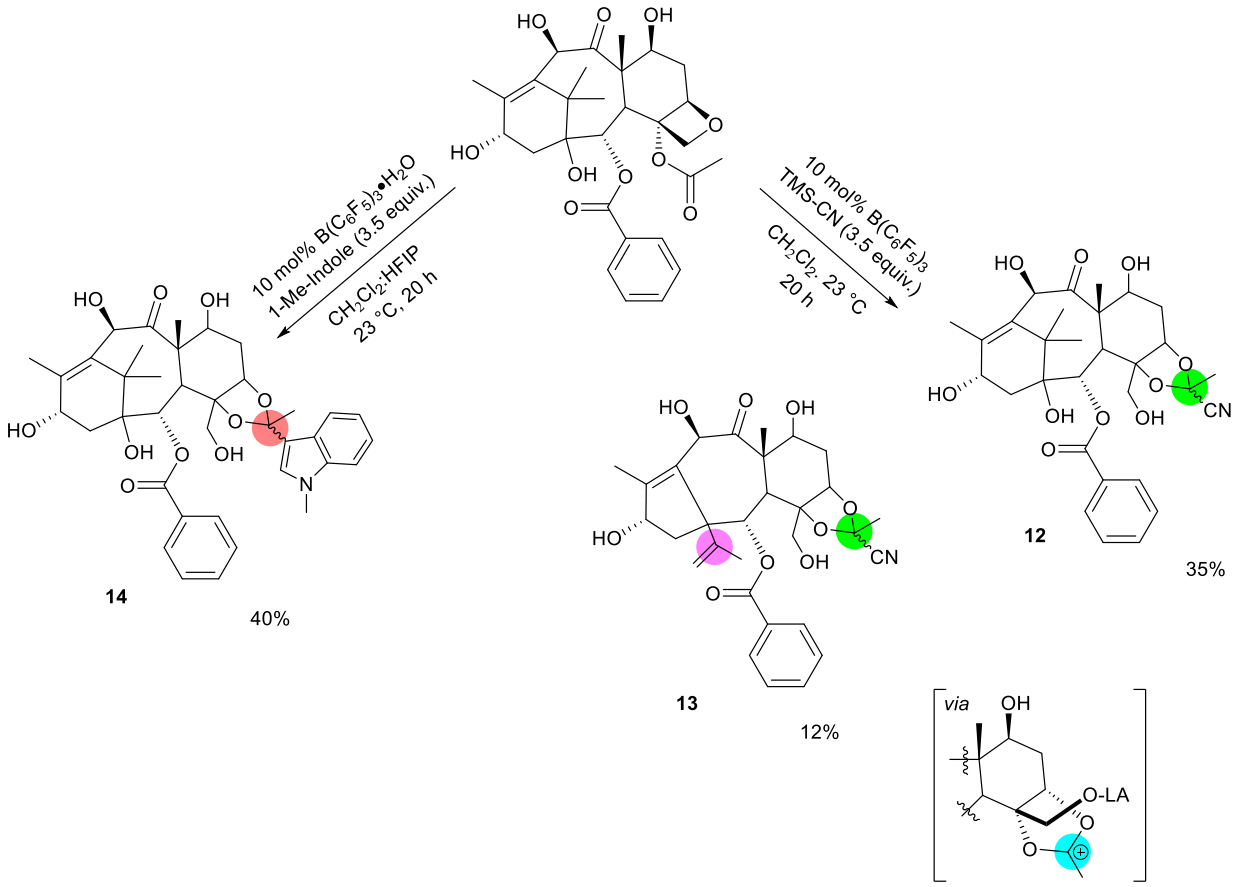

Figure 3.6. Summary of postulated new baccatin derivatives

3.6. Brønsted acid catalysis and Friedel-Crafts reactivity in HFIP

Recently, HFIP solvent has emerged as an important solvent for a variety of organic transformations that were traditionally challenging to accomplish in traditional solvents. Inspired by the recent work of the Hall and Moran labs on alcohol activation in HFIP,[74–76] we also decided to probe the possibility of activating the two alcohols present on the gibberellic acid molecule for Friedel-Crafts-type reactions. While the BCF•H_2O catalyst is not an effective Brønsted acid for these functionalizations, utilizing 10 mol% of triflic acid in combination with 3.0 equiv. of 1,4-dimethoxybenzene in HFIP led to the formation of previously unreported product **16** in moderate yields (Scheme 3.9).

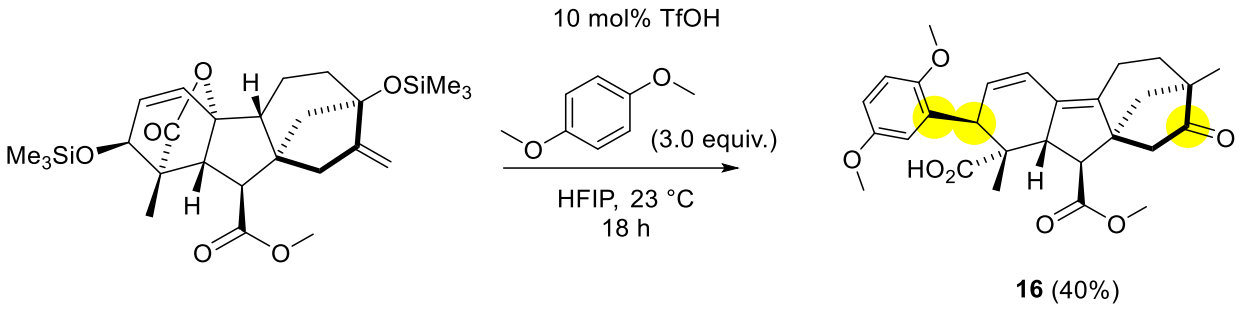

Scheme 3.9. TMS-Me-Gibb reaction with 1,4-dimethoxybenzene in HFIP

Interestingly, the tertiary alcohol on the right-hand-side of the molecule also reacts, but not to install the nucleophile at this position. Instead, the system undergoes the Wagner-Meerwein rearrangement[71] resulting in a new ketone species. Observation of the previously unreported product **16** establishes an exciting precedent from both synthetic organic and LSF-type perspectives since it demonstrates that a complex substrate can survive the relatively harsh conditions of a strong Brønsted acid catalyst in HFIP to yield a novel C–C bond containing derivative.

3.7. Assembled boronic acid catalysts for LSF

3.7.1. Scope of assembled boronic acid Brønsted acids catalysts

To further probe the role of the catalysts in Brønsted-acid catalyzed azidation of gibberellic acid, we decided to compare the BCF•H_2O catalyst to the previously reported assembled boronic acid ester systems (i.e. Scheme 3.10).[77] The literature-reported *in situ* assembly of these catalysts can be monitored by ^{19}F NMR spectroscopy, with the fluorine shifts providing evidence for the fully hydrated form of these Brønsted acidic species.[77,78]

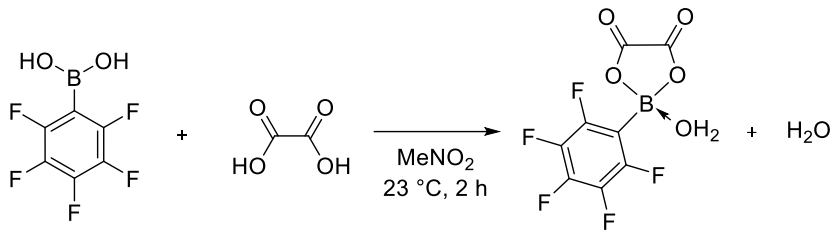

17

Scheme 3.10. Assembly example for a boronic acid ester catalyst

These hydrated catalysts, made from the combination of boronic acids and diacid ligands, are in principle much more economically attractive than BCF•H_2O due to the relatively low cost of the starting materials required for their assembly. Synthetically, they were shown to be active in Friedel-Crafts reactions of alcohols, leading to the formation of new C–C bonds in $MeNO_2$.[77] Since the boron center of these boronic acid esters was reported to possess slightly lower, but comparable Lewis acidity to that of BCF,[79] we hypothesized that they would exhibit similar reactivity in small molecule hydrosilylation reactions and, potentially, more complicated transformations like the azidation of gibberellic acid. Inspired by earlier reports by Hall[74] and Moran[77] on these catalysts' assembly, we studied the feasibility of assembling novel systems and their activity toward hydrosilylation. The results summarized in Figure 3.7 point to the fact that certain boronic acid and diacid combinations are more likely to assemble than others, as well as the fact that some of them are significantly more active than others for the proposed hydrosilylation of cyclohexanone (the test reaction). All of these catalysts exist in either partially or fully hydrated forms (dative bond to H_2O shown), rendering these systems Bronsted acidic with highly electrophilic boron centers.

Boronic acid	Diol ligand	Catalyst	Assembly (after 2 h)	Hydrosilylation of cyclohexanone rate
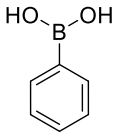	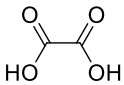	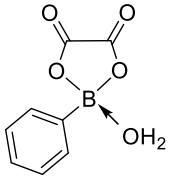 **18**	Partial	**Low** (63% conversion after 3 days)
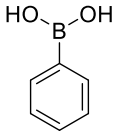	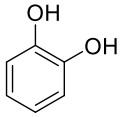	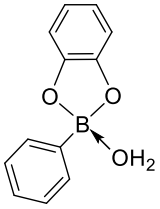 **19**	Partial	**Very low** (3% conversion after 5 days)
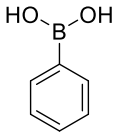	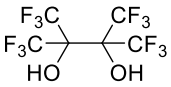	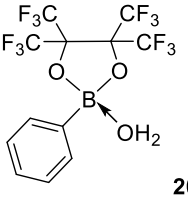 **20**	Partial	**Low** (56% conversion after 3 days)
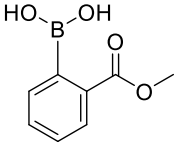	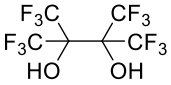	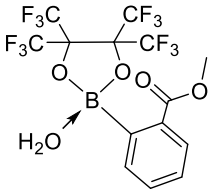 **21**	Full	**Moderate** (75% conversion after 2 days)
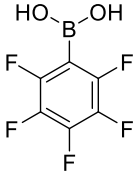	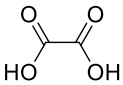	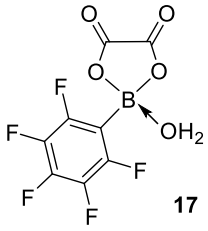 **17**	Full	**Moderate** (85% conversion after 1 day)
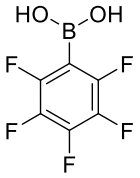	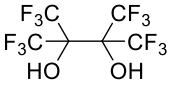	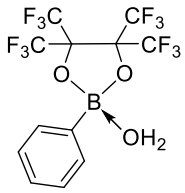 **22**	None	**None**

Figure 3.7. Assembled boronic acid systems

As seen from Figure 3.7, the two most active systems were either the catalyst **21** assembled from 2-methoxycarbonylphenylboronic acid and perfluoropinacol (reported by Hall) or the catalyst **17** assembled from pentafluorophenyl boronic acid and oxalic acid (reported by Moran). A speciation study was performed with catalyst **21** in which **21**, PPh_3, and Et_3SiH were combined to determine whether **21** can heterolytically activate Et_3SiH, operating under a Piers-like mechanism,[22] and generate an ion pair similar to the experiments extensively discussed in Chapter 2. However, only free PPh_3 was observed by ^{31}P NMR, indicating that this catalyst does not behave in the same manner as Lewis acidic BCF. However, **21** still proved to be active for cyclohexanone hydrosilylation, albeit at slower rates than **17**. For this reason, catalyst **17** – which was successful in earlier reported Friedel-Crafts reactions – was tested for gibberellic acid reactivity in the late-stage azidation reaction.

Gratifyingly, employing 10 mol% of boronic acid ester **17** in the presence of excess TMS–N_3 in $MeNO_2$ led to the formation of all three previously observed products (highlighted in Figure 3.8), with a net 91% yield. While the overall yield of products **4**, **6**, and **7** is only slightly lower than that obtained with BCF•H_2O, this result was very encouraging considering the much lower cost of this boronic acid ester system and its ease of assembly in $MeNO_2$ and CH_2Cl_2 under ambient conditions.

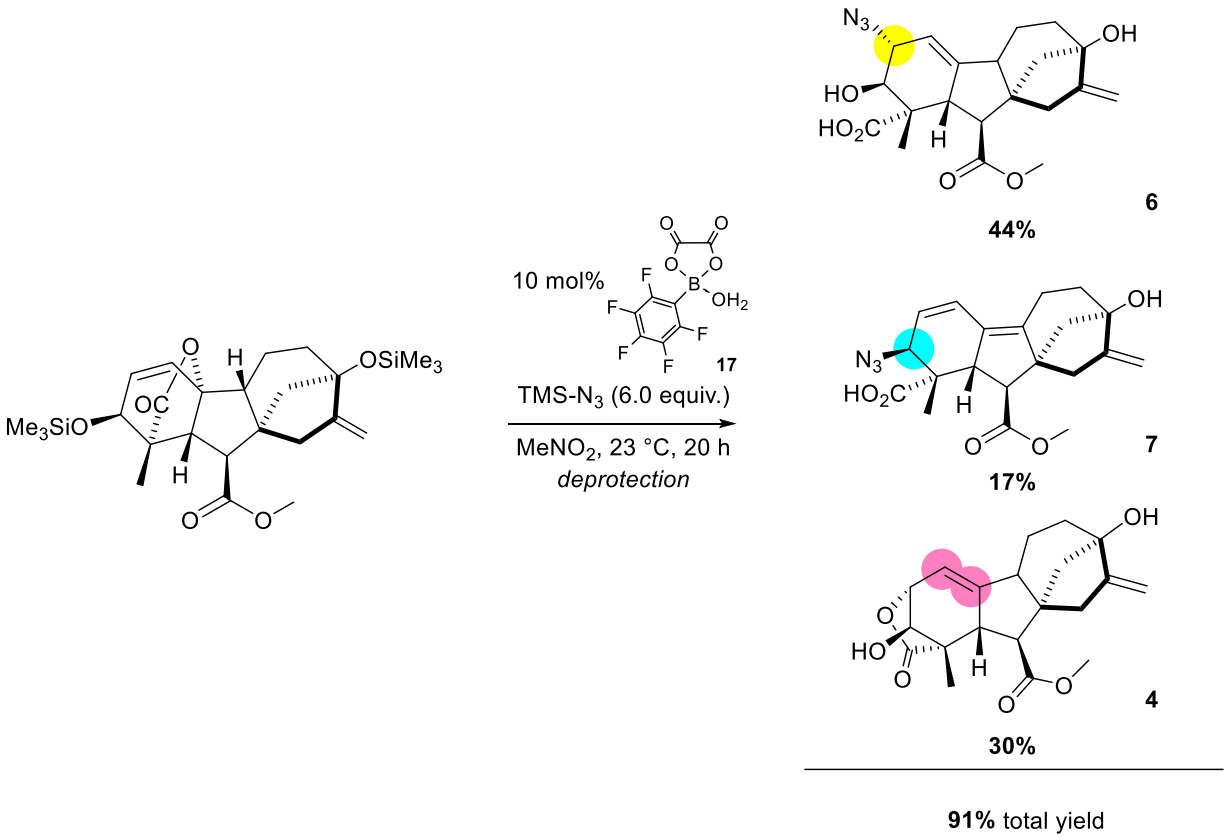

Figure 3.8. Assembled boronic acid catalyzed TMS-Me-Gibb azidation

3.7.2. Catalyst comparison for azidation of gibberellic acid

To complete the comparison between several structurally distinct Brønsted acid catalysts in $MeNO_2$ and CH_2Cl_2, we also studied the effect of utilizing triflic acid to achieve the desired LSF transformation. Reacting TMS-Me-Gibb with 10% of TfOH and excess TMS–N_3 in $MeNO_2$ led to 85% total yield of the reported products, with 37% attributed to elimination product **7** – the highest observed for the three catalysts. Carrying out the azidation reaction in CH_2Cl_2 with the same set of catalysts revealed that these solvents are both compatible with the system, but $MeNO_2$ provides greater overall yields and the aforementioned higher fraction of elimination product **7** irrespective of the catalyst.

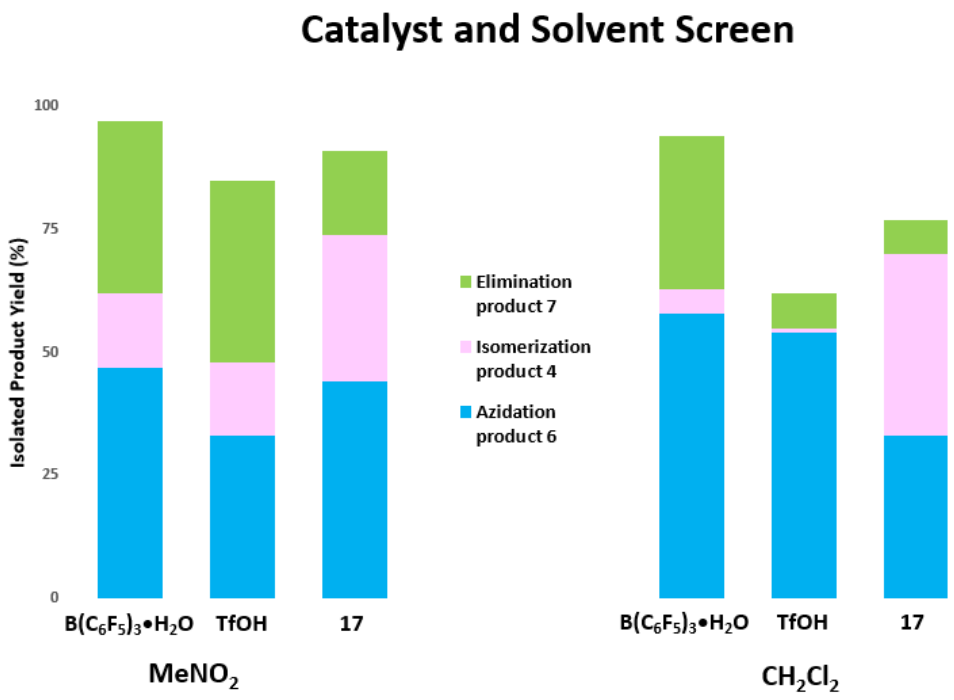

Figure 3.9. Catalyst and solvent comparison for TMS-Me-Gibb azidation

The results summarized in Figure 3.9 establish a series of interesting trends that can be referenced when a higher yield of a specific product is desired. Also, the relative assembly ease of catalyst **17** makes it an attractive general alternative to the commonly used BCF•H_2O or stronger classical Brønsted acid catalysts like TfOH.

3.8. Experimental section

3.8.1. General experimental considerations

All reactions were performed at ambient temperature (23 ºC, RT) unless otherwise specified. All workup procedures were performed under air with reagent grade reagents unless otherwise specified. Column chromatography was performed using SilaFlash P60 40-63 μm (230-400 mesh). Thin layer chromatography (TLC) was performed on SiliCycle Silica Gel 60 F254 plates and was visualized with ceric ammonium molybdate (CAM) stain. All NMR spectra were recorded on a Bruker Avance 600 or a Bruker Avance 400 MHz spectrometer at standard

temperature and pressure. All deuterated solvents were used as received from Cambridge Isotope Laboratories, Inc. The residual solvent protons (^{1}H) or the solvent carbons (^{13}C) were used as internal standards. The following abbreviations are used in reporting NMR data: s, singlet; d, doublet; dd, doublet of doublets; dt, doublet of triplets; td, triplet of doublets; ddd, doublet of doublet of doublets; and m, multiplet. Where necessary, 2D COSY, and HSQC data were used for peak assignment. High Resolution Mass spectra were obtained on Q Exactive™ HF-X Hybrid Quadrupole-Orbitrap™ Mass spectrometer.

All chemicals were used as received, or otherwise described on how it was treated before use. $Me_2EtSiCl$ was purchased from Gelest, and gibberellic acid was purchased from Carbonsynth Biosynth.

3.8.2. General experimental procedure for silyl protection

A magnetic stir-bar equipped 100-mL round bottom flask was charged with gibberellic acid (2.00 g, 5.77 mmol, 1.00 equiv.) and imidazole (1.97 g, 28.87 mmol, 5.00 equiv.) capped with a rubber septum, and a positive flow of nitrogen established. After dissolving the solids with CH_2Cl_2 (30.0 mL), the solution was cooled to 0 °C in an ice bath. Et_3SiCl (4.36 mL, 25.98 mmol, 4.50 equiv.) or $Me_2EtSiCl$ (3.65 mL, 25.97 mmol, 4.50 equiv.) were slowly added by syringe at 0 °C, and the reaction was allowed to stir overnight at room temperature. After starting material was consumed, water (20 mL) was added and the reaction contents transferred to a separatory funnel along with CH_2Cl_2 rinses from the reaction flask (2 x 10 mL). The layers were separated and the aqueous phase extracted with CH_2Cl_2 (2 x 20 mL). The combined organic fractions were washed with water (2 x 40 mL), brine (2 x 40 mL), then collected and dried over magnesium sulfate. The solvent was removed under vacuum, and the product was purified by silica gel chromatography

(20 x 4 cm column) using a gradient elution profile (100% hexanes to 20:1 to 15:1 to 10:1 to 5:1 to 4:1, hexanes: ethyl acetate) to afford Et_3Si-Gibb (81%) as white solid or Me_2EtSi-Gibb (89%).

Et_3Si-Gibb

^1H NMR (600 MHz, Acetone-d6): δ 6.39 (d, J = 9.3 Hz, 1H), 5.85 (dd, J = 9.3, 3.7 Hz, 1H), 5.20 (s, 1H), 4.91 (s, 1H), 4.15 (d, J = 3.6 Hz, 1H), 3.28 (d, J = 10.8 Hz, 1H), 2.73 (d, J = 10.8 Hz, 1H), 2.35 (dt, J = 15.6, 3.0 Hz, 1H), 2.32 – 2.25 (m, 1H), 2.11 – 2.06 (m, 1H), 2.04 – 1.98 (m, 2H), 1.95 (dd, J = 10.5, 1.3 Hz, 1H), 1.88 – 1.77 (m, 2H), 1.75 – 1.68 (m, 1H), 1.19 (s, 3H), 1.02 – 0.93 (m, 18H), 0.72 – 0.66 (m, 6H), 0.63 – 0.58 (m, 6H).

^{13}C NMR (151 MHz, Acetone) δ 178.7, 173.1, 158.6, 133.5, 132.9, 107.2, 91.2, 80.2, 71.1, 54.7, 53.5, 51.6, 51.4, 51.0, 45.1, 43.3, 41.7, 17.7, 15.5, 7.4, 7.1, 7.0, 5.5.

HRMS (EI) calculated for $C_{31}H_{50}O_6Si_2Na$ $[M+Na]^+$: 597.3039; found 597.3063.

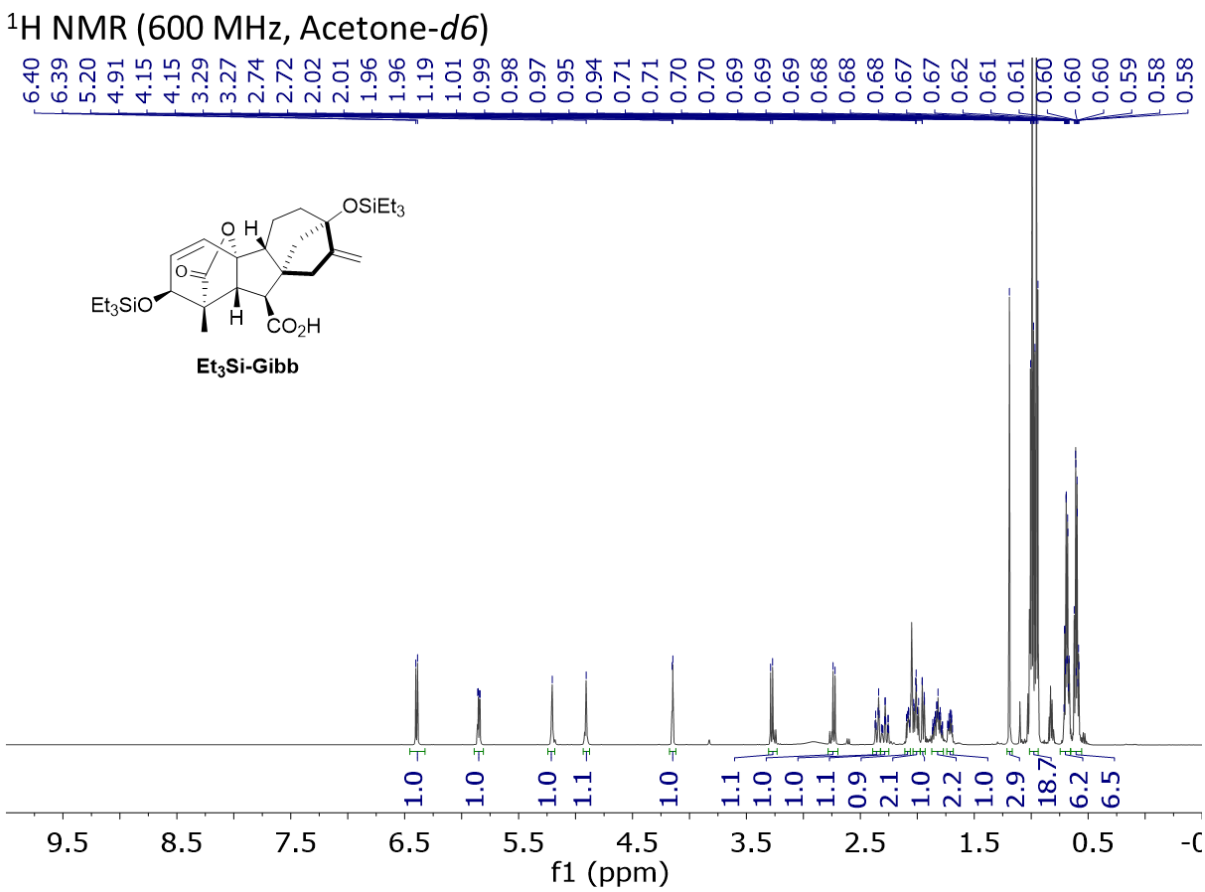

Figure 3.10. ^{1}H NMR spectrum of Et_3Si-Gibb protected material

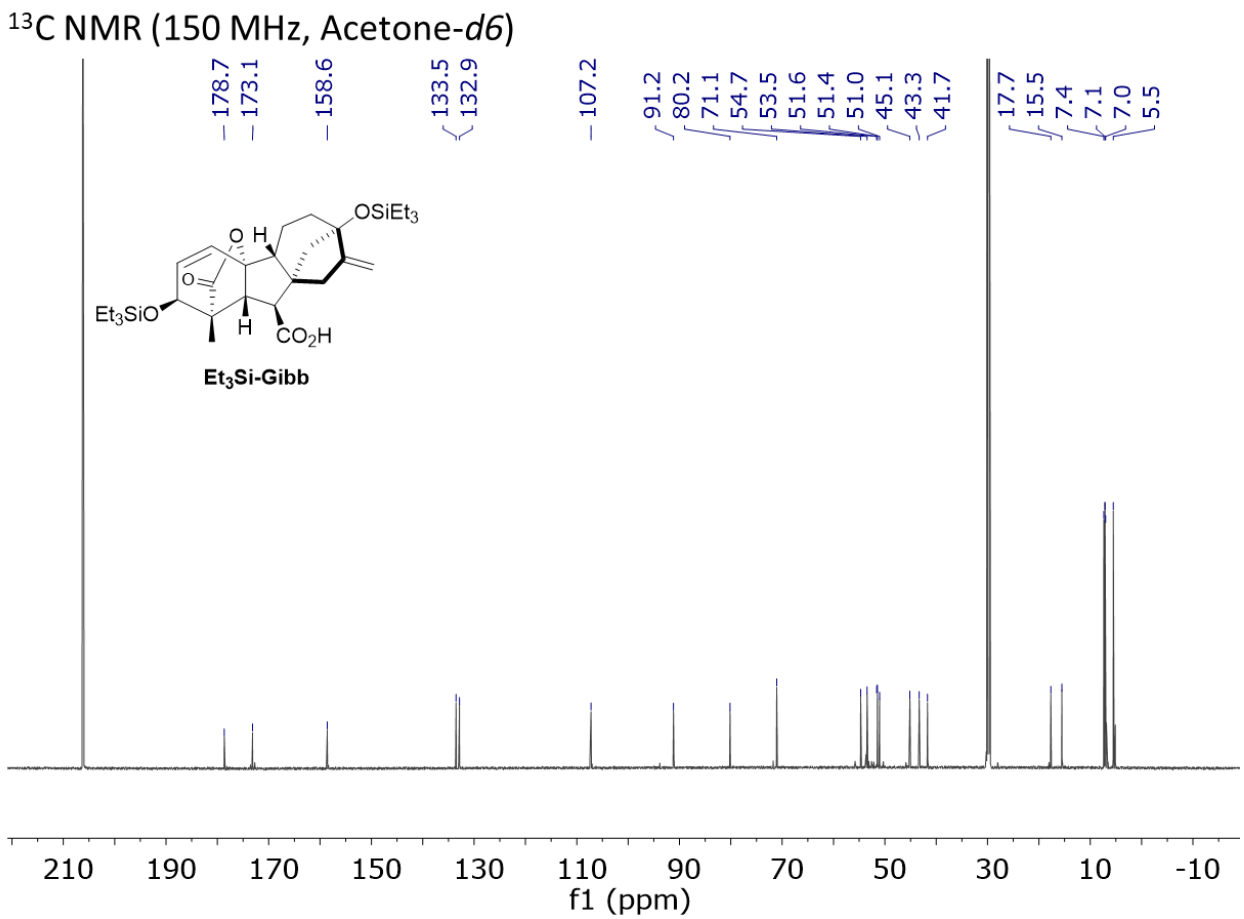

Figure 3.11. ^{13}C NMR spectrum of Et_3Si-Gibb protected material

Me_2EtSi-Gibb

^{1}H NMR (600 MHz, CD_2Cl_2) δ 6.25 (d, J = 9.3 Hz, 1H), 5.76 (dd, J = 9.3, 3.7 Hz, 1H), 5.21 (s, 1H), 4.92 (s, 1H), 4.11 (d, J = 3.7 Hz, 1H), 3.23 (d, J = 10.8 Hz, 1H), 2.80 (d, J = 10.8 Hz, 1H), 2.32 (dt, J = 15.5, 3.0 Hz, 1H), 2.22 (d, J = 15.5 Hz, 1H), 2.13 – 2.04 (m, 1H), 2.01 (dd, J = 10.6, 2.7 Hz, 1H), 1.96 – 1.75 (m, 4H), 1.70 – 1.62 (m, 1H), 1.18 (s, 3H), 0.99 – 0.89 (m, 6H), 0.61 (qd, J = 7.9, 2.8 Hz, 2H), 0.55 (qd, J = 7.9, 1.7 Hz, 2H), 0.14 (d, J = 3.3 Hz, 6H), 0.09 (d, J = 4.9 Hz, 6H).

^{13}C NMR (151 MHz, CD_2Cl_2) δ 179.1, 176.6, 157.6, 133.6, 132.0, 107.9, 91.2, 80.1, 70.6, 53.3, 51.4, 51.2, 51.1, 44.7, 43.2, 41.1, 17.6, 15.4, 10.6, 9.0, 7.2, 7.0, 0.2, 0.1, -1.6, -1.9.

HRMS (EI) calculated for $C_{27}H_{42}O_6Si_2Na$ $[M+Na]^+$: 541.2413; found 541.2433.

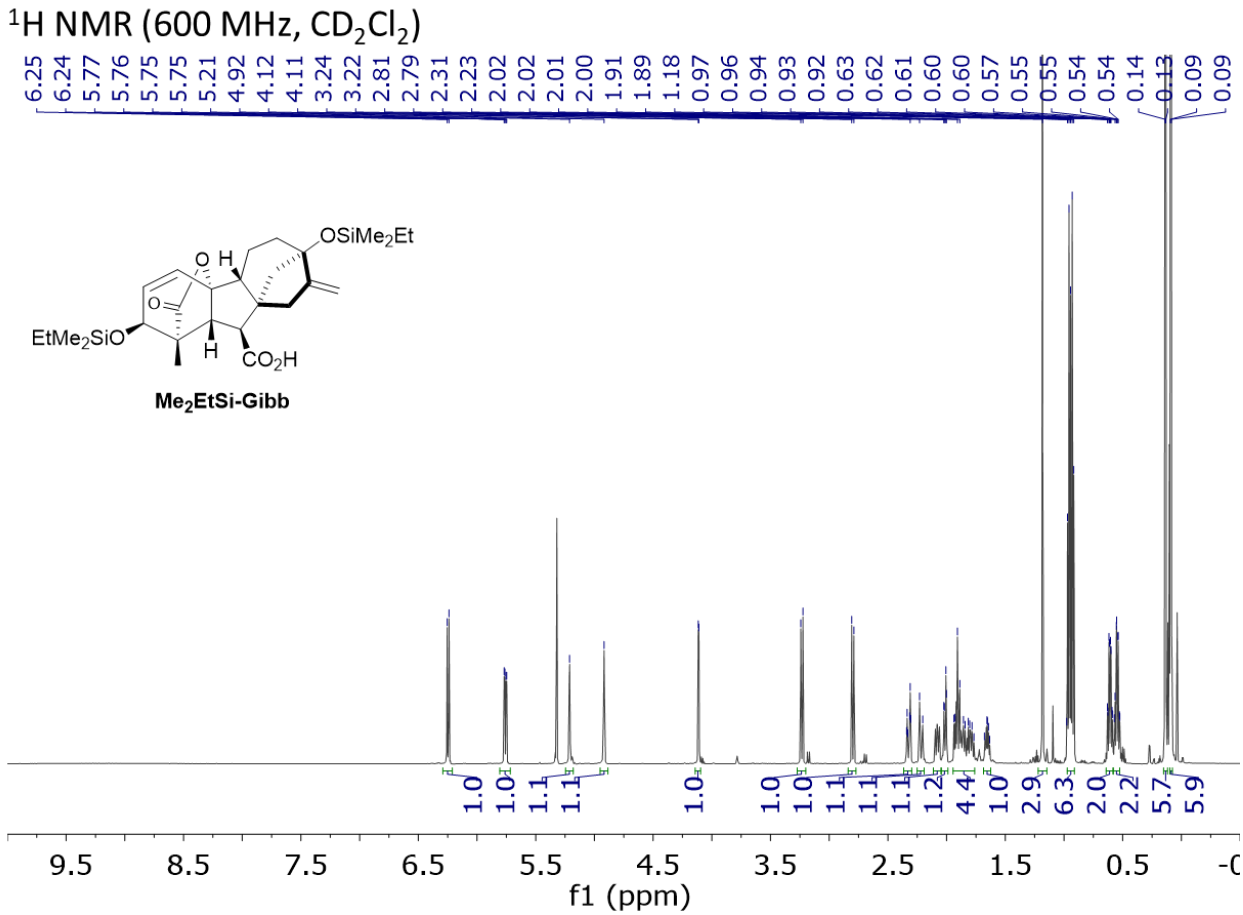

Figure 3.12. ^{1}H NMR spectrum of Me_2EtSi -Gibb. protected material

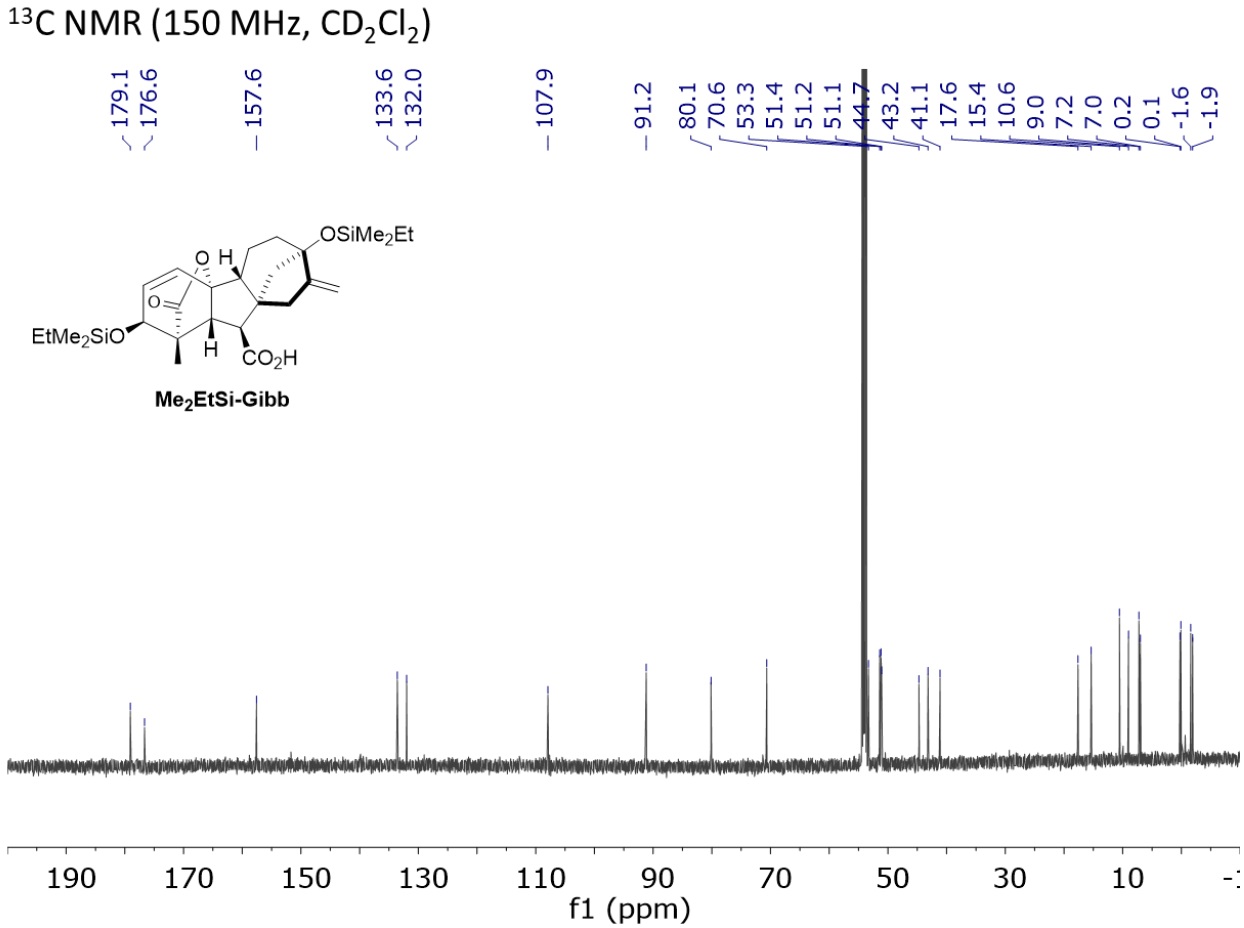

Figure 3.13. ^{13}C NMR spectrum of Me_2EtSi-Gibb protected material

3.8.3. Preparation of product 5

A magnetic stir-bar equipped 100-mL round bottom flask was charged with gibberellic acid (2.00 g, 5.77 mmol, 1.00 equiv.) and hydrazine monohydrate (10 mL), and the reaction was refluxed at 110 °C for 1 h. The reaction was then cooled in an ice bath, diluted with water (10 mL), and acidified to pH 3 with concentrated hydrochloric acid. The aqueous phase was extracted with ethyl acetate (3 x 30 mL) and the combined organic layers were washed with brine (2 x 40 mL), dried over magnesium sulfate and concentrated. The obtained crude mixture was used to prepare **5** without further purification. The same silyl protecting procedure was applied as

described above to afford a mixture of **5**-silyl ester (R=$SiEt_3$) and **5**-carboxylic acid (R=H) in 53% yield in 2 steps. The mixture of silyl ester and carboxylic acid was used.

5-silyl ester (R=$SiEt_3$)

^{1}H NMR (600 MHz, Acetone-d_6) δ 6.32 (d, *J* = 9.6 Hz, 1H), 5.93 (dd, *J* = 9.7, 5.4 Hz, 1H), 5.15 (s, 0H), 4.95 (s, 1H), 4.41 (d, *J* = 5.4 Hz, 1H), 3.78 (d, *J* = 8.9 Hz, 1H), 3.62 (dd, *J* = 8.9, 4.5 Hz, 1H), 2.60 (dd, *J* = 16.5, 6.3 Hz, 1H), 2.48 (dt, *J* = 16.3, 3.0 Hz, 1H), 2.36 (dd, *J* = 10.1, 2.8 Hz, 1H), 2.26 – 2.17 (m, 1H), 2.14 – 2.05 (m, 1H), 1.82 – 1.66 (m, 3H), 1.26 (s, 3H), 1.05 – 0.95 (m, 36H), 0.86 – 0.80 (m, 6H), 0.78 – 0.72 (m, 6H), 0.69 – 0.60 (m, 12H).

^{13}C NMR (151 MHz, Acetone) δ 175.6, 174.8, 155.4, 139.7, 131.1, 128.1, 123.7, 106.4, 81.2, 70.9, 56.8, 52.8, 51.7, 51.5, 48.4, 42.3, 39.7, 21.3, 21.1, 7.4, 7.3, 7.2, 6.9, 6.9, 5.8, 5.2, 5.2.

HRMS (EI) calculated for $C_{43}H_{78}O_6Si_4Na$ $[M+Na]^+$: 825.4768; found 825.4799.

^{1}H NMR (600 MHz, Acetone-d_6)

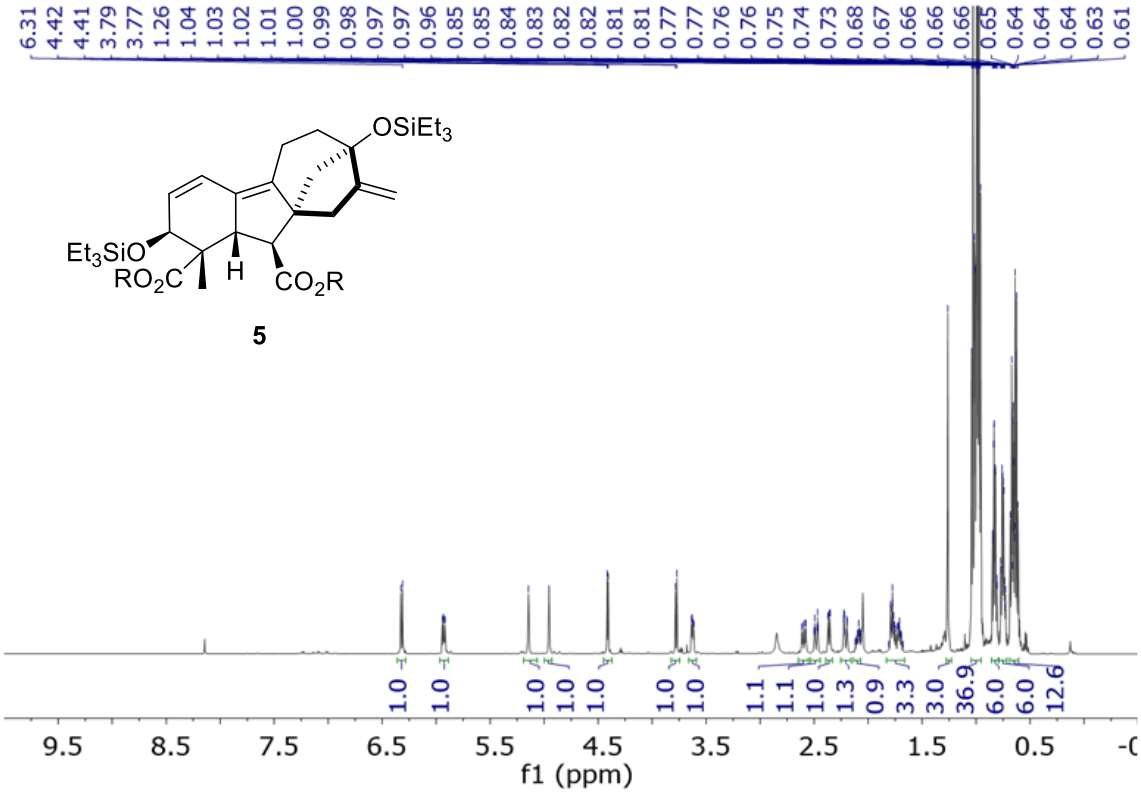

Figure 3.14. ^{1}H NMR spectrum of compound 5 when R = $SiEt_3$

^{13}C NMR (150 MHz, Acetone-d_6)

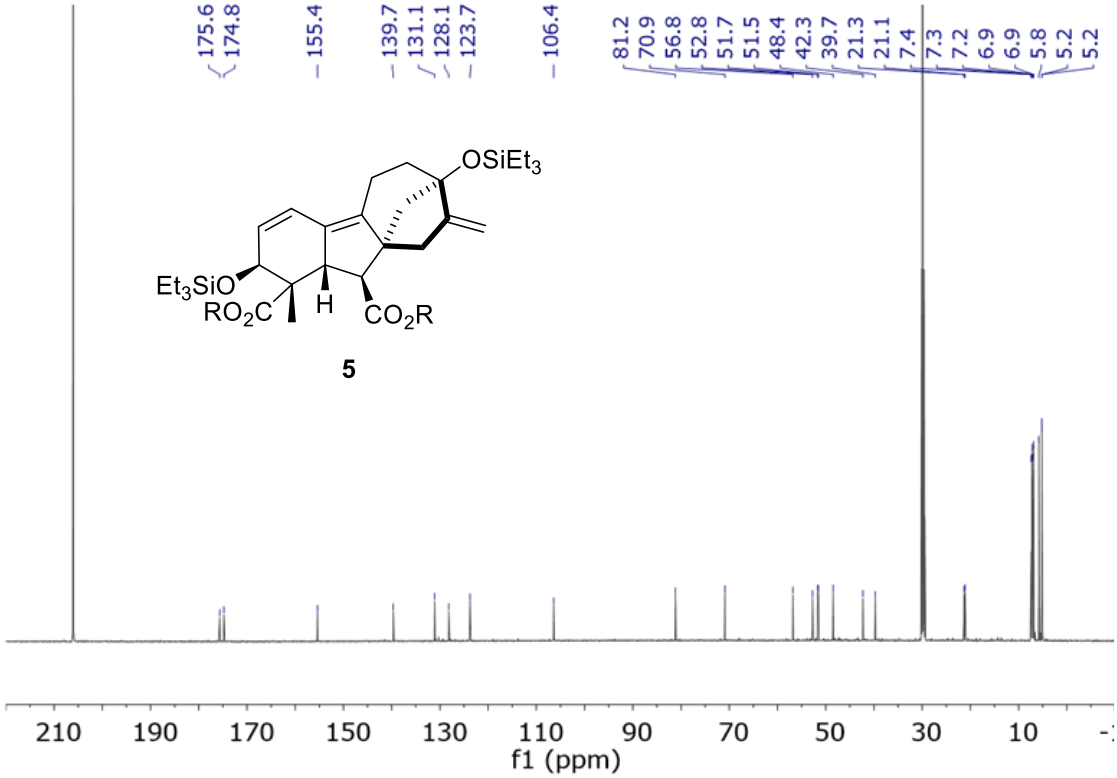

Figure 3.15. ^{13}C NMR spectrum of compound 5 when R = $SiEt_3$

5-carboxylic acid (R=H)

^{1}H NMR (600 MHz, Acetone-d_6) δ 6.33 (d, *J* = 9.7 Hz, 1H), 5.88 (dd, *J* = 9.7, 5.4 Hz, 1H), 5.13 (s, 1H), 4.93 (s, 1H), 4.45 (d, *J* = 5.5 Hz, 1H), 3.73 (d, *J* = 8.5 Hz, 1H), 3.65 (dd, *J* = 8.5, 4.4 Hz, 1H), 2.60 (dd, *J* = 16.3, 6.2 Hz, 1H), 2.51 (dt, *J* = 16.4, 3.0 Hz, 1H), 2.30 (dd, *J* = 10.1, 2.7 Hz, 1H), 2.20 (dd, *J* = 16.4, 2.2 Hz, 1H), 2.13 – 1.96 (m, 2H), 1.82 (dd, *J* = 10.1, 2.4 Hz, 1H), 1.77 (dt, *J* = 11.9, 6.4 Hz, 1H), 1.72 – 1.67 (m, 1H), 1.26 (s, 3H), 1.01 – 0.93 (m, 18H), 0.69 – 0.58 (m, 12H).

^{13}C NMR (151 MHz, Acetone) δ 176.2, 175.8, 155.7, 139.6, 130.3, 128.3, 124.3, 106.1, 81.3, 70.8, 56.8, 52.8, 50.3, 49.7, 48.3, 42.3, 39.5, 21.3, 20.8, 7.4, 7.2, 7.1, 5.8.

HRMS (EI) calculated for $C_{31}H_{50}O_6Si_2Na$ $[M+Na]^+$: 597.3039; found 597.3061.

^{1}H NMR (600 MHz, Acetone-d_6)

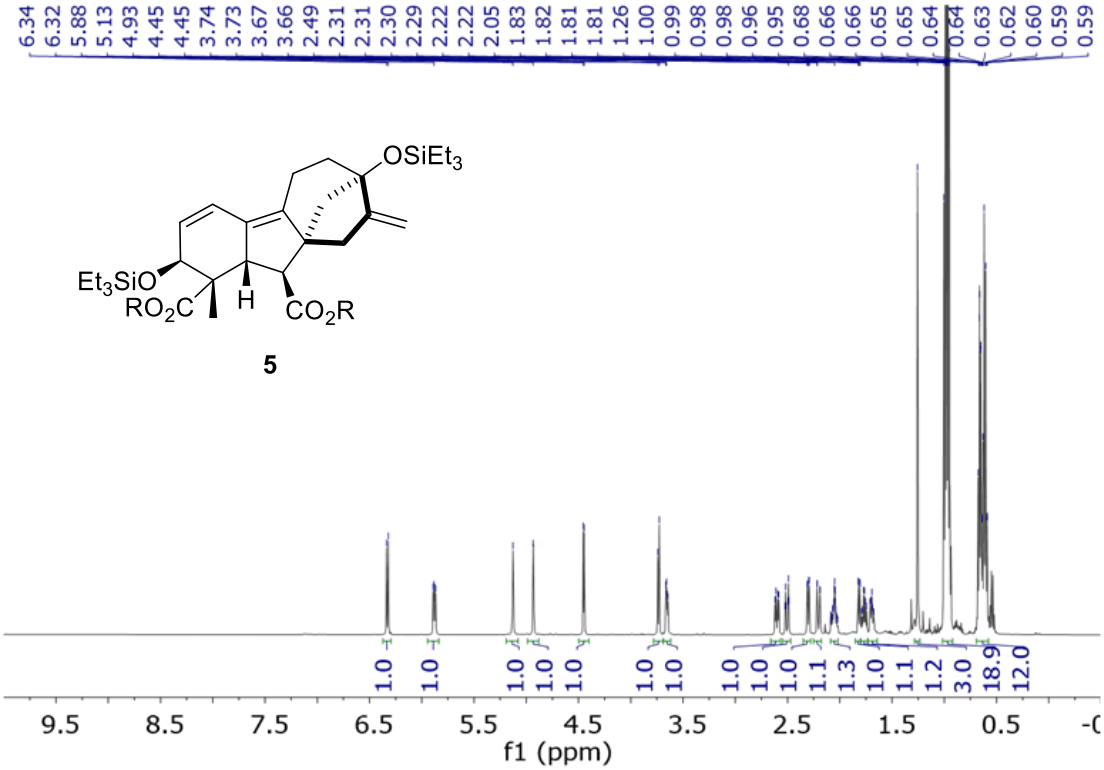

Figure 3.16. ^{1}H NMR spectrum of compound 5 when R = H

^{13}C NMR (150 MHz, Acetone-d_6)

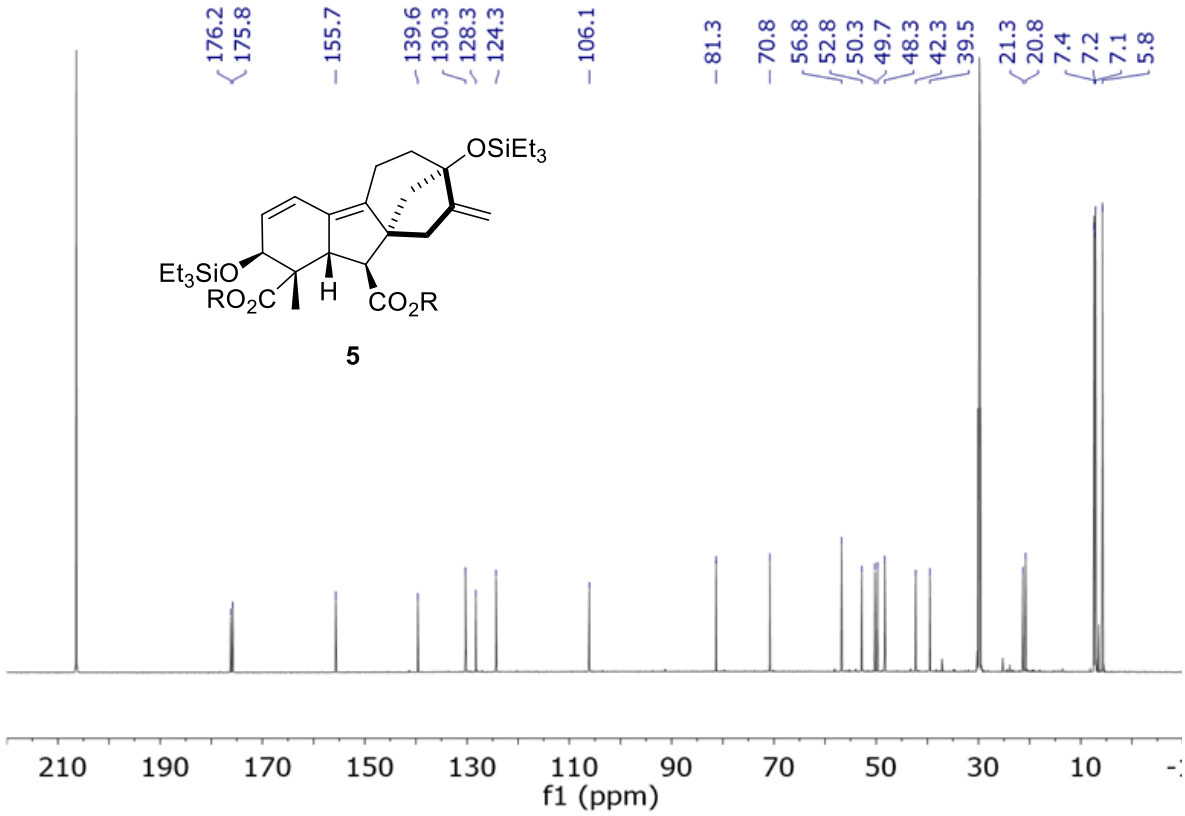

Figure 3.17. ^{13}C NMR spectrum of compound 5 when R = H

3.8.4. Preparation of products 2 and 3

In a N_2-filled glove box, BCF (4.93 mg, 0.010 mmol, 0.10 equiv.) was placed in a 1-dram vial and dissolved in 0.2 mL of CH_2Cl_2. To the catalyst solution, was added Me_2EtSiH (32 μL, 0.241 mmol, 2.50 equiv.) and mixed. In a separate vial, Me_2EtSi-Gibb (50 mg, 0.096 mmol, 1.00 equiv.) was diluted with 0.3 mL of CH_2Cl_2. The catalyst and borane mixture was then added to the substrate solution in one portion. The reaction mixture was transferred to NMR tube and sealed with a septum cap. After 24 h, the mixture was transferred to a vial and rinsed three times with 0.5 mL of MeOH. After concentrating the resulting solution in vacuo, the crude residue was purified by silica gel chromatography (30:1 CH_2Cl_2/MeOH to 20:1 to 10:1 to 5:1) to yield **2** (83%) and **3** (16%). NMR spectra for compounds **2** and **3** from Scheme 3.2 can be found below.

Compound **2**: ^{1}H NMR (600 MHz, Acetone-d_6) δ 5.19 (br s, 1H), 5.06 (br s, 1H), 4.90 (br s, 1H), 4.04 (dd, J = 4.3, 2.0 Hz, 1H), 3.17 (d, J = 5.5 Hz, 1H), 3.16 – 3.12 (m, 1H), 2.77 (dt, J = 18.2, 3.5 Hz, 1H), 2.68 (dt, J = 16.3, 3.0 Hz, 1H), 2.49 (br s, 1H), 2.28 – 2.23 (m, 1H), 2.13 (m, 1H), 1.96 – 1.88 (m, 1H), 1.74 (dd, J = 11.0, 2.9 Hz, 1H), 1.69 – 1.58 (m, 2H), 1.49 – 1.39 (m, 2H), 1.32 (s, 3H).

^{13}C NMR (151 MHz, Acetone-d_6) δ 177.5, 176.2, 156.6, 142.1, 111.0, 105.7, 79.3, 70.5, 50.5, 50.0, 49.8, 49.7, 48.8, 47.2, 46.6, 40.1, 38.8, 33.4, 22.2, 19.4.

HRMS (EI) calculated for $C_{19}H_{24}O_6Na$ $[M+Na]^+$:371.1465; found 371.1459.

^{1}H NMR (600 MHz, Acetone-d_6)

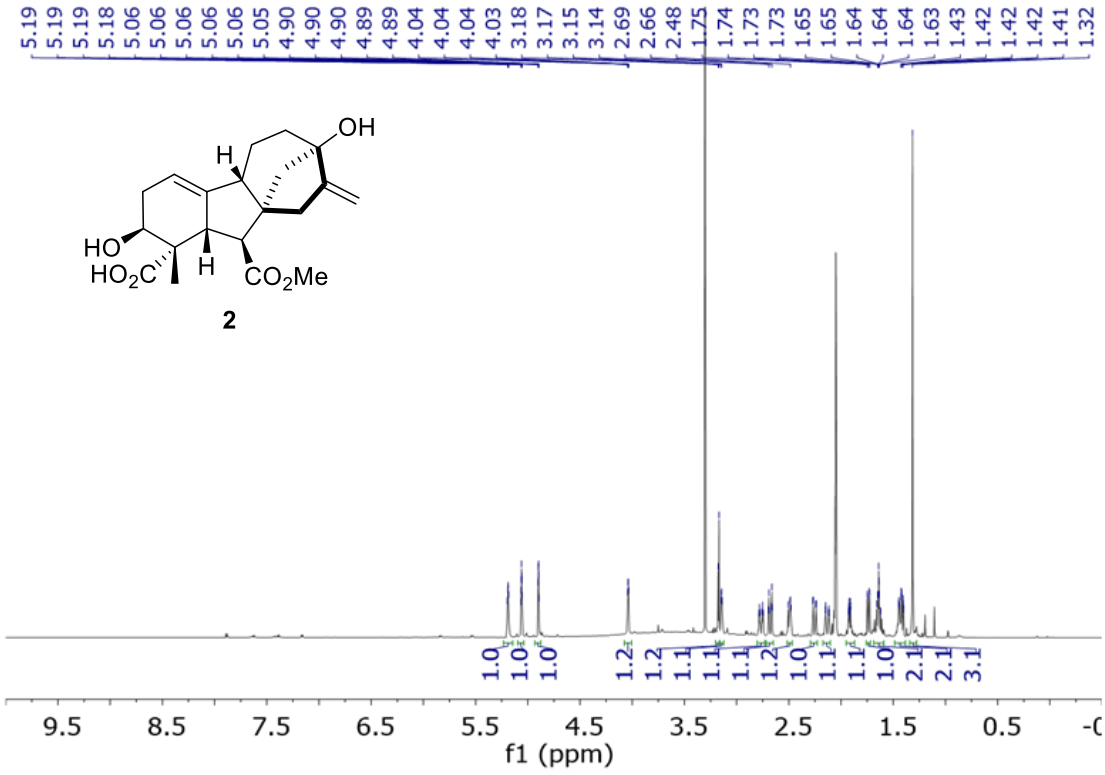

Figure 3.18. ^{1}H NMR spectrum of compound 2

^{13}C NMR (150 MHz, Acetone-d_6)

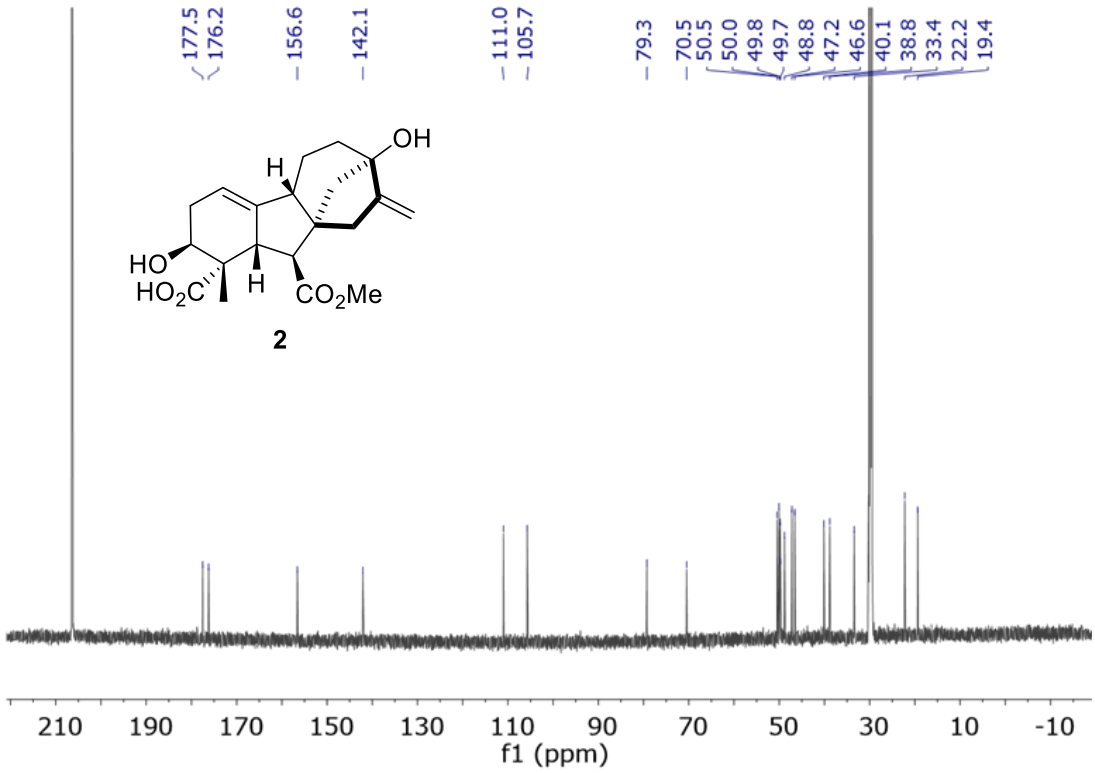

Figure 3.19. ^{13}C NMR spectrum of compound 2

Compound **3**: ^{1}H NMR (600 MHz, Methanol-d_4) δ 5.85 (d, J = 9.8 Hz, 1H), 5.51 (d, J = 9.8 Hz, 1H), 5.10 (t, J = 2.5 Hz, 1H), 3.15 – 3.01 (m, 1H), 2.98 – 2.81 (m, 2H), 2.75 – 2.64 (m, 1H), 2.60 – 2.42 (m, 2H), 2.31 – 2.12 (m, 1H), 2.06 (dd, J = 10.1, 2.6 Hz, 1H), 2.03 – 1.89 (m, 1H), 1.73 (td, J = 11.9, 6.4 Hz, 1H), 1.64 (ddd, J = 10.7, 7.0, 2.6 Hz, 1H), 1.59 (dd, J = 10.1, 2.5 Hz, 1H), 1.21 (s, 3H).

^{13}C NMR (151 MHz, Methanol-d_4) δ 178.2, 177.8, 156.0, 136.5, 132.4, 128.9, 127.8, 105.8, 80.0, 57.1, 55.9, 53.9, 52.4, 40.6, 40.5, 26.1, 24.5, 21.6.

HRMS (EI) calculated for $C_{19}H_{22}O_5Na$ $[M+Na]^+$: 353.1360; found: 353.1370.

^{1}H NMR (600 MHz, CD_3OD)

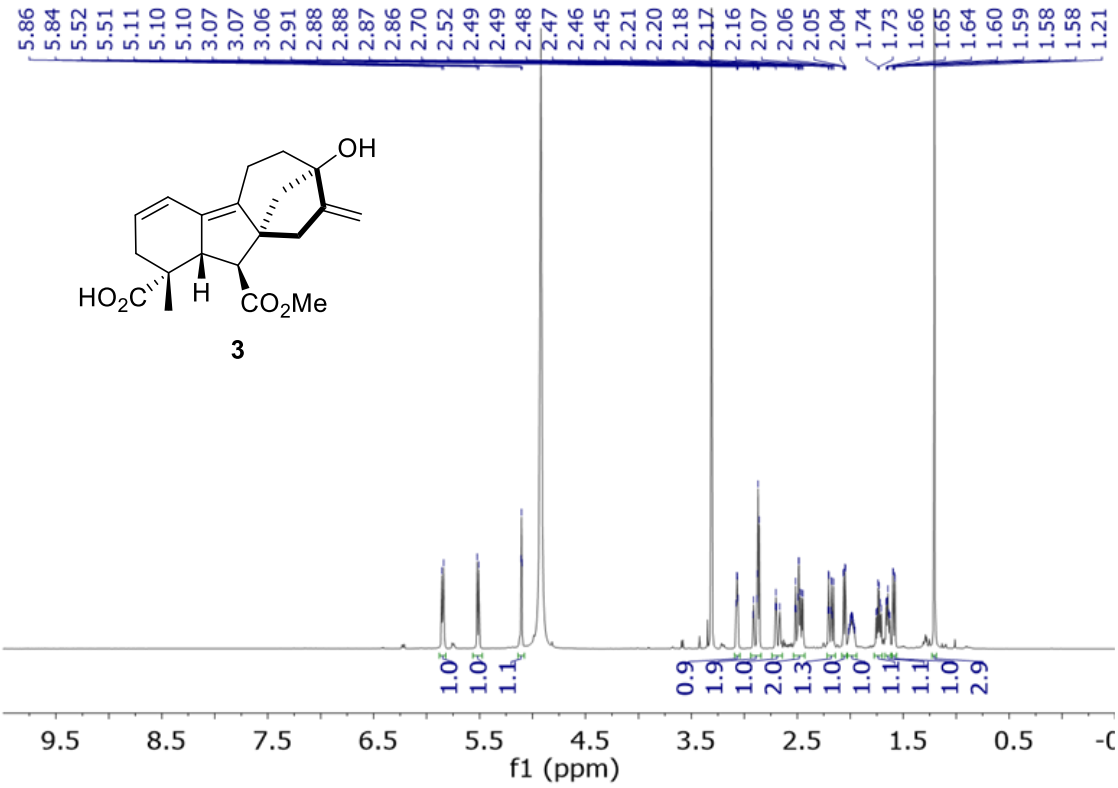

Figure 3.20. ^{1}H NMR spectrum of compound 3

^{13}C NMR (150 MHz, CD_3OD)

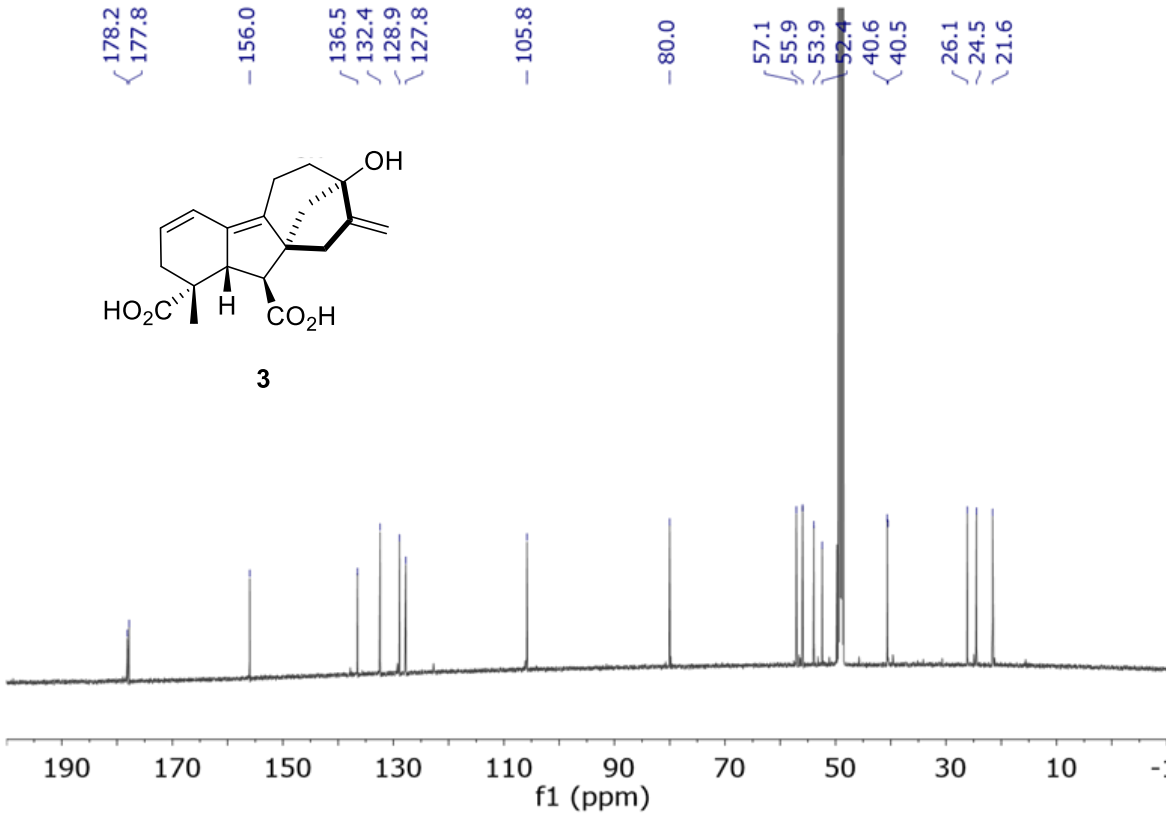

Figure 3.21. ^{13}C NMR spectrum of compound 3

3.8.5. BCF-catalyzed gibberelic acid reduction with HBCat

In a N_2-filled glove box, BCF (3.58 mg, 0.007 mmol, 0.10 equiv.) was placed in a 1-dram vial and dissolved in 0.2 mL of CH_2Cl_2. To the catalyst solution, was added HBCat (37 μL, 0.350 mmol, 5.00 equiv.) and mixed. In a separate vial, Me_2EtSi-Gibb (36 mg, 0.070 mmol, 1.00 equiv.) was diluted with 0.3 mL of CH_2Cl_2. The catalyst and borane mixture was then added to the substrate solution in one portion. The reaction mixture was transferred to NMR tube and sealed with a septum cap. After 24 h, the mixture was transferred to a vial and rinsed three times with 0.5 mL of MeOH. After concentrating the resulting solution in vacuo, the crude residue was purified

by silica gel chromatography (100% CH_2Cl_2 to 30:1 CH_2Cl_2/MeOH to 20:1 to 10:1 to 5:1) to yield **2** as a clear film in 90% yield.

3.8.6. Azidation of gibberellic acid to generate products 6 and 7

TMS-Me-Gibb starting material in the following experiments was synthesized in accordance to a previously reported procedure.[72] 10 mol% of BCF•H_2O (12.8 mg, 0.025 mmol, 0.10 equiv.) was placed in a scintillation vial and dissolved in 0.5 mL of $MeNO_2$ at room temperature. To the catalyst solution, was added TMS–N_3 (188 μL, 1.5 mmol, 6.00 equiv.) and mixed. In a separate vial, TMS-Me-Gibb (126 mg, 0.25 mmol, 1.00 equiv.) was diluted with 0.3 mL of $MeNO_2$. The catalyst and azide mixture was then added to the substrate solution in one portion. The reaction mixture was stirred for 24 h. After 24 h, the mixture was transferred to a separate vial and concentrated in vacuo, and the crude residue was purified by silica gel chromatography (9:1 Hex/EtOAc to 6:1 to 3:1 to 1:1) to yield **6** (47%), **7** (35%), and known compound **4** (15%). NMR spectra for compounds **6** and **7** can be found below. For ease of spectroscopic characterization, isolated version of product **6** bears three -TMS protecting groups and its spectra can be found below. Free alcohol version of compound **6** can also be generated if MeOH is added to the reaction mixture for deprotection of alcohols prior to concentrating the mixture in vacuo.

Compound **6**: ^{1}H NMR (500 MHz, $CDCl_3$) δ 5.30 (s, 1H), 5.08 (s, 2H), 4.93 (s, 1H), 4.00 (s, 1H), 3.87 (s, 1H), 3.70 (s, 3H), 3.02 (s, 2H), 2.61 – 2.53 (m, 2H), 2.29 (dd, *J* = 11.5, 2.5 Hz, 1H), 2.21 – 2.13 (m, 1H), 1.92 (dd, *J* = 14.0, 5.5 Hz, 1H), 1.74 (dd, *J* = 11.0, 5.8 Hz, 1H), 1.68 – 1.62 (m, 2H), 1.53 (d, *J* = 8.7 Hz, 1H), 1.17 (s, 3H), 0.27 (s, 9H), 0.14 (s, 9H), 0.11 (s, 9H).

^{13}C NMR (151 MHz, $CDCl_3$) δ 176.6, 172.5, 154.7, 149.9, 106.6, 106.3, 81.0, 74.9, 60.2, 60.2, 51.6, 50.9, 49.7, 49.4, 47.4, 46.5, 46.2, 39.4, 39.1, 22.6, 18.8, 2.2, 0.2, 0.2, -0.4, -0.4.

HRSM (EI) calculated for $C_{29}H_{49}N_3O_6Si_3Na$ $[M+Na]^+$: 642.2827; found 642.2805.

^{1}H NMR (400 MHz, $CDCl_3$)

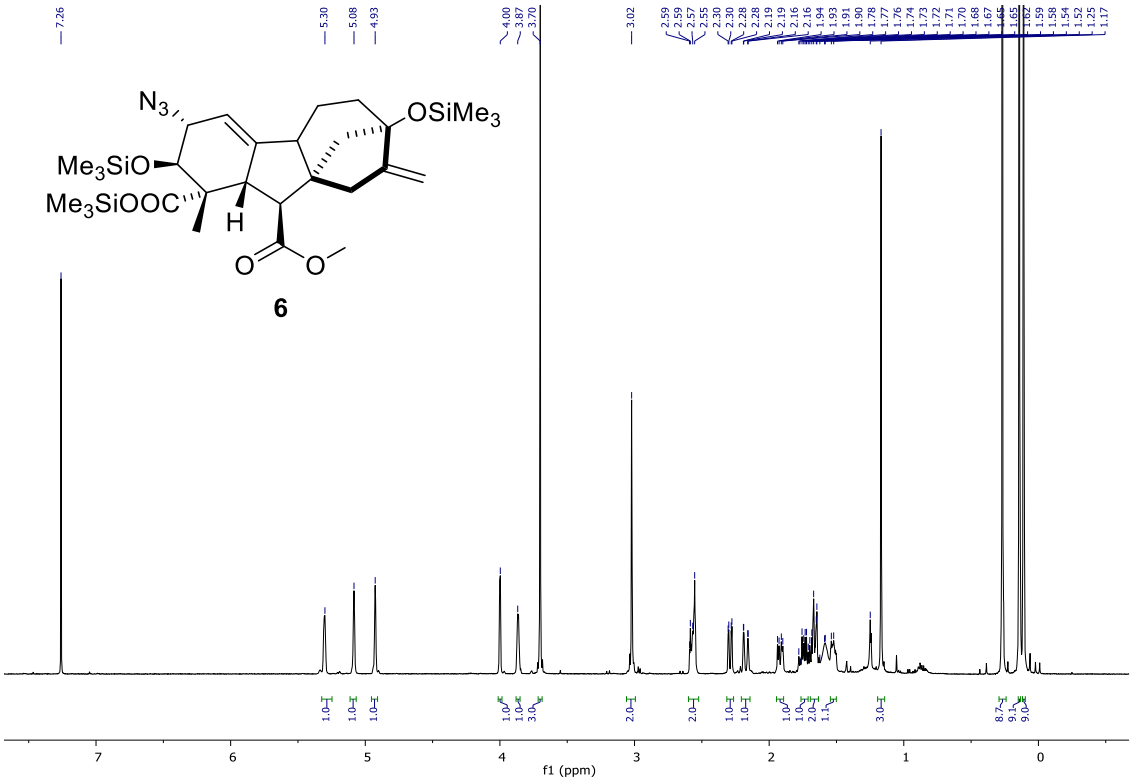

Figure 3.22. ^{1}H NMR spectrum of protected compound 6

^{13}C NMR (150 MHz, $CDCl_3$)

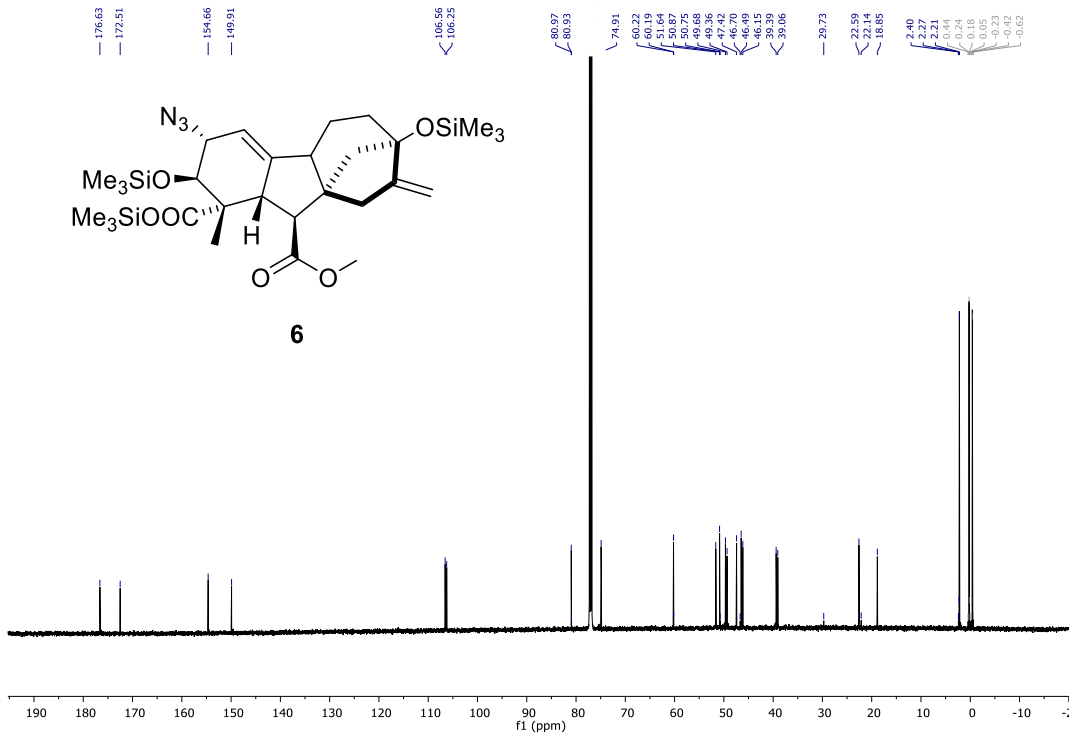

Figure 3.23. ^{13}C NMR spectrum of protected compound 6

For ease of spectroscopic characterization, isolated version of product **7** bears one -TMS protecting group and its spectra can be found below. Free alcohol version of compound **7** can also be generated if MeOH is added to the reaction mixture for deprotection of the alcohol prior to concentrating the mixture in vacuo.

Compound **7**: ^{1}H NMR (400 MHz, $CDCl_3$) δ 6.51 (d, J = 9.6 Hz, 1H), 5.86 (dd, J = 9.5, 5.7 Hz, 1H), 5.12 (s, 1H), 4.93 (s, 1H), 4.23 (d, J = 5.7 Hz, 1H), 3.71 (s, 3H), 3.64 (d, J = 8.4 Hz, 1H), 3.46 (dd, J = 8.2, 4.1 Hz, 1H), 2.55 (dd, J = 16.3, 5.7 Hz, 1H), 2.33 – 2.18 (m, 3H), 2.07 (dt, J = 12.2, 4.4 Hz, 1H), 1.83 – 1.65 (m, 3H), 1.27 (s, 3H), 0.93 – 0.80 (m, 1H), 0.13 (s, 9H).

^{13}C NMR (101 MHz, $CDCl_3$) δ 179.5, 174.5, 153.8, 142.1, 126.5, 125.5, 123.4, 106.7, 80.9, 61.8, 60.6, 56.6, 51.9, 51.8, 49.1, 49.1, 48.3, 41.1, 38.6, 21.1, 20.7, 2.4.

HRSM (EI) calculated for $C_{23}H_{31}N_3O_5SNa$ $[M+H]^+$: 458.2111; found 458.2145.

^{1}H NMR (400 MHz, $CDCl_3$)

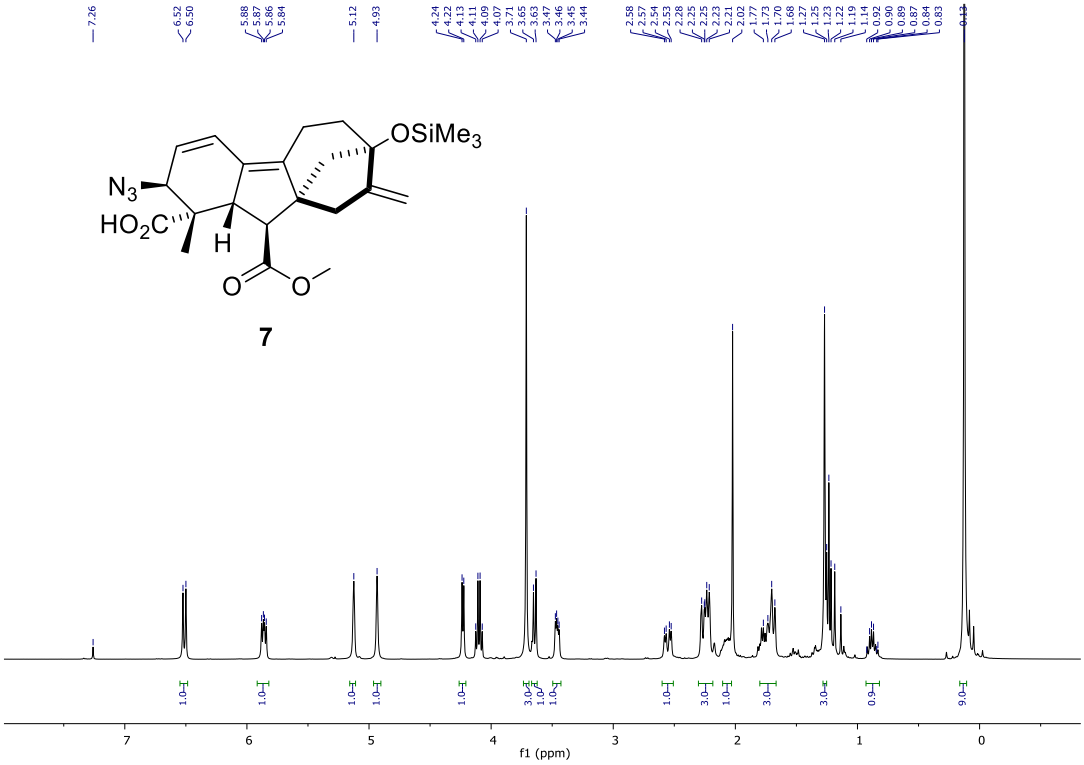

Figure 3.24. ^{1}H NMR spectrum of protected compound 7

^{13}C NMR (101 MHz, $CDCl_3$)

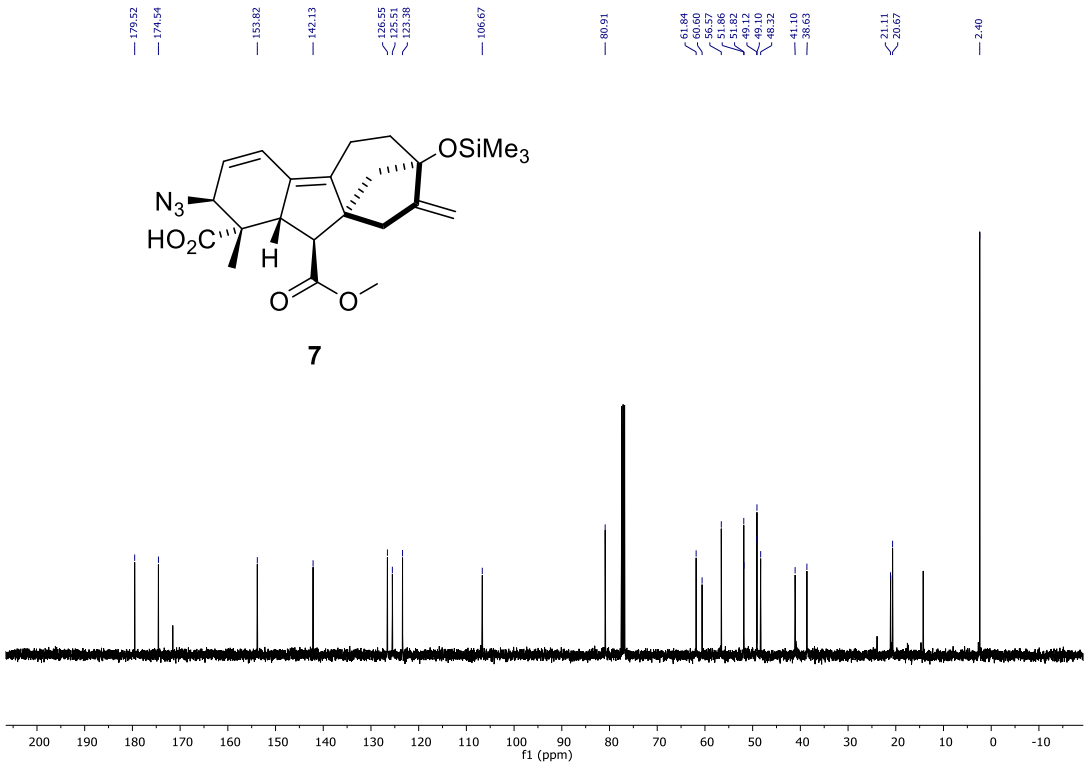

Figure 3.25. ^{13}C NMR spectrum of protected compound 7

3.8.7. Azidation of gibberellic acid to generate thiol product 8

10 mol% of BCF•H_2O (12.8 mg, 0.025 mmol, 0.10 equiv.) was placed in a scintillation vial and dissolved in 0.5 mL of CH_2Cl_2 at room temperature. To the catalyst solution, was added PhSH (77 µL, 0.75 mmol, 3.00 equiv.) and mixed. In a separate vial, TMS-Me-Gibb (126 mg, 0.25 mmol, 1.00 equiv.) was diluted with 0.3 mL of CH_2Cl_2. The catalyst and thiophenol mixture was then added to the substrate solution in one portion. The reaction mixture was stirred for 24 h. After 24 h, the mixture was transferred to a separate vial and concentrated in vacuo, and the crude residue was purified by silica gel chromatography (9:1 Hex/EtOAc to 6:1 to 3:1 to 1:1) to yield **8** (41%) and unknown byproducts. NMR spectra for compound **8** can be found below.

Compound **8**: ^{1}H NMR (400 MHz, $CDCl_3$): δ 7.47 (d, *J* = 7.4 Hz, 2H), 7.30 (dt, *J* = 13.7, 7.1 Hz, 3H), 5.42 – 5.35 (m, 1H), 5.28 (s, 1H), 5.09 (s, 1H), 4.93 (s, 1H), 3.99 (d, *J* = 4.4 Hz, 1H), 3.81 (d, *J* = 5.0 Hz, 1H), 3.62 (s, 3H), 3.00 (d, *J* = 7.2 Hz, 1H), 2.77 (d, *J* = 7.3 Hz, 1H), 2.48 (t, *J* = 12.3 Hz, 2H), 2.17 (d, *J* = 16.3 Hz, 1H), 1.90 – 1.82 (m, 1H), 1.78 (d, *J* = 11.4 Hz, 1H), 1.71 (d, *J* = 12.7 Hz, 2H), 1.53 (s, 1H), 1.46 (d, *J* = 11.3 Hz, 1H), 1.31 (s, 3H), 1.22 (dd, *J* = 13.4, 6.4 Hz, 1H).

^{13}C NMR (101 MHz, $CDCl_3$): δ 179.8, 175.9, 154.1, 145.0, 134.3, 132.8, 129.2, 127.8, 111.6, 106.6, 79.1, 77.4, 77.1, 76.7, 73.1, 53.5, 51.8, 50.6, 50.3, 50.0, 48.7, 47.3, 46.8, 46.5, 39.5, 37.8, 21.2, 18.8.

^{1}H NMR (400 MHz, $CDCl_3$)

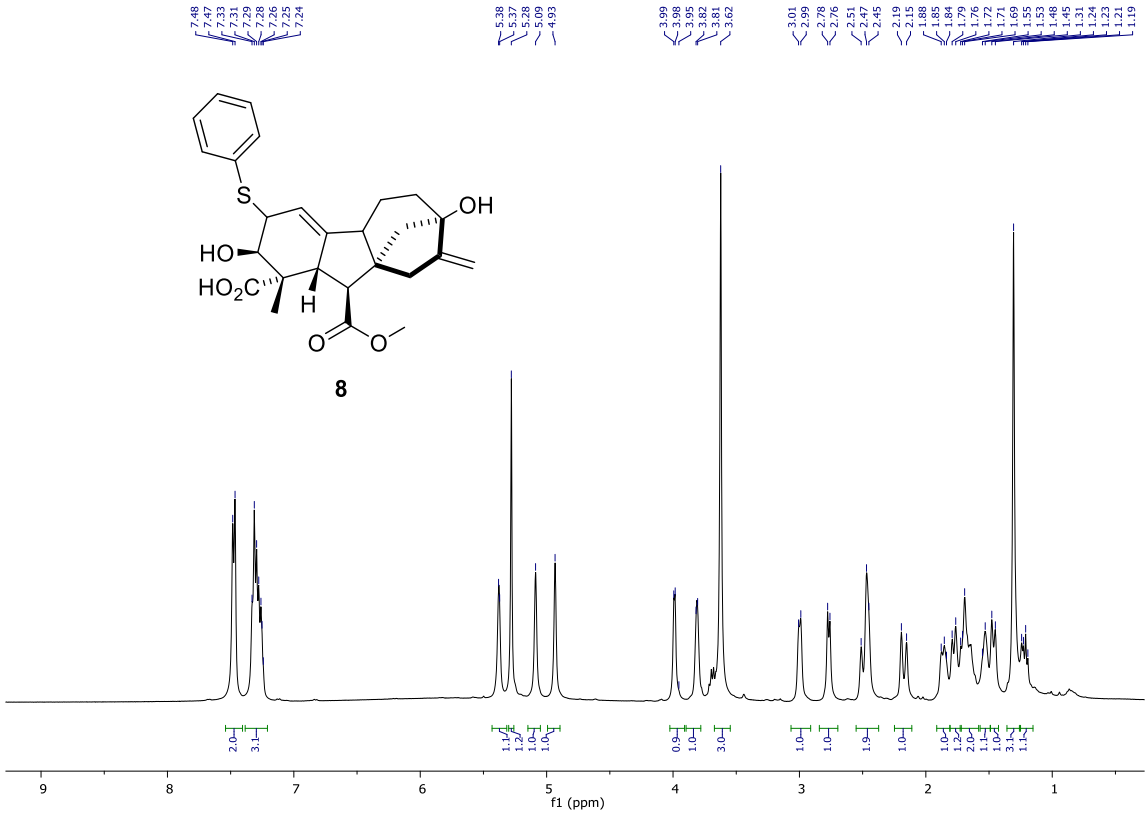

Figure 3.26. ^{1}H NMR spectrum of compound 8

^{13}C NMR (101 MHz, $CDCl_3$)

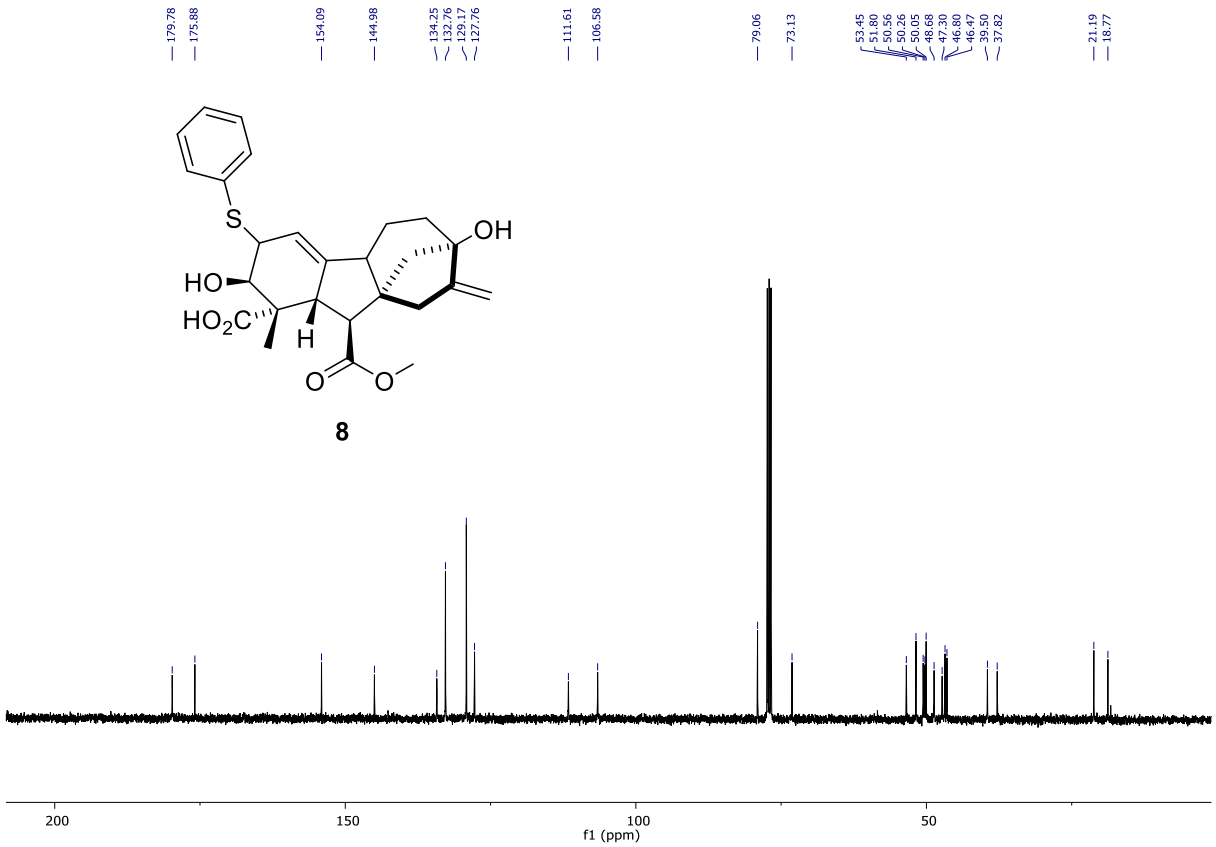

Figure 3.27. ^{13}C NMR spectrum of compound 8

3.8.8. Reaction with 1-methylindole to generate product 9

10 mol% of BCF•H_2O (12.8 mg, 0.025 mmol, 0.10 equiv.) was placed in a scintillation vial and dissolved in 0.5 mL of CH_2Cl_2 at room temperature. To the catalyst solution, was added 1-methylindole (94 µL, 0.75 mmol, 3.50 equiv.) and mixed. In a separate vial, TMS-Me-Gibb (126 mg, 0.25 mmol, 1.00 equiv.) was diluted with 0.3 mL of CH_2Cl_2. The catalyst and 1-methylindole mixture was then added to the substrate solution in one portion. The reaction mixture was stirred for 20 h. After 20 h, the mixture was transferred to a separate vial and concentrated in vacuo, and the crude residue was purified by silica gel chromatography (3:1 Hex/EtOAc to 2:1 to 1:1) to yield **9** (31%) and known compound **4** (49%). For ease of spectroscopic characterization, isolated version of product **9** bears one -TMS protecting group and its spectra can be found below. Free

alcohol version of compound **9** can also be generated if MeOH is added to the reaction mixture for deprotection of the alcohol prior to concentrating the mixture in vacuo.

Compound **9**: ^{1}H NMR (600 MHz, CD_2Cl_2) δ 7.67 (d, *J* = 7.9 Hz, 1H), 7.30 (d, *J* = 8.2 Hz, 1H), 7.20 (t, *J* = 8.0 Hz, 1H), 7.08 (t, *J* = 7.9 Hz, 1H), 6.80 (s, 1H), 6.10 (dd, *J* = 9.7, 3.3 Hz, 1H), 5.59 (dd, *J* = 9.7, 2.4 Hz, 1H), 5.06 (t, *J* = 2.3 Hz, 1H), 4.88 (s, 1H), 4.50 (s, 1H), 3.73 (s, 3H), 3.72 (s, 3H), 3.48 (s, 1H), 3.05 (d, *J* = 6.0 Hz, 1H), 2.50 (d, *J* = 9.7 Hz, 1H), 2.33 (dt, *J* = 16.6, 2.8 Hz, 1H), 2.16 – 2.14 (m, 1H), 2.12 (s, 2H), 2.10 (d, *J* = 2.5 Hz, 1H), 1.67 – 1.64 (m, 2H), 1.63 – 1.59 (m, 1H), 1.31 (s, 3H), 1.21 (s, 1H).

^{13}C NMR (151 MHz, $CDCl_3$) δ 178.7, 175.0, 154.3, 137.7, 137.2, 133.7, 129.0, 129.0, 126.6, 126.1, 121.7, 119.1, 119.0, 116.0, 109.5, 106.1, 81.3, 55.9, 54.6, 52.8, 51.9, 50.9, 48.8, 41.2, 39.0, 32.9, 32.8, 29.8, 23.8, 21.6, 2.5.

HRSM (EI) calculated for $C_{29}H_{31}NO_5Na$ $[M+Na]^+$: 496.2100; found 496.2134.

^{1}H NMR (400 MHz, CD_2Cl_2)

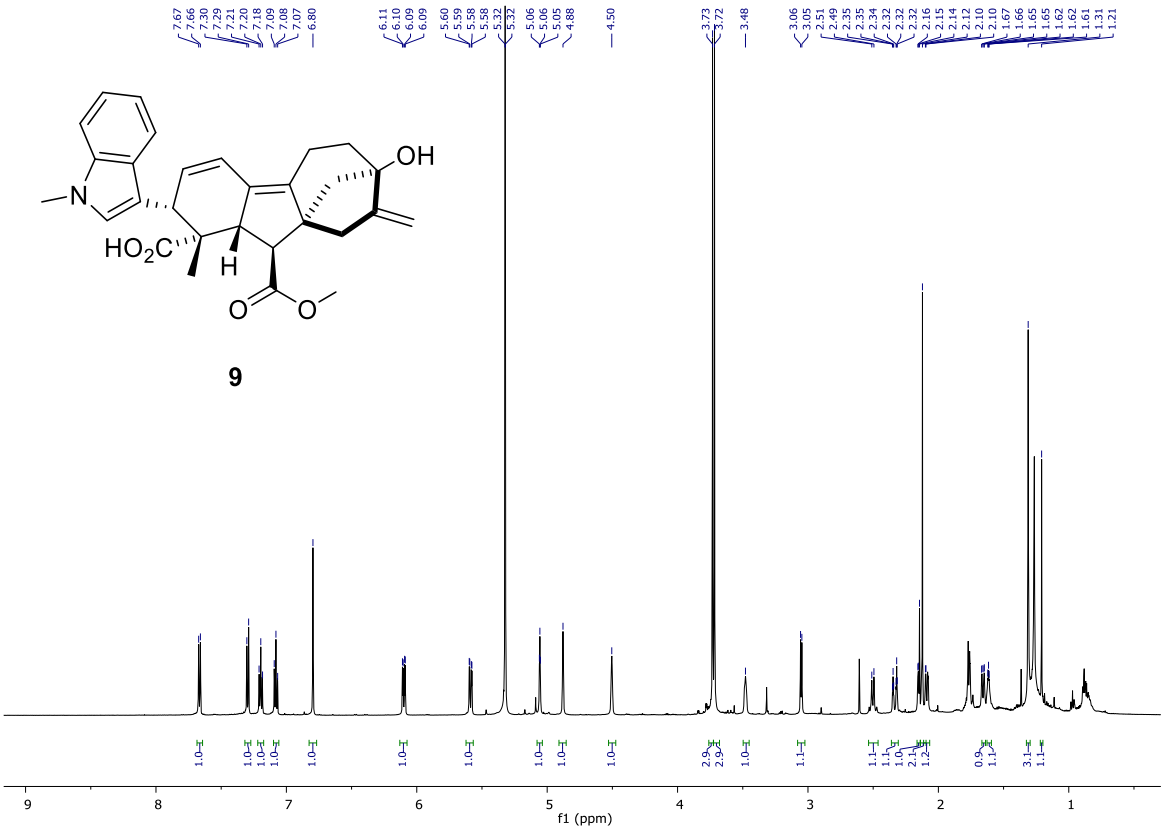

Figure 3.28. ^{1}H NMR spectrum of compound 9

^{13}C NMR (150 MHz, $CDCl_3$)

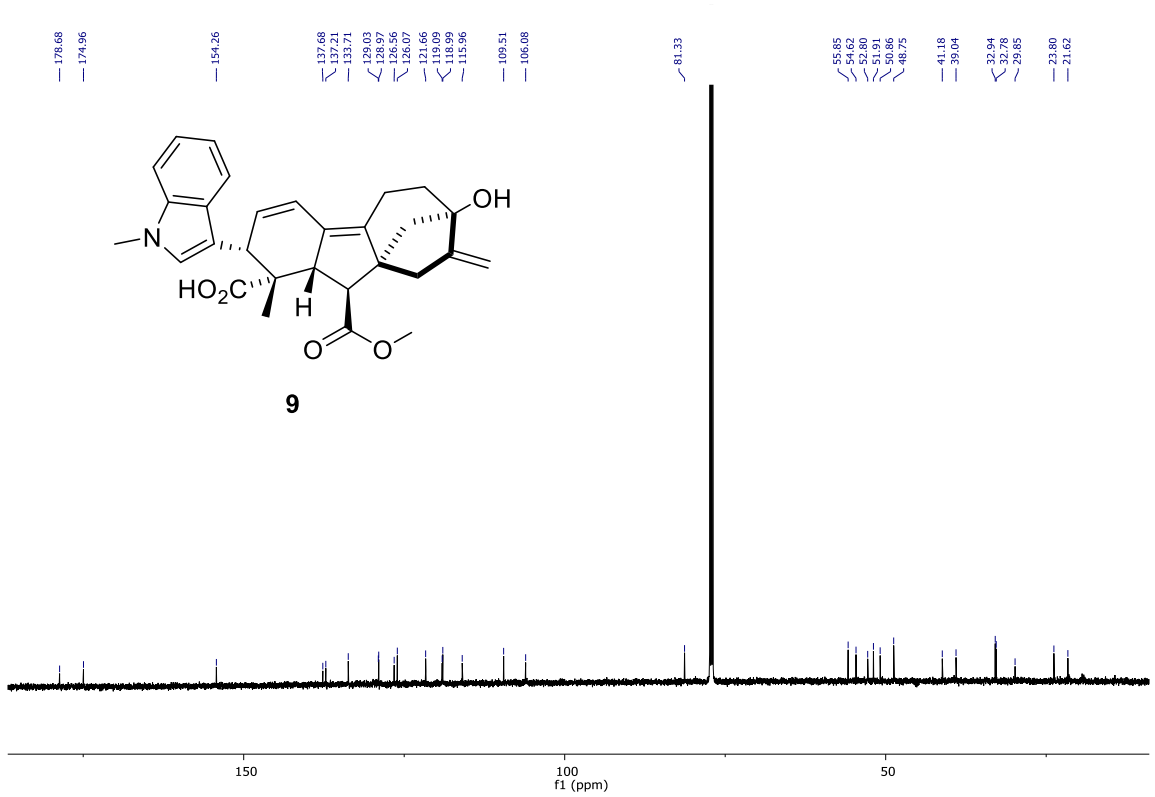

Figure 3.29. ^{13}C NMR spectrum of compound 9

3.8.9. Friedel-Crafts reaction in HFIP to generate product 16

TMS-Me-Gibb (126 mg, 0.25 mmol, 1.00 equiv.) and 1,4-dimethoxybenzene (99 µL, 0.75 mmol, 3.00 equiv.) were dissolved with 0.5 mL of HFIP in a scintillation vial. To this solution, 10 mol% of TfOH (2.2 µL, 0.025 mmol, 0.10 equiv.) was added slowly via microsyringe. The reaction mixture was stirred for 18 h at room temperature After 18 h, the reaction mixture was transferred to a separate vial and concentrated in vacuo, and the crude residue was purified by silica gel chromatography (99:1 CH_2Cl_2/MeOH to 95:5 to 9:1) to yield **16** (40%) several unknown decomposition byproducts. NMR spectra for compound **16** can be found below.

Compound **16**: ^{1}H NMR (400 MHz, $CDCl_3$) δ 6.79 (d, J = 9.5 Hz, 1H), 6.72 (s, 2H), 5.89 (d, J = 12.5 Hz, 1H), 5.55 (d, J = 12.1 Hz, 1H), 4.52 (s, 1H), 3.80 (s, 3H), 3.77 (s, 3H), 3.74 (s, 3H), 3.52 (d, J = 4.9 Hz, 1H), 3.02 (d, J = 7.3 Hz, 1H), 2.48 (d, J = 18.3 Hz, 1H), 2.31 (s, 1H),

2.27 (s, 1H), 1.97 – 1.82 (m, 1H), 1.62 (d, J = 11.8 Hz, 2H), 1.50 – 1.43 (m, 1H), 1.30 (s, 3H), 1.14 (s, 1H), 0.97 (s, 3H), 0.92 – 0.86 (m, 1H).

^{13}C NMR (101 MHz, $CDCl_3$) δ 220.8, 179.6, 174.0, 153.8, 150.7, 136.9, 133.1, 132.5, 130.1, 129.5, 114.1, 112.0, 111.6, 56.0, 55.8, 54.2, 53.9, 52.0, 50.7, 50.6, 50.3, 48.4, 46.8, 36.7, 35.3, 23.6, 21.2, 21.1, 20.3.

HRMS (EI) calculated for $C_{28}H_{32}O_7$ $[M+H]^+$: 481.2226; found 481.2210.

^{1}H NMR (400 MHz, $CDCl_3$)

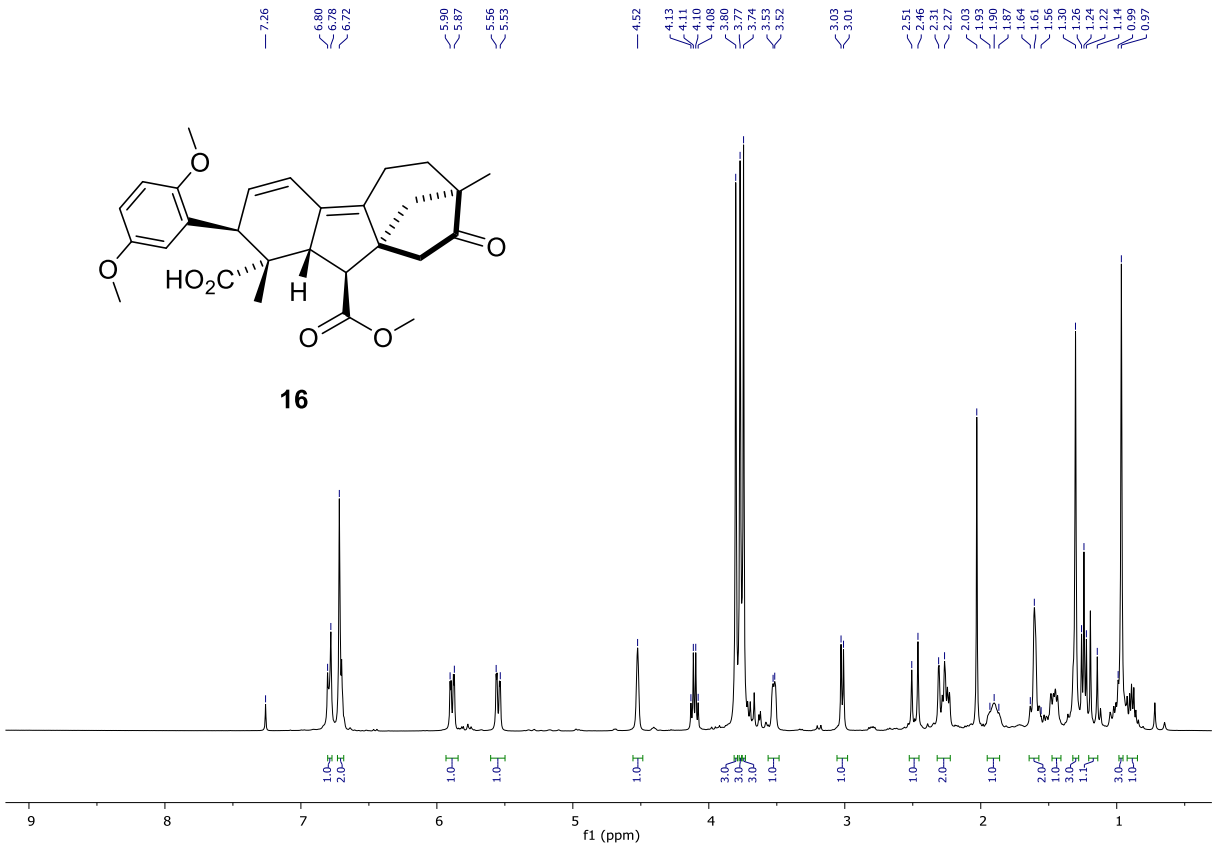

Figure 3.30. ^{1}H NMR spectrum of compound 16

^{13}C NMR (150 MHz, $CDCl_3$)*

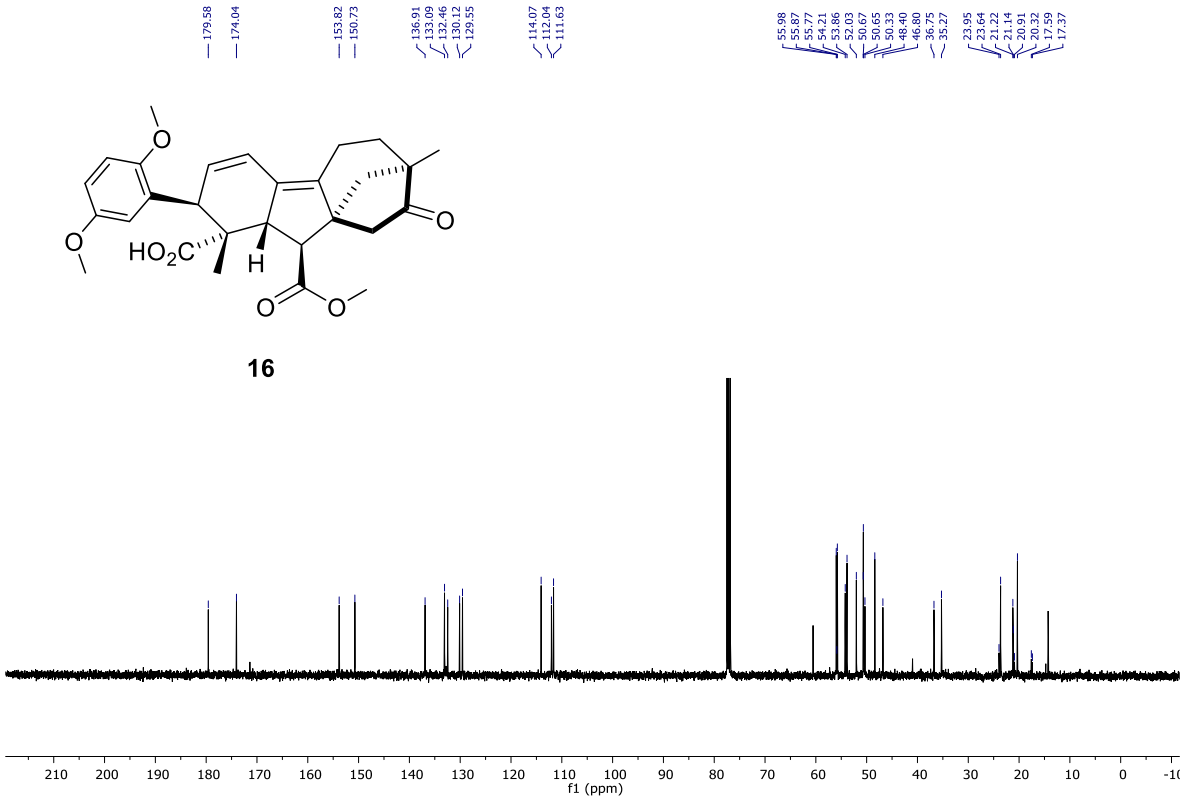

Figure 3.31. ^{13}C NMR spectrum of compound 16

***Additional peak at 220.8 ppm corresponding to the ketone falls outside the collected spectral range but was observed when the range is expanded beyond the standard experimental parameters.**

3.8.10. General experimental procedures for azidation of baccatin

In a N_2-filled glove box, BCF (12.8 mg, 0.025 mmol, 0.10 equiv.) was placed in a 1-dram vial and dissolved in 0.2 mL of CH_2Cl_2. To the catalyst solution, was added TMS–N_3 (116 µL, 0.88 mmol, 3.50 equiv.) and mixed. In a separate vial, free baccatin (136 mg, 0.25 mmol, 1.00 equiv.) was diluted with 0.3 mL of CH_2Cl_2. The catalyst and azide mixture was then added to the substrate solution in one portion. The reaction mixture was transferred to a J-Young NMR tube and sealed with a septum cap. After 20 h, the mixture was transferred to a vial and concentrated in vacuo, and the crude residue was purified by silica gel chromatography (9:1 Hexane/EtOAc to 6:1 to 4:1 to

2:1) to yield **10** (22%) and known compound **11** (35%).[5] NMR spectra for compound **10** can be found below. Relevant 2D NMR experiments are also included.

Product **10:** ^{1}H NMR (600 MHz, $CDCl_3$) δ 8.00 (ddt, *J* = 7.8 Hz, 2H), 7.61 (t, *J* = 7.4 Hz, 1H), 7.49 (t, *J* = 7.5 Hz, 2H), 5.62 (d, *J* = 6.9 Hz, 1H), 5.20 (m, 1H), 5.10 (s, 1H), 5.02 (t, *J* = 8.3 Hz, 1H), 4.28 (d, *J* = 4.5 Hz, 1H), 3.96 (d, *J* = 4.6 Hz, 1H), 3.81 (d, *J* = 4.4 Hz, 1H), 3.23 (d, *J* = 6.9 Hz, 1H), 2.63 – 2.57 (m, 1H), 2.55 (s, 1H), 2.28 – 2.23 (m, 2H), 2.22 (s, 3H), 2.17 (s, 1H) 1.85 (s, 3H), 1.74 (dd, *J* = 15.6, 3.7 Hz, 1H), 1.29 (s, 3H), 1.27 (s, 3H), 1.24 (s, 3H), 0.17 (s, 9H).

^{13}C NMR (151 MHz, $CDCl_3$) δ 206.6, 170.7, 167.2, 146.4, 137.6, 134.0, 129.8, 129.0, 85.0, 81.3, 79.9, 77.1, 75.3, 68.7, 65.2, 46.2, 42.1, 41.2, 37.5, 37.4, 30.3, 27.0, 21.8, 21.7, 18.4, 17.4, 0.2.

HRSM (EI) calculated for $C_{32}H_{43}N_3O_9SiNa$ $[M+Na]^+$: 664.2666; found 664.26591.

^{1}H NMR (400 MHz, $CDCl_3$)

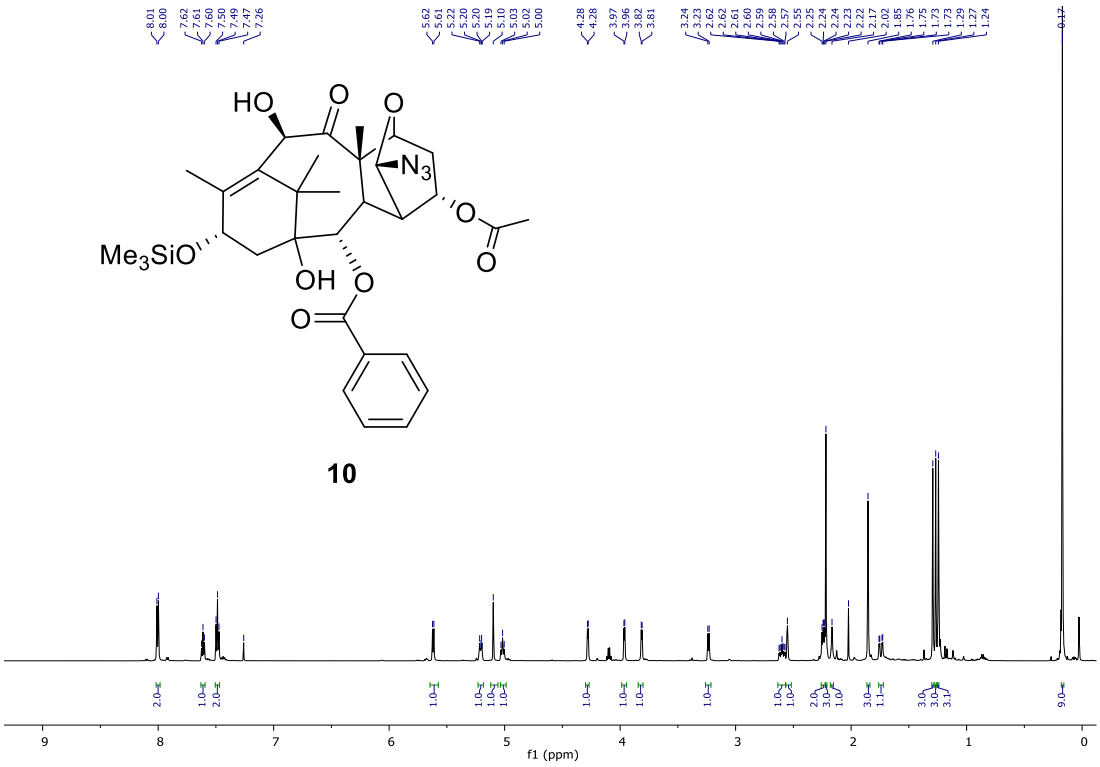

Figure 3.32. ^{1}H NMR spectrum of compound 10

^{13}C NMR (150 MHz, $CDCl_3$)

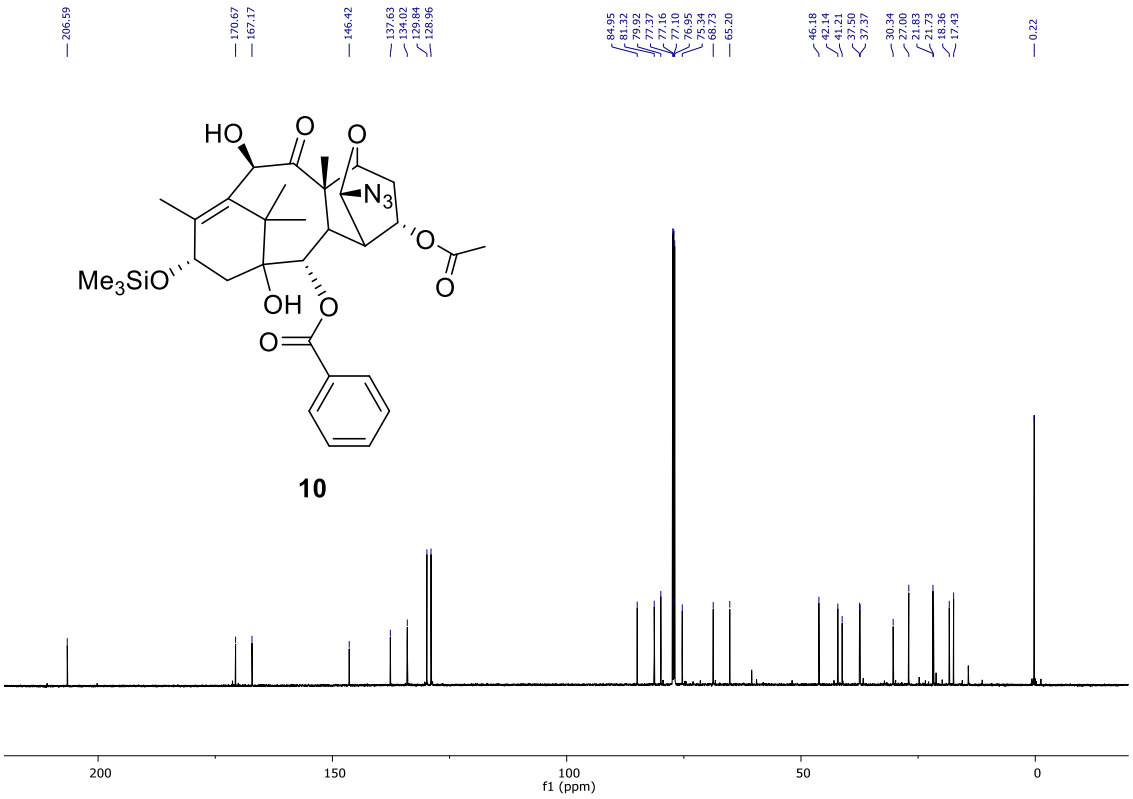

Figure 3.33. ^{13}C NMR spectrum of compound 10

Selected 2D correlations that facilitated spectroscopic assignment:

HSQC

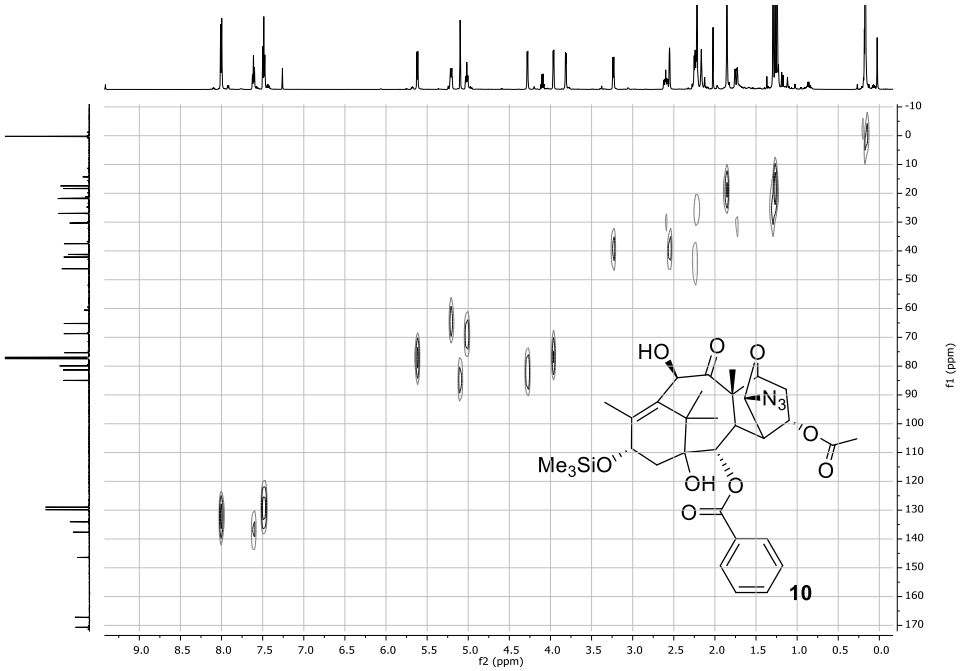

Figure 3.34. HSQC NMR spectrum of compound 10

COSY

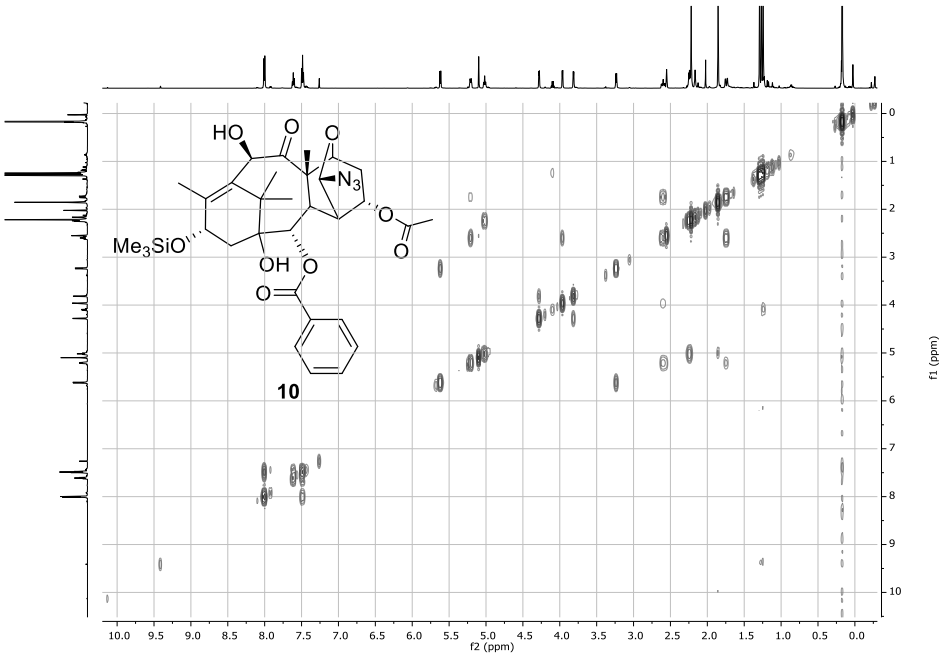

Figure 3.35. COSY NMR spectrum of compound 10

Crystallography data for compound **10** was also obtained and is described in detail below. The crystal mounted had approximate dimensions of 0.218 mm x 0.226 mm x 0.530 mm, and was a colorless block fragment. The crystal was mounted using a MiTeGen and the diffraction carried out on a Bruker Apex2 Diffractometer, with data collected at 150K.

Data Collection

Initial unit cell measurements and constants were determined from reflections harvested from a series of 3 sets of 12 images. The resulting matrices gave 219 reflections used for unit cell determination. The data collection was carried out with Cu Kα radiation. The frame time used during collection was 2θ dependent, and varied from 10 seconds at low angles to 30 seconds at high angles. Frames were collected in 0.50° intervals in a series of ω and φ scans. The average redundancy for the data collection was 5.52. Data collection was carried out to a resolution limit of 0.809 Å, with all data to that limit used in data reduction. Data integration was carried out using the SAINT program by Bruker. Absorption correction was completed using the Multi-Scan method. During data reduction, one scan was found to have an abnormally high error value, and so was omitted from the subsequent integration, presumably due to the crystal quality. Additional details can be found in crystallographic information tables.

Structure Solution and Refinement

The space group was determined to be $P2_1$ after data integration, with the determination being made based on unit cell parameters, systematic absences, and general intensity statistics. Each cell contains four formula units, consisting of the baccatin derivative ($C_{33}H_{45}O_9N_3Si$) of interest as well as four molecules of dichloromethane (CH_2Cl_2), which was used in the recrystallization of the substrate. The structure was solved using Superflip and refined through a full matrix, least squares approach using the Oxford University Crystals program.

Initial solution provided most of the non-hydrogen atoms, which were then refined through a least squares approach. The Fourier map was used to isolate remaining electron density which was modeled as several instances of disorder. One of the dichloromethane molecules was disordered. All disorder was modeled in multiple parts, with restraints then used to ensure the similarity of the parts. Vibrational restraints were then applied to ensure oblate ellipsoids. Vibrational restraints were also applied on several atoms in the phenyl rings of the palladium complex, again to ensure oblate ellipsoids. All non-hydrogen atoms were refined anisotropically. Hydrogen atoms were placed geometrically in appropriate positions and subsequently refined as riding atoms. The final refinement gave an R1 = 4.06% and a GooF of 1.007.

Structure Solution

Azidated baccatin structure.

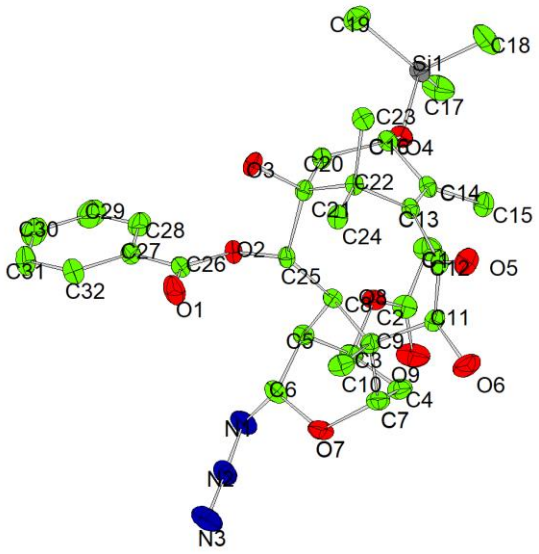

Figure 3.36. Graphics with numbering for compound 10

The graphic omits one of the molecules of interest in the formula unit for clarity, as well as the solvent dichloromethane molecules. Hydrogens also omitted for clarity.

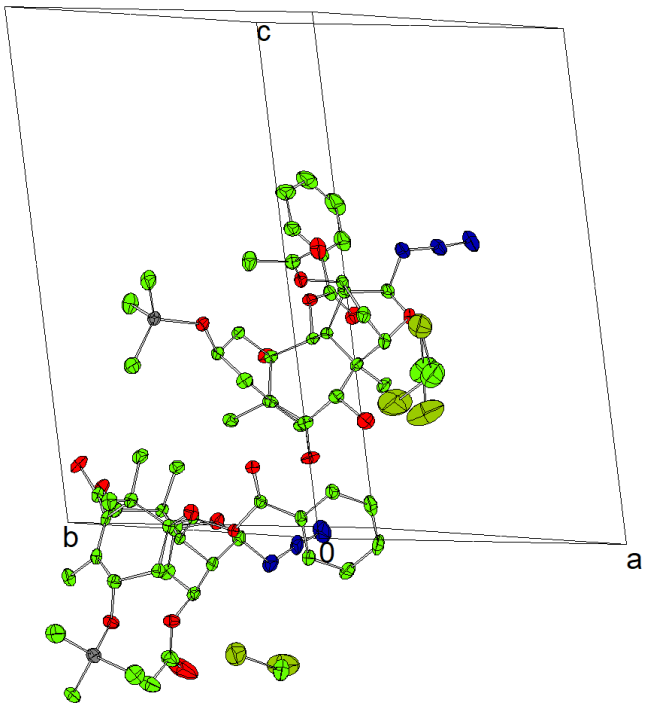

Figure 3.37. Structure solution of 10 with cell axes

Asymmetric unit with cell

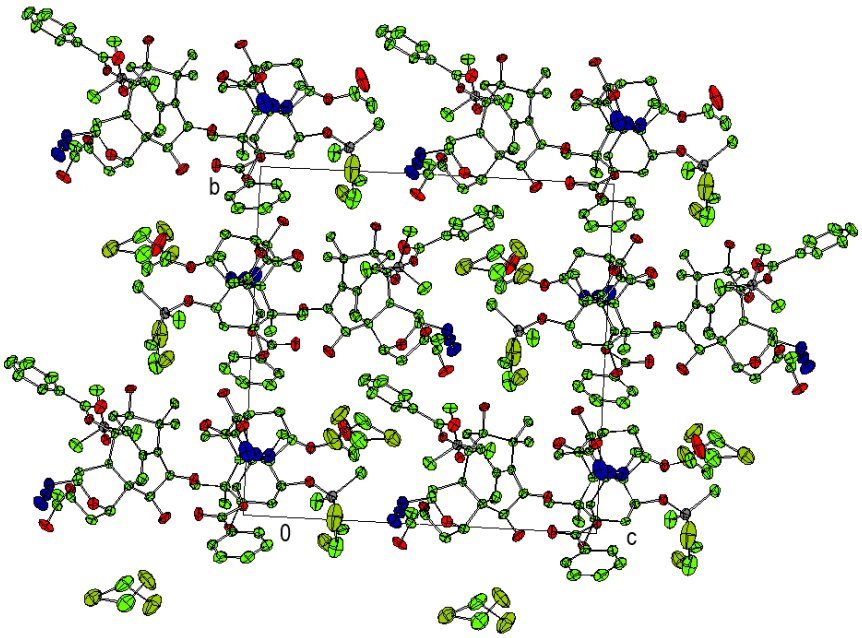

Figure 3.38. Compound 10 cell view along a-axis

Hydrogens omitted for clarity.

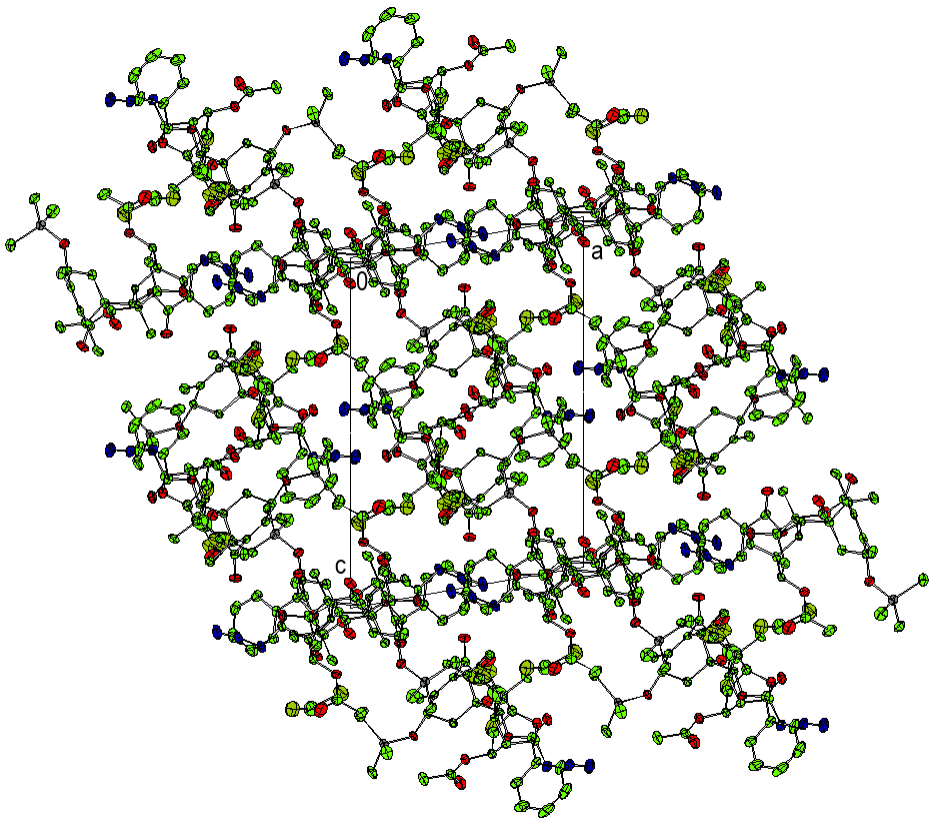

Figure 3.39. Compound 10 cell view along b-axis

Hydrogens omitted for clarity.

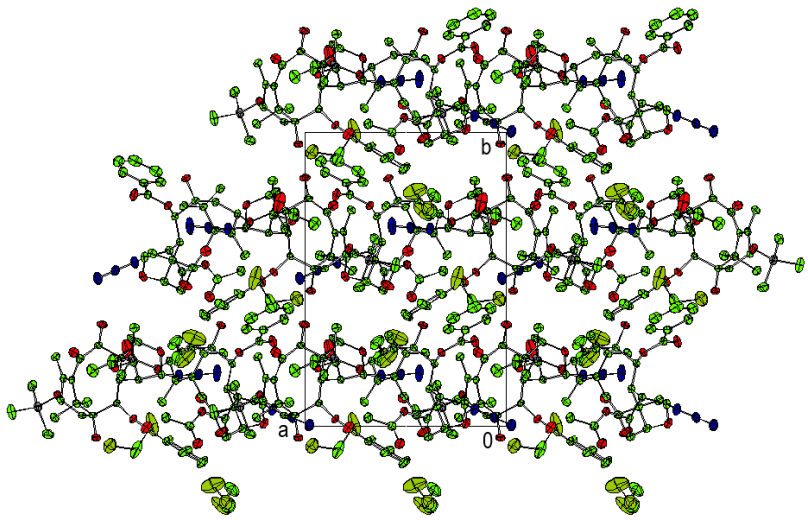

Figure 3.40. Compound 10 cell view along c-axis

Hydrogens omitted for clarity.

Table 3.1. Structure and refinement details for product 10

Formula	$C_{66}H_{90}Cl_4N_6O_{18}Si_2$
Formula Weight	1453.45
Crystal Color, shape, size	colorless block fragment, 0.218 x 0.226 x 0.530 mm^3
Temperature	150 K
Crystal Class	monoclinic
Space Group	$P2_1$
Unit Cell Dimensions	a = 12.0450(2) Å α = 90.0°
	b = 17.2262(3) Å β = 99.9587(9)°
	c = 17.7282(3) Å γ = 90.0°
Volume	3622.99(11) $Å^3$
Z	2
Density (calculated)	1.33 mg/m^3
Absorption Coefficient	2.396 mm^{-1}
F(000)	1536.000

Data Collection

Diffractometer	Bruker Apex2
Wavelength	1.54187 Å (Cu Kα)
Theta range for data collection	4.5254 –72.4882 °
Index Ranges	h = -14 → 14
	k = -21 → 21
	l = -19 → 21
Reflections measured	76817
Independent reflections	13905 [R_{int} = 0.0256]
Observed Reflections	9678
Completeness to theta	.969

Solution and Refinement

Absorption Correction	Multi-scan
Transmission range	0.55 to 0.59
Solution	Charge Flipping
Refinement Method	Full-matrix, least-squares on F^2
Weighting Scheme	$w = 1/[\sigma^2(Fobs^2) + (0.068 \times P)^2 + 1.990 \times P + 0.000 + 0.000 \times \sin\theta]$,
	$P = 0.333 \times \max(F_{obs}^2,0) + 0.667 \times F_{calc}^2$
Data/Restraints/Parameters	13929/80/901
GooF on F^2	1.007
Flack	0.027(11)
Final R values [I>2sigma(I)]	R1 = 0.0406, wR2 = 0.1087
R indices (all data)	R1 = 0.0403, wR2 = 0.1083
Largest diff. peak and hole	0.54 and -0.56 e $Å^{-3}$

Table 3.2. Atomic coordinates for product 10*

*(× 10^4) and equivalent isotropic displacement parameters (Å^2 × 10^3). U(eq) is defined as one third of the trace of the orthogonalized Uij tensor.

Label	*x*	*y*	*z*	$U_{iso/equiv}$	Occupancy
Cl1	0.61086(8)	0.24255(7)	0.41069(6)	0.0696	1
C12	0.5458(2)	0.30115(12)	0.25981(11)	0.1221	0.791(4)
Cl101	0.24492(10)	0.50692(12)	0.25932(7)	0.1043	1
Cl102	0.03715(8)	0.43512(7)	0.23776(6)	0.064	1
Cl1002	0.5842(6)	0.2306(4)	0.2425(2)	0.1003	0.209(4)
Si1	0.14564(5)	0.73224(4)	0.40462(4)	0.0219	1
Si101	0.32013(5)	0.56702(5)	0.24850(4)	0.0262	1
O1	0.84361(15)	0.78916(12)	0.41668(12)	0.0358	1
O2	0.67691(13)	0.75230(9)	0.44633(9)	0.0216	1
O3	0.58648(14)	0.84507(9)	0.33432(10)	0.0242	1
O4	0.27181(13)	0.69628(10)	0.39684(9)	0.0233	1
O5	0.48854(16)	0.59688(11)	0.14260(10)	0.0317	1
O6	0.5898(2)	0.48110(12)	0.21946(12)	0.0436	1
O7	0.80000(14)	0.51169(11)	0.42308(10)	0.0294	1
O8	0.49193(13)	0.55110(9)	0.48982(10)	0.0244	1
O9	0.47086(17)	0.44198(12)	0.55320(13)	0.0414	1
O101	0.21658(16)	0.49736(12)	0.12460(10)	0.0347	1
O102	0.15187(12)	0.52597(9)	0.00014(9)	0.0198	1
O103	0.03142(14)	0.46176(9)	0.03499(10)	0.0265	1
O104	0.21947(14)	0.60549(10)	0.18396(10)	0.0265	1
O105	0.14188(16)	0.75233(11)	0.11845(11)	0.0331	1
O106	0.00108(15)	0.84712(10)	0.07128(11)	0.0298	1
O107	0.28792(13)	0.75443(10)	0.01282(10)	0.0274	1
O108	0.05814(14)	0.70225(10)	0.18209(9)	0.027	1
O109	0.1246(2)	0.7622(2)	0.27526(16)	0.0851	1
N1	0.84105(17)	0.55854(14)	0.55043(13)	0.0335	1
N2	0.93705(17)	0.53099(13)	0.55826(13)	0.0305	1
N3	1.0238(2)	0.50473(16)	0.57169(16)	0.0441	1
N101	0.37923(18)	0.67368(15)	0.06566(14)	0.0349	1
N102	0.47603(18)	0.67702(14)	0.02879(14)	0.0352	1
N103	0.5673(2)	0.6824(2)	0.00186(19)	0.0619	1
C1	0.3143(2)	0.53014(16)	0.52421(18)	0.0352	1
C2	0.4318(2)	0.50201(14)	0.52533(14)	0.0269	1
C3	0.60678(18)	0.52737(13)	0.48676(13)	0.0229	1
C4	0.6126(2)	0.46534(14)	0.42589(15)	0.028	1
C5	0.66848(19)	0.59996(13)	0.46717(13)	0.0217	1
C6	0.79168(19)	0.57719(15)	0.47022(14)	0.0259	1
C7	0.69356(19)	0.49338(14)	0.37467(14)	0.0259	1
C8	0.61731(17)	0.62776(12)	0.38492(12)	0.018	1

C9	0.65326(18)	0.56714(13)	0.32652(13)	0.0214	1
C10	0.7532(2)	0.59017(14)	0.28703(15)	0.0278	1
C11	0.5524(2)	0.54031(13)	0.26436(14)	0.0261	1
C12	0.49264(19)	0.60315(13)	0.21127(13)	0.0223	1
C13	0.44314(18)	0.66903(13)	0.24850(12)	0.0195	1
C14	0.36060(18)	0.65751(13)	0.28986(12)	0.0204	1
C15	0.2946(2)	0.58409(14)	0.29088(15)	0.0274	1
C16	0.33211(17)	0.72405(13)	0.33964(12)	0.0201	1
C17	0.0951(2)	0.67522(18)	0.48032(18)	0.0385	1
C18	0.0455(2)	0.7204(2)	0.31272(17)	0.0434	1
C19	0.1577(2)	0.83634(15)	0.43060(19)	0.0382	1
C20	0.44071(18)	0.76496(13)	0.37930(13)	0.0208	1
C21	0.54032(18)	0.76858(12)	0.33384(12)	0.019	1
C22	0.50043(18)	0.74830(12)	0.24774(12)	0.0196	1
C23	0.41694(19)	0.80976(13)	0.20819(14)	0.024	1
C24	0.59870(19)	0.75102(13)	0.20303(13)	0.0238	1
C25	0.64112(17)	0.71579(12)	0.37183(12)	0.018	1
C26	0.77582(19)	0.78974(13)	0.45960(14)	0.0236	1
C27	0.7946(2)	0.82950(13)	0.53545(14)	0.0275	1
C28	0.7126(2)	0.83210(15)	0.58199(15)	0.0325	1
C29	0.7353(3)	0.86932(18)	0.65240(18)	0.0454	1
C30	0.8390(3)	0.90499(19)	0.67603(19)	0.0534	1
C31	0.9200(3)	0.90263(19)	0.6300(2)	0.0513	1
C32	0.8985(2)	0.86547(17)	0.55968(19)	0.0398	1
C33	0.6237(5)	0.2319(3)	0.31637(17)	0.0773	0.791(4)
C101	-0.0485(3)	0.6912(2)	0.30479(18)	0.0477	1
C102	0.0545(2)	0.72198(19)	0.25520(17)	0.0397	1
C103	0.15762(18)	0.72301(13)	0.12827(13)	0.0222	1
C104	0.1431(2)	0.80075(13)	0.08883(14)	0.026	1
C105	0.17846(17)	0.65934(13)	0.06827(13)	0.0201	1
C106	0.29091(18)	0.67752(14)	0.01755(14)	0.024	1
C107	0.17644(19)	0.78797(13)	0.00268(14)	0.0247	1
C108	0.08210(17)	0.65865(12)	0.02014(12)	0.0164	1
C109	0.09550(17)	0.73334(12)	0.03230(12)	0.0187	1
C110	0.15035(19)	0.72008(14)	0.11687(13)	0.0245	1
C111	0.01908(19)	0.77676(12)	0.02996(14)	0.0213	1
C112	0.11084(18)	0.73028(14)	0.06042(13)	0.0233	1
C113	0.15127(17)	0.65889(13)	0.01637(13)	0.0205	1
C114	0.19312(17)	0.66392(13)	0.05840(14)	0.0221	1
C115	-0.2314(2)	0.73726(14)	0.10147(15)	0.0297	1
C116	0.20525(18)	0.58958(13)	0.10446(13)	0.0225	1
C117	-0.4494(2)	0.5498(2)	0.20694(19)	0.0498	1
C118	-0.3470(2)	0.63844(17)	0.32804(15)	0.0347	1
C119	-0.2695(3)	0.47379(17)	0.28264(19)	0.0414	1
C120	0.10041(18)	0.53749(12)	0.08080(13)	0.0208	1

C121	0.04733(18)	0.53875(12)	0.00581(13)	0.0188	1
C122	0.12802(18)	0.57892(13)	0.05394(14)	0.0225	1
C123	-0.2376(2)	0.53047(15)	0.05181(16)	0.0302	1
C124	-0.0764(2)	0.58255(15)	0.13958(15)	0.0293	1
C125	0.07050(17)	0.58003(12)	0.02156(12)	0.0174	1
C126	0.22381(19)	0.49201(13)	0.05790(13)	0.0224	1
C127	0.31576(18)	0.45021(13)	0.02833(14)	0.023	1
C128	0.3268(2)	0.45234(15)	0.04790(15)	0.0296	1
C129	0.4185(2)	0.41731(16)	0.07154(17)	0.0363	1
C130	0.4993(2)	0.38036(17)	0.01908(19)	0.0391	1
C131	0.4884(2)	0.37700(17)	0.05734(18)	0.0388	1
C132	0.3969(2)	0.41147(14)	0.08156(15)	0.0281	1
C133	0.1667(2)	0.42145(13)	-0.2671(2)	0.0721	1
C1033	0.6410(18)	0.2864(8)	0.3249(3)	0.073	0.209(4)
H2	-0.012(3)	0.4345(19)	0.0004(16)	0.039(2)	1
H5	0.573(3)	0.8704(18)	0.3697(15)	0.036(2)	1
H7	-0.034(3)	0.848(2)	0.1072(16)	0.044(2)	1
H11	0.2746(2)	0.49374(16)	0.54979(18)	0.0425	1
H12	0.3167(2)	0.57884(16)	0.54959(18)	0.0425	1
H13	0.2770(2)	0.53589(16)	0.47274(18)	0.0425	1
H21	0.565(4)	0.493(3)	0.1763(14)	0.065(2)	1
H31	0.64136(18)	0.50827(13)	0.53545(13)	0.0274	1
H41	0.6391(2)	0.41785(14)	0.44969(15)	0.0334	1
H42	0.5398(2)	0.45772(14)	0.39628(15)	0.0334	1
H51	0.66286(19)	0.63977(13)	0.50340(13)	0.0252	1
H61	0.83144(19)	0.61952(15)	0.45318(14)	0.0304	1
H71	0.70529(19)	0.45260(14)	0.34085(14)	0.0306	1
H81	0.53789(17)	0.62313(12)	0.38075(12)	0.0216	1
H101	0.7800(2)	0.64002(14)	0.30440(15)	0.0339	1
H102	0.7288(2)	0.59146(14)	0.23313(15)	0.0339	1
H103	0.8120(2)	0.55320(14)	0.29925(15)	0.0339	1
H111	0.4978(2)	0.51780(13)	0.29048(14)	0.0309	1
H151	0.2415(2)	0.58993(14)	0.32437(15)	0.0331	1
H152	0.3445(2)	0.54260(14)	0.30823(15)	0.0331	1
H153	0.2559(2)	0.57308(14)	0.24064(15)	0.0331	1
H161	0.28634(17)	0.76048(13)	0.30819(12)	0.0241	1
H171	0.0230(2)	0.69367(18)	0.48682(18)	0.0451	1
H172	0.1466(2)	0.68058(18)	0.52710(18)	0.0451	1
H173	0.0897(2)	0.62207(18)	0.46585(18)	0.0451	1
H181	-0.0258(2)	0.7412(2)	0.31807(17)	0.0513	1
H182	0.0735(2)	0.7471(2)	0.27303(17)	0.0513	1
H183	0.0376(2)	0.6668(2)	0.30030(17)	0.0513	1
H191	0.0854(2)	0.85612(15)	0.43474(19)	0.0438	1
H192	0.2070(2)	0.84216(15)	0.47826(19)	0.0438	1
H193	0.1870(2)	0.86416(15)	0.39211(19)	0.0438	1

H201	0.42154(18)	0.81683(13)	0.38999(13)	0.0249	1
H202	0.46660(18)	0.73842(13)	0.42600(13)	0.0249	1
H231	0.45425(19)	0.85837(13)	0.20834(14)	0.0287	1
H232	0.35547(19)	0.81442(13)	0.23501(14)	0.0287	1
H233	0.38975(19)	0.79437(13)	0.15686(14)	0.0287	1
H241	0.62925(19)	0.80198(13)	0.20562(13)	0.0282	1
H242	0.65537(19)	0.71532(13)	0.22487(13)	0.0282	1
H243	0.57238(19)	0.73758(13)	0.15104(13)	0.0282	1
H251	0.70056(17)	0.71980(12)	0.34312(12)	0.0218	1
H281	0.6412(2)	0.80851(15)	0.56561(15)	0.0384	1
H291	0.6798(3)	0.87036(18)	0.68453(18)	0.0539	1
H301	0.8540(3)	0.93124(19)	0.72383(19)	0.0635	1
H311	0.9911(3)	0.92649(19)	0.6467(2)	0.0608	1
H321	0.9546(2)	0.86478(17)	0.52806(19)	0.0482	1
H331	0.7012(5)	0.2367(3)	0.31164(17)	0.0846	0.791(4)
H332	0.5975(5)	0.1819(3)	0.29921(17)	0.0846	0.791(4)
H1011	-0.0488(3)	0.7062(2)	0.35640(18)	0.0563	1
H1012	-0.1134(3)	0.7116(2)	0.28810(18)	0.0563	1
H1013	-0.0491(3)	0.6362(2)	0.30140(18)	0.0563	1
H1031	0.22026(18)	0.72626(13)	0.15415(13)	0.0268	1
H1034	0.7233(18)	0.2880(8)	0.3276(3)	0.0888	0.209(4)
H1035	0.6135(18)	0.3364(8)	0.3211(3)	0.0888	0.209(4)
H1041	0.1903(2)	0.83902(13)	0.10545(14)	0.0311	1
H1042	0.0667(2)	0.81713(13)	0.10075(14)	0.0311	1
H1051	0.18227(17)	0.61046(13)	0.09251(13)	0.024	1
H1061	0.30603(18)	0.64084(14)	0.02294(14)	0.0291	1
H1071	0.17844(19)	0.83693(13)	0.02217(14)	0.029	1
H1081	0.01397(17)	0.66531(12)	0.05555(12)	0.0188	1
H1101	0.15884(19)	0.76847(14)	0.14294(13)	0.0287	1
H1102	0.22221(19)	0.69663(14)	0.11898(13)	0.0287	1
H1103	0.10356(19)	0.68696(14)	0.14062(13)	0.0287	1
H1111	0.04722(19)	0.78956(12)	0.02195(14)	0.0251	1
H1151	-0.2573(2)	0.72535(14)	0.15388(15)	0.0362	1
H1152	-0.2908(2)	0.76008(14)	0.08025(15)	0.0362	1
H1153	-0.1701(2)	0.77262(14)	0.09737(15)	0.0362	1
H1161	0.26977(18)	0.56253(13)	0.09424(13)	0.0265	1
H1171	-0.5061(2)	0.5277(2)	0.24478(19)	0.0586	1
H1172	-0.4757(2)	0.5976(2)	0.18994(19)	0.0586	1
H1173	-0.4325(2)	0.5152(2)	0.16483(19)	0.0586	1
H1181	-0.4045(2)	0.61926(17)	0.36711(15)	0.0422	1
H1182	-0.3704(2)	0.68634(17)	0.30934(15)	0.0422	1
H1183	-0.2799(2)	0.64622(17)	0.34837(15)	0.0422	1
H1191	-0.3271(3)	0.45150(17)	0.31970(19)	0.0505	1
H1192	-0.2046(3)	0.48296(17)	0.30506(19)	0.0505	1
H1193	-0.2509(3)	0.43920(17)	0.24061(19)	0.0505	1

H1201	0.04430(18)	0.55383(12)	0.10898(13)	0.0252	1
H1202	0.12159(18)	0.48550(12)	0.09415(13)	0.0252	1
H1231	-0.2194(2)	0.48158(15)	0.07553(16)	0.0358	1
H1232	-0.2878(2)	0.55750(15)	0.07836(16)	0.0358	1
H1233	-0.2725(2)	0.52278(15)	0.00007(16)	0.0358	1
H1241	-0.0642(2)	0.53135(15)	0.15917(15)	0.0359	1
H1242	-0.1265(2)	0.60904(15)	0.16660(15)	0.0359	1
H1243	-0.0066(2)	0.60952(15)	0.14580(15)	0.0359	1
H1251	0.08971(17)	0.58894(12)	0.07511(12)	0.0208	1
H1281	0.2714(2)	0.47788(15)	0.08413(15)	0.0359	1
H1291	0.4255(2)	0.41851(16)	0.12409(17)	0.0429	1
H1301	0.5629(2)	0.35740(17)	0.03529(19)	0.0462	1
H1311	0.5437(2)	0.35097(17)	0.09322(18)	0.0466	1
H1321	0.3889(2)	0.40885(14)	0.13388(15)	0.0332	1
H1331	0.1537(2)	0.40535(13)	-0.3191(2)	0.0861	1
H1332	0.2081(2)	0.38246(13)	-0.2363(2)	0.0861	1

Table 3.3. Anisotropic displacement parameters for product 10*

*The anisotropic displacement factor exponent takes the form: $-2\pi^2$ [h^2 a^2 U[11] + ... + 2 hkab U[12]]

Label	U_{11}	U_{22}	U_{33}	U_{23}	U_{13}	U_{12}
Cl1	0.0550(5)	0.0757(6)	0.0723(6)	-0.0189(5)	-0.0051(4)	-0.0069(4)
Cl2	0.199(2)	0.0941(14)	0.0830(13)	0.0486(10)	0.0513(14)	0.0384(14)
Cl101	0.0550(6)	0.1970(17)	0.0601(6)	-0.0113(8)	0.0074(5)	-0.0449(8)
Cl102	0.0574(5)	0.0742(6)	0.0645(6)	0.0194(4)	0.0223(4)	0.0107(4)
Cl1002	0.115(4)	0.112(4)	0.084(4)	-0.044(3)	0.046(3)	-0.076(4)
Si1	0.0173(3)	0.0260(3)	0.0236(3)	-0.0001(2)	0.0065(2)	-0.0015(2)
Si101	0.0204(3)	0.0315(3)	0.0253(3)	-0.0025(2)	0.0006(2)	-0.0027(2)
O1	0.0214(8)	0.0500(11)	0.0373(11)	-0.0099(8)	0.0086(7)	-0.0094(8)
O2	0.0214(7)	0.0246(8)	0.0187(7)	-0.0026(6)	0.0030(6)	-0.0056(6)
O3	0.0297(8)	0.0173(7)	0.0273(9)	-0.0041(6)	0.0095(7)	-0.0063(6)
O4	0.0193(7)	0.0286(8)	0.0240(8)	0.0038(6)	0.0092(6)	-0.0006(6)
O5	0.0437(10)	0.0330(9)	0.0194(9)	-0.0061(7)	0.0080(7)	-0.0020(8)
O6	0.0572(13)	0.0337(10)	0.0357(11)	-0.0161(8)	-0.0037(9)	0.0173(9)
O7	0.0227(8)	0.0338(9)	0.0316(9)	0.0007(7)	0.0044(7)	0.0089(7)
O8	0.0205(7)	0.0247(8)	0.0292(8)	0.0069(6)	0.0074(6)	0.0016(6)
O9	0.0354(10)	0.0357(10)	0.0564(13)	0.0245(9)	0.0173(9)	0.0048(8)
O101	0.0369(10)	0.0472(11)	0.0199(9)	0.0011(7)	0.0048(7)	0.0176(8)
O102	0.0198(7)	0.0204(7)	0.0195(8)	-0.0005(6)	0.0040(6)	0.0055(6)
O103	0.0305(8)	0.0173(8)	0.0322(9)	0.0054(6)	0.0072(7)	0.0000(6)
O104	0.0250(8)	0.0303(8)	0.0228(8)	0.0023(6)	0.0005(6)	-0.0053(6)
O105	0.0372(10)	0.0325(9)	0.0348(10)	-0.0104(7)	0.0206(8)	-0.0024(7)
O106	0.0370(9)	0.0193(8)	0.0368(10)	-0.0094(7)	0.0170(7)	-0.0026(7)

O107	0.0177(7)	0.0299(8)	0.0350(9)	-0.0079(7)	0.0056(6)	-0.0069(6)
O108	0.0268(8)	0.0334(9)	0.0210(8)	0.0002(6)	0.0042(6)	-0.0080(7)
O109	0.0483(14)	0.150(3)	0.0522(15)	0.0520(18)	-0.0035(12)	-0.0323(17)
N1	0.0243(10)	0.0453(13)	0.0293(11)	0.0034(9)	-0.0001(8)	0.0049(9)
N2	0.0237(11)	0.0335(11)	0.0323(11)	0.0085(9)	-0.0005(8)	-0.0035(9)
N3	0.0278(12)	0.0496(14)	0.0523(16)	0.0178(12)	-0.0006(10)	0.0045(10)
N101	0.0204(10)	0.0504(13)	0.0362(12)	-0.0034(10)	0.0115(9)	-0.0030(9)
N102	0.0200(11)	0.0447(13)	0.0444(13)	0.0077(10)	0.0150(9)	0.0045(9)
N103	0.0215(13)	0.106(3)	0.0599(19)	0.0192(17)	0.0120(12)	0.0044(14)
C1	0.0272(12)	0.0342(13)	0.0474(16)	0.0075(11)	0.0149(11)	0.0013(10)
C2	0.0271(11)	0.0279(12)	0.0272(12)	0.0059(9)	0.0089(9)	-0.0008(9)
C3	0.0200(10)	0.0255(11)	0.0235(11)	0.0063(8)	0.0048(8)	0.0035(8)
C4	0.0287(12)	0.0225(11)	0.0334(13)	0.0040(9)	0.0069(10)	0.0029(9)
C5	0.0219(10)	0.0226(10)	0.0203(11)	0.0026(8)	0.0034(8)	0.0007(8)
C6	0.0189(10)	0.0338(12)	0.0243(11)	0.0023(9)	0.0021(8)	0.0002(9)
C7	0.0240(11)	0.0241(11)	0.0302(12)	-0.0003(9)	0.0061(9)	0.0053(9)
C8	0.0175(9)	0.0206(10)	0.0161(10)	0.0013(7)	0.0032(7)	0.0006(8)
C9	0.0217(10)	0.0221(10)	0.0212(10)	-0.0042(8)	0.0065(8)	0.0003(8)
C10	0.0296(12)	0.0300(12)	0.0273(12)	-0.0001(9)	0.0147(9)	0.0041(9)
C11	0.0301(11)	0.0227(11)	0.0245(12)	-0.0061(9)	0.0018(9)	0.0006(9)
C12	0.0223(10)	0.0236(10)	0.0213(11)	-0.0028(8)	0.0050(8)	-0.0067(8)
C13	0.0197(9)	0.0218(10)	0.0158(10)	-0.0004(8)	-0.0002(8)	-0.0017(8)
C14	0.0189(10)	0.0233(10)	0.0177(10)	0.0007(8)	0.0000(8)	-0.0024(8)
C15	0.0269(11)	0.0269(12)	0.0292(12)	-0.0032(9)	0.0071(9)	-0.0062(9)
C16	0.0170(9)	0.0241(10)	0.0204(10)	0.0017(8)	0.0062(8)	-0.0016(8)
C17	0.0276(12)	0.0463(16)	0.0462(16)	0.0150(12)	0.0191(11)	0.0029(11)
C18	0.0229(12)	0.073(2)	0.0323(14)	-0.0123(13)	0.0002(10)	0.0026(13)
C19	0.0362(14)	0.0261(12)	0.0538(17)	-0.0014(11)	0.0123(12)	0.0003(10)
C20	0.0194(10)	0.0231(10)	0.0205(10)	-0.0036(8)	0.0056(8)	-0.0016(8)
C21	0.0195(10)	0.0183(10)	0.0198(10)	-0.0011(7)	0.0052(8)	-0.0038(8)
C22	0.0204(10)	0.0203(10)	0.0179(10)	-0.0003(8)	0.0031(8)	-0.0025(8)
C23	0.0253(11)	0.0254(11)	0.0215(11)	0.0056(8)	0.0048(9)	-0.0031(9)
C24	0.0253(11)	0.0259(11)	0.0213(11)	0.0003(8)	0.0074(8)	-0.0051(8)
C25	0.0175(9)	0.0213(10)	0.0158(10)	-0.0032(7)	0.0045(7)	-0.0040(7)
C26	0.0192(10)	0.0237(10)	0.0261(12)	0.0000(8)	-0.0010(9)	-0.0008(8)
C27	0.0274(11)	0.0223(11)	0.0285(12)	-0.0003(9)	-0.0066(9)	0.0003(9)
C28	0.0387(14)	0.0299(12)	0.0267(12)	-0.0063(10)	-0.0009(10)	0.0030(10)
C29	0.0603(19)	0.0427(16)	0.0303(15)	-0.0105(12)	-0.0002(14)	0.0095(14)
C30	0.068(2)	0.0427(17)	0.0387(17)	-0.0188(13)	-0.0209(16)	0.0121(15)
C31	0.0449(17)	0.0412(16)	0.057(2)	-0.0161(14)	-0.0201(15)	-0.0033(13)
C32	0.0289(13)	0.0363(14)	0.0492(18)	-0.0083(12)	-0.0077(12)	-0.0016(11)
C33	0.071(3)	0.083(3)	0.080(3)	-0.016(3)	0.019(3)	0.002(3)
C101	0.0474(17)	0.0601(19)	0.0309(14)	0.0068(13)	-0.0068(13)	-0.0070(14)
C102	0.0315(13)	0.0561(17)	0.0312(14)	0.0131(12)	0.0048(11)	-0.0013(12)
C103	0.0178(10)	0.0268(11)	0.0234(11)	-0.0014(9)	0.0079(8)	-0.0034(8)

C104	0.0282(12)	0.0217(11)	0.0301(13)	0.0000(9)	0.0103(9)	-0.0052(9)
C105	0.0169(10)	0.0203(10)	0.0240(11)	-0.0025(8)	0.0065(8)	-0.0005(8)
C106	0.0168(10)	0.0271(11)	0.0290(12)	-0.0026(9)	0.0066(9)	-0.0024(8)
C107	0.0226(11)	0.0214(10)	0.0313(13)	-0.0057(9)	0.0082(9)	-0.0059(8)
C108	0.0141(9)	0.0183(9)	0.0171(10)	-0.0033(7)	0.0039(7)	-0.0007(7)
C109	0.0181(9)	0.0170(9)	0.0216(10)	-0.0042(8)	0.0052(8)	-0.0032(8)
C110	0.0242(10)	0.0268(11)	0.0221(11)	-0.0054(8)	0.0026(8)	-0.0055(9)
C111	0.0234(10)	0.0169(10)	0.0252(11)	-0.0035(8)	0.0089(8)	0.0005(8)
C112	0.0206(10)	0.0236(10)	0.0273(12)	-0.0014(9)	0.0090(8)	0.0032(9)
C113	0.0144(9)	0.0201(10)	0.0291(12)	-0.0016(8)	0.0097(8)	0.0014(8)
C114	0.0154(9)	0.0224(10)	0.0298(12)	0.0007(9)	0.0077(8)	0.0012(8)
C115	0.0254(11)	0.0241(11)	0.0375(13)	0.0012(10)	-0.0007(9)	0.0049(9)
C116	0.0190(10)	0.0244(11)	0.0237(11)	0.0003(8)	0.0027(8)	-0.0040(8)
C117	0.0245(12)	0.083(3)	0.0415(16)	-0.0036(16)	0.0042(11)	-0.0130(14)
C118	0.0318(12)	0.0408(14)	0.0281(13)	0.0018(10)	-0.0040(10)	0.0063(11)
C119	0.0469(16)	0.0292(13)	0.0466(16)	-0.0059(11)	0.0034(13)	-0.0040(11)
C120	0.0213(10)	0.0161(9)	0.0248(11)	-0.0044(8)	0.0035(8)	-0.0017(8)
C121	0.0209(10)	0.0122(9)	0.0236(11)	0.0013(7)	0.0047(8)	-0.0002(7)
C122	0.0218(10)	0.0212(10)	0.0263(11)	0.0021(8)	0.0091(9)	-0.0022(8)
C123	0.0250(11)	0.0291(12)	0.0390(14)	0.0078(10)	0.0129(10)	-0.0051(9)
C124	0.0310(12)	0.0324(13)	0.0279(13)	0.0039(9)	0.0146(10)	0.0007(9)
C125	0.0172(9)	0.0170(9)	0.0191(10)	-0.0020(7)	0.0061(7)	0.0029(7)
C126	0.0240(10)	0.0198(10)	0.0222(12)	-0.0014(8)	0.0009(8)	0.0028(8)
C127	0.0191(10)	0.0186(10)	0.0301(12)	-0.0040(8)	0.0005(9)	0.0016(8)
C128	0.0313(12)	0.0293(12)	0.0284(12)	-0.0003(9)	0.0062(10)	0.0109(10)
C129	0.0397(15)	0.0360(14)	0.0358(15)	-0.0065(11)	0.0134(11)	0.0071(11)
C130	0.0284(12)	0.0384(14)	0.0513(18)	-0.0118(12)	0.0098(12)	0.0128(11)
C131	0.0292(13)	0.0333(13)	0.0496(17)	-0.0059(12)	-0.0053(11)	0.0124(10)
C132	0.0281(12)	0.0258(11)	0.0284(12)	-0.0036(9)	-0.0007(9)	0.0060(9)
C133	0.0476(19)	0.110(3)	0.057(2)	-0.015(2)	0.0051(16)	0.036(2)
C1033	0.071(5)	0.070(6)	0.081(6)	-0.037(5)	0.021(5)	-0.030(5)

Table 3.4. Bond lengths [Å] for product 10

Cl1	C33	1.715(3)Å	Cl1	C1033	1.790(3)Å
Cl2	Cl1002	1.354(8)Å	Cl2	C33	1.727(3)Å
Cl2	C1033	1.501(18)Å	Cl2	H1035	1.381Å
Cl101	C133	1.740(2)Å	Cl102	C133	1.744(2)Å
Cl1002	C33	1.313(6)Å	Cl1002	C1033	1.782(3)Å
Cl1002	H332	1.298Å	Si1	O4	1.6687(16)Å
Si1	C17	1.849(3)Å	Si1	C18	1.863(3)Å
Si1	C19	1.851(3)Å	Si101	O104	1.6548(17)Å
Si101	C117	1.858(3)Å	Si101	C118	1.857(3)Å
Si101	C119	1.856(3)Å	O1	C26	1.209(3)Å

O2	C25	1.459(2)Å	O2	C26	1.339(3)Å
O3	C21	1.430(2)Å	O3	H5	0.803(18)Å
O4	C16	1.428(3)Å	O5	C12	1.215(3)Å
O6	C11	1.415(3)Å	O6	H21	0.800(19)Å
O7	C6	1.418(3)Å	O7	C7	1.449(3)Å
O8	C2	1.339(3)Å	O8	C3	1.452(3)Å
O9	C2	1.206(3)Å	O101	C126	1.204(3)Å
O102	C125	1.449(2)Å	O102	C126	1.355(3)Å
O103	C121	1.425(2)Å	O103	H2	0.839(18)Å
O104	C116	1.417(3)Å	O105	C112	1.215(3)Å
O106	C111	1.413(3)Å	O106	H7	0.804(19)Å
O107	C106	1.433(3)Å	O107	C107	1.444(3)Å
O108	C102	1.333(3)Å	O108	C103	1.442(3)Å
O109	C102	1.193(4)Å	N1	N2	1.235(3)Å
N1	C6	1.479(3)Å	N2	N3	1.126(3)Å
N101	N102	1.235(3)Å	N101	C106	1.476(3)Å
N102	N103	1.124(4)Å	C1	C2	1.493(3)Å
C1	H11	0.950Å	C1	H12	0.950Å
C1	H13	0.950Å	C3	C4	1.529(3)Å
C3	C5	1.525(3)Å	C3	H31	0.950Å
C4	C7	1.521(3)Å	C4	H41	0.950Å
C4	H42	0.950Å	C5	C6	1.527(3)Å
C5	C8	1.557(3)Å	C5	H51	0.950Å
C6	H61	0.950Å	C7	C9	1.561(3)Å
C7	H71	0.950Å	C8	C9	1.583(3)Å
C8	C25	1.568(3)Å	C8	H81	0.950Å
C9	C10	1.545(3)Å	C9	C11	1.563(3)Å
C10	H101	0.950Å	C10	H102	0.950Å
C10	H103	0.950Å	C11	C12	1.530(3)Å
C11	H111	0.950Å	C12	C13	1.488(3)Å
C13	C14	1.348(3)Å	C13	C22	1.531(3)Å
C14	C15	1.496(3)Å	C14	C16	1.521(3)Å
C15	H151	0.950Å	C15	H152	0.950Å
C15	H153	0.950Å	C16	C20	1.544(3)Å
C16	H161	0.950Å	C17	H171	0.950Å
C17	H172	0.950Å	C17	H173	0.950Å
C18	H181	0.950Å	C18	H182	0.950Å
C18	H183	0.950Å	C19	H191	0.950Å
C19	H192	0.950Å	C19	H193	0.950Å
C20	C21	1.558(3)Å	C20	H201	0.950Å
C20	H202	0.950Å	C21	C22	1.559(3)Å
C21	C25	1.572(3)Å	C22	C23	1.543(3)Å
C22	C24	1.535(3)Å	C23	H231	0.950Å
C23	H232	0.950Å	C23	H233	0.950Å
C24	H241	0.950Å	C24	H242	0.950Å

C24	H243	0.950Å	C25	H251	0.950Å
C26	C27	1.491(3)Å	C27	C28	1.394(4)Å
C27	C32	1.396(4)Å	C28	C29	1.388(4)Å
C28	H281	0.950Å	C29	C30	1.390(5)Å
C29	H291	0.950Å	C30	C31	1.377(6)Å
C30	H301	0.950Å	C31	C32	1.386(5)Å
C31	H311	0.950Å	C32	H321	0.950Å
C33	C1033	0.967(10)Å	C33	H331	0.956Å
C33	H332	0.949Å	C101	C102	1.489(4)Å
C101	H1011	0.950Å	C101	H1012	0.950Å
C101	H1013	0.950Å	C103	C104	1.535(3)Å
C103	C105	1.518(3)Å	C103	H1031	0.950Å
C104	C107	1.527(3)Å	C104	H1041	0.950Å
C104	H1042	0.950Å	C105	C106	1.523(3)Å
C105	C108	1.555(3)Å	C105	H1051	0.950Å
C106	H1061	0.950Å	C107	C109	1.559(3)Å
C107	H1071	0.950Å	C108	C109	1.579(3)Å
C108	C125	1.561(3)Å	C108	H1081	0.950Å
C109	C110	1.547(3)Å	C109	C111	1.564(3)Å
C110	H1101	0.950Å	C110	H1102	0.950Å
C110	H1103	0.950Å	C111	C112	1.536(3)Å
C111	H1111	0.950Å	C112	C113	1.493(3)Å
C113	C114	1.337(3)Å	C113	C122	1.535(3)Å
C114	C115	1.507(3)Å	C114	C116	1.512(3)Å
C115	H1151	0.950Å	C115	H1152	0.950Å
C115	H1153	0.950Å	C116	C120	1.547(3)Å
C116	H1161	0.950Å	C117	H1171	0.950Å
C117	H1172	0.950Å	C117	H1173	0.950Å
C118	H1181	0.950Å	C118	H1182	0.950Å
C118	H1183	0.950Å	C119	H1191	0.950Å
C119	H1192	0.950Å	C119	H1193	0.950Å
C120	C121	1.558(3)Å	C120	H1201	0.950Å
C120	H1202	0.950Å	C121	C122	1.561(3)Å
C121	C125	1.569(3)Å	C122	C123	1.556(3)Å
C122	C124	1.539(3)Å	C123	H1231	0.950Å
C123	H1232	0.950Å	C123	H1233	0.950Å
C124	H1241	0.950Å	C124	H1242	0.950Å
C124	H1243	0.950Å	C125	H1251	0.950Å
C126	C127	1.490(3)Å	C127	C128	1.381(4)Å
C127	C132	1.404(3)Å	C128	C129	1.385(4)Å
C128	H1281	0.950Å	C129	C130	1.380(4)Å
C129	H1291	0.950Å	C130	C131	1.385(5)Å
C130	H1301	0.950Å	C131	C132	1.384(4)Å
C131	H1311	0.950Å	C132	H1321	0.950Å
C133	H1331	0.950Å	C133	H1332	0.950Å

C1033	H331	1.171Å	C1033	H1034	0.985Å
C1033	H1035	0.922Å			

Table 3.5. Bond angles [°] for product 10

C33	Cl1	C1033	31.9(3)°	Cl1002	Cl2	C33	48.6(3)°
Cl1002	Cl2	C1033	77.1(7)°	C33	Cl2	C1033	34.0(4)°
Cl1002	Cl2	H1035	113.235°	C33	Cl2	H1035	70.108°
C1033	Cl2	H1035	37.020°	Cl2	Cl1002	C33	80.7(3)°
Cl2	Cl1002	C1033	55.2(8)°	C33	Cl1002	C1033	32.1(4)°
Cl2	Cl1002	H332	113.974°	C33	Cl1002	H332	42.643°
C1033	Cl1002	H332	74.673°	O4	Si1	C17	106.35(11)°
O4	Si1	C18	110.38(11)°	C17	Si1	C18	109.39(15)°
O4	Si1	C19	110.29(11)°	C17	Si1	C19	110.83(14)°
C18	Si1	C19	109.56(16)°	O104	Si101	C117	110.72(12)°
O104	Si101	C118	105.68(11)°	C117	Si101	C118	111.02(15)°
O104	Si101	C119	109.22(12)°	C117	Si101	C119	109.67(16)°
C118	Si101	C119	110.46(14)°	C25	O2	C26	118.76(17)°
C21	O3	H5	112(3)°	Si1	O4	C16	121.11(14)°
C11	O6	H21	104(3)°	C6	O7	C7	112.14(16)°
C2	O8	C3	115.83(17)°	C125	O102	C126	116.92(17)°
C121	O103	H2	107(3)°	Si101	O104	C116	123.94(14)°
C111	O106	H7	112(3)°	C106	O107	C107	112.42(16)°
C102	O108	C103	117.64(19)°	N2	N1	C6	113.9(2)°
N1	N2	N3	174.1(3)°	N102	N101	C106	113.6(2)°
N101	N102	N103	173.1(3)°	C2	C1	H11	109.512°
C2	C1	H12	109.210°	H11	C1	H12	109.475°
C2	C1	H13	109.678°	H11	C1	H13	109.477°
H12	C1	H13	109.475°	O8	C2	O9	122.0(2)°
O8	C2	C1	112.2(2)°	O9	C2	C1	125.8(2)°
O8	C3	C4	112.54(19)°	O8	C3	C5	106.41(17)°
C4	C3	C5	109.19(19)°	O8	C3	H31	109.531°
C4	C3	H31	109.442°	C5	C3	H31	109.669°
C3	C4	C7	108.16(19)°	C3	C4	H41	109.952°
C7	C4	H41	109.758°	C3	C4	H42	109.631°
C7	C4	H42	109.851°	H41	C4	H42	109.466°
C3	C5	C6	106.87(18)°	C3	C5	C8	109.63(18)°
C6	C5	C8	109.69(18)°	C3	C5	H51	110.093°
C6	C5	H51	110.120°	C8	C5	H51	110.367°
O7	C6	N1	109.6(2)°	O7	C6	C5	110.54(18)°
N1	C6	C5	108.46(19)°	O7	C6	H61	109.424°
N1	C6	H61	109.367°	C5	C6	H61	109.383°
O7	C7	C4	108.0(2)°	O7	C7	C9	107.85(18)°
C4	C7	C9	114.46(18)°	O7	C7	H71	108.777°
C4	C7	H71	108.822°	C9	C7	H71	108.840°
C5	C8	C9	107.51(17)°	C5	C8	C25	112.53(17)°

C9	C8	C25	117.62(18)°	C5	C8	H81	106.085°
C9	C8	H81	106.227°	C25	C8	H81	106.094°
C7	C9	C8	105.89(17)°	C7	C9	C10	105.31(18)°
C8	C9	C10	116.72(18)°	C7	C9	C11	105.98(18)°
C8	C9	C11	112.90(17)°	C10	C9	C11	109.15(19)°
C9	C10	H101	109.448°	C9	C10	H102	109.453°
H101	C10	H102	109.476°	C9	C10	H103	109.498°
H101	C10	H103	109.475°	H102	C10	H103	109.477°
O6	C11	C9	108.97(19)°	O6	C11	C12	109.0(2)°
C9	C11	C12	116.75(19)°	O6	C11	H111	107.172°
C9	C11	H111	107.242°	C12	C11	H111	107.289°
O5	C12	C11	119.1(2)°	O5	C12	C13	124.2(2)°
C11	C12	C13	116.64(19)°	C12	C13	C14	121.2(2)°
C12	C13	C22	117.41(19)°	C14	C13	C22	120.8(2)°
C13	C14	C15	125.1(2)°	C13	C14	C16	117.78(19)°
C15	C14	C16	117.15(19)°	C14	C15	H151	109.547°
C14	C15	H152	109.408°	H151	C15	H152	109.476°
C14	C15	H153	109.445°	H151	C15	H153	109.475°
H152	C15	H153	109.476°	O4	C16	C14	110.67(18)°
O4	C16	C20	108.93(17)°	C14	C16	C20	110.47(17)°
O4	C16	H161	108.858°	C14	C16	H161	108.871°
C20	C16	H161	109.003°	Si1	C17	H171	109.430°
Si1	C17	H172	109.585°	H171	C17	H172	109.476°
Si1	C17	H173	109.384°	H171	C17	H173	109.477°
H172	C17	H173	109.475°	Si1	C18	H181	109.335°
Si1	C18	H182	109.618°	H181	C18	H182	109.476°
Si1	C18	H183	109.445°	H181	C18	H183	109.476°
H182	C18	H183	109.476°	Si1	C19	H191	109.459°
Si1	C19	H192	109.489°	H191	C19	H192	109.476°
Si1	C19	H193	109.451°	H191	C19	H193	109.476°
H192	C19	H193	109.477°	C16	C20	C21	116.77(17)°
C16	C20	H201	107.711°	C21	C20	H201	107.518°
C16	C20	H202	107.555°	C21	C20	H202	107.693°
H201	C20	H202	109.466°	O3	C21	C20	111.55(17)°
O3	C21	C22	105.43(17)°	C20	C21	C22	111.29(17)°
O3	C21	C25	105.06(16)°	C20	C21	C25	111.23(17)°
C22	C21	C25	111.98(17)°	C13	C22	C21	104.73(17)°
C13	C22	C23	110.90(17)°	C21	C22	C23	110.95(17)°
C13	C22	C24	114.88(18)°	C21	C22	C24	111.36(17)°
C23	C22	C24	104.16(18)°	C22	C23	H231	109.435°
C22	C23	H232	109.492°	H231	C23	H232	109.477°
C22	C23	H233	109.472°	H231	C23	H233	109.476°
H232	C23	H233	109.476°	C22	C24	H241	109.277°
C22	C24	H242	109.496°	H241	C24	H242	109.476°
C22	C24	H243	109.625°	H241	C24	H243	109.476°

H242	C24	H243	109.476°	O2	C25	C8	108.41(16)°
O2	C25	C21	102.93(16)°	C8	C25	C21	118.38(16)°
O2	C25	H251	108.757°	C8	C25	H251	108.892°
C21	C25	H251	109.032°	O1	C26	O2	124.2(2)°
O1	C26	C27	123.9(2)°	O2	C26	C27	111.8(2)°
C26	C27	C28	122.4(2)°	C26	C27	C32	118.0(2)°
C28	C27	C32	119.6(2)°	C27	C28	C29	119.8(3)°
C27	C28	H281	120.159°	C29	C28	H281	119.996°
C28	C29	C30	120.2(3)°	C28	C29	H291	119.884°
C30	C29	H291	119.953°	C29	C30	C31	120.0(3)°
C29	C30	H301	120.157°	C31	C30	H301	119.801°
C30	C31	C32	120.4(3)°	C30	C31	H311	119.720°
C32	C31	H311	119.906°	C27	C32	C31	120.0(3)°
C27	C32	H321	120.298°	C31	C32	H321	119.707°
Cl1	C33	Cl2	111.17(4)°	Cl1	C33	Cl1002	153.6(5)°
Cl2	C33	Cl1002	50.7(4)°	Cl1	C33	C1033	78.3(3)°
Cl2	C33	C1033	60.1(11)°	Cl1002	C33	C1033	101.8(6)°
Cl1	C33	H331	109.292°	Cl2	C33	H331	109.279°
Cl1002	C33	H331	96.000°	C1033	C33	H331	75.065°
Cl1	C33	H332	109.162°	Cl2	C33	H332	108.880°
Cl1002	C33	H332	67.801°	C1033	C33	H332	168.851°
H331	C33	H332	109.028°	C102	C101	H1011	109.624°
C102	C101	H1012	109.339°	H1011	C101	H1012	109.477°
C102	C101	H1013	109.438°	H1011	C101	H1013	109.475°
H1012	C101	H1013	109.476°	O108	C102	O109	122.1(3)°
O108	C102	C101	111.5(2)°	O109	C102	C101	126.3(3)°
O108	C103	C104	111.75(18)°	O108	C103	C105	107.59(17)°
C104	C103	C105	109.23(18)°	O108	C103	H1031	109.485°
C104	C103	H1031	109.353°	C105	C103	H1031	109.393°
C103	C104	C107	107.38(19)°	C103	C104	H1041	110.031°
C107	C104	H1041	110.004°	C103	C104	H1042	109.898°
C107	C104	H1042	110.033°	H1041	C104	H1042	109.467°
C103	C105	C106	106.70(18)°	C103	C105	C108	109.96(17)°
C106	C105	C108	110.46(18)°	C103	C105	H1051	109.780°
C106	C105	H1051	109.981°	C108	C105	H1051	109.911°
O107	C106	N101	109.03(19)°	O107	C106	C105	109.54(18)°
N101	C106	C105	107.82(19)°	O107	C106	H1061	110.181°
N101	C106	H1061	110.107°	C105	C106	H1061	110.119°
O107	C107	C104	108.88(19)°	O107	C107	C109	107.92(18)°
C104	C107	C109	114.24(18)°	O107	C107	H1071	108.587°
C104	C107	H1071	108.485°	C109	C107	H1071	108.603°
C105	C108	C109	107.87(16)°	C105	C108	C125	113.76(16)°
C109	C108	C125	115.89(17)°	C105	C108	H1081	106.134°
C109	C108	H1081	106.219°	C125	C108	H1081	106.246°
C107	C109	C108	105.36(16)°	C107	C109	C110	106.44(17)°

C108	C109	C110	115.67(18)°	C107	C109	C111	108.09(18)°
C108	C109	C111	111.97(16)°	C110	C109	C111	108.86(17)°
C109	C110	H1101	109.505°	C109	C110	H1102	109.537°
H1101	C110	H1102	109.475°	C109	C110	H1103	109.358°
H1101	C110	H1103	109.476°	H1102	C110	H1103	109.475°
O106	C111	C109	109.93(18)°	O106	C111	C112	108.66(18)°
C109	C111	C112	115.25(18)°	O106	C111	H1111	107.460°
C109	C111	H1111	107.580°	C112	C111	H1111	107.675°
O105	C112	C111	118.7(2)°	O105	C112	C113	125.5(2)°
C111	C112	C113	115.79(18)°	C112	C113	C114	119.9(2)°
C112	C113	C122	119.6(2)°	C114	C113	C122	119.8(2)°
C113	C114	C115	125.9(2)°	C113	C114	C116	117.7(2)°
C115	C114	C116	116.4(2)°	C114	C115	H1151	109.548°
C114	C115	H1152	109.371°	H1151	C115	H1152	109.475°
C114	C115	H1153	109.478°	H1151	C115	H1153	109.477°
H1152	C115	H1153	109.478°	O104	C116	C114	110.92(18)°
O104	C116	C120	109.54(18)°	C114	C116	C120	110.28(17)°
O104	C116	H1161	108.810°	C114	C116	H1161	108.559°
C120	C116	H1161	108.676°	Si101	C117	H1171	109.458°
Si101	C117	H1172	109.637°	H1171	C117	H1172	109.476°
Si101	C117	H1173	109.306°	H1171	C117	H1173	109.475°
H1172	C117	H1173	109.476°	Si101	C118	H1181	109.425°
Si101	C118	H1182	109.491°	H1181	C118	H1182	109.477°
Si101	C118	H1183	109.484°	H1181	C118	H1183	109.475°
H1182	C118	H1183	109.476°	Si101	C119	H1191	109.480°
Si101	C119	H1192	109.476°	H1191	C119	H1192	109.477°
Si101	C119	H1193	109.445°	H1191	C119	H1193	109.475°
H1192	C119	H1193	109.475°	C116	C120	C121	115.83(17)°
C116	C120	H1201	107.897°	C121	C120	H1201	107.824°
C116	C120	H1202	107.932°	C121	C120	H1202	107.782°
H1201	C120	H1202	109.466°	O103	C121	C120	110.57(17)°
O103	C121	C122	105.75(17)°	C120	C121	C122	110.89(17)°
O103	C121	C125	107.26(16)°	C120	C121	C125	112.72(17)°
C122	C121	C125	109.35(16)°	C113	C122	C121	104.17(17)°
C113	C122	C123	112.36(18)°	C121	C122	C123	110.76(18)°
C113	C122	C124	113.82(19)°	C121	C122	C124	111.93(18)°
C123	C122	C124	104.01(19)°	C122	C123	H1231	109.545°
C122	C123	H1232	109.588°	H1231	C123	H1232	109.476°
C122	C123	H1233	109.267°	H1231	C123	H1233	109.476°
H1232	C123	H1233	109.474°	C122	C124	H1241	109.485°
C122	C124	H1242	109.462°	H1241	C124	H1242	109.475°
C122	C124	H1243	109.454°	H1241	C124	H1243	109.477°
H1242	C124	H1243	109.475°	O102	C125	C108	108.27(16)°
O102	C125	C121	107.11(16)°	C108	C125	C121	117.48(16)°
O102	C125	H1251	107.856°	C108	C125	H1251	107.870°

C121	C125	H1251	107.914°	O101	C126	O102	124.3(2)°
O101	C126	C127	124.5(2)°	O102	C126	C127	111.10(19)°
C126	C127	C128	122.3(2)°	C126	C127	C132	117.8(2)°
C128	C127	C132	119.8(2)°	C127	C128	C129	120.1(2)°
C127	C128	H1281	119.920°	C129	C128	H1281	120.006°
C128	C129	C130	120.2(3)°	C128	C129	H1291	119.865°
C130	C129	H1291	119.907°	C129	C130	C131	120.2(2)°
C129	C130	H1301	120.030°	C131	C130	H1301	119.775°
C130	C131	C132	120.1(3)°	C130	C131	H1311	120.035°
C132	C131	H1311	119.878°	C127	C132	C131	119.6(3)°
C127	C132	H1321	120.134°	C131	C132	H1321	120.236°
Cl101	C133	Cl102	111.23(4)°	Cl101	C133	H1331	108.648°
Cl102	C133	H1331	108.837°	Cl101	C133	H1332	109.278°
Cl102	C133	H1332	109.355°	H1331	C133	H1332	109.466°
Cl1	C1033	Cl2	119.0(10)°	Cl1	C1033	Cl1002	111.31(4)°
Cl2	C1033	Cl1002	47.8(4)°	Cl1	C1033	C33	69.8(3)°
Cl2	C1033	C33	85.9(8)°	Cl1002	C1033	C33	46.2(3)°
Cl1	C1033	H331	94.955°	Cl2	C1033	H331	112.738°
Cl1002	C1033	H331	66.748°	C33	C1033	H331	52.036°
Cl1	C1033	H1034	108.722°	Cl2	C1033	H1034	131.382°
Cl1002	C1033	H1034	107.167°	C33	C1033	H1034	102.884°
H331	C1033	H1034	51.454°	Cl1	C1033	H1035	109.506°
Cl2	C1033	H1035	64.389°	Cl1002	C1033	H1035	111.183°
C33	C1033	H1035	146.138°	H331	C1033	H1035	153.524°
H1034	C1033	H1035	108.864°	C33	H331	C1033	52.899°
Cl1002	H332	C33	69.556°	Cl2	H1035	C1033	78.591°

Chapter 4 – Comparative functional group reactivity ranking in the context of LSF

4.1. Motivation behind functional groups reactivity comparison

Chemoselective modification of natural products by the strategic employment of fluoroarylborane catalysts and silanes has been quite successful on a variety of natural products.[5] As discussed in detail in the previous chapter, the late-stage functionalization (LSF) approach led to excellent chemoselectivities and good to excellent yields for a host of new natural product derivatives. Despite this success, some of reported results were rather exciting serendipitous discoveries rather than targeted predetermined synthetic outcomes. In fact, prior to the experiments outlined in Chapter 3, very little was known about comparative rates of reduction of numerous functional groups present on the complex natural product scaffolds.

Since a chemoselective reaction is inherently a competition between functional groups, baseline reactivity trends are needed to gain insight into the structure-activity relationships of the chosen natural products. This kinetic data on simple small molecules provides important context for how structure can enhance or diminish reactivity. Changing the reaction conditions such as catalyst, reductant, or temperature also helps us gain important understanding regarding chemoselectivity trends observed in natural product reactions. Ultimately, the vast complexity and diversity of natural products mean that the reported reactivity trends will vary on a case by case basis, but the baseline data can help in *a priori* selection of the catalyst/reductant combinations with the highest chance of success for a given structure or region of a molecule.

4.2. Competition experiments – NMR approach

4.2.1. Precedent and competition analysis by Proton NMR

Establishing background comparative reactivity ranking of small molecules in catalysis has been precedented in the literature by Stephan and colleagues for a novel Lewis acidic phosphonium cation catalyst.[80] The synthesized salts, $[(C_6F_5)_3PX][B(C_6F_5)_4]$ (X=F, Cl, Br), catalyze the hydrosilylation of ketones, imines, nitriles, and olefins. Inherently, there was no prior established method of predicting the reactivity of these functional groups with respect to each other for this new catalytic system. Utilizing ^{1}H NMR spectroscopy and observing the hydrosilylated product distributions, a relative reactivity ranking was successfully established (Scheme 4.1).

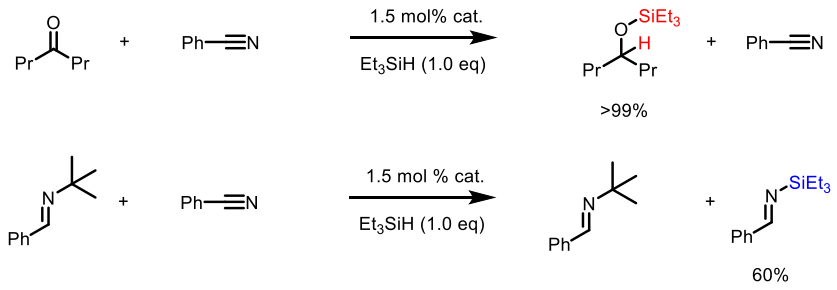

Scheme 4.1. Stephan functional group competition experiments*

***Percentage values in parentheses are yields determined by ^{1}H NMR spectroscopy.**

For example, the ketone in Scheme 4.1 was selectively reduced in the presence of nitrile, therefore indicating the highest relative propensity of the catalyst to reduce this family of functional groups. The established trend in order of decreasing preference was reported as: ketone>nitrile>imine>olefin. Further intramolecular experiments confirmed this when a molecule containing both a ketone and a terminal olefin was subjected to the reaction conditions. Since the olefin fragment was unchanged, as seen by ^{1}NMR, it was evident that ketone reduction to the silyl ether is the dominant outcome.[80]

Similar to the method reported by Stephan et al., our experiments set out to establish a relative reactivity ranking between various functional groups observed in complicated substrates as gibberellic acid and natamycin (Figure 4.1).

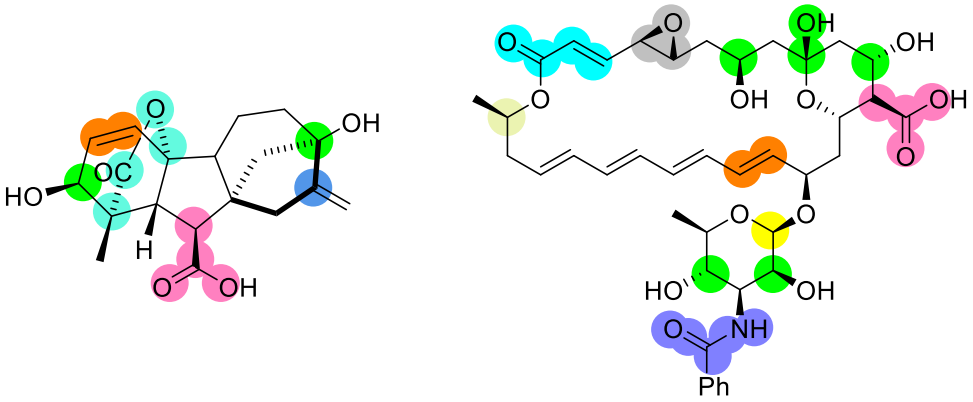

Figure 4.1. Functional group diversity in natural products

Several key functional groups (i.e. carboxylic acids, epoxides, esters, olefins, amides) were identified and small molecules containing these moieties were chosen for pairwise experiments. To best mimic catalytic reaction conditions used in prior natamycin experiments, BCF and Et_3SiH combinations in toluene or dichloromethane was chosen. Due to the propensity of side product formation in small-molecule BCF-catalyzed reductions, the rate of consumption of starting materials was tracked over time to determine the more competitive functional group. By tracking the disappearance of the diagnostic starting material peaks with respect to an internal standard, a successful NMR experiment was designed to probe comparative reactivity (Figure 4.2).

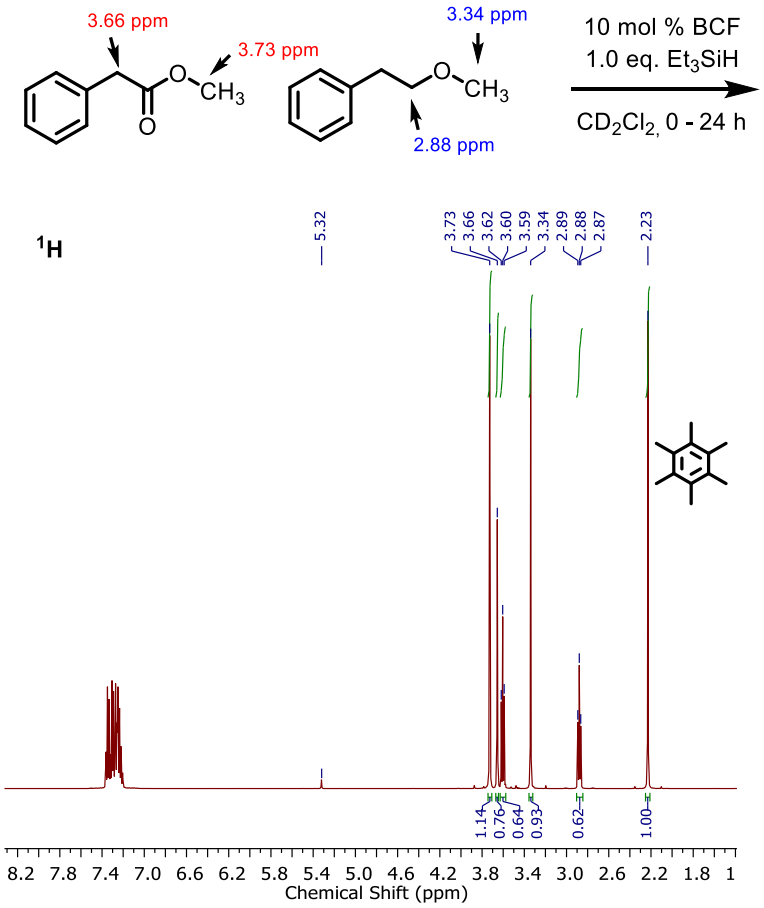

Figure 4.2. A representative ^{1}H NMR for a pairwise competition

In a nitrogen-filled glovebox atmosphere at room temperature, 10 mol % of BCF catalyst, hexamethylbenzene (HMB) internal standard, and CD_2Cl_2 were added to a 1-dram vial. The chosen substrates (1 equiv.) were then added to the same vial and the mixture was transferred to a septum-capped NMR tube. Upon initial ^{1}H NMR spectrum collection, 1 equivalent of Et_3SiH was added by syringe via the septum cap and the tube was immediately placed into the spectrometer to acquire a ^{1}H NMR spectrum, with the first at approximately 5 minutes after silane addition. ^{1}H NMR spectroscopy was then tracked after 2, 12, and 24 h intervals to monitor the starting material disappearance. Using this approach allowed for a quick assessment of substrate conversion over time, as each of the starting material peaks can be compared to the normalized internal standard

integration, providing accurate quantitative data. Due to rapid consumption of certain substrate classes, silylium ion carriers needed to be employed in some experiments, as discussed in the following section.

4.2.2. Silylium ion carriers for facile NMR analysis

While the general ^{1}H NMR approach is useful, some of the hydrosilylation reactions were too rapid to allow successful tracking of starting material disappearance by obtaining consecutive ^{1}H NMR spectra. Since the BCF/Et_3SiH combination is very reactive toward several small molecule reductions (i.e. epoxide ring-opening), the silylium attenuation methodology outlined in Chapter 2 had to be employed to lower the overall reaction rate and allow for more facile data analysis. Appropriate control experiments established that employing a silylium ion carrier influences the rate but not the chemoselectivity of the reaction. In this manner, various triarylphosphines and amides (Figure 4.3) were probed in pairwise experiments.

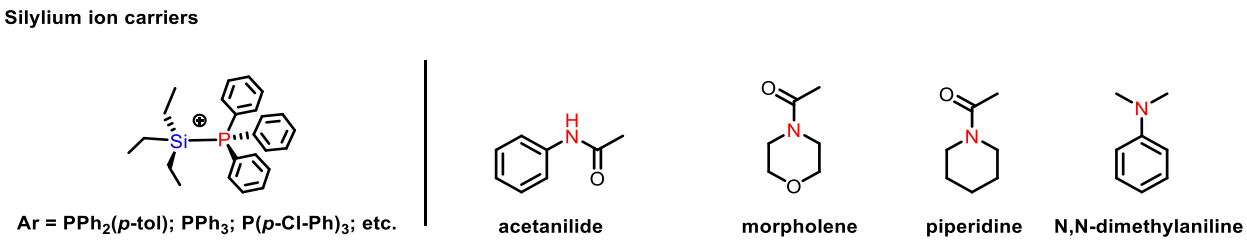

Figure 4.3. Lewis base silylium ion carriers

N,N-dimethylaniline was identified as the optimal silylium carrier for the reactions reported herein, since it both speciated the BCF and Et_3SiH fully to the $[Et_3Si–NC_8H_{11}^+][H–B(C_6F_5)_3^-]$ ion pair (Figure 4.4) and reacted with C–O bond containing substrates at rates that could be comfortably tracked by ^{1}H NMR over 24 hours.

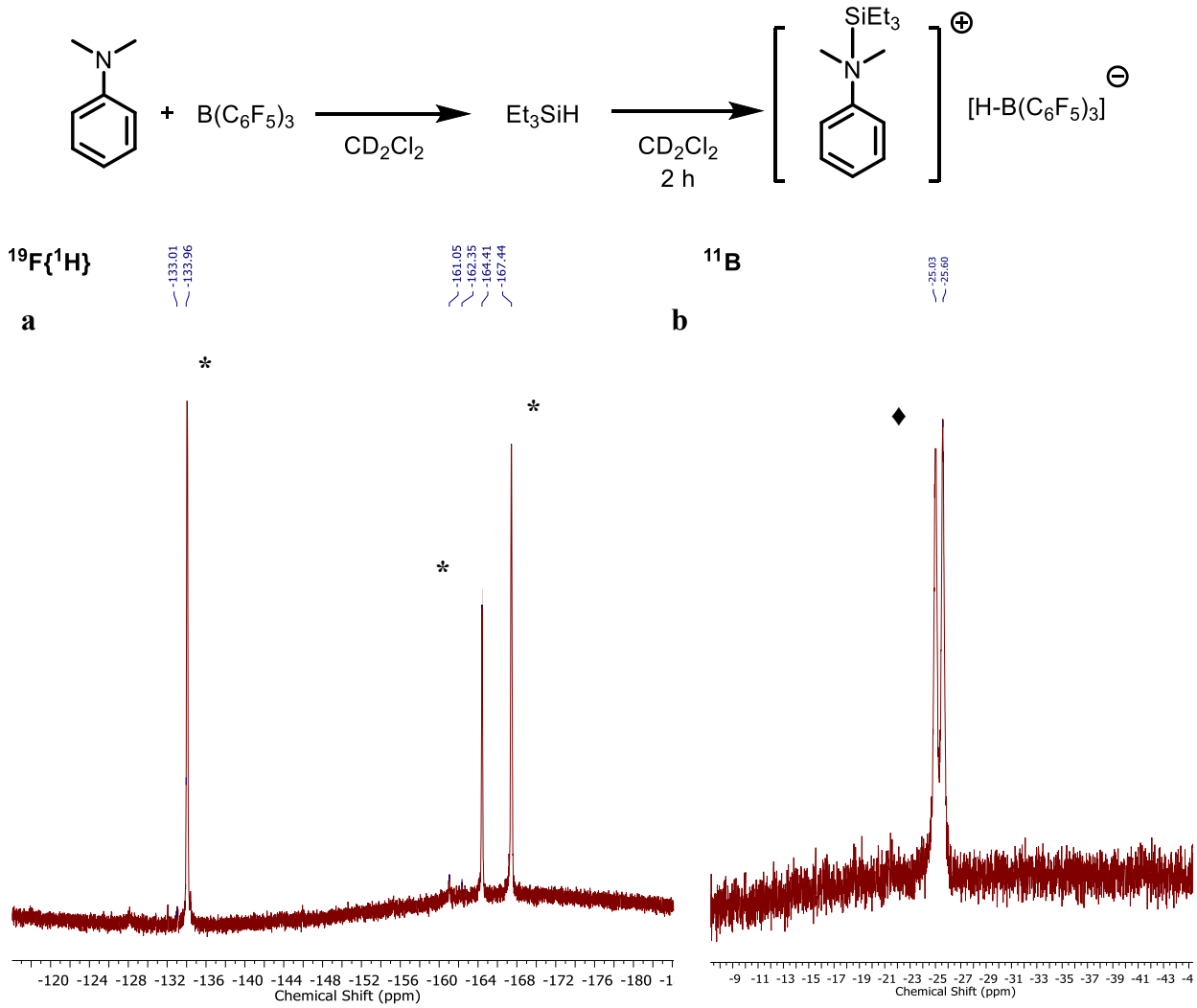

Figure 4.4. Speciation experiment with N,N-dimethylaniline

BCF, Et_3SiH, and N,N-dimethylaniline speciate fully to the ion pair. a. The peaks indicated with (*) correspond to the H–$B(C_6F_5)_3^-$ anion.[54] b. ^{11}B NMR spectrum (proton coupled) of $[Et_3Si–NC_8H_{11})^+][H–B(C_6F_5)_3^-]$. The peak indicated with (♦) corresponds to the H–$B(C_6F_5)_3^-$ anion.[54]

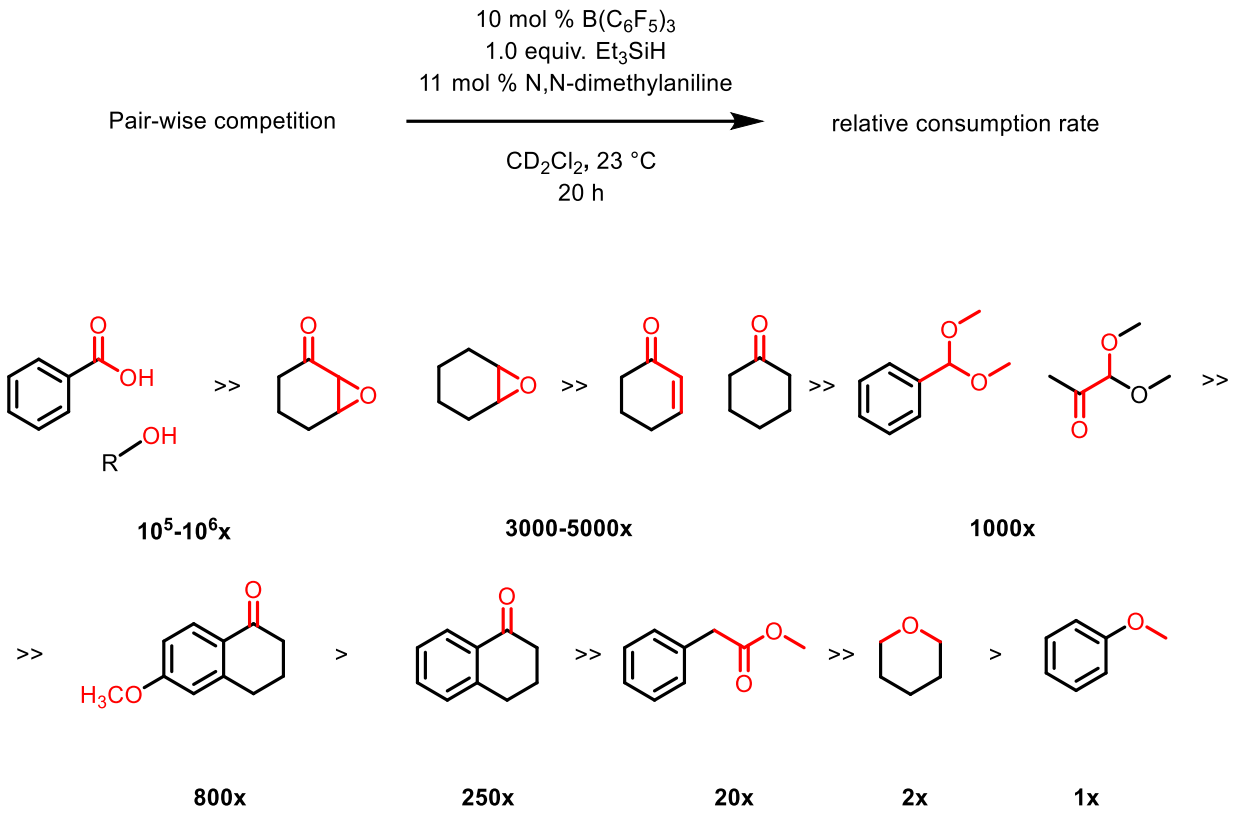

Figure 4.5. Relative rates of substrate consumption via ^{1}H NMR

The trend observed as a result of the conducted NMR experiments is summarized in Figure 4.5. It is immediately apparent that dehydrocoupling of free alcohols and carboxylic acids is much faster than any other reaction. It is estimated to be on the order of 30-50 times faster than the next fastest process. Rapid H_2 gas evolution was observed in the form of bubbling almost immediately after the silane addition in each of the carried-out tests. This observation is corroborated further by the clean dehydrosilylation of the carboxylic acid in natamycin to generate the corresponding silyl ester in a previously reported example (see Chapter 3). In fact, such reactivity can be used to one's advantage in a predictive sense for directed stepwise reduction experiments as illustrated in Figure 4.6. In this example, knowing with certainty that the dehydrocoupling was likely to occur at the carboxylic acid allowed for facile experimental design to generate the shown enol ether product. 2,4.6-BCF and PPh_3 mixture first reacts with Et_2SiH_2 to rapidly evolve H_2 gas, followed by BCF

and PPh_3 addition to the resulting intermediate to form the final product. It is noteworthy that this stepwise reaction occurs without a competitive enoate reduction in the NW corner of the parent molecule, resulting in a novel natamycin derivative in only two simple synthetic steps.[5]

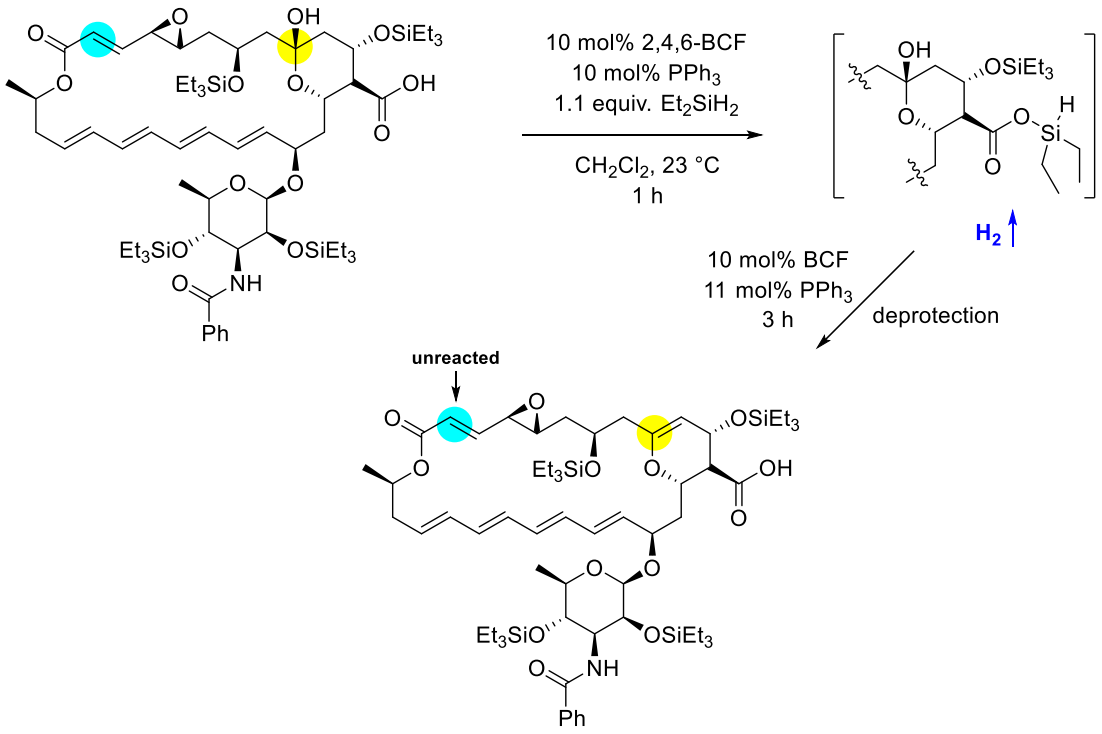

Figure 4.6. Predictive stepwise reactivity example in natamycin

The next most reactive functional groups in Figure 4.5, following the dehydrocoupling of carboxylic acids and alcohols, were epoxides. It is worth noting that less hindered epoxides, such as cyclohexene oxide, generally provided a complex product mixture under the BCF/Et_3SiH conditions. However, adding a Lewis base silylium ion carrier attenuated this reactivity and allowed for successful completion of pairwise NMR experiments.

Epoxides react approximately twice as fast as cyclic ketones, the next class of functional groups found in the natamycin structure. The major product of the cyclic ketone reactions was determined to be the ketone hydrosilylation with minor over-reductions products also detected. Cyclohexenone and cyclohexanone react at similar rates with respect to each other, both being

consumed approximately 3-5 times faster than the tested acetals. Acetals, in turn, are slightly more reactive than the substituted tetralones and significantly (4x) more reactive than the 1-tetralone substrate. Hydrosilylation at the ketone was the major product of the tetralone reactions, with any substituents remaining untouched. When esters were reacted against the tetralones in pairwise competitions, the 1,2-hydrosilylation of the sp^2 carbon was the major reaction for both compounds. The consumption of the tetralone starting materials, however, was about 8-10 times faster than that of the esters.

Finally, the least reactive of the tested functional groups were ethers. Tetrahydropyran (THP) ring-opening reaction is approximately 20 times slower than any of the ester reductions, an observation that can be attributed to the difference between the sp^3 and the sp^2 C–O center reactivity. Electrophilicity difference in these two cases is what is responsible for the slower ether reactivity toward borohydride-induced reduction of the C–O bond. Cyclic ethers in particular are more reactive toward reduction (and ring-opening) than the linear ones, as evidenced by the anisole reduction to CH_4 and the silyl ether being twice as slow as the THP ring-opening.

As can be seen from the results summarized in Figure 4.5, NMR pairwise competition experiments helped establish several key reactivity trends that were previously not explicitly defined in a quantitative manner. The key observations include the fact that dehydrocoupling is faster than any other reaction as well as the fact that sp^2 C–O centers react much faster than the sp^3 ones. Additionally, a large range of reactivity rates was observed (on the order of several thousand), which was a relatively surprising, yet important observation. Ultimately such data can be used to make an informed prediction as to which C–O bond is most likely to react first under BCF/silane reaction conditions when given a more complex substrate or a natural product.

4.3. Competition experiments – GC approach

Despite the general trends established in the NMR experiments providing useful baseline data, utilizing gas chromatography with flame ionization detection (GC-FID) allowed for an even more in-depth comparison within various functional groups. The GC approach also simplified the separation, identification (from retention times), and quantification of the starting materials and the products. To obtain quantitative yields for each compound, calibration plots of relative integrations were constructed for each substrate (see Experimental section). Hexamethylbenzene was used as an internal standard, and the GC-FID spectra were taken at 5 min, 20 min, and 2 h intervals following the silane addition to the competing molecules. Utilizing the FID detector allowed for more rapid reaction tracking, without the need for a Lewis base silylium ion carrier. As such, 10 mol % of the BCF catalyst was used with 1 equivalent of Et_3SiH in toluene.

The utility of the GC data is particularly evident from the in-depth analysis of the epoxide and the cyclic ketone functional group reactivity (Figure 4.7). While the NMR approach estimated both of these to be 3-5 times more reactive than the acetals (the next functional group on the ranking), there is an interesting trend established within the epoxides and the cyclic ketones themselves. Trans-stilbene oxide, for example, is more reactive than cyclohexanone which, in turn, is slightly more reactive than both the cyclohexenone and the terminal epoxide of 1,2-epoxy-5-hexene.

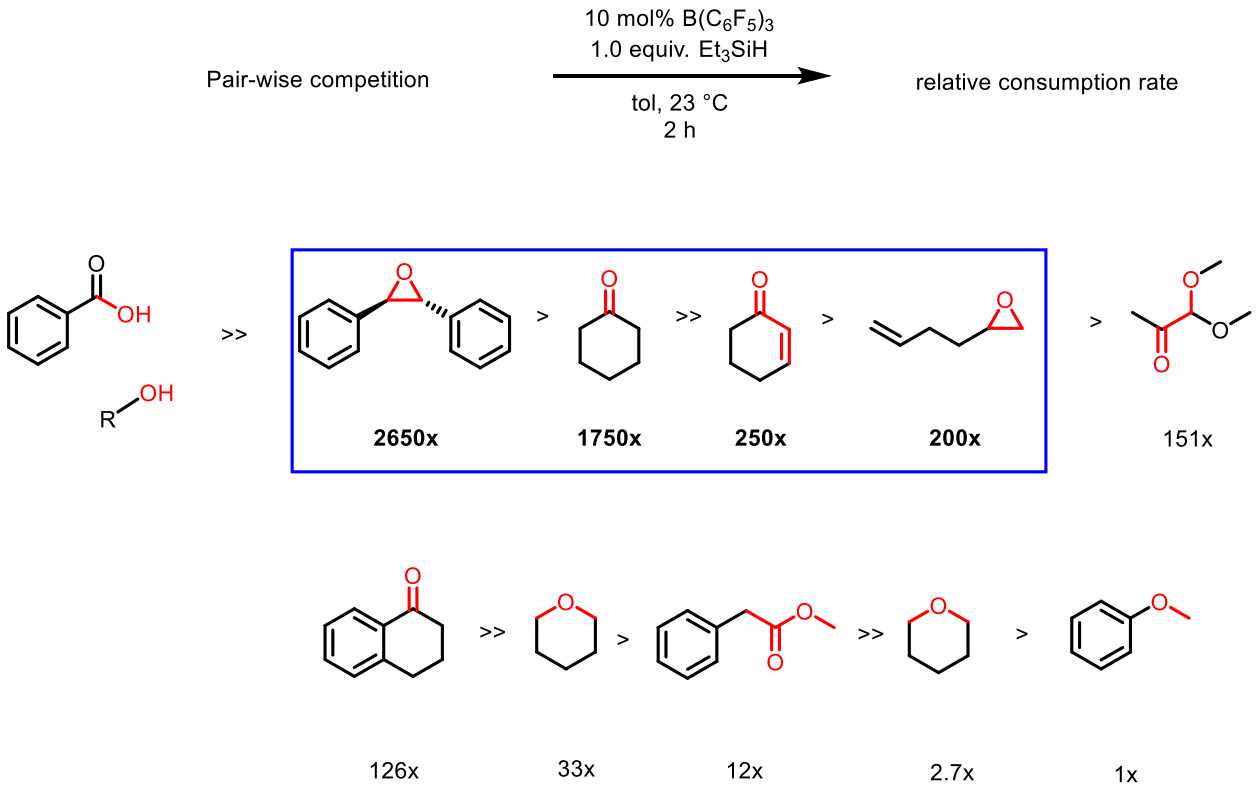

Figure 4.7. Relative rates of substrate consumption via GC-FID

Additionally, the GC approach allowed for a deeper study of the electronic effects responsible for observed reactivity. Within the carboxylic acid substrate class, for example, the chain length of the alkyl group was varied to observe the impact of electron-donating effects of the neighboring aromatic group (Scheme 4.2). In the case of hydrocinnamic and benzoic acid, however, it was observed that regardless of the chain length, the carboxylic acid dehydrocoupling proceeds rapidly with no selectivity.

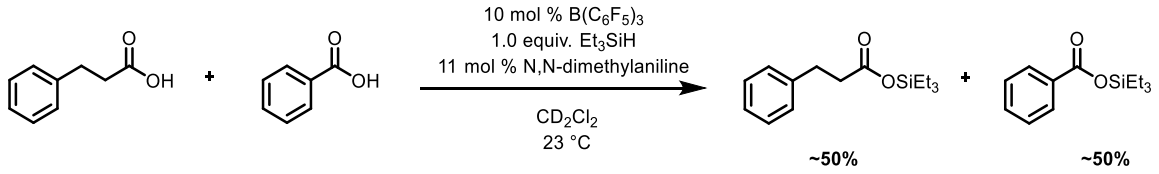

Scheme 4.2. Hydrocinnamic and benzoic acid GC competition experiment

In the tetralone family, the effect of the electron-donating methoxy group was probed by comparing 1-tetralone to its 6-methoxy-1-tetralone derivative. Since the 6-methoxy-1-tetralone was consumed at a rate approximately 3 times greater than 1-tetralone, several conclusions can be drawn. The increased Lewis basicity of the ketone oxygen in the 6-methoxy-1-tetralone versus the unsubstituted compound is responsible for the propensity of this substrate to attack the silylium ion to generate the key silyl oxonium intermediate. As such, the carbonyl oxygen attack at silicon must be the rate-determining step in this reaction, with the most Lewis basic sites reacting first.

The ether family of substrates also exhibited several interesting reactivity trends upon a deeper analysis of the GC data (Figure 4.8). Simple cyclic ethers with fairly Lewis basic oxygens, such as THP, are reduced faster to the ring-opened products than either the anisole or ethoxybenzene molecules. While anisole reacted slower when compared to THP, further increasing the alkyl chain length next to the aromatic ring resulted in an even more sluggish reaction, as demonstrated by ethoxybenzene being consumed 1.7 times slower than anisole. Due to the increased steric bulk associated with the secondary carbon of ethoxybenzene, ethane product formation for this substrate is less favored than that of methane in the anisole case.

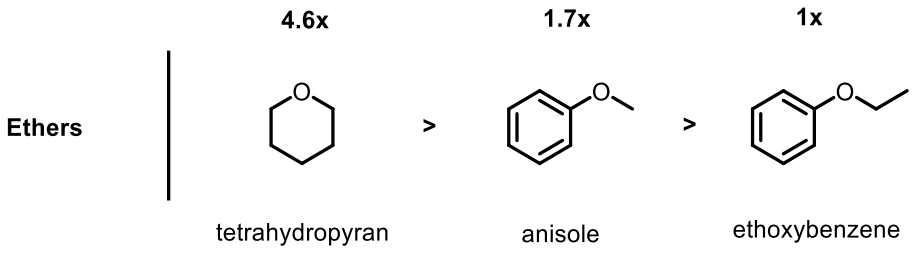

Figure 4.8. Comparative ether family reactivity data

After establishing the reactivity ranking outlined in Figures 4.5 and 4.7, several additional experiments were carried out to determine how changing the catalyst or the reductant influences

the observed trends. One such experiment involved changing the traditionally used BCF catalyst to $MesB(C_6F_5)_2$ derivative synthesized via a previously reported procedure.[81] Due to its significantly lower Lewis acidity, this catalyst was much less reactive in combination with Et_3SiH and a given substrate even in the absence of a Lewis basic silylium carrier. Despite the slower overall reaction, however, the reactivity trends established above still held true. For example, both the cyclohexanone (14.9x) and the 1,1-dimethylglyoxal acetal (1.2x) were more reactive than 1-tetralone, suggesting that changing the catalyst keeps the same magnitude of relative rates as the BCF-catalyzed systems (Scheme 4.3).

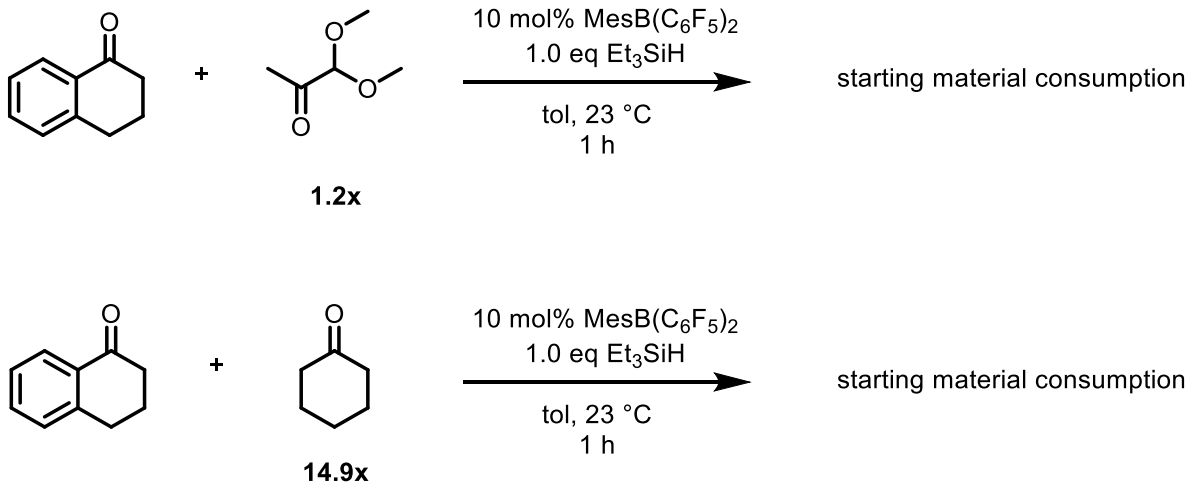

Scheme 4.3. Comparative reactivity data for $MesB(C_6F_5)_2$ catalyst

Similarly, changing the silane to the traditionally more reactive Me_2EtSiH or the stereoelectronically different Ph_3SiH maintained similar comparative results.

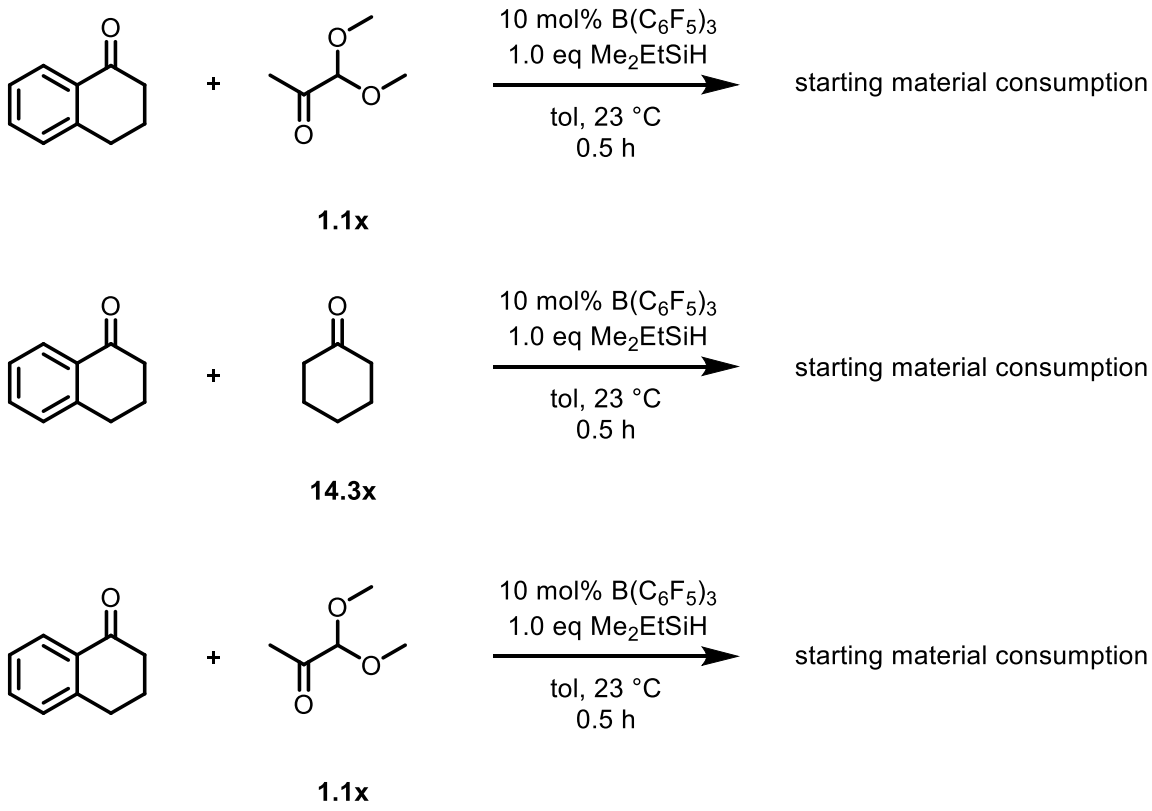

Scheme 4.4. Comparative reactivity data for Me_2EtSiH and Ph_3SiH reductants

4.4. Results in the context of natamycin experiments

While the data reported in this chapter is important and useful presented as such, it is worth recalling that complex natural products, and in particular the structurally diverse natamycin molecule, served as the initial inspiration for these experiments. Putting the obtained results in the context of natamycin reactivity, several interesting observations can be made. Since free carboxylic acids are the most reactive functional group, one would predict rapid dehydrocoupling of the natamycin carboxylic acid to occur first (see Figure 4.6), followed by reactivity at the epoxide, hydrosilylation of the ester, and finally the hemi-acetal reduction. However, under the reported reaction conditions (Figure 4.9), all of the above reactivity predictions hold true except the epoxide reactivity.[5]

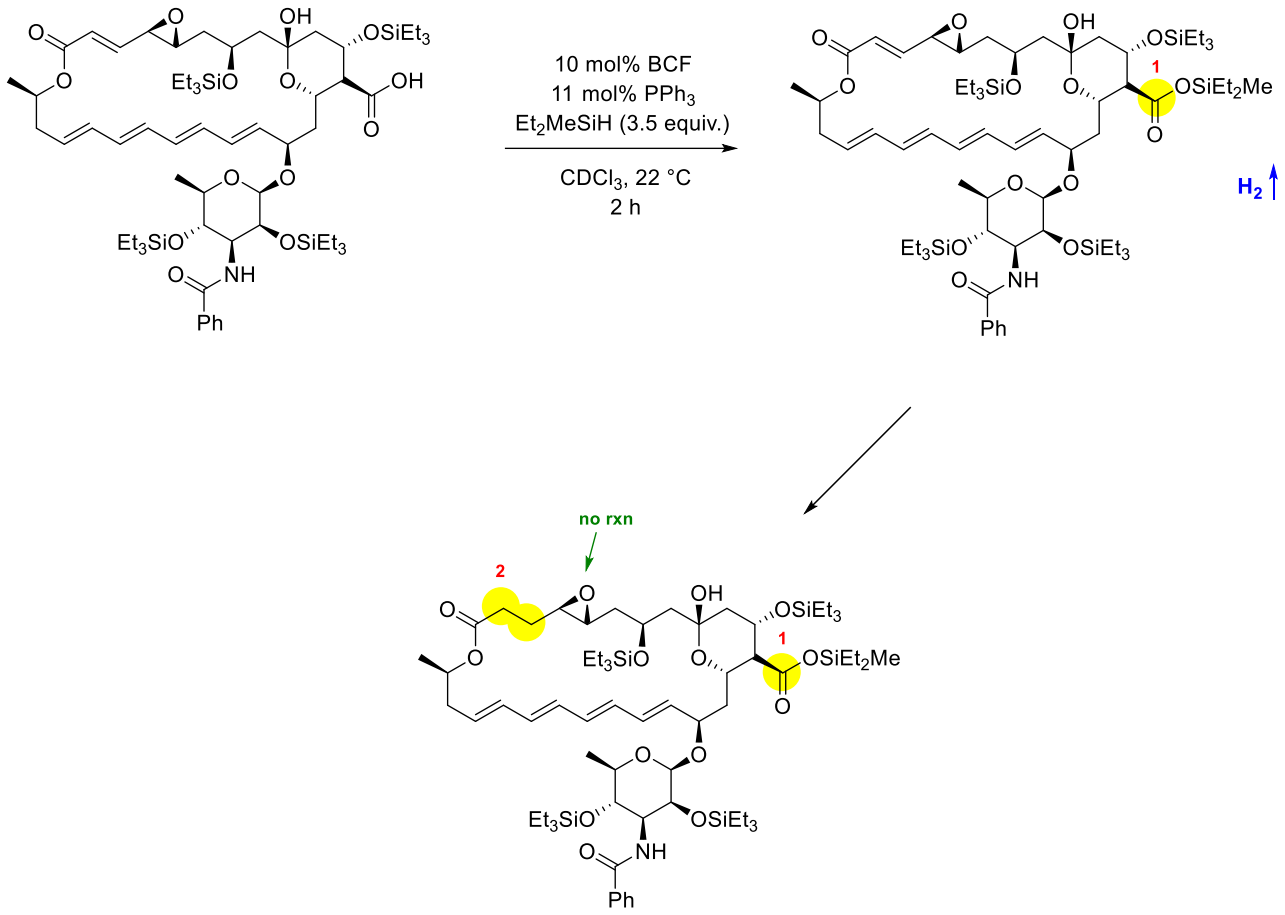

Figure 4.9. Functional group reactivity order in natamycin

As expected, when BCF and PPh_3 combination is used, the first equivalent of Et_2MeSiH is consumed to firm a silyl ester at the carboxylic acid. The second equivalent, however, hydrosilylates the enoate in the NW corner of the molecule instead of reacting with the adjacent epoxide. This disconnect with respect to the competition experiment data suggests than the epoxide in natamycin lies buried within the structure and is thus inaccessible for the generation of a silyl-oxonium cation. This observation raises the important question of whether certain functionalities are inherently less reactive for a given catalytic system or may lie buried within complex natural product scaffolds. As such, it is always essential to consider the three-dimensional structures of the chosen substrates prior to making assumptions regarding their expected reactivity.

When it comes to completely altering the catalyst/reductant pairs, it is also important to consider the changes in baseline reactivity trends. For example, amide functional groups are unreactive with BCF/trialkylsilanes combinations, but when one of three pentafluorophenyl rings on BCF is exchanged for an alkyl chain (i.e. *trans*-3-hexene **3-hex-B** based catalyst, Scheme 4.5), amide reduction proceeds with excellent chemoselectivity.[82] The reactivity rankings, therefore, may change given the diversity of potential outcomes observed in natamycin reactions under different catalytic conditions.

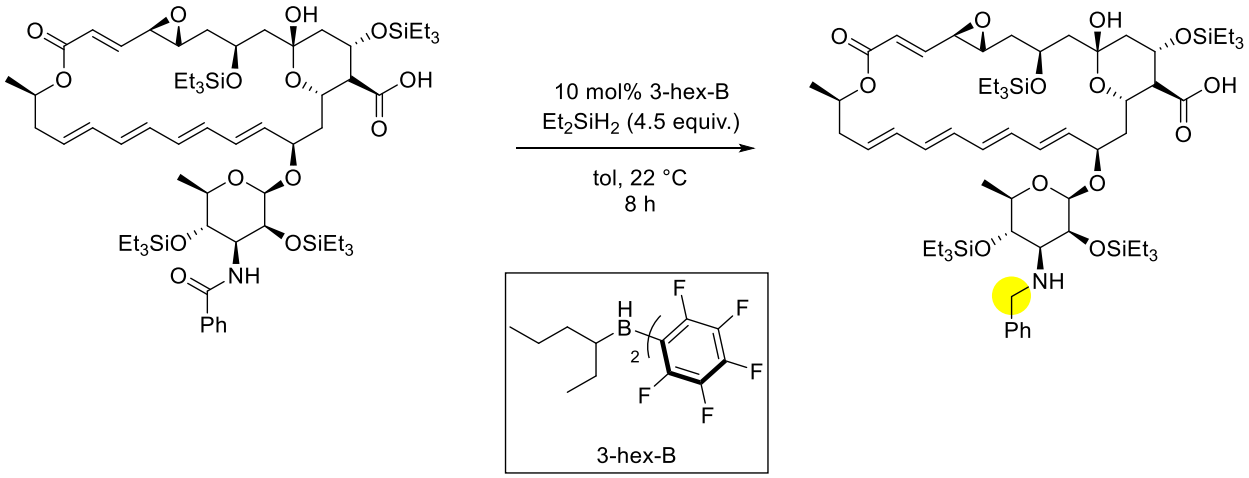

Scheme 4.5. Chemoselective amide reduction in natamycin

4.5. Conclusions

In summary, a reactivity series was established for various functional groups with the BCF/silane catalytic system that is generally utilized in late-stage natural product functionalization chemistry. Using gibberellic acid and natamycin natural products as inspiration for the ranking, small molecules of varying diversity were tested in pairwise competition experiments, with the results quantified by either NMR or GC-FID. The obtained reactivity series was used to illustrate the predictive power of site-selective functional group modifications, with the trends generally holding true. The noted inconsistencies of the series can be attributed to the structural attributes of

a given natural product, highlighting the importance of structural complexity influencing reactivity trends. Ultimately, the reported data can be used to predict the most likely reactive sites with the BCF/Et_3SiH catalytic system and also to assess which different catalysts and reductants may exhibit diverging LSF behavior.

4.6 Experimental section

For complex natural products discussed in this Chapter, namely natamycin, full comprehensive NMR and Mass Spectrometry data has been previously published and reported in the following publications.[5,82]

4.6.1. General experimental considerations – NMR

In a nitrogen-filled glovebox atmosphere at room temperature, 10 mol % of BCF catalyst, 2.7 mg hexamethylbenzene (HMB) internal standard, and 0.5 mL CD_2Cl_2 were added to a 1-dram vial. The chosen substrates (1 equiv.) were then added to the same vial and the mixture was transferred to a septum-capped NMR tube. Upon initial ^1H NMR spectrum collection, 1 equivalent of Et_3SiH was added by syringe via the septum cap and the tube was immediately placed into the spectrometer to acquire a ^1H NMR spectrum at approximately 5 minutes after silane addition. ^1H NMR was then tracked after 2 h, 12 h, and 24 h intervals to observe the starting material disappearance. Each of the starting material peak areas compared to the constant internal standard integration, providing quantitative data.

4.6.2. General experimental considerations – GC-FID

In a nitrogen-filled glovebox atmosphere at room temperature, 10 mol % of BCF catalyst, 2.7 mg hexamethylbenzene (HMB) internal standard, and 0.4 mL of toluene were added to a 1-dram vial. The chosen substrates (1 equiv. each) were then added to the same vial and the mixture was transferred to a GC vial and sealed with a septum cap. In a separate 1-dram vial, 1 equiv. of

Et_3SiH was dissolved in 0.1 mL of toluene and the vial was capped with a septum cap and transferred outside of the glovebox. After an initial GC-FID chromatogram was obtained for the mixture of starting materials, the silane was added via syringe to the GC vial containing both substrates and the GC-FID spectra were acquired at 5 min, 20 min, and 2 h intervals.

To obtain quantitative data for each reaction, a calibration curve was constructed for each of the individual substrates analyzed. The integrations of the peak areas were taken with respect to an internal standard, hexamethylbenzene. Calibration curves can be found below.

Table 4.1 Trans-stilbene oxide raw GC data

Trans-stilbene oxide			
[sub] mM	[std] mM	Area substrate	Area standard
160	15.63	8835.9	801.15
130	15.63	7104.4	784.99
110	15.63	6087.7	797.69
80	15.63	4317.8	816.00
50	15.63	2634.9	808.45
[s]/[std]	$A_{substrate}/A_{standard}$		
10.237	11.029		
8.3173	9.0503		
7.0377	7.6315		
5.1183	5.2914		
3.1989	3.2592		

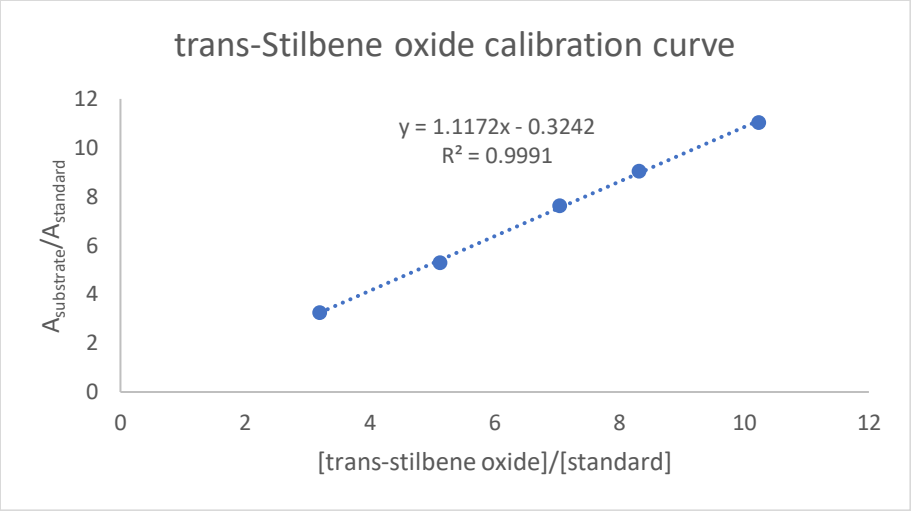

Figure 4.10. Trans-stilbene oxide calibration curve

Table 4.2. Cyclohexanone raw GC data

Cyclohexanone			
[sub] mM	[std] mM	Area substrate	Area standard
160	14.261	4195.0	826.21
130	14.261	3321.9	818.62
110	14.261	2819.5	823.71
80	14.261	2050.0	801.90
50	14.261	1311.3	825.48
[s]/[std]	$A_{substrate}/A_{standard}$		
11.21941	5.0774		
9.11577	4.0580		
7.713344	3.4229		
5.609705	2.5564		
3.506065	1.5885		

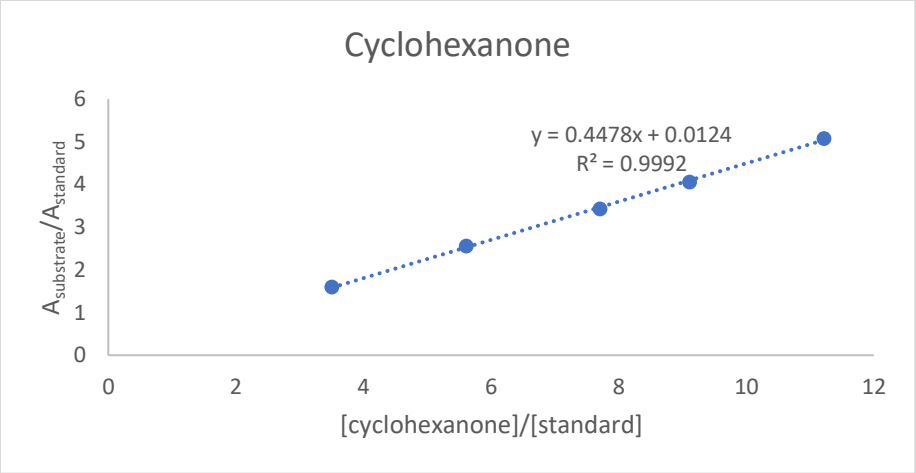

Figure 4.11. Cyclohexanone calibration curve

Table 4.3. Cyclohexeone raw GC data

Cyclohexenone			
[sub] mM	[std] mM	Area substrate	Area standard
160	14.261	3729.5	802.10
130	14.261	3246.6	851.51
110	14.261	2244.5	762.66
80	14.261	1726.7	774.97
50	14.261	1033.8	748.35
[s]/[std]	$A_{substrate}/A_{standard}$		
11.219	4.6497		
9.1158	3.8128		
7.7133	2.9430		
5.6097	2.2281		
3.5061	1.3814		

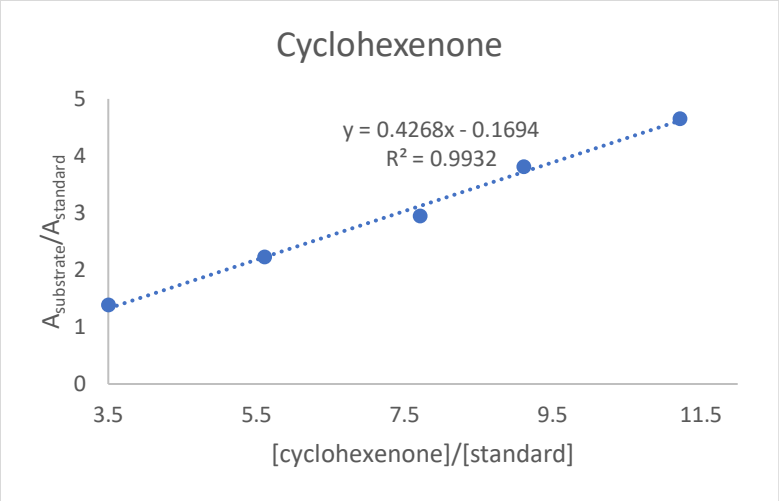

Figure 4.12. Cyclohexenone calibration curve

Table 4.4. 1,2-epoxy-5-hexene raw GC data

1,2-epoxy-5-hexene			
[sub] mM	[std] mM	Area substrate	Area standard
160	15.630	3258.1	848.30
130	15.630	3344.2	1009.8
110	15.630	2521.4	894.10
80	15.630	1861.9	884.10
50	15.630	1148.1	925.12
[s]/[std]	$A_{substrate}/A_{standard}$		
10.236	3.8407		
8.3173	3.3117		
7.0377	2.8200		
5.1184	2.1060		
3.1990	1.2410		

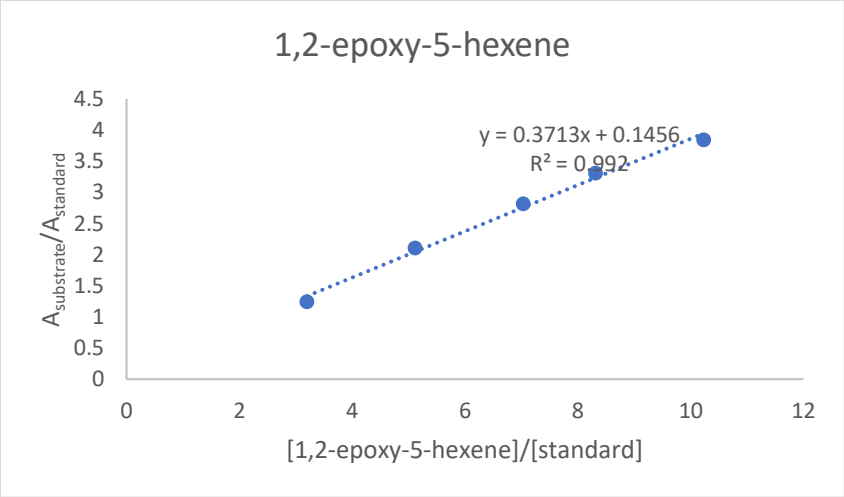

Figure 4.13. 1,2-epoxy-5-hexene calibration curve

Table 4.5. 1,1-dimethylglyoxal acetal raw GC data

1,1-dimethylglyoxal acetal			
[sub] mM	[std] mM	Area substrate	Area standard
160	15.630	1901.3	773.80
130	15.630	1522.4	802.30
110	15.630	1330.4	793.42
80	15.630	953.57	820.81
50	15.630	561.08	849.31
[s]/[std]	$A_{substrate}/A_{standard}$		
10.237	2.4571		
8.3173	1.8975		
7.0377	1.6768		
5.1183	1.1617		
3.1990	0.66063		

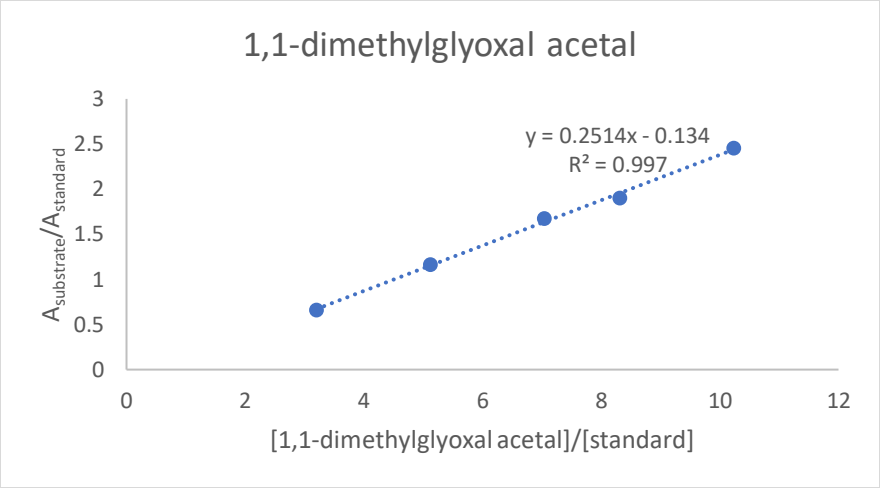

Figure 4.14. 1,1-dimethylglyoxal acetal calibration curve

Table 4.6. 1-tetralone raw GC data

1-tetralone			
[sub] mM	[std] mM	Area substrate	Area standard
160	14.261	6644.8	837.20
130	14.261	5846.9	888.50
110	14.261	4562.1	813.00
80	14.261	3291.7	838.40
50	14.261	2169.5	883.90
[s]/[std]	$A_{substrate}/A_{standard}$		
11.219	7.9369		
9.1158	6.5807		
7.7133	5.6114		
5.6097	3.9262		
3.5061	2.4544		

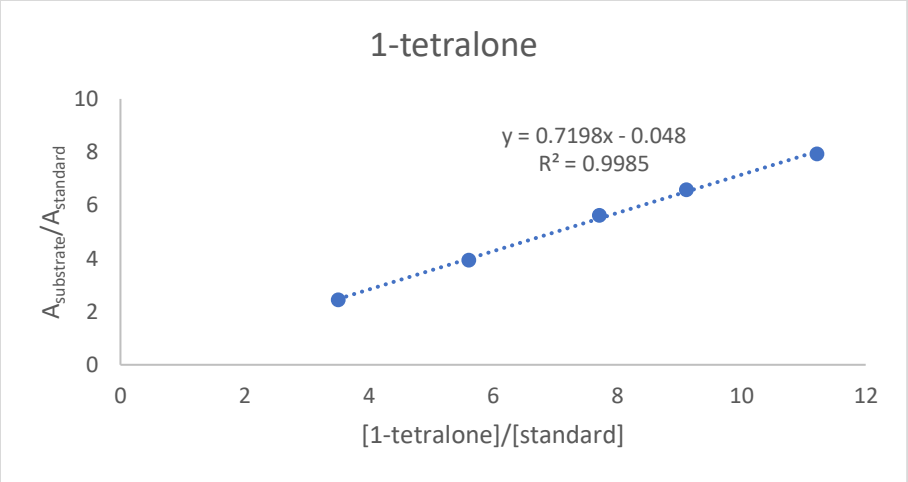

Figure 4.15. 1-tetralone calibration curve

Table 4.7. 6-methoxy-1-tetralone raw GC data

6-methoxy-1-tetralone			
[sub] mM	[std] mM	Area substrate	Area standard
160	15.630	6200.9	740.18
130	15.630	4966.1	767.53
110	15.630	4207.0	755.45
80	15.630	2990.9	786.65
50	15.630	1823.9	793.50
[s]/[std]	$A_{substrate}/A_{standard}$		
10.237	8.3776		
8.3173	6.4703		
7.0377	5.5689		
5.1184	3.8021		
3.1990	2.2987		

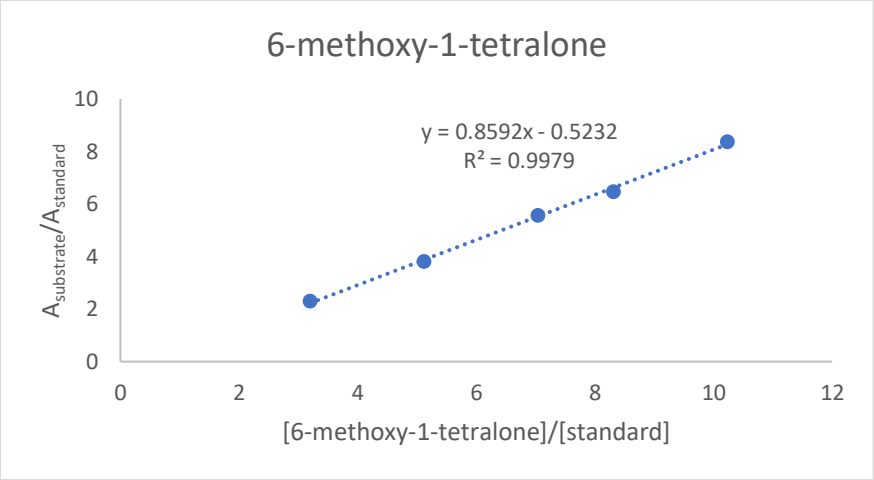

Figure 4.16. 6-methoxy-1-tetralone calibration curve

Table 4.8. Methyl phenyl acetate raw GC data

Methyl Phenyl Acetate			
[sub] mM	[std] mM	Area substrate	Area standard
160	14.261	6247.8	792.30
130	14.261	4947.7	791.90
110	14.261	3771.9	720.98
80	14.261	2679.3	654.40
50	14.261	1633.4	718.20
[s]/[std]	$A_{substrate}/A_{standard}$		
11.219	7.8857		
9.1158	6.2479		
7.7133	5.2316		
5.6097	4.0943		
3.5061	2.2743		

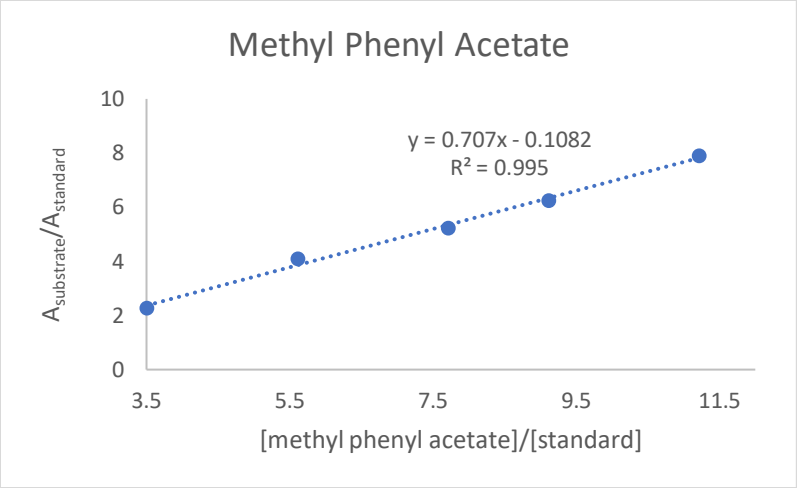

Figure 4.17. Methyl phenyl acetate calibration curve

Table 4.9. Tetrahydropyran raw GC data

Tetrahydropyran			
[sub] mM	[std] mM	Area substrate	Area standard
160	15.630	2919.7	822.70
130	15.630	2634.3	913.60
110	15.630	2253.1	928.90
80	15.630	1539.3	897.20
50	15.630	1021.6	921.00
[s]/[std]	$A_{substrate}/A_{standard}$		
10.237	3.5489		
8.3173	2.8834		
7.0377	2.4256		
5.1184	1.7157		
3.1990	1.1092		

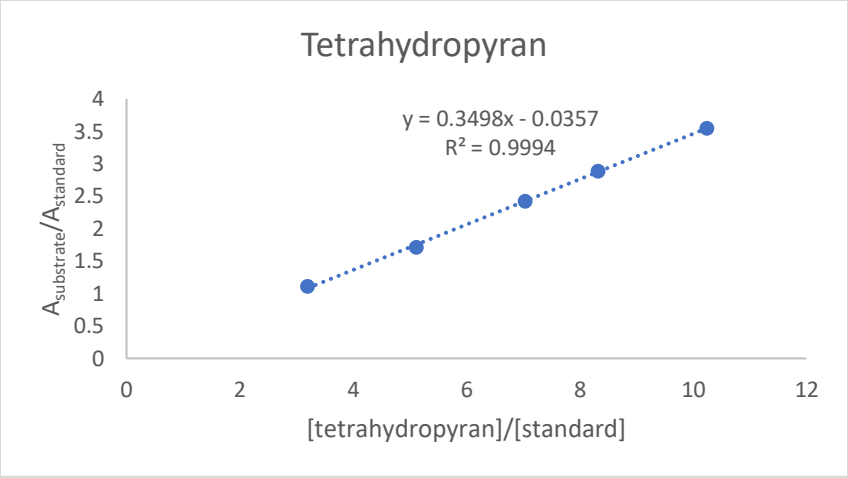

Figure 4.18. Tetrahydropyran calibration curve

Table 4.10. Anisole raw GC data

Anisole			
[sub] mM	[std] mM	Area substrate	Area standard
160	15.630	4658.4	901.30
130	15.630	3880.3	911.90
110	15.630	3465.9	942.20
80	15.630	2531.2	974.30
50	15.630	1280.3	873.90
[s]/[std]	$A_{substrate}/A_{standard}$		
10.23672	5.1685		
8.317338	4.2552		
7.037748	3.6785		
5.118362	2.5980		
3.198976	1.4650		

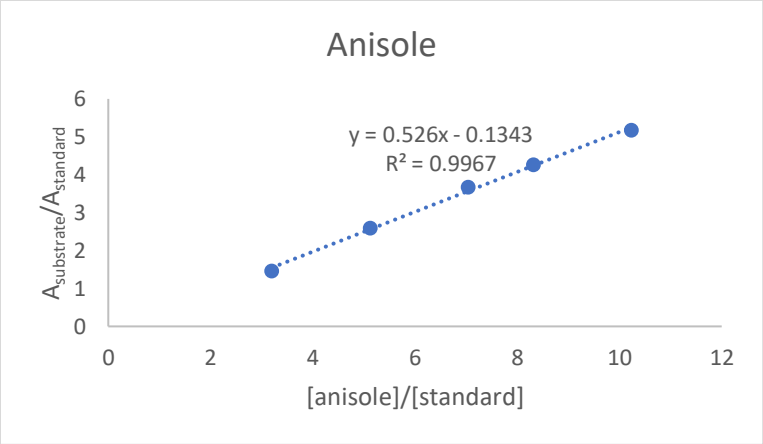

Figure 4.19. Anisole calibration curve

Table 4.11. Ethoxybenzene raw GC data

Ethoxybenzene			
[sub] mM	[std] mM	Area substrate	Area standard
160	14.261	6201.3	764.40
130	14.261	5106.1	760.16
110	14.261	4598.0	858.82
80	14.261	3175.6	810.66
50	14.261	1914.7	887.18
[s]/[std]	$A_{substrate}/A_{standard}$		
11.219	8.1127		
9.1158	6.7171		
7.7133	5.3538		
5.6097	3.9173		
3.506`	2.1582		

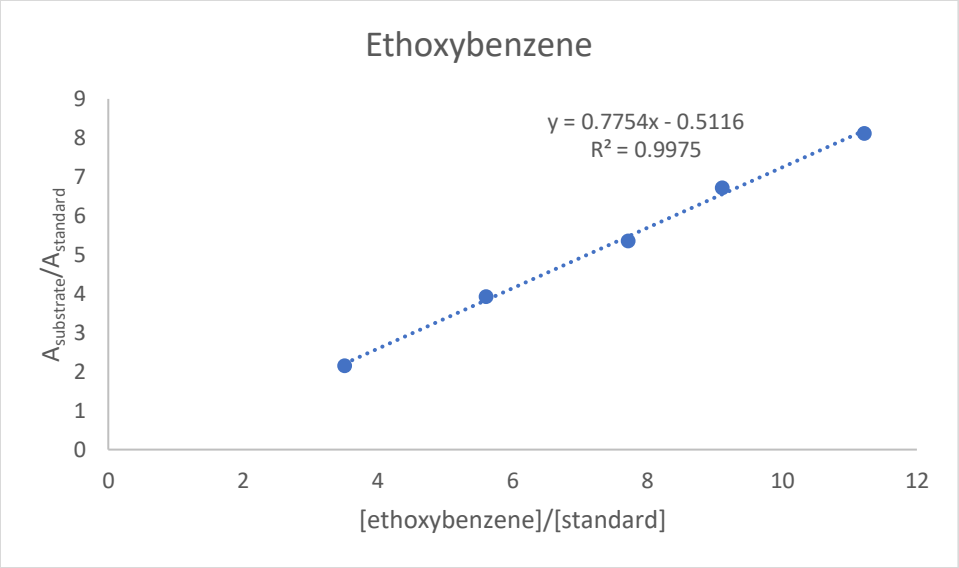

Figure 4.20. Ethoxybenzene calibration curve

REFERENCES

(1) Peng, L.; Lin, L.; Zhang, J.; Shi, J.; Liu, S. *Appl. Catal. A Gen.* **2011**, *397*, 259–265.

(2) Kuo, C.-H.; Poyraz, A. S.; Jin, L.; Meng, Y.; Pahalagedara, L.; Chen, S.-Y.; Kriz, D. A.; Guild, C.; Gudz, A.; Suib, S. L. *Green Chem.* **2014**, *16*, 785.

(3) Adduci, L. L.; Bender, T. A.; Dabrowski, J. A.; Gagné, M. R. *Nat. Chem.* **2015**, *7*, 576–581.

(4) Karimov, R. R.; Sharma, A.; Hartwig, J. F. *ACS Cent. Sci.* **2016**, *2*, 715–724.

(5) Bender, T. A.; Payne, P. R.; Gagné, M. R. *Nat. Chem.* **2018**, *10*, 85–90.

(6) Seo, Y.; Gudz, A.; Lowe, J. M.; Gagné, M. R. *Tetrahedron* **2019**, *75*, 130712.

(7) Bender, T. A.; Dabrowski, J. A.; Gagné, M. R. *Nat. Rev. Chem.* **2018**, *2*, 35–46.

(8) Chheda, J. N.; Huber, G. W.; Dumesic, J. A. *Angew. Chemie Int. Ed.* **2007**, *46*, 7164–7183.

(9) Huber, G. W. *Science.* **2005**, *308*, 1446–1450.

(10) Metzger, J. O. *Angew. Chemie Int. Ed.* **2006**, *45*, 696–698.

(11) Liu, Dajiang Chen, E. Y. X. *ACS Catal.* **2014**, *4*, 1302–1310.

(12) Liu, D.; Chen, E. Y. X. *ChemSusChem* **2013**, *6*, 2236–2239.

(13) Shiramizu, M.; Toste, F. D. *Angew. Chemie Int. Ed.* **2012**, *51*, 8082–8086.

(14) Adlington, M. G.; Orfanopoulos, M.; Fry, J. L. *Tetrahedron Lett.* **1976**, *17*, 2955–2958.

(15) Corma Canos, A.; Iborra, S.; Velty, A. *Chem. Rev.* **2007**, *107*, 2411–2502.

(16) Fry, J. L.; Orfanopoulos, M.; Adlington, M. G.; Dittman, W. P.; Silverman, S. B. *J. Org. Chem.* **1978**, *43*, 374–375.

(17) Adduci, L. L.; McLaughlin, M. P.; Bender, T. a.; Becker, J. J.; Gagné, M. R. *Angew. Chemie - Int. Ed.* **2014**, *53*, 1646–1649.

(18) Bender, T. A.; Dabrowski, J. A.; Gagné, M. R. *Nat. Rev. Chem.* **2018**, *2*, 35–46.

(19) Parks, D. J.; Piers, W. E. *J. Am. Chem. Soc.* **1996**, *118*, 9440–9441.

(20) Piers, W. E.; Chivers, T. *Chem. Soc. Rev.* **1997**, *26*, 345.

(21) Gevorgyan, V.; Rubin, M.; Benson, S.; Liu, J. X.; Yamamoto, Y. *J. Org. Chem.* **2000**, *65*, 6179–6186.

(22) Parks, D. J.; Blackwell, J. M.; Piers, W. E. *J. Org. Chem.* **2000**, *65*, 3090–3098.

(23) Gudz, A.; Payne, P. R.; Gagné, M. R. *Organometallics* **2017**, *36*, 4047–4053.

(24) Bézier, D.; Park, S.; Brookhart, M. *Org. Lett.* **2013**, *15*, 496–499.

(25) Houghton, A. Y.; Hurmalainen, J.; Mansikkamäki, A.; Piers, W. E.; Tuononen, H. M. *Nat. Chem.* **2014**, *6*, 983–988.

(26) Rendler, S.; Oestreich, M. *Angew. Chemie - Int. Ed.* **2008**, *47*, 5997–6000.

(27) Sakata, K.; Fujimoto, H. *J. Org. Chem.* **2013**, *78*, 12505–12512.

(28) Stephan, D. W.; Erker, G. *Angew. Chemie - Int. Ed.* **2015**, *54*, 6400–6441.

(29) Oestreich, M.; Hermeke, J.; Mohr, J. *Chem. Soc. Rev.* **2015**, *44*, 2202–2220.

(30) Stephan, D. W. *Org. Biomol. Chem.* **2008**, *6*, 1535.

(31) Stephan, D. W. *Science.* **2016**, *354*, 7229.

(32) Chen, D.; Leich, V.; Pan, F.; Klankermayer, J. *Chem. - A Eur. J.* **2012**, *18*, 5184–5187.

(33) Heshmat, M.; Privalov, T. *Chem. - A Eur. J.* **2017**, *23*, 1–17.

(34) Scott, D. J.; Fuchter, M. J.; Ashley, A. E. *J. Am. Chem. Soc.* **2014**, *136*, 15813–15816.

(35) Greb, L.; Tussing, S.; Schirmer, B.; Oña-Burgos, P.; Kaupmees, K.; Lõkov, M.; Leito, I.; Grimme, S.; Paradies, J. *Chem. Sci.* **2013**, *4*, 2788–2796.

(36) Mewald, M.; Oestreich, M. *Chem. - A Eur. J.* **2012**, *18*, 14079–14084.

(37) Zhu, X.; Du, H. *Org. Biomol. Chem.* **2015**, *13*, 1013–1016.

(38) Gandhamsetty, N.; Park, S.; Chang, S. *J. Am. Chem. Soc.* **2015**, *137*, 15176–15184.

(39) Blackwell, J. M.; Morrison, D. J.; Piers, W. E. *Tetrahedron* **2002**, *58*, 8247–8254.

(40) Drosos, N.; Ozkal, E.; Morandi, B. *Synlett* **2016**, *27*, 1760–1764.

(41) Bender, T. A.; Dabrowski, J. A.; Zhong, H.; Gagné, M. R. *Org. Lett.* **2016**, *18*, 4120–4123.

(42) Chatterjee, I.; Porwal, D.; Oestreich, M. *Angew. Chemie - Int. Ed.* **2017**, *56*, 3389–3391.

(43) Ren, X.; Du, H. *J. Am. Chem. Soc.* **2016**, *138*, 810–813.

(44) Ren, X.; Li, G.; Wei, S.; Du, H. *Org. Lett.* **2015**, *17*, 990–993.

(45) Weicker, S. A.; Stephan, D. W. *Chem. - A Eur. J.* **2015**, *21*, 13027–13034.

(46) Holthausen, M. H.; Bayne, J. M.; Mallov, I.; Dobrovetsky, R.; Stephan, D. W. *J. Am. Chem. Soc.* **2015**, *137*, 7298–7301.

(47) Herrington, T. J.; Ward, B. J.; Doyle, L. R.; McDermott, J.; White, A. J. P.; Hunt, P. A.; Ashley, A. E. *Chem. Commun. (Camb).* **2014**, *50*, 12753–12756.

(48) Seo, Y.; Gudz, A.; Lowe, J. M.; Gagné, M. R. *Tetrahedron* **2019**, *75*, 130712.

(49) Jordan, P. A.; Miller, S. J. *Angew. Chemie - Int. Ed.* **2012**, *51*, 2907–2911.

(50) Yoganathan, S.; Miller, S. J. *J. Med. Chem.* **2015**, *58*, 2367–2377.

(51) Dai, X. J.; Li, C. J. *J. Am. Chem. Soc.* **2016**, *138*, 5433–5440.

(52) Fasano, V.; Radcliffe, J. E.; Ingleson, M. J. *ACS Catal.* **2016**, *6*, 1793–1798.

(53) Dryzhakov, M.; Hellal, M.; Wolf, E.; Falk, F. C.; Moran, J. *J. Am. Chem. Soc.* **2015**, *137*, 9555–9558.

(54) Longobardi, L. E.; Mahdi, T.; Stephan, D. W. *Dalt. Trans.* **2015**, *44*, 7114–7117.

(55) Henderson, W. A.; Streuli, C. A. *J. Am. Chem. Soc.* **1960**, *82*, 5791–5794.

(56) Welch, G. C.; Holtrichter-Roessmann, T.; Stephan, D. W. *Inorg. Chem.* **2008**, *47*, 1904–1906.

(57) Frisch, M. J.; Trucks, G.W.; Schlegel, H. B.; Scuseria, G. E.; Robb, M. A.; Cheeseman, J. R.; Scalmani, G.; Barone, V.;Mennucci, B.; Petersson, G. A.; Nakatsuji, H.; Caricato, M.; Li, X.; Hratchian, H. P.; Izmaylov, A. F.; Bloino, J.; Zheng, G.; Sonnenber, D. J. *Gaussian, Inc. Wallingford CT* **2009**.

(58) Zhao, Y.; Truhlar, D. G. *Theor. Chem. Acc.* **2008**, *120*, 215–241.

(59) Hehre, W. J.; Radom, L.; Schleyer, P. v. R.; Pople, J. A. *Ab Initio Molecular Orbital Theory*; Wiley: New York, 1986.

(60) Miertuš, S.; Scrocco, E.; Tomasi, J. *Chem. Phys.* **1981**, *55*, 117–129.

(61) Huigens III, R. W.; Morrison, K. C.; Hicklin, R. W.; Flood Jr, T. A.; Richter, M. F.; Hergenrother, P. J. *Nat. Chem.* **2013**, *5*, 195–202.

(62) Hamasaka, G.; Tsuji, H.; Uozumi, Y. *Synlett* **2015**, *26*, 2037–2041.

(63) Yin, Q.; Kemper, S.; Klare, H. F. T.; Oestreich, M. *Chem. - A Eur. J.* **2016**, *22*, 13840–13844.

(64) Lawson, J. R.; Wilkins, L. C.; Melen, R. L. *Chem. - A Eur. J.* **2017**, *23*, 10997–11000.

(65) Seo, Y.; Lowe, J. M.; Gagné, M. R. *ACS Catal.* **2019**, 6648–6652.

(66) Lowe, J. M.; Seo, Y.; Gagné, M. R. *ACS Catal.* **2018**, *8*, 8192–8198.

(67) Heiden, Z. M.; Lathem, A. P. *Organometallics* **2015**, *34*, 1818–1827.

(68) Sivaev, I. B.; Bregadze, V. I. *Coord. Chem. Rev.* **2014**, *270–271*, 75–88.

(69) MacK, D. J.; Guo, B.; Njardarson, J. T. *Chem. Commun.* **2012**, *48*, 7844–7846.

(70) Bender, T. A.; Dabrowski, J. A.; Gagné, M. R. *ACS Catal.* **2016**, *6*, 8399–8403.

(71) Wu, M.-J.; Wu, D.-M.; Chen, J.-B.; Zhao, J.-F.; Gong, L.; Gong, Y.-X.; Li, Y.; Yang, X.-D.; Zhang, H. *Bioorg. Med. Chem. Lett.* **2018**, *28*, 2543–2549.

(72) Bon, D. J.-Y. D.; Mander, L. N.; Lan, P. *J. Org. Chem.* **2018**, *83*, 6566–6572.

(73) Chen, S.-H.; Farina, V. In *Taxane Anticancer Agents*; 1994; pp 247–261.

(74) Mo, X.; Morgan, T. D. R.; Ang, H. T.; Hall, D. G. *J. Am. Chem. Soc.* **2018**, *140*, 5264–5271.

(75) Vuković, V. D.; Richmond, E.; Wolf, E.; Moran, J. *Angew. Chemie* **2017**, *129*, 3131–3135.

(76) Dryzhakov, M.; Richmond, E.; Moran, J. *Synthesis (Stuttg).* **2016**, *48*, 935–959.

(77) Wolf, E.; Richmond, E.; Moran, J. *Chem. Sci.* **2015**, *6*, 2501–2505.

(78) Richmond, E.; Moran, J. *Synlett* **2016**, *27*, 2637–2643.

(79) Adamczyk-Woźniak, A.; Jakubczyk, M.; Sporzyński, A.; Żukowska, G. *Inorg. Chem. Commun.* **2011**, *14*, 1753–1755.

(80) Pérez, M.; Qu, Z. W.; Caputo, C. B.; Podgorny, V.; Hounjet, L. J.; Hansen, A.; Dobrovetsky, R.; Grimme, S.; Stephan, D. W. *Chem. - A Eur. J.* **2015**, *21*, 6491–6500.

(81) Cummings, S. A.; Iimura, M.; Harlan, C. J.; Kwaan, R. J.; Trieu, I. V.; Norton, J. R.; Bridgewater, B. M.; Jäkle, F.; Sundararaman, A.; Tilset, M. *Organometallics* **2006**, *25*, 1565–1568.

(82) Peruzzi, M. T.; Mei, Q. Q.; Lee, S. J.; Gagné, M. R. *Chem. Commun.* **2018**, *54*, 5855–5858.